A study on the effect of lateral interactions on methanation over Fe(100)

THESIS

Presented for the degree of

Doctor of Philosophy at the

University of Cape Town

By

Robin Kyle Abrahams

Centre for Catalysis Research

Department of Chemical Engineering University of Cape Town Private Bag
Rondebosch, 7701 South Africa

Robin Kyle Abrahams

A study on the effect of lateral interactions on methanation over Fe(100)

Keywords:

Fischer-Tropsch / Iron / Adsorption / Syngas /

Lateral Interaction / Methanation / Microkinetic

The work described in this thesis has been carried out at the Catalysis Research Unit, Department of Chemical Engineering, University of Cape Town, South Africa. This work is part of the Fe focus area of the 'Fischer-Tropsch molecular modelling' research project, which is financially supported by SASOL and NRF.

This document was compiled on March 29, 2017

Synopsis

In this thesis, the lateral interactions involved in conversion of synthesis gas, a mixture of H_2 and CO, to methane over Fe(100) and the effect they have on the kinetics of the process is explored. Understanding the methanation of syngas allows for a better understanding of the initial stages of Fischer-Tropsch synthesis.

Density functional theory was used to calculate the energies and properties of simple methanation adsorbates on an Fe(100) surface. All of the parameters were tested and optimized in order to find a balance between efficiency and accuracy. A number of configurations were calculated to investigate nearest neighbour and next nearest neighbour interactions. An energetic break down of the lateral interactions is postulated using the components of the Hamiltonian. The charges associated with the different atoms in each configuration were identified using the Mulliken population analysis and the Bader population analysis. These gave insights into configurations which displayed large electrostatic lateral interactions.

Lateral interactions were investigated using larger unit cells than typically utilized in molecular modelling up to now (viz. p(4x4) and p(3x2) unit cells) to enable the estimation of nearest neighbour and next nearest neighbour interactions. When using larger p(4x4) unit cells for CO adsorption on Fe(100), the results showed that the heat of adsorption can differ by as much as 0.24 eV at 0.25 ML. It was concluded that lateral interactions are a function of local coverage (i.e. number of nearest and next nearest neighbours) and not necessarily global coverage. Nearest neighbour interactions are typically repulsive and much larger than next nearest neighbour interactions, which varied between repulsive and attractive interactions. While this is not a unique conclusion it did allow for the creation lateral interaction matrices that vary with temperature.

The study has shown that lateral interactions can be broken down into kinetic and potential energy and an inverse relationship exists between these component energies. If this relationship is truly understood, then the total energy can be calculated knowing either kinetic or potential energy instead of both. This would then give additional value to well explored electrostatic interaction models.

The lateral interactions were empirically related to nearest neighbour and next nearest neighbour interactions. Two kinetic studies were investigated in this thesis and in both cases, mean field approximations and quasi chemical approximation (QCA) were used and compared to incorporate lateral interactions into the kinetics. The mean field approximation over estimates the lateral interactions and considers global coverage while the QCA approximation considers probability of local combinations.

The first kinetic study was a simulated CO TPD experiment on Fe(100). The mean field approximation was an improvement on systems which considered no lateral interactions but did not describe all the aspects observed in the experimental TPD. The prediction by the quasi-chemical approximation shows good agreement for the desorption of associatively bound CO. The deviation observed for the dissociatively adsorbed CO is attributed to the presence of alternative pathways for the adsorbed species (specifically the diffusion of oxygen into the lattice of the solid).

A microkinetic model for the methanation of syngas over Fe(100) was also created. The results showed that different methods of lateral interaction incorporation resulted in significantly different coverage profiles and reaction energy profiles. Both methods showed a build-up of oxygen on the surface towards the end of the simulation. The build-up of oxygen on the surface of Fe(100) may indicate that iron-based catalysts need to undergo phase changes to complete the catalytic cycle.

Contents

List of Figures

1 Introduction

Heterogeneous catalysis has become essential to chemical industries, as at present, the production of many product compounds involves one or more catalytic processes. There are both homogeneous and heterogeneous systems of catalysis, the focus of this thesis will be on heterogeneous catalysis. In heterogeneous catalysis, the catalytic reaction takes place on active sites at the surface of a solid. To date the kinetics of heterogeneously catalysed reactions is typically based on the adsorption isotherm proposed by Langmuir and the kinetic formalism of Hinshelwood [1]. The Langmuir-Hinshelwood approach is postulates ideal surfaces and assumes that the adsorption sites are energetically equivalent, and that adsorbates are randomly mixed and have no interactions with each other.

Developments in catalysis analyse the validity of these assumptions and refine the kinetics accordingly. Examples of these refinements include the adsorption isotherms proposed by Temkin, which portrays a linear decline of the heat of adsorption with coverage, and Freundlich, which portrays an exponential decline of the heat of adsorption with coverage [2]. These adaptations to the Langmuir isotherm pertain to adsorption sites which are energetically different and/or interactions between adsorbates particularly at higher coverages.

The effectiveness of a catalyst is given by the extent to which it accelerates the rate of formation of the desired product compounds. Evaluating the effectiveness of a catalyst relies on our understanding of the kinetics and mechanisms involved in a catalytic process.

The advancements in the field of computational chemistry allow us to evaluate the mechanistic steps of a processes at a microscopic level. We can evaluate the energy, geometry and vibrations of a system with a high degree of accuracy. Furthermore, kinetic steps that occur within a fraction of a second can be reconstructed and understood in their entirety.

The current computational chemistry software allows for a considerable amount of repeatability and a significant number of configurations can be tested. The *theoretical approach* has led to finding novel catalysts [3,4] and should be used as a tool in conjunction with experimental work.

Once the energetics of a system is known, the kinetics can theoretically be determined and modelled using either a stochastic method, like Monte-Carlo simulations [5,6], or from a deterministic method, like a Mean-Field approximation [1,7,8]. The latter is computationally less demanding [8] and should converge to the results obtained in a Monte-Carlo type of method if all interactions are captured correctly. Focusing on heterogeneously catalysed systems, the so-called lateral interactions between adsorbed species [9] are of particular importance.

1.1 Lateral interactions

Studies on Lateral interactions, both experimental [10,11] and theoretical [12–15], are numerous for the adsorption of CO on metal surfaces, for ammonia synthesis [16,17,8] and for O adsorption on Pt (111) [18,19]. Lateral interactions can be classified as through-surface or through-space interactions.

Through-space interactions are typically "long" range interactions such electrostatics/van der Waals interactions [20–22]. If the chemisorption involves a charge transfer, dipole moments are created on the surface and these can be modelled using the classical physics dipole-dipole interactions. For large dipole moments the interactions are measurable over a distance as large as 32 Å [23].

Through-surface interactions are seen as changes in adsorption and reaction energy as a result of the electronic interactions through the substrate surface due to co-adsorption of adsorbates. The chemisorption of an adsorbate involves the overlapping of adsorbate and substrate orbitals. The occupancy of the substrates orbitals is thus altered, altering the overlapping with other adsorbates. This interaction is dependent on the number of surface atoms shared amongst adsorbates. Chemisorbed adsorbates which are close enough for orbitals to overlap show strong interactions

[9,21]. As the lateral distance between these adsorbates increases the interactions energy decreases exponentially [22].[1]

Typical through-surface interaction models such as the bond order conservation and other nearest neighbour models are independent of the adsorbates involved i.e. H-H though surface interactions and CO-CO though surface interactions are equivalent. This is obviously an oversimplification as it is well documented that changes in heats of adsorption for H and CO are significantly different. For example, on the Fe (100) surface, H has a saturation coverage of 1 ML and CO has a saturation coverage of approximately 0.65 ML at Fischer-Tropsch conditions [12,24–26]. These saturation coverages being a result of lateral interactions.

Even though the refinements by Temkin and Freundlich are an improvement on the Langmuir isotherm, experimental results show that adsorption isotherms are more complex. Figure 1-1 below shows the change in heat of adsorption of CO with respect to coverage on the Fe (211) surface at 300 K [11]. At lower coverages, less than 0.25 ML, the adsorbates are considered to be spaced far apart. Hence, the main lateral interactions involved in this regime are through-space interactions. As coverage increases, adsorbates are thought to be spaced more closely and through-surface interactions come into play. Thus, the extent of lateral interactions increases with coverage. This can be seen by the changes in heat of adsorption of CO [10,27] and NO [28] with respect to coverage.

Even though classifications have been made for lateral interactions, very little is written about the explicit energetic contributions made by each type of lateral interactions i.e. how much of the interaction is contributed to electrostatics, orbital overlap, etc. The general trend in literature is to calculate the overall changes in activation energy or heat of adsorption due to lateral interactions and postulate reasons for these changes [11,17,28–30,8].

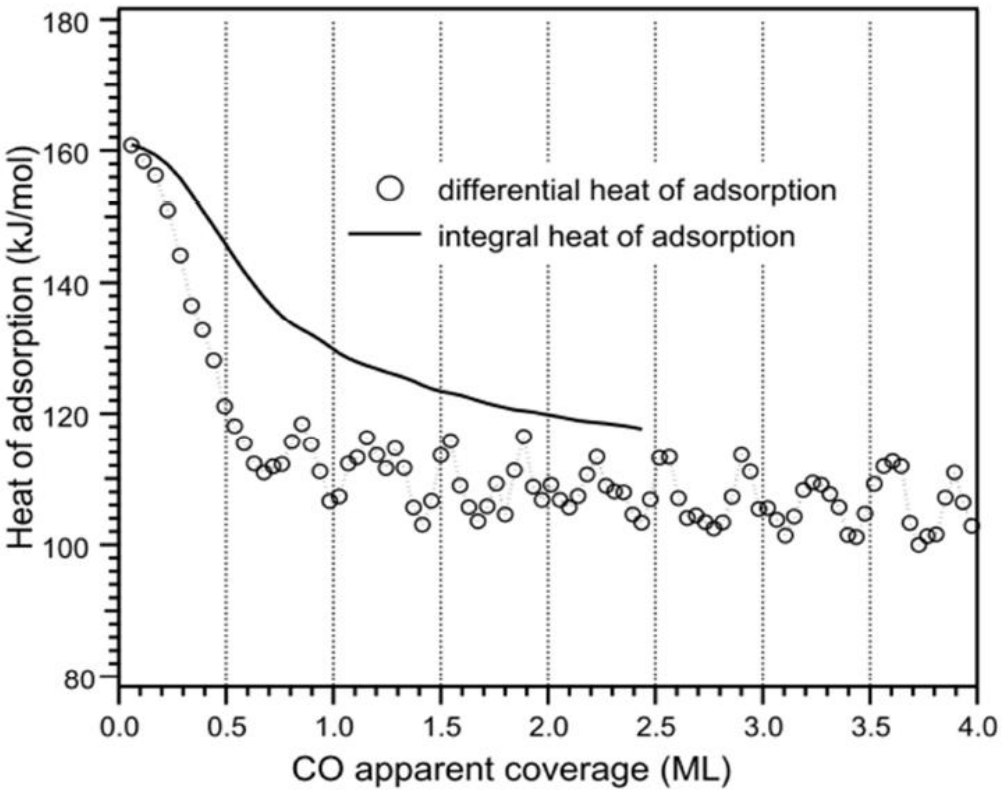

Figure 1-1: Experimental data showing the dependence of the heat of adsorption of CO on the Fe (211) surface at 300K [10]

[1] This particularly true for metal surfaces. Oxide surfaces can have long range surface mediated interactions

A vast collection of data on lateral interactions exists in literature. For instance, for the ammonia synthesis, the overall lateral interactions between N, H, NH_x (x=1-3) are well defined [17,8]. Table 1-1 below summaries adsorbate-adsorbate interactions for ammonia synthesis on the stepped Ru (1011) surface. For most cases, the lateral interactions are repulsive (positive energies) but certain cases do exist where the interactions are attractive (negative energies). Looking at the N-N interaction on the upper step, the interactions are largely repulsive and it is thought that this is due to the through-surface interactions which exist due to shared ruthenium atoms. The NH_3-NH_3 interaction on the lower step is also largely repulsive and it is thought that this is due to the repulsions of the large dipole moments created for the adsorbed NH_3. The N-NH_3 interaction on the upper step is attractive due to the favourable interaction between the dipole moment created by the NH_3 adsorbate and the N adsorbate.

As mentioned before, the extent of lateral interaction increases for higher coverage. However, it is important to note that for low coverage, lateral interactions cannot be neglected since adsorbates with strong dipole moments can exhibit interactions over large ranges and some systems display formations of islands i.e. local coverage might be significantly higher.

Experimental and theoretical results show that for certain cases, island formation exists [31,11,28,29,32,33]. Island formation may occur when the lateral interactions between adsorbates are attractive.

Table 1-1: Lateral interactions for ammonia synthesis. US and LS are abbreviations for upper step and lower step respectively. Energies are given in eV. A positive energy represents a repulsive interaction while and negative energy represents an attractive interaction [8]

US_{H-H} $E_{int}=0.024$	US_{H-N} $E_{int}=0.13$	US_{H-NH} $E_{int}=0.075$	US_{H-NH_2} $E_{int}=-0.05$	US_{H-NH_3} $E_{int}=0.0$
US_{N-N} $E_{int}=0.38$	US_{N-NH} $E_{int}=0.24$	US_{N-NH_2} $E_{int}=0.12$	US_{N-NH_3} $E_{int}=-0.16$	US_{NH-NH} $E_{int}=0.21$
US_{NH-NH_2} $E_{int}=0.25$	US_{NH-NH_3} $E_{int}=0.18$	$US_{NH_2-NH_2}$ $E_{int}=0.43$	$US_{NH_2-NH_3}$ $E_{int}=0.30$	$US_{NH_2-NH_3}$ $E_{int}=0.16$
LS_{H-H} $E_{int}=0.06$	LS_{H-N} $E_{int}=0.16$	LS_{H-NH} $E_{int}=0.14$	LS_{H-NH_2} $E_{int}=0.05$	LS_{H-NH_3} $E_{int}=0.12$
LS_{N-N} $E_{int}=0.35$	LS_{N-NH} $E_{int}=0.27$	LS_{N-NH_2} $E_{int}=0.21$	LS_{N-NH_3} $E_{int}=-0.02$	LS_{NH-NH} $E_{int}=0.27$
LS_{NH-NH_2} $E_{int}=0.29$	LS_{NH-NH_3} $E_{int}=0.08$	$LS_{NH_2-NH_2}$ $E_{int}=0.30$	$LS_{NH_2-NH_3}$ $E_{int}=0.30$	$LS_{NH_3-NH_3}$ $E_{int}=0.59$

Trost et al. [29] showed experimental and theoretical evidence of oxygen island formation on Ru (0001). The same study shows the absence of nitrogen island formation on Ru (0001) due to strong repulsive interactions between adsorbates.

Lateral interactions can also reveal information about catalyst deactivation. Swart et al. [33] showed that lateral interactions played a role in the type of coking precursors in cobalt. The study revealed that since repulsive interactions between individually adsorbed carbon atoms exist, structures with C-C bonds and carbon clusters are more stable particularly at high coverage. Hence, it was concluded that atomic carbon can be considered an unlikely coking precursor.

While majority of the work on lateral interactions is theoretical, experimentally obtained results have also been used to approximate lateral interactions. For example, van Bavel et al. [11] showed that by comparing the TPD spectra of CO desorbing from clean Rh (100) and CO desorbing from a nitrogen pre-covered surface, a repulsive lateral interaction between N and CO was found to be 20 kJ/mol.

1.1.1 Modelling Lateral interactions

There have been models that try to predict and extrapolate the effects of these lateral interactions. Lateral interactions can be modelled by either using fixed energies to approximate the interactions between species or by directly modelling the different components the lateral interactions are comprised of [23,34]. The former is the more popular and simpler of the two approaches. The study shown above by Hellman [8], used fixed 1-2 interactions to create a microkinetic model for ammonia synthesis. Implementing 1-2 (pairwise) interactions and 1-2-3 interactions has produced favourable approximations. These pairwise interactions are also easy to implement into a microkinetic model, an additional advantage.

Kokalj [23] used a polarized point-dipole model to predict the adsorption of highly polarized adsorbates, triazole and benzotriazole. Maschhoff and Cowin [34] created a dipole-dipole interaction model and showed how the dipole interaction energy alone could influence the total interaction energy. While there is no doubt that electrostatics contribute significantly to the lateral interactions, it is still unclear as to whether an electrostatic model alone is sufficient to accurately describe lateral interactions. An attempt will be made to quantify the different component energies to the lateral interactions

1.2 Methanation of syngas

While converting syngas into methane may not be a desired catalytic process itself, understanding the methanation of syngas is beneficial for understanding Fischer-Tropsch synthesis. CO and hydrogen adsorption, CO dissociation and formulation and interaction of CH_x species are all events that are identical in both processes. The first step, the adsorption of CO on the surface, has been a field of much interest. A great deal of experimental [35–39] and theoretical [14,24,22,40] work has contributed to the understanding of CO adsorption and behaviour on the surface.

1.2.1 CO on Fe (100)

The adsorption and dissociation of CO is a crucial step in the Fischer-Tropsch process [12,41,42]. This reaction is industrially either catalysed using iron or cobalt-based catalysts. Metallic iron is a simple model system used to investigate the reaction pathway for the Fischer-Tropsch synthesis [24,40,43] and can still provide insight into the fundamentals of Fischer-Tropsch synthesis. The lower miller index structures of iron metal surfaces have been extensively studied [44,24,15,25,45]. On the Fe (111) surface, CO adsorption is studied up to a coverage of 2 ML [44]. At lower coverages (< 0.5 ML) the most stable configuration of CO is the adsorption in the shallow-hollow site with the C-O bond normal to the surface. Above a coverage of 1 ML, the energetically most stable configuration of CO is on the on-top site with the C-O bond slightly tilted from the surface normal at an angle of 10°. It has been shown both experimentally and theoretically to bind strongly on the Fe (110) surface and is most stable on the on-top site with the C-O bond normal to the surface. This is shown both experimentally and theoretically [25],[46]. On the Fe (100) surface, CO can adsorb in either the four-fold hollow site, bridge site or the on-top site. The C-O bond can either be normal to the surface or tilted away from the normal. It is seen both experimentally and theoretically that CO absorbed in the hollow site and tilted 45±10° away from the normal is the most stable configuration [12,15,22,24,45]. On all the lower

miller index surfaces the heat of adsorption decreases with increasing coverage [12,15,22,24,25,44–46]. This decrease in heat of adsorption can be attributed to the lateral interactions between the adsorbed molecules on the surface.

1.2.2 Other methanation species on the surface

Several studies reported on the stability of CH_x species adsorbed on Fe (100) [24,27,31,47,48,15,49], Fe (110) [50–52] and several Fe_5C_2 Hagg iron carbide surfaces[53–55]. The studies on Fe (100) imply that the four-fold hollow site is the stable adsorption site for C, CH and CH_2, while the CH_3 species is stable on the two-fold bridge site. CH_4 only displays weak physisorption. On an active catalyst, all these species may co-exist, some in higher concentrations than others. In order to truly understand the energetics of a catalytic system, the lateral interactions of all species involved need to be considered.

The inter-species lateral interactions can be used to explain the change in the heat of adsorption/binding energy with change in coverage i.e. *"Coverage Effects"*. Numerous studies have documented the change in energy with the change in coverage for single species [22,24,37,56], but few have considered intra-species interactions.

Sorescu [48] looked at the effects of co-adsorption on C with H, O, CH_x (x = 1-4) and CO. Only next nearest neighbour interactions on a c(2x2) cell were considered. For all the species considered (except for CH_3), a stabilization was observed. Sorescu believed that this was possibly due to the local surface environment being expanded, this stemming from another study of his [15] which shows that the binding energy of CO increases with lattice expansion.

For the methanation of syngas, a wide variety of intra- species lateral interactions will be seen and the effects that these interactions will have on the kinetics of the process will be investigated.

1.3 Aim of this study

The study will explore the lateral interactions of the methanation system in detail. While the existence and classifications of lateral interactions are well documented, a detailed understanding of what it comprises is still lacking. In this thesis two cases will be investigated in an attempt to achieve a better understanding of lateral interactions.

The first case will be a theoretical TPD model of CO on Fe (100). The general objectives of this study are:

- To study the adsorption of CO on Fe (100) and to quantify the interactions of between CO adsorbates on the surface
- To breakdown the interaction energies into its different component energies
- Create a microkinetic model of CO TPD and determine what is the most effective method of incorporating lateral interactions into the model

The second case is a theoretical study of syngas methanation on Fe (100). The general objectives of this study are:

- To study the methanation of syngas on Fe (100) and to quantify the interactions of between CO adsorbates on the surface
- To break down the interaction energies into its different component energies
- Create a microkinetic model of the methanation of syngas and determine what is the most effective method of incorporating lateral interactions into the model

In both studies, two key questions are asked:

Can a breakdown of interaction energy develop the understanding of lateral interactions?

What is the most effective and efficient method of incorporating lateral interactions into a microkinetic model?

1.4 References

[1] Chorkendroff, I., Niemantsverdriet, J.W., *Concepts of modern catalysis and kinetics*, vol. 2, Wiley-VCH, **2007**.

[2] Boudart, M., Djega-Mariadassou, G., *Kinetics of heterogeneous catalytic reactions*, Princeton University Press, Princeton **1984**.

[3] Nørskov, J.K., *Prog. Surf. Sci.* **1991**, 38, 103–144.

[4] Hammer, B., Nørskov, J.K., in:, *Adv. Catal.*, vol. 45, **2000**, pp. 71–129.

[5] Kang, H.C., Weinberg, W.H., *Chem. Rev.* **1995**, 95, 667–676.

[6] Zhdanov, V.P., *Surf. Sci. Rep.* **2002**, 45, 231–326.

[7] van Santen, R.A., Niemantsverdriet, J.W., *Chemical kinetics and catalysis*, Plenum Press, New York and London **1995**.

[8] Hellman, A., Honkala, K., *J. Chem. Phys.* **2007**, 127, 194704: 1-6.

[9] Einstein, T.L., *Handb. Surf. Sci.* **2005**, 4111, 1-43.

[10] Borthwick, D., Fiorin, V., Jenkins, S.J., King, D. a., *Surf. Sci.* **2008**, 602, 2325–2332.

[11] van Bavel, A.P., Hermse, C.G.M., Hopstaken, M.J.P., Jansen, A.P.J., Lukkien, J.J., Hilbers, P.A.J., Niemantsverdriet, J.W., *Phys. Chem. Chem. Phys.* **2004**, 6, 1830-1835.

[12] van Helden, P., van Steen, E., *J. Phys. Chem. C* **2008**, 112, 16505–16513.

[13] Ma, Z.-Y., Huo, C.-F., Liao, X.-Y., Li, Y.-W., Wang, J., Jiao, H., *J. Phys. Chem. C* **2007**, 111, 4305–4314.

[14] Cao, D., Zhang, F., Li, Y., Jiao, H., *J. Phys. Chem. B* **2004**, 108, 9094–9104.

[15] Sorescu, D., Thompson, D., Hurley, M., Chabalowski, C., *Phys. Rev. B* **2002**, 66, 35416, 1-13.

[16] Honkala, K., Hellman, A., Remediakis, I.N., Logadottir, A., Carlsson, A., Dahl, S., Christensen, C.H., Nørskov, J.K., *Science* **2005**, 307, 555–558.

[17] Mhadeshwar, A.B., Kitchin, J.R., Barteau, M.A., Vlachos, D.G., *Catal. Letters* **2004**, 96, 13–22.

[18] Tang, H., Van der Ven, A., Trout, B., *Phys. Rev. B* **2004**, 70, 45420.

[19] Tang, H., Van Der Ven, A., Trout, B.L., *Mol. Phys.* **2004**, 102, 273–279.

[20] Neurock, M., An Ab Initio Approach towards Engineering Fischer-Tropsch Surface Chemistry. University of Viginia, **2006**.

[21] Plata, J.J., Collico, V., Márquez, A.M., Sanz, J.F., *Theor. Chem. Acc.* **2012**, 132, 1311, 1-7.

[22] Zeinalipour-Yazdi, C.D., van Santen, R. a., *J. Phys. Chem. C* **2012**, 116, 8721–8730.

[23] Kokalj, A., *Phys. Rev. B* **2011**, 84, 45418, 1-17.

[24] Bromfield, T.C., Ferré, D.C., Niemantsverdriet, J.W., *Chemphyschem* **2005**, 6, 254–260.

[25] Jiang, D.E., Carter, E. a., *Surf. Sci.* **2004**, 570, 167–177.

[26] van Steen, E., van Helden, P., *J. Phys. Chem. C* **2010**, 114, 5932–5940.

[27] Van Helden, P., Initial Steps of the Fischer-Tropsch Synthesis on Fe(100): The Role of Hydrogen. University of Cape Town, **2010**.

[28] Yeo, Y.Y., Vattuone, L., King, D.A., *J. Chem. Phys.* **1996**, 104, 3810-3821.

[29] Trost, J., Zambelli, T., Wintterlin, J., Ertl, G., *Phys. Rev. B* **1996**, 54, 17850–17857.

[30] Chen, J., Liu, Z.-P., *J. Am. Chem. Soc.* **2008**, 130, 7929–7937.

[31] Lo, J.M.H., Ziegler, T., *J. Phys. Chem. C* **2007**, 111, 11012–11025.

[32] Rodriguez, J.A., Goodman, D.W., *J. Phys. Chem.* **1991**, 95, 4196–4206.

[33] Swart, J.C.W., Ciobîcă, I.M., van Santen, R.A., van Steen, E., *J. Phys. Chem. C* **2008**, 112, 12899–12904.

[34] Maschhoff, B.L., Cowin, J.P., *J. Chem. Phys.* **1994**, 101, 8138–8151.

[35] Blyholder, G., *J. Phys. Chem.* **1964**, 68, 2772–2777.

[36] Hoffmann, R., *Angew. Chemie Int. Ed. English* **1987**, 26, 846–878.

[37] Moon, D.W., Dwyer, D.J., Bernasek, S.L., *Surf. Sci.* **1985**, 163, 215–229.

[38] Sung, S.S., Hoffmann, R., *J. Am. Chem. Soc.* **1985**, 107, 578–584.

[39] van Daelen, M.A., Neurock, M., van Santen, R.A., *Surf. Sci.* **1998**, 417, 247–260.

[40] Curulla-Ferré, D., Govender, A., Bromfield, T.C., Niemantsverdriet, J.W.H., *J. Phys. Chem. B* **2006**, 110, 13897–904.

[41] Van Santen, R.A., De Koster, A., Koerts, T., *Catal. Letters* **1990**, 7, 1–14.

[42] van der Laan, G.P., Beenackers, A.A.C.M., *Catal. Rev.* **1999**, 41, 255–318.

[43] Govender, A., Ferré, D.C., Niemantsverdriet, J.W., *Chemphyschem* **2012**, 13, 1583–90.

[44] Chen, Y., Cao, D., Jun, Y., Li, Y., Wang, J., Jiao, H., *Chem. Phys. Lett.* **2004**, 400, 35–41.

[45] Nayak, S.K., Nooijen, M., Bernasek, S.L., Blaha, P., *J. Phys. Chem. B* **2001**, 105, 164–172.

[46] Stibor, A., Kresse, G., Eichler, A., Hafner, J., *Surf. Sci.* **2002**, 507–510, 99–102.

[47] Govender, A., Ferré, D.C., Niemantsverdriet, J.W.H., *NaCatSoc. Extr.* **2009**.

[48] Sorescu, D., *Phys. Rev. B* **2006**, 73, 155420.

[49] Jiang, D., Carter, E., *Phys. Rev. B* **2005**, 71, 45402.

[50] Mavrikakis, M., Gokhale, A.A., *Am. Chem. Soc.* **2005**, 229, 861–865.

[51] Erley, W., McBreen, P.H., Ibach, H., *J. Catal.* **1983**, 84, 229–234.

[52] McBreen, P.H., Erley, W., Ibach, H., *Surf. Sci.* **1984**, 148, 292–310.

[53] Zhao, S., Liu, X.-W., Huo, C.-F., Li, Y.-W., Wang, J., Jiao, H., *J. Catal.* **2012**, 294, 47–53.

[54] Cao, D.-B., Li, Y.-W., Wang, J., Jiao, H., *J. Mol. Catal. A Chem.* **2011**, 346, 55–69.

[55] Gracia, J.M., Prinsloo, F.F., Niemantsverdriet, J.W., *Catal. Letters* **2009**, 133, 257–261.

[56] Sorescu, D.C., *Catal. Today* **2005**, 105, 44–65.

2 Model background and validation

Computational chemists and physicists today are capable of calculating a large number of systems at faster speeds with a high degree of accuracy. Computational methods are used to compliment and understand experimental observations. As versatile as quantum mechanics is, we are still limited by the uncertainty principle. The expectation value of quantum mechanical observables can however be described with any desired accuracy. Furthermore, complex many body systems are best handled with numerical methods and thus another limit is the computational power and efficiency. This is a field that is experiencing significant developments and the rate at which processors can calculate is growing exponentially also known as Koomey's law, as shown in Figure 2-1.

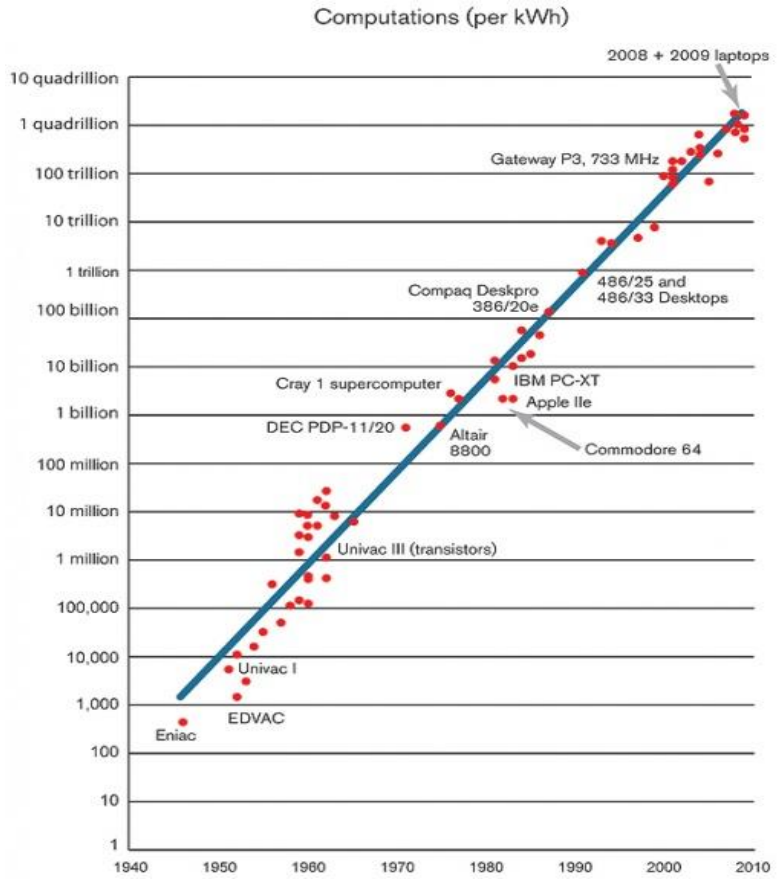

Figure 2-1: Koomey's law, the number of calculations per joule of energy dissipated doubles approximately every 1.57 years. [1]

The methods used by computational scientists are encoded in relatively easily available programs; for DFT calculations these include CASTEP [2,3], DMol3 [4], Siesta [5], VASP [6] and Quantum Espresso [7] as well as modelling suites such as Materials Studio software package [8], which have allowed the scientific community to generate computational chemistry results with ease and accuracy.

2.1 Computational chemistry

The methods for computational chemistry are normally divided into two categories, molecular mechanics and quantum mechanics or *ab initio* (from first-principle).

The molecular mechanics or force fields approaches traditionally use parameters which are based on empirical observations[2]. Classical mechanics are used to model molecular systems with bonds being considered as springs. This method is typically used to model systems with a large number of atoms, like biological systems, which are less amenable to quantum-mechanical methods due to the size of the system.

Ab initio methods use quantum mechanics to solve many body systems with nuclei and electrons. This is done by solving the Schrödinger equation. To quote Dronskowski [9]: *"All available experimental (and theoretical) knowledge is in agreement that any given system composed of nuclei and electrons, i.e. atoms, molecules and infinite molecules (crystals), can be described in its entirety by solving the fundamental QM equation of Schrödinger"*.

The time-independent form of the Schrödinger equation is given by:

$$\hat{H}\varphi = E\varphi \qquad (2.1)$$

With $\hat{H}$,the Hamiltonian given by:

$$\hat{H} = \frac{-\hbar}{2m}\nabla^2 + V \qquad (2.2)$$

Here, φ is the wave function, E is the energy of the system, m is the mass of the system, $\hbar$ is Planck's constant divided by 2π, ∇^2 is the Laplace operator and V is the potential. For chemical systems the Schrödinger equation can only be solved explicitly for systems containing one electron (e.g. a hydrogen atom) [10,11]. The solution of systems with more than one electron requires some approximations to simplify the calculations.

The first is the Born-Oppenheimer approximation [12]. Here it is assumed that the wave function of the electrons and the nuclei are independent. This approximation can be made since the movement of the nuclei relative to the electrons is negligible. This means that solving the Schrödinger equation only requires solving the electronic wave function.

The second approximation needs to account for electron-electron interactions in many electron systems. This is achieved with the self-consistent field (SCF) method [9].

2.1.1 Development of *ab initio* computational chemistry

In 1927 English mathematician and physicist Douglas Hartree developed the SCF method which approximates wave functions and energies of atoms and ions [9,13]. In the same year German physicists Walter Heitler and Fritz London used quantum mechanics and the SCF method to describe bonding properties of a H_2 molecule [14]. This was the first time the Schrödinger equation was used to describe the covalent bond of a molecule.

Hartree wanted to do away with empirical approximations and solve the time independent Schrödinger equations. In 1928 he proposed a solution to this in the Hartree-Method [13,15,16]. Two years later both Soviet physicist Vladimir Fock [17] and American physicist John Slater [18] pointed out that the Hartree method did not account of the exchange symmetry of the wave function. Several improvements have been proposed on HF theory. One of the first was the Møller-Plesset perturbation theory in 1934 [9]. Danish chemist Christian Møller and American physicist Milton Plesset improved on HF theory by accounting for electron correlation [19]. In the same year German physicist Hans Hellmann introduced the idea of using pseudopotentials to simplify solving the Schrödinger equation [20].

In 1950 British chemist Samuel Boys showed that by using Gaussian Basis Sets the accuracy of solving many body problems can be significantly improved [21]. One year later Dutch physicist Clemens

[2] Some potentials do exist which are parameterized from first principle results

Roothaan [22] and Irish mathematician George Hall [23] utilized the Gaussian Basis sets in Hartree-Fock theory in what is known as Roothaan-Hall theory.

What followed next was one of the most successful developments in computational chemistry, the birth of density functional theory. In 1964 French-American theoretical physicist Pierre Hohenberg and American theoretical physicist Walter Kohn showed that a one-to-one mapping exists between the ground state wave function of a many-particle system and the ground state electron density [24]. They showed that an energy functional of a system can be written as:

$$E(\rho) = \int V(r) \cdot \rho(r)\, dr + F(\rho) \tag{2.3}$$

where

$$F(\rho) = T(\rho) + W_{CL}(\rho) + W_{NCL}(\rho) \tag{2.4}$$

Here ρ is the electron density, T is the kinetic energy, V is the nucleus-electron potential, W_{CL} is the Coulombic electron-electron potential, W_{NCL} is the non-Coulombic electron-electron potential. When the energy functional

$$E(\rho) = \int V(r) \cdot \rho(r)\, dr + F(\rho) \tag{2.3}$$

is minimized, the exact ground state energy and electron density is given. This expression significantly reduces the degrees of freedom of a system. For HF and post HF calculations, a system of N electrons requires a wave function of 4N degrees of freedom. Simplifying to electron density reduces the degrees of freedom to 3. A problem arose however with respect to what exactly are the expressions for T and W. A year later, Kohn with the help of Chinese physicist Lu Jeu Sham showed that if a reference system, with the same number of electrons, was to interact with the external potential (V) it would produce the same electron density as that of the real system [25]. The reference system has the special property that the electrons interact only with the nucleus and not each other. The energy functional can then be written as:

$$E(\rho) = \iint \frac{\rho(r')\rho(r)}{2|r' - r|} dr' dr + \int V(r) \cdot \rho(r)\, dr + T_0(\rho) + E_{XC}(\rho) \tag{2.5}$$

Here T_0 is the kinetic energy of the reference system and E_{XC} is a combination of the exchange energy, correlation energy and the change in kinetic energy between the reference and real systems. It is important to note that the exact expression for E_{XC} is unknown [9]. Thus, the accuracy with which the energy functional can be minimized is dependent on the accuracy of the term E_{XC}.

2.1.2 Exchange-Correlation potential

Over the past 50 years, the greatest challenge of implementing DFT is finding a suitable exchange-correlation potential. The exchange-correlation potential includes the effects of the Pauli Principle and long range dipole interactions. The first attempt at approximating the exchange-correlation potential was the local density approximation (LDA). Here, the potential at a specific point is modelled as a homogeneous free electron gas [9]. The potential is then:

$$E_{XC}^{LDA}(\rho) = \int dr \rho(r) \mu_{XC}(\rho) \tag{2.6}$$

Here μ_{XC} is the exchange-correlation potential and is a functional of the density. Examples of DFT calculations using the LDA approximation can produce satisfactory geometries, charge densities and vibrational frequencies but over-estimates for binding energies [9,26]. While other calculations using

the LDA approximation produce rather poor approximations for magnetic moments [27,28] and can even give completely erroneous molecular structures [29].

An improvement on the LDA approximation is the generalized gradient approximation (GGA). Here the exchange-correlation potential is both a functional of the electron density and the gradient of the electron density. The potential is then written as:

$$E_{XC}^{GGA}(\rho) = \int dr\rho(r)\mu_{XC}(\rho, \nabla\rho) \tag{2.7}$$

Here, ∇ρ is the gradient of the electron density. This addition improves the exchange-correlation energy particularly at regions of low density. DFT calculations which utilize the GGA approximation typically give better results for geometries, charge densities, vibrational frequencies and binding energies when compared to LDA calculations [26,30]. However, GGA calculations a computationally more demanding than LDA calculations. The popular GGA functional include Perdew-Wang 91 (PW91) Burke-Enzerhof (PBE) and revised Perdew-Burke-Enzerhof (rPBE) [29,31] and Wu-Cohen (WC) [32] .

Even though the GGA approximations significantly improve DFT calculations, there are still some shortcomings. These include a poor estimation of van der Waals interactions [33] and a poor estimation of band gap [34,35]. To improve on these short comings, Hybrid GGA [36,37], here the Fock-potential is used to describe the exchange-correlation, and Meta GGA [30], the potential is a functional of higher order derivatives of the electron density as well and the kinetic energy density, approximations are made. These improvements are much more computationally demanding.

2.1.3 Periodicity

Periodic models are used to model crystals and/or catalytic surface systems. In these periodic systems, a unit cell is repeated infinitely in some or all three special dimensions. The wave-functions for these systems are generated with Blöch's theorem [38] in mind. In Blöch's theorem electronic wave-functions in a periodic cell are generated as discrete plane-wave basis sets. The periodicity is exploited and instead of generating an infinite number of electron wave-functions only the wave functions for the electrons in the unit cell are required. Crystalline wave-functions are the linear combinations of the electron wave-functions and these expansions can be reduced to plane waves. The expansions can be written as:

$$\varphi_{n,k} = \sum_{g} e^{i(k+g)r} u_{n,g,k} \tag{2.8}$$

Here $e^{i(k+g)r}$ is the modulating function and $u_{n,g,k}$ is the periodic function. For large kinetic energies, this expansion tends to zero. For small kinetic energies, however, the basis set needs to be truncated at a specified cut off energy. The expansion takes place in reciprocal space and is different for every k-point (the boundaries of the first Brillouin zone).

For systems which have a large number of core electrons, a large number of plane-waves is required and would in turn increase the computational cost. To simplify the plane-wave problem, pseudopotentials are used. Core electrons are not involved in chemical bonding and thus these electrons can be fixed [20,39,40]. This reduces the number of plane waves required and simplifies the simulation. The pseudopotential needs to be created in such a way that the charge density of the real system and pseudo system are the same, at least usually up to a cut-off radius. The "softness" of a pseudopotential is related to the number of basis sets required, i.e. the fewer basis sets, the "softer" the pseudo potential.

If the norm of the pseudo potential and the real system are the same (up to the cut off radius), the pseudo potential is said to be norm conserving [41–44]. Even with the incorporation of pseudopotentials, first row transition metals still require a large number of basis sets. The number of basis sets can be further reduced if the condition of norm conservation is relaxed potentials which

relax the condition of norm conservation are called “Ultra Soft”. These ultra-soft pseudo potentials do no compromise the accuracy of the model [45].

2.2 Fe model

The DFT calculations in this study were completed using the Cambridge Sequential Total Energy Package (CASTEP) [3], as implemented in the Materials Studio software package [8]. The program uses the SCF approach to solve the Kohn-Sham equations for periodic systems. The ion-electron interactions are described with pseudopotential approximations using plane wave basis sets. The exchange-correlation energy was calculated using the generalized gradient approximation (GGA). Gaussian smearing was used for the electron distribution at the Fermi level sampling of the k-space was generated using the Monkhorst-Pack procedure [46].

In order generate results from a Fe (100) surface model, the validity of the model is first scrutinized.

2.2.1 Bulk iron model verification

A first step in ensuring the validity of results in a computational chemistry study is to compare experimentally observed properties of the bulk material with the theoretical equivalents. Ideally we would like to use parameters that give the most accurate representations, but the computational cost is strongly dependent on how fine the parameters are set and how many atoms are represented [47].

The surface model will depend on the converged bulk Fe model. It is thus important to obtain and accurate representation of the electronic and structural properties of bulk iron, Fe. The RPBE functional was chosen as it tends to give reasonable predictions of adsorption energies [29]. The PW91 functional was considered but it has been reported in literature that it over-binds the adsorbates, particularly for CO [48,49]. Since no pseudopotential that is optimized for the RPBE functional was available, the generic iron ultrasoft pseudopotential with nonlinear core correction was selected from the available pseudopotentials provided by material studio. A pseudopotential with nonlinear core corrections was used as these tend to give more accurate lattice parameters [50]. Nonlinear core corrections are required since there exists a nonlinear relationship between the energy and the core charge density.

The results from this study were compared to several studies in literature as well as experimental observations. It is important to note the difference in code, functional and pseudopotential may give different results. The accuracy of the different models can be seen by the calculation of bulk properties of Fe in Table 2-1. When optimizing the structure for bulk Fe we allowed for the correction of the Finite Basis set, allowing the cell volume to vary. Thus, an accurate lattice parameter (a_0) can be calculated and it provides enough information to calculate the bulk modulus (B_0), as it describes the change in cell energy with change in cell volume($\frac{d^2E}{dV^2}$). Furthermore, since Fe is a magnetic system, the magnetic moment (M_0) was determined by utilizing spin-polarized DFT-calculations. These were compared to the equivalent of the different studies and experimental values.

Table 2-1: Comparison of bulk properties calculated in this study (USPP-RPBE, 500 eV, 16x16x16) with the other studies

Authors and Method	Code	a_0 (Å)	B_0 (GPa)	M_0 (μ_B)
Borthwick et al. (USPP-PW91) [51]	CASTEP	2.850		2.24
Chen et al. (USSP-PBE) [52]	CASTEP	2.826	-	2.24
Huo et al. (USPP-PBE) [53]	CASTEP	2.826	-	2.24
Ziegler and Lo (USPP-PW91) [54]	VASP	2.865	156.0	2.30
Govender (PAW-PW91) [55]	VASP	2.810	-	2.16
Sorescu (USPP-PW91)[56]	VASP	2.865	159.7	2.33
Sorescu (PAW-PW91) [56]	VASP	2.831	173.0	2.20
Sorescu (PAW-PBE) [56]	VASP	2.833	171.0	-
Present Work (USPP-RPBE)	CASTEP	2.854	173.0	2.30
Experimental [57]		2.867	170.0	2.22

The 3d electrons are responsible for the magnetic moment of transition metals and contribute to the structure of transition metals. Shiga [58] shows that an empirical correlation can exist between the lattice constant and the magnetic moment. It would be reasonable to think that as the positions and geometries change between substrate atoms, the positions and orientations of the d electrons will change and hence the magnetic moment would change. Jing et al. [59] have shown that for Fe_xMn_{1-x} systems the magnetic properties change "*from paramagnetism to antiferromagnetism (or ferrimagnetism) and finally to ferromagnetism with an increase of the lattice constants*".

For bulk bcc Fe, it appears that the magnetic moment can be predicted accurately at the expense of a small error in the lattice parameter and vice versa, Figure 2-2. The representation of the bulk phase in this study gives a reasonably accurate representation of the structure of Fe and its bulk modulus with a small sacrifice in the accuracy of the determination of the magnetic moment. The model created by Borthwick et al. [51] appears to be the most accurate of the CASTEP models. However, this model uses the PW91 functional and as mentioned above, this could result in over-binding of adsorbates.

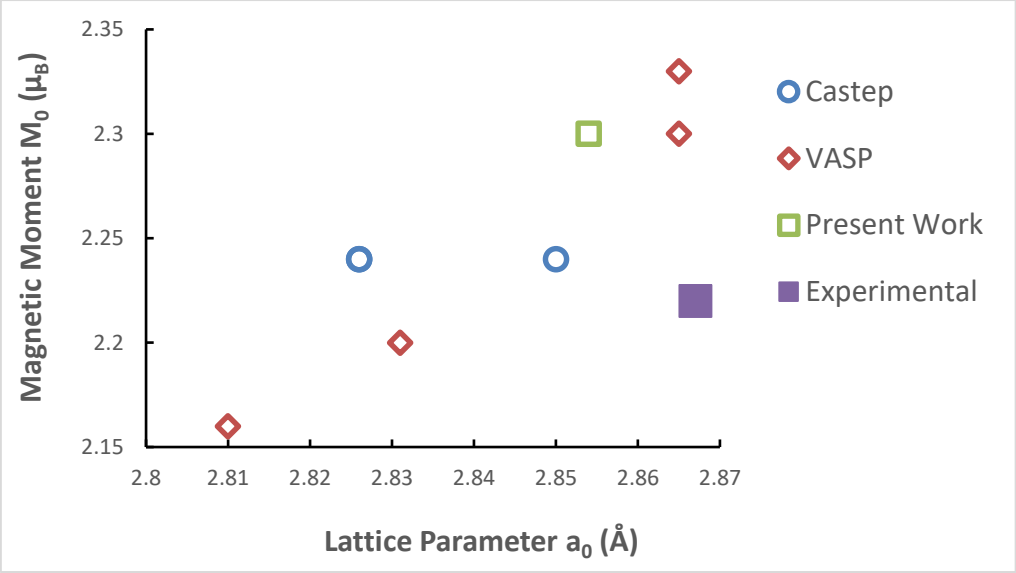

Figure 2-2: Magnetic moment on Fe as determined in various computational studies as a function of the optimized lattice parameter in comparison to the experimental value.

2.2.2 Modelling Fe Surfaces

Literature has shown [60–62] that the findings from low miller index metallic surface studies provide insight into micro kinetic world and when scaled agree with macro scale experiments and studies for Ammonia synthesis and water-gas-shift reactions. For iron, three lower miller index surfaces have been studied extensively. Those are the Fe (100), the Fe (110) and the Fe (111), the geometries and sites are shown in Figure 2-3 below. The Fe (110) and Fe (100) surfaces represent the prevalent facets on Fe nanocrystals [63].

With regard to methanation species, several studies reported on the stability of CH_x species adsorbed on Fe (100) [48,50,54,55,64,65,56], Fe (110) [66–68] and several Fe_5C_2 Hagg iron carbide surfaces [69–71]. The studies on Fe (100) imply that the four-fold hollow site is the stable adsorption site for C, CH and CH_2, while the CH_3 species is stable on the two-fold bridge site. CH_4 only displays weak physisorption.

For the purposes of studying lateral interactions, the Fe (100) sites are well defined the species show very little site variability. This makes it easy to define and identify orientations with expected lateral interactions. Additionally, microkinetic studies on Fe (100) [54] show results that agree with experimental equivalents. For this reason, the Fe (100) surface will be used.

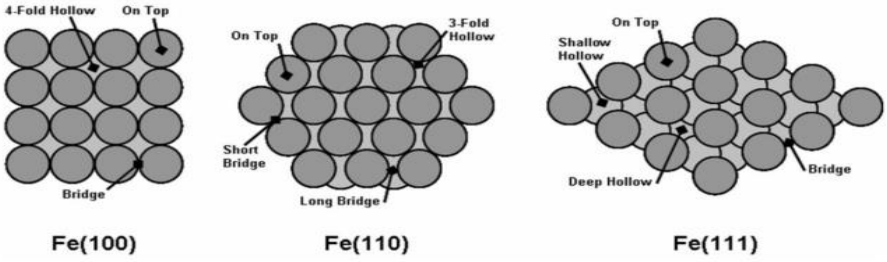

Figure 2-3: The sites available on lower miller indices surfaces

2.2.3 Fe (100) surface model

Once the bulk structure has been optimized, the cleaved surfaces can then be calculated. The surface of interest in this study is Fe (100). This surface has well defined sites that are easy to understand and identify. It is simpler than the carbide and high Miller index surfaces, and will allow for well-defined energies and potentially well-defined lateral interactions, the focus of this study. Cleaving the surfaces requires additional parameters to be optimized, these being the vacuum spacing, cut-off energy and k-point spacing.

2.2.3.1 Vacuum spacing

The vacuum spacing between iron slabs needs to be large enough such that the interactions between the slabs are negligible. The computational time however increases the size of the vacuum spacing increases. Thus, an optimization between vacuum spacing and computational time needs to be made. In this study, the vacuum spacing was varied in a range of 4-20 Å in increments of 2 Å while keeping the k-point mesh fixed at 7x7x1 and cut-off energy at 450 eV. The results of this exercise are shown in Figure 2-4. The results appear to converge after 8 Å but to ensure that the interactions between adjacent slabs are negligible and considering that we plan to adsorb adsorbates on the surface of the slab, a vacuum spacing of 10 Å was selected. This appears to be a number used consistently in literature [72–74]. As the vacuum spacing increases the computational time required to calculate the total energy of the system also increases.

2.2.3.2 Cut-off energy

As mentioned above, wave-functions are the linear combinations of the electron wave-functions and these expansions can be reduced to plane waves**.**

$$\varphi_{n,k} = \sum_{g} e^{i(k+g)r} u_{n,g,k} \qquad (2.8)$$

Instead of generating an infinite number of plane wave basis sets, the basis sets are truncated at a cut off energy. While this truncation will result in an error in total energy, it is possible to minimize this error by increasing the cutoff energy. To select the optimum cut-off energy for our model, the parameter was increased until the total energy of the system converged to within 0.005 eV/atom. The cut-off energy was varied in increments of 20 eV from 280 eV (the recommended minimum cut-off energy for the Fe pseudopotential used) to 500 eV while keeping the k-point mesh fixed at 7x7x1 and vacuum spacing at 10 Å. The results of this exercise can be seen in Figure 2-5. The system appears to converge after 360 eV but as with the vacuum spacing, a larger selection of 400 eV was chosen to ensure an accurate description of the system and to account for pseudopotentials of the adsorbates.

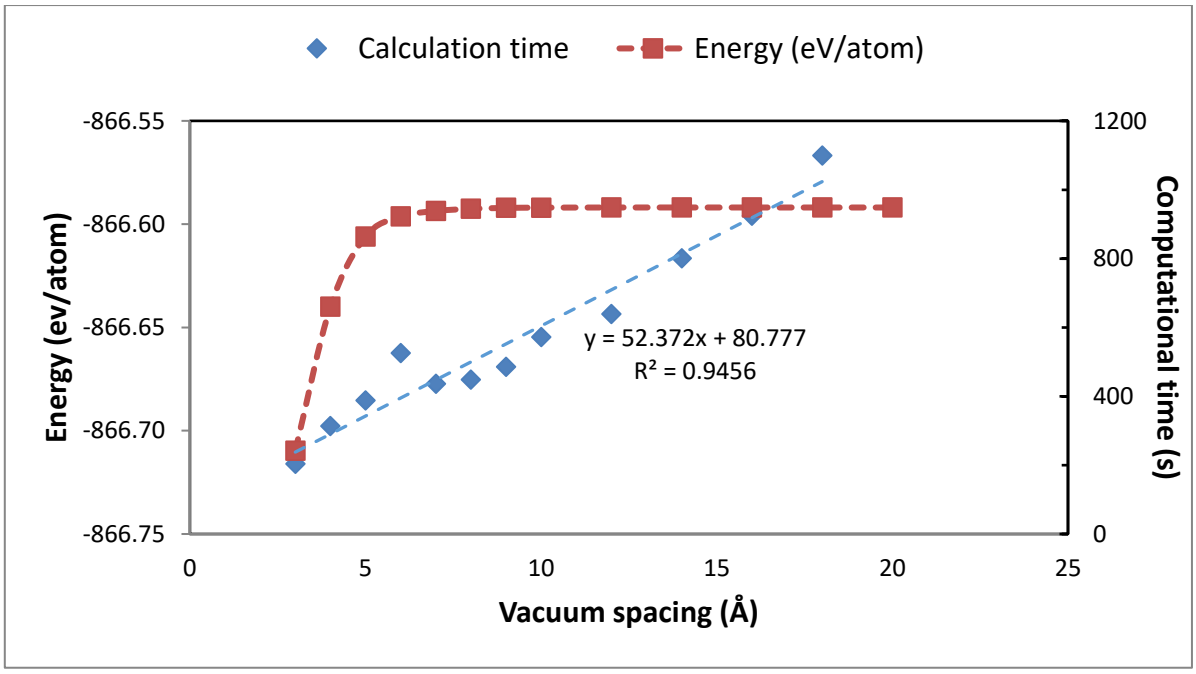

Figure 2-4: Total energy of a p(1x1) 5-layer Fe (100)-slab[3] as a function of the vacuum spacing (also shown the effect of the vacuum spacing on the computational time).

[3] Fe (100)-slab, top 3 layers relaxed and bottom 2 layers fixed, a cut-off energy of 450 eV, 7x7x1 k-point mesh

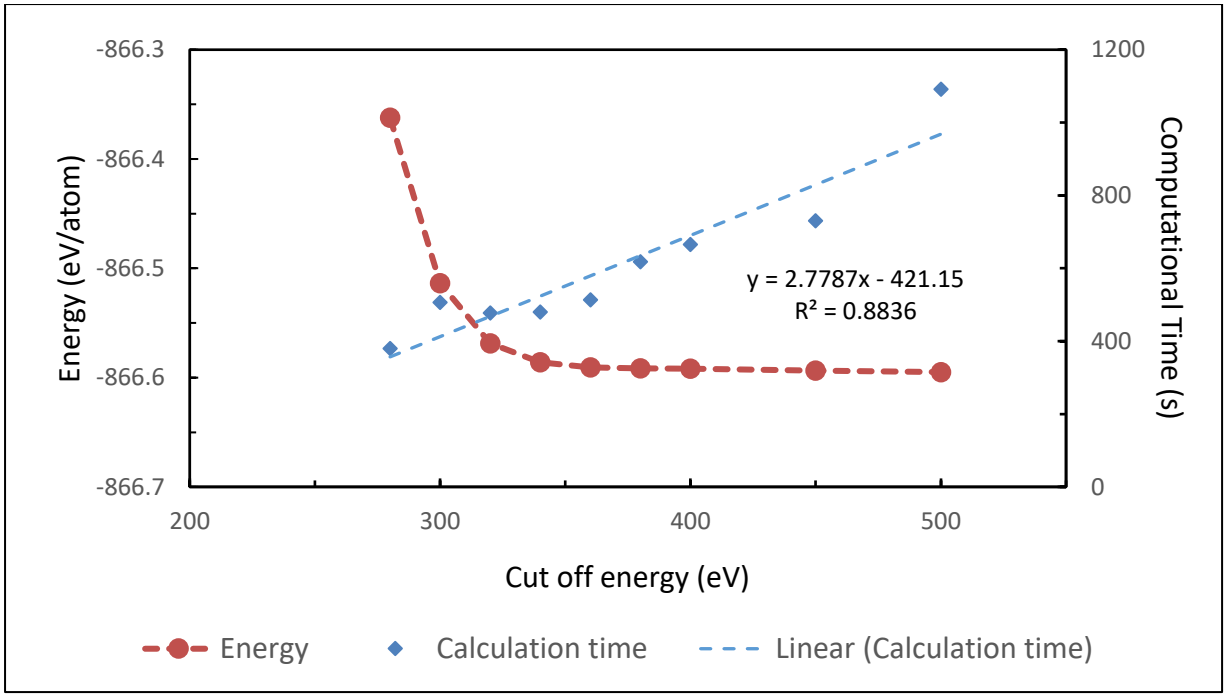

Figure 2-5: Total energy of a p(1x1) 5-layer Fe (100)-slab[4] as a function of the cut-off energy (also shown the effect of computational time for this system as a function of cut-off energy)

2.2.3.3 Sampling the k-point space

In this study, different size unit cells will be used. It is thus important to reach a consensus on k-point spacing instead of k-point mesh. To optimize the k-point spacing the system was calculated for k-point meshes of 4x4x1 to 20x20x1 while keeping the vacuum spacing at 10 Å and the cut-off energy at 400 eV. The results of this exercise can be seen in Figure 2-6. The energy oscillates around the converged solution and the system appears to converge after 5x5x1, which relates to a k-point spacing of <0.03 $Å^{-1}$. As expected the results show that the variation in k-point spacing has a much stronger effect on computational time than either the cut-off energy or vacuum spacing. This is because the wave function is calculated at each k-point set. The plane waves that is then needed to describe the wave function is dependent on each k-point set. Figure 2-6 also shows that there is a strong linear relationship between the computational time and the number of irreducible k-points.

[4] Fe (100)-slab, top 3 layers relaxed and bottom 2 layers fixed, vacuum spacing of 10 Å, 7x7x1 k-point mesh

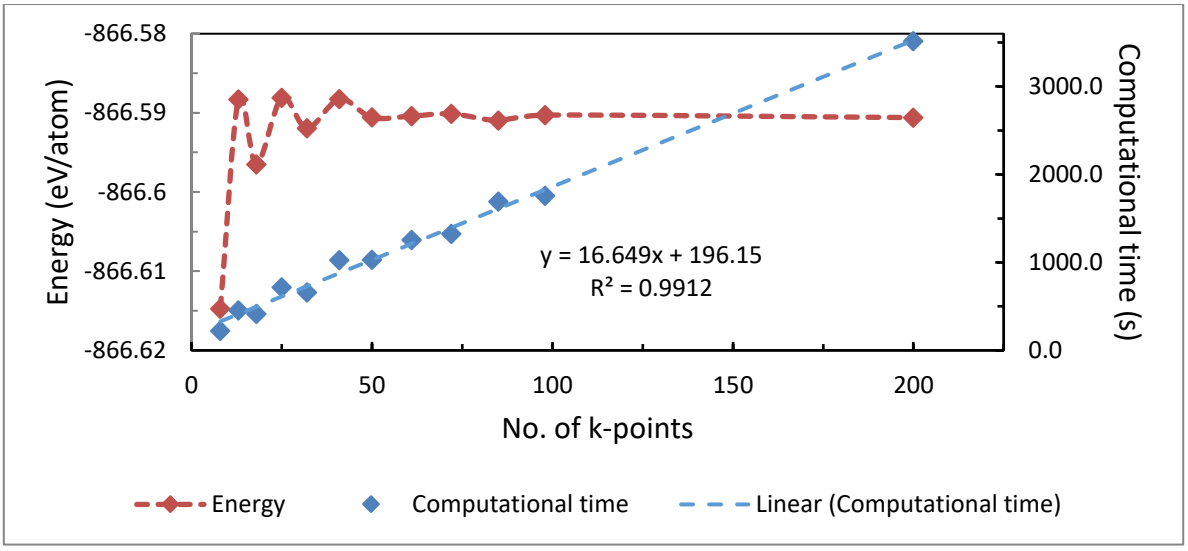

Figure 2-6: The total energy of a p(1x1) 5-layer Fe (100)-slab[5] as a function of the number of k-point density of the k-point mesh and the effect of the k-point sampling on the computational time

2.2.4 General optimized simulation

The DFT calculations in this study were completed using the Cambridge Sequential Total Energy Package (CASTEP) [3], as part of the Materials Studio software package[8]. The exchange-correlation energy was calculated using the generalized gradient approximation (GGA), making use of the RPBE functional [29]. A Gaussian smearing width of σ = 0.1 eV was utilized in all calculations. The ion-electron interactions were approximated using ultrasoft pseudopotentials with core corrections and a cutoff energy of 400 eV was set[6]. Spin-polarization was allowed for all calculations.

A five-layer slab with three layers relaxed was used with an optimized vacuum spacing of 10 Å between surfaces. Adsorption was performed on only one side of the slab. K-point sampling was generated using the Monkhorst-Pack procedure [46] with a k-point spacing of <0.03 $Å^{-1}$. All of the parameters were tested and optimized in order to find a balance between efficiency and accuracy. Geometry optimizations were completed when all the forces were less than 0.03 $eV.Å^{-1}$. The convergence test of 1 ML CO on Fe (100) is available in **Appendix A**.

2.2.5 Gas phase molecules

The approximation of molecules in the gas phase can also give insight to the accuracy of the different models. In Table 2-2 the bond angles, bond lengths and vibrational analysis of the molecules in 10 Å x 10 Å x 10 Å box is compared with experimental gas phase molecules. We see that our results are converged to within 0.001 Å for bond lengths and 0.1° for bond angle in CH, CH_2 and CH_4. The bond length of CH2 is converged to within 0.001 Å for bond lengths, but only to 4 ° for the bond angles[7]. The bond lengths for CO and H_2 are also accurate to 0.001 Å. The vibrational frequencies are in agreement with their experimental equivalents. Furthermore, the vibrational frequencies are all positive real numbers, indicating that the structures are all minima.

[5] Fe (100)-slab, top 3 layers relaxed and bottom 2 layers fixed, 450 eV cut off energy, Vacuum spacing of 10 Å

[6] 400 eV was high enough to ensure precision calculations for both Fe and O pseudopotentials. C and H pseudopotentials required lower cut-off energies

[7] Could this be a result of over approximated repulsion between the H atoms.

Table 2-2: Comparing the calculated bond distance (in Å) and vibrational frequencies (cm^{-1}) with reported computational data [56] and experimental values [75–77].

CO

Species	**r(C-O)**	**v_1**
Present Work (USPP-rPBE)	1.13	2158
Experimental	***1.128***	***2170***

H_2

Species	**r(H-H)**	**v_1**
Present Work	0.742	4397
Experimental	***0.741***	***4401***

H_2O

Species	**r(O-H)**	**Θ(H-O-H)**	**v_1**	**v_2**	**v_3**
Present Work	0.962	105	1668	3668	3781
Experimental	***0.957***	***104.5***	***1595***	***3659***	***3755***

CH

Species	**r(C-H)**	**v_1**
Sorescu (USPP-PW91)	1.133	2774
Sorescu (PAW-PBE)	1.138	2752
Present Work	1.119	2820
Experimental	***1.12***	***2858***

CH_2

Species	**r(C-H)**	**Θ(H-C-H)**	**v_1**	**v_2**	**v_3**
Sorescu (USPP-PW91)	1.082	135.2	3324	3082	1003
Sorescu (PAW-PBE)	1.086	135.1	3313	3076	1015
Present Work	1.088	126.1	3234	3026	968
Experimental	***1.078***	***130***	***3190***	***2806***	***963***

CH_3

Species	r(C-H)	Θ(H-C-H)	v_1	v_2	v_3	v_4
Sorescu (USPP-PW91)	1.083	120	3247	3064	1362	542
Sorescu (PAW-PBE)	1.087	120	3234	3054	1356	527
Present Work	1.079	120	3283	3090	1403	618
Experimental	***1.08***	***120***	***3161***	***3044***	***1396***	***606***

CH_4

Species	r(C-H)	Θ(H-C-H)	v_1	v_2	v_3	v_4
Sorescu (USPP-PW91)	1.094	109.47	3099	2984	1516	1295
Sorescu (PAW-PBE)	1.097	109.47	3091	2973	1510	1284
Present Work	1.088	109.53	3137	3016	1524	1307
Experimental	***1.087***	***109.47***	***3019***	***2917***	***1534***	***1306***

2.2.6 Energetic breakdown

A principal method for decomposition of interaction energies was proposed by Kitaura and Morokuma [78]. This method decomposes molecular interaction energies into electrostatic, exchange-repulsion, polarization, and charge transfer terms by systematically solving a series of model Hartree-Fock equations.

Mo et al. [79] built on this method and proposed a block-localized wave-function approach which decomposed the molecular interaction energies into the same components . They stated that electrostatic effects account for approximately 65%[8] of the interaction energy.

Philipsen and Baerends [80] attempted an energetic breakdown of adsorbate interaction with metals to Bond energy, steric energy, orbital interaction energy and preparation energy or energy required to change geometries and positions. The break down provided good insights into quantifying Pauli repulsion effects.

A different kind of energetic breakdown is attempted here in order to quantify the lateral interactions. All the terms included in the Hamiltonian will be considered. For CASTEP [3] the resulting energies are the kinetic energy, Hartree energy, local and non-local pseudopotential energies, exchange-correlation energy, Ewald energy and non-Coulombic energy.

The Hartree energy describes the electrostatic contribution of the electron-electron interaction. The local and non-local pseudopotential energies describe the electrostatic interactions between the ions and electrons. The Ewald energy describes the Coulombic energy of the ions in the system. A non-Coulombic energy arises since the pseudopotentials are not purely Coulombic. The potential within the core region of the ion deviates from a pure Coulomb potential. The non-Coulombic energy accounts for this deviation [81]. Hartree, Ewald, pseudopotential and Non-Coulombic energies combined will give an overall electrostatic interaction.

[8] Since the energetic components can be either negative or positive, this percentage is relative to the sum of the absolute values of the contributing energies

The exchange-correlation potential includes the effects of the Pauli Exclusion Principle. It should be noted that all exchange-correlation functionals are only approximations. This will be considered a general correction energy term which accounts for the deviations from ideal systems.

The remaining energy is the kinetic energy. The kinetic energy operator is the sum of the Laplacian operator over all points, seen in equation 2.9 below. This means that the kinetic energy is the sum of the relative magnitude of the curvature of the wave-function at each point. A simple analogy can be made with water waves where the water moves fastest in the regions of highest curvature, i.e. the peaks and troughs.

$$\hat{T} = \frac{1}{2}\sum_{i=1}^{N} \nabla_i^2 \qquad (2.9)$$

The kinetic energy gives us an idea of the shape of the electron density. A system with that has sharper changes in concavity will have a higher kinetic energy. This change in concavity could be the result of a number of changes to the system including large columbic interactions forcing a change in electron density and/or changes in position and geometry that brings about a large change in electron density.

A more detailed look at how each of these component energies and how they converge with changing parameters can be seen in **Appendix A**. It should be noted that the component energies are sensitive to small changes in the system.

2.3 Population analysis and charge representation

In classical chemistry, chemical bonding is classified into ionic or covalent bonds (sharing of electrons). Various methods are available to quantify atomic charges [82]. The differences in these methods arise from the algorithm used to partition the electron density. A graphical representation of the different methods can be seen in Figure 2-7.

2.3.1 Mulliken charge separation

The Mulliken population analysis is the oldest known partitioning of electron density. This method utilizes the representation of molecular wave-functions from basis functions and the electrons are distributed amongst the atomic orbitals of the atom [82–85].

The wave-functions ($\boldsymbol{\varphi(r)_k}$) are expanded in terms of the basis function ($\boldsymbol{\chi_\mu(r)}$):

$$\varphi(r)_k = \sum_i \sum_{\mu \in i} c_{\mu i}\, \chi_\mu(r) \qquad (2.10)$$

The total number of electrons is defined as:

$$N_e = \sum_{k}^{occupied} n_k \int |\varphi(r)_k|^2\, dr \qquad (2.11)$$

where n_k is the number of orbital occupation.

Substituting equation 2.10 in 2.11:

$$N_e = \sum_{i,j} \sum_{\mu \in i, \nu \in j} \sum_{k}^{occupied} n_k c_{\mu k} c_{\nu k} \int \chi_\mu \cdot \chi_\nu dr \qquad (2.12)$$

Defining a Density matrix as:

$$D_{\mu v} = \sum_{k}^{occupied} n_k c_{\mu k} c_{vk} \tag{2.13}$$

and an overlap integral between χ_μ and χ_v:

$$S_{\mu,v} = \int \chi_\mu \cdot \chi_v dr \tag{2.14}$$

The total number of electrons can be written as:

$$N_e = \sum_{i,j} \sum_{\mu \in i} \sum_{v \in j} D_{\mu,v} \cdot S_{\mu,v} \tag{2.15}$$

Since different basis functions represent the wave functions describing a system (e.g. a molecule) differently, the analysis becomes strongly dependent on the basis set chosen. Segall et al. [85] show that the magnitude of the atomic charge on a C atom in CO in the gas phase can differ by as much 0.3e depending on the basis set. Fonseca Guerra et al. [82] believe that the atomic charges resulting from a Mulliken population analysis are not of much use. The Natural Population analysis by Reed et al. [86] is an improvement on the Mulliken analysis as they consider orthonormal natural atomic orbitals instead of basis atomic orbitals.

2.3.2 Hirshfeld charge separation

The Hirshfeld analysis separates the electron density of the system in proportion to the atomic ground states. The algorithm defines an electron density of a "promolecule" system which is typically the sum of the electron densities of the atomic ground states ($\boldsymbol{p(r)_i^0}$) [82,87,88].

$$\rho(r)_{Promolecule} = \sum_i p(r)_i^0 \tag{2.16}$$

The atomic ground states are typically spherical in nature. The weight function is then defined as:

$$w(r)_i = \frac{p(r)_i^0}{\rho(r)_{Promolecule}} \tag{2.17}$$

Using the electron density of the system ($\boldsymbol{p(r)}$) and the nuclear charge ($\boldsymbol{Z_i}$) the Hirshfeld atomic charge is then:

$$Q_{i_{Hirshfeld}} = Z_i - \int w(r)_i \; p(r) dr \tag{2.18}$$

2.3.3 Bader charge separation

The Bader analysis looks purely at the topology of the electron density [82,88,89]. The regions which the electron density are divided into Bader volumes, which are separated by curves representing the minimum of the electron density is a minimum ($\boldsymbol{\nabla \rho = 0}$) [82,88,89].

Typical algorithms from the Bader analysis require a large amount computational effort in finding the critically points where the electron density is a minimum [90]. The algorithm proposed by Henkelman et al. [89] uses the FFT grids produced from DFT calculations and finds the maxima on the grid using a steepest accent procedure. The procedure is significantly faster than previous algorithms with minimal losses in accuracy. This method was recoded in MATLAB and uses a CASTEP formatted density file to conduct the analysis.

Fonseca Geurrara et al. [82] believe the Bader charges to be too large and resulting in a misrepresentation of the partial atomic charges. However, the Bader charge assignment does not

originate from a full and complete charge separation and the calculated charge does therefore not represent the classical “charge” on a specific atom. The Bader charge analysis is still a popular method of electron density decomposition

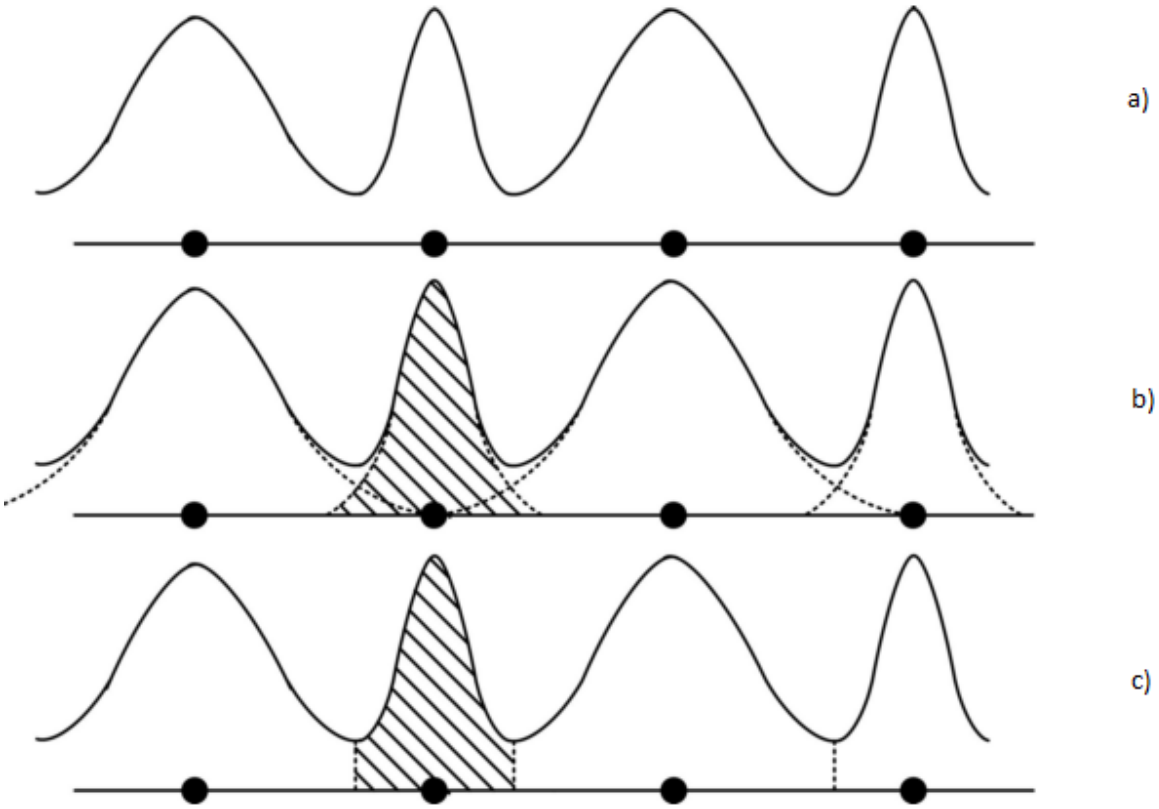

Figure 2-7: Charge assignment for a hypothetical 1-D charge distribution (per the Mulliken charge separation (b) and the Hirshfeld and Bader charge separation method (c).

While all three methods mentioned above are widely used, the empirical assignment of charges to atoms can lead to poor approximations of the actual charge distribution, particularly if electron delocalization is prevalent in the system.

2.3.4 Mapping the electron density

Instead of assigning approximate charges to the atoms in the system, the electron density could be mapped out and slices of specific planes could be analysed. Figure 2-8 shows the electron density of a free CO molecule in a vacuum cut at a plane running through the C-O bond. As to be expected, the electron density is highest around the oxygen atom.

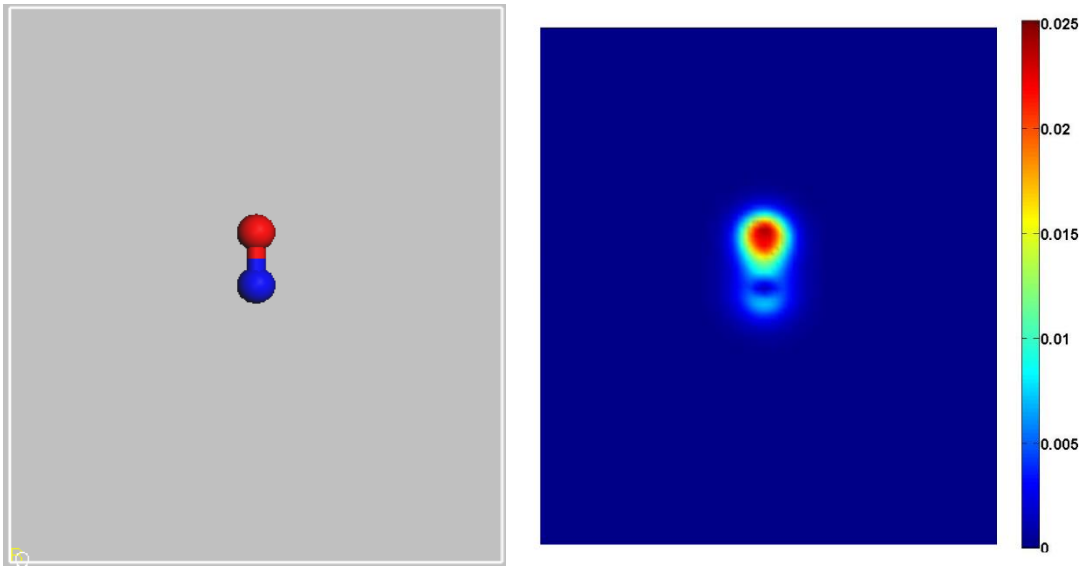

Figure 2-8: Electron density of CO in the gas phase (right)

While representations of the gas phases are easily understood, for surface models, the raw density map appears not to yield any insight into changes induced by the adsorption of CO on the surface or by lateral interactions involved as the electron density around the Fe cores overshadowed the density of the CO. This can be circumvented by subtracting the electron density of the clean surface, as shown in Figure 2-9. The result is electron density of the adsorbed CO and the electron density changes it induces on the metal. It is expected that the electrons not involved in the CO-Fe interaction will cancel each other out and the picture that remains will show the change in the electrons that are involved in the CO-Fe interaction. The changes to the metal are seen as a change in colour from dark blue to teal, which indicates the repositioning of electrons relative to the clean surface.

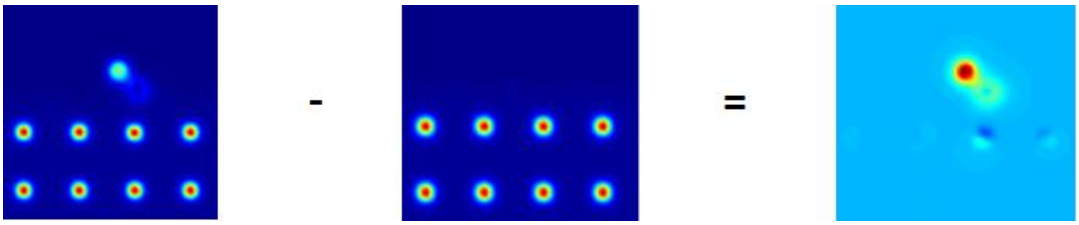

Figure 2-9: Electron density of the system of CO adsorbed on Fe (100) (left), Fe (100) (middle) and the resulting change electron density upon adsorption of CO on Fe (100 (right)

The electron density maps appear to give the same insights as the population analysis with the advantage of being a product (i.e. output) of a DFT simulation. Furthermore, a visual representation can at times be more easily understood then numerical values.

2.4 Lateral interactions

On the Fe (100) surface the lateral interactions of concern are the nearest neighbour (a) and next nearest neighbour (b) interactions:

a) b)

Figure 2-10: Representation of a) nearest neighbour and b) next nearest neighbour pairs

For adsorption / binding energies of an adsorbate can be calculated as follows

$$E_{ads} = \frac{E_{(Fe+nCO)} - E_{(Fe\ Slab)}}{n} - E_{CO} \qquad (2.19)$$

If a system with no lateral interactions is identified, then the deviation in adsorption / binding energies from this system is the resulting lateral interaction. For the CO adsorption study several p(4x4) unit cells were studied to investigate nearest neighbour and next nearest neighbour.

For the other methanation species nearest neighbour and next nearest neighbour interactions were considered as well. In order to investigate these interactions three configurations are considered; two configurations a 0.5 ML (called the "Diagonal" and "Adjacent" configurations) and a 0.33 ML configuration. The 0.5 ML "Adjacent" configuration and 0.33 ML configuration looks at the nearest neighbour interactions while the 0.5 ML "Diagonal" configuration investigates the next nearest neighbour interactions. For CH_3 and OH which are stable on the bridge site, only the bridge sites adjacent to the considered hollow site were investigated.

The lateral interactions are quantified here by calculating the excess energy of the configuration, defined as

$$E_{Excess} = E_{AB} - E_{A,0.25ML} - E_{B,0.25ML} + E_{xFe} \quad (2.20)$$

Where E_{AB} is the total coadsorption energy of the system, $E_{A,\ 0.25\ ML}$ and $E_{B,\ 0.25\ ML}$ are the total energies of the individual species at 0.25 ML and E_{xFe} is the total energy of a clean Fe surface. The number of Fe atoms used in the E_{xFe} surface is determined by balancing the total number of Fe atoms of the co-adsorbed configuration with the 0.25 ML configurations (i.e. if the co-adsorption configuration was calculated on a 2x2 unit cells and the two 0.25 ML individual configurations are always 2x2 unit cells, a clean Fe 2x2 unit cell will be used to balance the system.)

2.5 Kinetic models

The main objective of catalysis is to increase the rate of a chemical reaction by providing an alternative reaction pathway. Kinetics is used to describe the rate at which chemical reactions take place. It provides a relationship between measurable macroscopic properties, such as temperature, pressure and concentration, and the microscopic properties, the way in which molecules interact [91]. By understanding the mechanism, the kinetics of the process can be derived and a rate expression can then be postulated. The mechanism can also give insights into the selectivity of different catalysts.

While macrokinetic modelling will always have practical applications (reactor design, understanding catalyst deactivation, catalyst quality control [92,93]) they reveal little information about the mechanistic steps involved in the process. Furthermore, Corma et al. [94] showed that different

macrokinetic models with different underpinnings can fit kinetic data equally well, indicating that "the effect of distribution of site energies on the global kinetics is weak.". This is indeed the case for systems which have low to moderate variations with respect to site energies.

Microkinetic modelling examines catalytic reactions in terms of elementary kinetic steps and their relation to each other during the catalytic process [95]. Several publications [92,93,96,97] consider microkinetic modelling an important tool in understanding and developing the field of catalysis. The energetics required to build a microkinetic model can be obtained experimentally, through single crystal surfaces studies [60–62], or theoretically, popularly with DFT studies or UBI-QEP studies [93,95,96,98]. Microkinetic analysis can be approached either deterministically or stochastically.

Stochastic microkinetic models or Monte Carlo simulations are the popular choice for microkinetic models but are computationally expensive while deterministic simulations are computationally less demanding [96] and should converge to the results obtained in a Monte-Carlo type method if all interactions are captured correctly. It is easier to incorporate lateral interactions as well as specific spatial arrangements i.e. different adsorption sites, different adsorption geometries, etc. [96].

Deterministic microkinetic analysis involves directly solving a set of differential kinetic equations. In order to simplify the set of differential equations most microkinetic models in literature use the mean fields approach to approximate reaction barriers [54]. As a result, the effects of lateral interactions on the system are often poorly represented. Furthermore, the complexity of the set of differential equations increases if different adsorption sites are considered.

The density functional theory models calculate absolute energies and vibrational frequencies of initial, final and transition states of reactions. From this, heats of reactions, activation barriers and temperature corrections can be determined.

2.5.1 Kinetic model formulation

The elementary steps of a kinetic model involve adsorption and desorption of particles and surface reactions. Each of these elementary steps has an initial, final and a transition state. Each of these states has an associated partition function i.e. a function of the state variables like temperature or volume. Thermodynamic variables like the Gibbs free energy, enthalpy, entropy and pressure can be expressed in terms of the partition function or as a derivate of the partition function.

The partition function differs with respect to the degrees of freedom. For surface reactions, the partition functions correspond to 3N-5 and 3N-6 vibration degrees of freedom for linear and non-linear molecules. The partition function for vibrations is written as:

$$p.f_{\cdot vibrational} = \sum_{n=0}^{\infty} e^{-\left(n+\frac{1}{2}\right)\cdot\frac{h\cdot\nu}{k_b\cdot T}} = \frac{e^{-\frac{1}{2}\cdot\frac{h\cdot\nu}{k_b\cdot T}}}{1-e^{-\frac{h\cdot\nu}{k_b\cdot T}}} \quad (2.21)$$

where k_B is the Boltzmann constant, h is Planck constant, T is temperature and v is the vibrational frequency[9].

For adsorption and desorption, the translational and rotational degrees of freedom of the particles in the gas phase should also be considered.

$$p.f_{\cdot trans} = V \cdot \left(\frac{2\cdot m\cdot k_b\cdot T}{h^2}\right)^{\frac{3}{2}} \quad (2.22)$$

[9] This derivation of the vibrational partition function includes the ZPE correction. If it the ZPE correction is calculated separately the partition function is of the form : $p.f_{\cdot vibrational} = 1/(1-e^{-\frac{h\cdot\nu}{k_b\cdot T}})$

The rotational partition function for linear molecules:

$$p.f_{\cdot rotational} = \frac{8\cdot\pi^2\cdot I}{\sigma\cdot h^2}\cdot k_b\cdot T \quad (2.23)$$

The rotational partition function for nonlinear molecules:

$$p.f_{\cdot rotational} = \frac{1}{\sigma}\left(\frac{8\cdot\pi^2\cdot k_b\cdot T}{h^2}\right)^{\frac{3}{2}}\cdot\sqrt{\pi\cdot I_A\cdot I_B\cdot I_C} \quad (2.24)$$

Where I is the rotational moment of inertia

For elementary reactions steps, the rate constant, k, of an elementary reaction can be determined using the Eyring equation:

$$\mathrm{k} = \frac{k_B T}{h} e^{-\Delta E_R(T,LI)/k_B T} = \frac{k_B T}{h}\frac{Q^+}{Q} e^{-\Delta E_R(LI)/k_B T} \quad (2.25)$$

where LI is the lateral interactions involved, ΔE is the activation barrier, Q is the partition function of the reactants and Q^+ is the partition function of activated complex or transition state. The formulation above shows that the ratio of the partition functions accounts of the temperature corrections of the activation barrier.

For adsorption of gasses on the catalytic surface, the rate constant for adsorption can be determined using collision frequency or collision rate theory.

$$k_{\mathrm{Ads}} = \mathrm{A}_s\sqrt{\frac{2\pi\cdot m_{gas}}{kb\cdot T}} e^{-\Delta \mathrm{e}^{\mathrm{f}}(T,LI)/k_B T} \quad (2.26)$$

Where P_{Gas} is the partial pressure of the gas, θ_{ES} is the coverage of empty sites, k_{Ads} is the rate constant derived from Collision frequency, A_s is the area of a single site and m_{gas} is the mass of the gas particle. This equation can be derived by substitution the appropriate partition functions into the Eyring equation above.

Once a mechanism is proposed the rate equation and the rate constants for each elementary step can be expressed. The rate of adsorption can be expressed as

$$r_{Ads} = k_{\mathrm{Ads}} P_{Gas}\theta_{ES} \quad (2.27)$$

And for a simple surface reaction of A +B ↔ C +D:

$$r_1 = k_{\mathrm{fwd}}(\theta_A\theta_B - {\theta_C\theta_D}/{K_e}) \quad (2.28)$$

$$k_{\mathrm{fwd}} = \frac{k_B T}{h} e^{-eb_2^f/k_B T} \quad (2.29)$$

$$Ke_2 = \prod Q_{v_i} Q_{T_i} Q_{R_i}\, e^{-(eb_2^f - eb_2^r)/k_B T} \quad (2.30)$$

where Θ_x is the coverage of species x, k_B is the Boltzmann constant, h is Planck constant, LI is the lateral interactions, eb^f is the forward barrier, eb^r is the reverse barrier and ΔG_{Rxn} is the Gibbs free energy of reaction.

The rate equation for each species can be written as a differential equation of the form:

$$\frac{d\theta_i}{dt} = \sum_j^R v_{i,j}\cdot r_j \quad (2.31)$$

Where $v_{i,j}$ is the stoichiometric coefficient of species I in reactions j and r_j is the rate of reaction j.

The differential equations were then solved with ode23 solver[99], which was recommended for stiff ode's as part of the MatLab [100] package.

2.6 References

[1] Koomey, J., http://www.koomey.com, **2012**.

[2] Segall, M.D., Lindan, P.J.D., Probert, M.J., Pickard, C.J., Hasnip, P.J., Clark, S.J., Payne, M.C., *J. Phys. Condens. Matter* **2002**, 14, 2717–2744.

[3] Clark, S.J., Segall, M.D., Pickard, C.J., Hasnip, P.J., Probert, M.I.J., Refson, K., Payne, M.C., *Zeitschrift für Krist.* **2005**, 220, 567–570.

[4] Delley, B., *Comput. Mater. Sci.* **2000**, 17, 122–126.

[5] Soler, J.M., Artacho, E., Gale, J.D., García, A., Junquera, J., Ordejón, P., Sánchez-Portal, D., *J. Phys. Condens. Matter* **2002**, 14, 2745–2779.

[6] Kresse, G., Furthmüller, J., *Phys. Rev. B* **1996**, 54, 169-175.

[7] Giannozzi, P., Baroni, S., Bonini, N., Calandra, M., Car, R., Cavazzoni, C., Ceresoli, D., Chiarotti, G.L., Cococcioni, M., Dabo, I., Dal Corso, A., de Gironcoli, S., Fabris, S., Fratesi, G., Gebauer, R., Gerstmann, U., Gougoussis, C., Kokalj, A., Lazzeri, M., Martin-Samos, L., Marzari, N., Mauri, F., Mazzarello, R., Paolini, S., Pasquarello, A., Paulatto, L., Sbraccia, C., Scandolo, S., Sclauzero, G., Seitsonen, A.P., Smogunov, A., Umari, P., Wentzcovitch, R.M., *J. Phys. Condens. Matter* **2009**, 21, 395502.

[8] Accelrys Software Inc., Material Studio Modeling Environment, San Diego: Accelrys Software Inc., **2010**.

[9] Dronskowski, R., *Computational chemistry of solid state materials*, Wiley. com, **2008**.

[10] Engel, T., Reid, P., *Physical Chemistry*, Pearson Education, San Francisco **2006**.

[11] Dronskowski, R., *Computational chemistry of solid state materials*, Wiley-VCH, London **2005**.

[12] Born, M., *Ann. Phys* **1927**, 84, 457–484.

[13] Hartree, D.R., in:, *Math. Proc. Cambridge Philos. Soc.*, vol. 24, Cambridge Univ Press, **1928**, pp. 111–132.

[14] Heitler, W., London, F., *Zeitschrift für Phys.* **1927**, 44, 455–472.

[15] Hartree, D.R., in:, *Math. Proc. Cambridge Philos. Soc.*, vol. 24, Cambridge Univ Press, **1928**, pp. 89–110.

[16] Hartree, D.R., in:, *Math. Proc. Cambridge Philos. Soc.*, vol. 24, Cambridge Univ Press, **1928**, pp. 426–437.

[17] Fock, V., *Zeitschrift für Phys.* **1930**, 61, 126–148.

[18] Slater, J.C., *Phys. Rev.* **1930**, 35, 210-215.

[19] Møller, C., Plesset, M.S., *Phys. Rev.* **1934**, 46, 618-623.

[20] Hellmann, H., *J. Chem. Phys.* **1935**, 3, 61-70.

[21] Boys, S.F., *Proc. R. Soc. London. Ser. A. Math. Phys. Sci.* **1950**, 200, 542–554.

[22] Roothaan, C.C.J., *Rev. Mod. Phys.* **1951**, 23, 69-75.

[23] Hall, G.G., *Proc. R. Soc. London. Ser. A. Math. Phys. Sci.* **1951**, 205, 541–552.

[24] Hohenberg, P., Kohn, W., *Phys. Rev.* **1964**, 136, 864-871.

[25] Kohn, W., Sham, L.J., *Phys. Rev.* **1965**, 140, A1133–A1138.

[26] Perdew, J.P., Jackson, K.A., Pederson, M.R., Singh, D.J., Fiolhais, C., *Phys. Rev. B* **1992**, 46, 6671–6687.

[27] Bagno, P., Jepsen, O., Gunnarsson, O., *Phys. Rev. B* **1989**, 40, 1997–2000.

[28] Singh, D., Pickett, W., Krakauer, H., *Phys. Rev. B* **1991**, 43, 11628–11634.

[29] Hammer, B., Hansen, L., Nørskov, J., *Phys. Rev. B* **1999**, 59, 7413–7421.

[30] Perdew, J.P., Ruzsinszky, A., Tao, J., Staroverov, V.N., Scuseria, G.E., Csonka, G.I., *J. Chem. Phys.* **2005**, 123, 62201-62209.

[31] Perdew, J.P., Burke, K., Ernzerhof, M., *Phys. Rev. Lett.* **1996**, 77, 3865–3868.

[32] Wu, Z., Cohen, R., *Phys. Rev. B* **2006**, 73, 235116, 1-6.

[33] Dion, M., Rydberg, H., Schröder, E., Langreth, D.C., Lundqvist, B.I., *Phys. Rev. Lett.* **2004**, 92, 246401-246404.

[34] Muscat, J., Wander, A., Harrison, N.M., *Chem. Phys. Lett.* **2001**, 342, 397–401.

[35] Lebègue, S., Klintenberg, M., Eriksson, O., Katsnelson, M., *Phys. Rev. B* **2009**, 79, 245117.

[36] Adamo, C., Barone, V., *J. Chem. Phys.* **1999**, 110, 6158-6170.

[37] Becke, A.D., *J. Chem. Phys.* **1993**, 98, 5648-5652.

[38] Bloch, F., *Zeitschrift für Phys.* **1929**, 52, 555–600.

[39] Phillips, J., Kleinman, L., *Phys. Rev.* **1959**, 116, 287–294.

[40] Yin, M., Cohen, M., *Phys. Rev. B* **1982**, 25, 7403–7412.

[41] Hamann, D., *Phys. Rev. B* **1989**, 40, 2980–2987.

[42] Kresse, G., Hafner, J., *J. Phys. Condens. Matter* **1994**, 6, 8245–8257.

[43] Vanderbilt, D., *Phys. Rev. B* **1985**, 32, 8412–8415.

[44] Hamann, D., Schlüter, M., Chiang, C., *Phys. Rev. Lett.* **1979**, 43, 1494–1497.

[45] Moroni, E., Kresse, G., Hafner, J., Furthmüller, J., *Phys. Rev. B* **1997**, 56, 15629–15646.

[46] Monkhorst, H.J., Pack, J.D., *Phys. Rev. B* **1976**, 13, 5188–5192.

[47] Whitten, J., *Surf. Sci. Rep.* **1996**, 24, 55–124.

[48] Bromfield, T.C., Ferré, D.C., Niemantsverdriet, J.W., *Chemphyschem* **2005**, 6, 254–60.

[49] Kresse, G., Gil, A., Sautet, P., *Phys. Rev. B* **2003**, 68, 73401.

[50] Van Helden, P., Initial Steps of the Fischer-Tropsch Synthesis on Fe(100): The Role of Hydrogen. University of Cape Town, **2010**.

[51] Borthwick, D., Fiorin, V., Jenkins, S.J., King, D. a., *Surf. Sci.* **2008**, 602, 2325–2332.

[52] Chen, Y., Cao, D., Jun, Y., Li, Y., Wang, J., Jiao, H., *Chem. Phys. Lett.* **2004**, 400, 35–41.

[53] Huo, C., Li, Y., Wang, J., Jiao, H., *J. Phys. Chem. B* **2005**, 109, 14160–7.

[54] Lo, J.M.H., Ziegler, T., *J. Phys. Chem. C* **2007**, 111, 11012–11025.

[55] Govender, A., Ferré, D.C., Niemantsverdriet, J.W.H., *NaCatSoc. Extr.* **2009**.

[56] Sorescu, D., *Phys. Rev. B* **2006**, 73, 155420.

[57] Kittel, C., *Introduction to Solid State*, Wiley, New York **1996**.

[58] Shiga, M. (Kyoto U., *AIP Conf. Proc* **1974**, 18, 463–477.

[59] Jing, C., Cao, S.X., Zhang, J.C., *Phys. Rev. B* **2003**, 68, 224407.

[60] Stoltze, P., Nørskov, J.K., *J. Catal.* **1988**, 110, 1–10.

[61] Stoltze, P., Nørskov, J.K., *Phys. Rev. Lett.* **1985**, 55, 2502-2515.

[62] Ovesen, C. V, Clausen, B.S., Hammershøi, B.S., Steffensen, G., Askgaard, T., Chorkendorff, I., Nørskov, J.K., Rasmussen, P.B., Stoltze, P., Taylor, P., *J. Catal.* **1996**, 158, 170–180.

[63] Błoński, P., Kiejna, A., Hafner, J., *Surf. Sci.* **2005**, 590, 88–100.

[64] Sorescu, D., Thompson, D., Hurley, M., Chabalowski, C., *Phys. Rev. B* **2002**, 66, 35416.

[65] Jiang, D., Carter, E., *Phys. Rev. B* **2005**, 71, 45402.

[66] Mavrikakis, M., Gokhale, A.A., *Am. Chem. Soc.* **2005**, 229, 861–865.

[67] Erley, W., McBreen, P.H., Ibach, H., *J. Catal.* **1983**, 84, 229–234.

[68] McBreen, P.H., Erley, W., Ibach, H., *Surf. Sci.* **1984**, 148, 292–310.

[69] Zhao, S., Liu, X.-W., Huo, C.-F., Li, Y.-W., Wang, J., Jiao, H., *J. Catal.* **2012**, 294, 47–53.

[70] Cao, D.-B., Li, Y.-W., Wang, J., Jiao, H., *J. Mol. Catal. A Chem.* **2011**, 346, 55–69.

[71] Gracia, J.M., Prinsloo, F.F., Niemantsverdriet, J.W., *Catal. Letters* **2009**, 133, 257–261.

[72] Curulla-Ferré, D., Govender, A., Bromfield, T.C., Niemantsverdriet, J.W.H., *J. Phys. Chem. B* **2006**, 110, 13897–904.

[73] Jiang, D.E., Carter, E. a., *Acta Mater.* **2004**, 52, 4801–4807.

[74] Spencer, M.J.., Hung, A., Snook, I.K., Yarovsky, I., *Surf. Sci.* **2002**, 513, 389–398.

[75] Montgomery, J.A., Ochterski, J.W., Petersson, G.A., *J. Chem. Phys.* **1994**, 101, 5900.

[76] Lide, D.R., *CRC handbook of chemistry and physics*, CRC press, **2004**.

[77] Moon, D.W., Bernasek, S.L., Dwyer, D.J., Gland, J.L., *J. Am. Chem. Soc.* **1985**, 107, 4363–4364.

[78] Kitaura, K., Morokuma, K., *Int. J. Quantum Chem.* **1976**, 10, 325–340.

[79] Mo, Y., Gao, J., Peyerimhoff, S.D., *J. Chem. Phys.* **2000**, 112, 5530–5538.

[80] Philipsen, P.H.T., Baerends, E.J., *J. Phys. Chem. B* **2006**, 110, 12470–12479.

[81] Payne, M.C., Arias, T. a., Joannopoulos, J.D., *Rev. Mod. Phys.* **1992**, 64, 1045–1097.

[82] Fonseca Guerra, C., Handgraaf, J., Baerends, E.J., Bickelhaupt, F.M., *J. Comput. Chem.* **2004**, 25, 189–210.

[83] Segall, M., Shah, R., Pickard, C., Payne, M., *Phys. Rev. B* **1996**, 54, 16317–16320.

[84] Mulliken, R.S., *J. Chem. Phys.* **1955**, 23, 1833-1863.

[85] Segall, M.D., *Mol. Phys.* **1996**, 89, 571–577.

[86] Reed, A.E., Weinstock, R.B., Weinhold, F., *J. Chem. Phys.* **1985**, 83, 735-739.

[87] Hirshfeld, F.L., *Theor. Chim. Acta* **1977**, 44, 129–138.

[88] Parr, R.G., Ayers, P.W., Nalewajski, R.F., *J. Phys. Chem. A* **2005**, 109, 3957–2959.

[89] Henkelman, G., Arnaldsson, A., Jónsson, H., *Comput. Mater. Sci.* **2006**, 36, 354–360.

[90] Bader, R.F.W., *Atoms in molecules*, Wiley Online Library, **1990**.

[91] Chorkendroff, I., Niemantsverdriet, J.W., *Concepts of modern catalysis and kinetics*, vol. 2, Wiley-VCH, **2007**.

[92] Hansen, A.G., Well, W.J.M., Stoltze, P., *Top. Catal.* **2007**, 45, 219–222.

[93] Davis, M.E., Davis, R.J., in:, *Fundam. Chem. React. Eng.*, vol. 217, MGraw-Hill Companies, New York **1993**, pp. 240–259.

[94] Corma, A., Llopis, F., Monton, J.B., Weller, S.W., *Chem. Eng. Sci.* **1988**, 43, 785–792.

[95] Dumesic, J.A., *The microkinetics of heterogeneous catalysis*, American Chemical Society, Washington D.C. **1993**.

[96] Hellman, A., Honkala, K., *J. Chem. Phys.* **2007**, 127, 194704: 1-6.

[97] Storsæter, S., Chen, D., Holmen, A., *Surf. Sci.* **2006**, 600, 2051–2063.

[98] Fishtik, I., Datta, R., *Surf. Sci.* **2002**, 512, 229–254.

[99] Lamba, H., Stuart, A.M., *BIT Numer. Math.* **1998**, 38, 751–780.

[100] MATLAB User's Guide, *The mathworks*, vol. 5, **1998**.

3 Energetic study on lateral interactions for CO adsorption on Fe (100)

3.1 Introduction

The Fischer-Tropsch is initiated by CO adsorption on a catalytically active metal [1–3]. There are numerous studies of CO adsorption on metals, e.g. on Fe [4–8], Co [9,10], Ru [11] and Pt [12–14].[10]

The interaction between CO and metal surfaces was first described by Blyholder [15] in terms of the Molecular Orbital theory. Blyholder only considered the π-interactions and assumed the σ-bonds are constant. Even with these simplifications, Blyholder could explain the stretching frequencies of CO in the infra-red spectra as well as band shifts and band positions.

Föhlisch et al. [17] showed that the Blyholder model does not give a complete description. It was shown that hybridization of the entire π-electronic structure should be considered. Furthermore, orbital mixing of the σ-electronic structure should also be considered. The latter is known as the Nilsson-Pettersson model. Both models agree that π-interactions stabilize the CO-metal interaction, while σ-interactions destabilize the CO-metal interaction. Zeinalipour-Yazdi and van Santen [18] showed that the π back-donation is sensitive to the number of bonds connected to a metal atom.

The HOMO of CO (the 5σ molecular orbital) can overlap with the unoccupied d_{z^2} and *s* orbitals of the transition metals, allowing for electron donation from CO to the metal. The LUMO of CO (the 2π* molecular orbital) can overlap with the occupied d_{xz} and d_{yz} orbitals of the transition metal. If the LUMO 2π* orbital is shifted below the Fermi level back-donation of electrons from the metal to CO can take place. The spreading of the 2π* orbital to below the Fermi level of the surface occurs on metallic iron surfaces [3,5] and iron carbide surfaces [16].

Metallic iron is a simple model system that can be used to investigate the reaction pathway for the Fischer-Tropsch synthesis [4,19,20]. The lower Miller index structures of iron metal surfaces have been extensively studied [4–8]. On the Fe (111) surface, CO adsorption has been studied up to a coverage of 2 ML [5]. At lower coverages (<0.5 ML) the most stable configuration of CO is the adsorption in the shallow-hollow site with the C-O bond normal to the surface. Above a coverage of 1 ML, the energetically most stable configuration of CO is on the on-top site with the C-O bond slightly tilted from the surface normal at an angle of 10°. It has been shown that CO adsorbs strongly on the Fe (110) surface and is most stable on the on-top site with the C-O bond normal to the surface as shown both experimentally and theoretically [6],[21]. On the Fe (100) surface, CO can adsorb in either the four-fold hollow site, bridge site or the on-top site. For the hollow site, the C-O bond can either be normal to the surface or tilted away from the normal. It is seen both experimentally and theoretically that CO is absorbed in its most favoured state in the hollow site and is tilted 45° ± 10° away from the normal is the most stable configuration [3,4,7,8,18] at lower coverages but re-orientates to in the hollow site and normal to the surface at higher coverages. On all the lower Miller index surfaces the heat of adsorption decreases with increasing coverage [3–8,18,21]. This decrease in heat of adsorption can be attributed to the lateral interactions between the adsorbates.

Lateral interactions have been investigated both experimentally [22,23] and theoretically [3,8,16,24] for the adsorption of CO on metal surfaces. Lateral interactions can be classified as through-surface or through-space interactions [25]. Even though these classifications have been made, very little is written about the explicit energetic contributions to the lateral interactions i.e. how much of the interaction can be contributed to electrostatic interactions, orbital overlap, etc. The general trend in

[10] This is only a small sample of hundreds

literature is to calculated the overall changes in activation energy or adsorption energy due to lateral interactions and postulate reasons for these changes [22,26–31].

Through-space interactions are typically "long" range interactions such as electrostatics/van der Waals interactions [18,31,32]. If the chemisorption involves a charge transfer, dipole moments are created on the surface, which can be modelled using the classical physics dipole-dipole interactions. For large dipole moments the interactions are measurable over a distance as large as 32 Å [33].

Through-surface interactions are seen as changes in adsorption and reaction energy as a result of the electronic interactions through the substrate surface due to co-adsorption of adsorbates. The chemisorption of an adsorbate involves the overlapping of adsorbate and substrate orbitals. The occupancy of the substrates orbitals is thus altered, altering the overlapping with other adsorbates. This interaction is dependent on the number of surface atoms shared amongst adsorbates [25]. Chemisorbed adsorbates which are close enough for orbitals to overlap show strong interactions [25,31]. As the lateral distance between these adsorbates increases the interactions energy decreases exponentially [18].

Typical through-surface interaction models such as the bond order conservation and other nearest neighbour models are independent of the adsorbates involved i.e. through surface interactions when the surface is covered with H and through surface interactions when the surface is covered with CO are seen to be equivalent. This is obviously an oversimplification as it is well documented that changes in heats of adsorption for H and CO are significantly different. Furthermore, it has been shown [3,4,6,34] that at Fischer-Tropsch conditions the coverage of CO is limited to a coverage 0.65 ML and the coverage of H is limited to 1 ML. These limited coverages being a result of lateral interactions

In this study, density functional theory (DFT) calculations were used to model the adsorption of CO on Fe (100). Larger p(4x4) unit cells were used to create a greater variety of configurations than those traditionally used i.e. the p(2x2) unit cells. An energetic breakdown of the lateral interactions involved is proposed.

3.2 Methodology

3.2.1 DFT Calculations

The CASTEP suite [35], part of the Materials Studio software package [36] was used for the calculations. The RPBE functional [37] was used, hence GGA was used to calculate the exchange-correlation energy. A Gaussian smearing width of σ = 0.1 eV was utilized in all calculations. The ion-electron interactions were approximated using ultrasoft pseudopotentials with core corrections and a cutoff energy was set at 400 eV. A five-layer slab with three layers relaxed was used with an optimized vacuum spacing of 10 Å between surfaces. The k-point grid was generated using the Monkhorst-Pack[38] procedure with a k-point spacing of <0.03 $Å^{-1}$. Spin-polarization was allowed for all calculations

The integral adsorption energy is the average adsorption energy of a configuration and is calculated as follows:

$$E_{ads,CO} = \frac{E_{(Fe+nCO)} - E_{(Fe\ Slab)}}{n} - E_{CO} \qquad (3.1)$$

Where $E_{(Fe+nCO)}$ is the energy of *n* CO molecules on an iron surface, $E_{(Fe\ Slab)}$ is the energy of a clean iron surface and E_{CO} is the energy of CO in the gas phase

The differential adsorption energy can be used to describe the adsorption of individual adsorbates of a particular configuration as is calculated as follows:

$$\bar{E}_{ads,CO} = E_{(Fe+nCO)} - E_{(Fe+(n-1)CO)} - E_{CO} \qquad (3.2)$$

The interaction between the CO molecules and the iron surface caused a shift in the position of the iron atoms. This shift in positions occurs mainly with the first Fe layer even though three layers are relaxed. If the configuration is frozen and the adsorbate(s) removed, we can compare this 'deformed' structure with the clean Fe (100) surface. The energetic contribution due to this shift in metal surface was considered part of the lateral interactions. To measure this quantity, the adsorbates were removed and a single point energy calculation was completed. The deformation energy was then the difference in energy between the clean optimised Fe surface and the single point energy calculation. The deformation of the iron surface was then calculated as follows:

$$E_{deform} = E_{[(Fe+nCO)-nCO]} - E_{(Fe\ Slab)} \qquad (3.3)$$

Where $E_{[(Fe+nCO)-nCO]}$ is the energy of the geometry optimized iron/CO surface having removed the CO molecules and $E_{(Fe\ Slab)}$ is the energy of a clean geometry optimized iron surface. [11]

The mapped difference in the electron density for the configurations considered is also produced. This is achieved by subtracting the electron density of the clean surface from the electron density of the slab with adsorbed molecules as shown in Figure 2-9. The result is electron density of the adsorbed CO and the electron density changes it induces on the metal. It is expected that the electron density attributed to the electrons not involved in the interactions, for the most part core electrons, would cancel each other out and only deviations in what was classically know as frontier orbitals [25,39–41] will be seen. The changes to the metal are seen as a change in colour from dark blue to teal, which indicates the repositioning of electrons relative to the clean surface.

3.2.2 Energetic breakdown

In order to find an energetic breakdown for the lateral interactions, all the terms included in the Hamiltonian need to be considered. For CASTEP [35] the resulting energies are the kinetic energy, Hartree energy, local and non-local pseudopotential energies, exchange-correlation energy, Ewald energy and non-Coulombic energy.

The energy contribution to the total electronic energy of each of the terms was considered and the change in each energy on adsorption was considered. This was calculated using the same procedure to calculate the integral adsorption energy was calculated. This means:

$$E_{i,ads} = \frac{E_{i,(Fe+nCO)} - E_{i,(Fe\ Slab)}}{n} - E_{i,CO} \qquad (3.5)$$

Where i is either the kinetic energy, Hartree energy, local or non-local pseudopotential energies, exchange-correlation energy, Ewald energy or non-Coulombic energy.

3.2.3 Unique configurations

Due to computational time and the resources available, DFT calculations for periodic systems were traditionally calculated on p(2x2) unit cells for Fe (100) [4,8,34,43]. As a result, the number of geometric configurations per unit cell was limited and only coverages of 0.25 ML, 0.5 ML, 0.75 ML, and 1.0 ML have typically been calculated [3,4,34]. In principle, at a coverage of $\theta = n/m$ where n is the number of adsorbates and m is the total number of adsorption sites, the total number of configurations is given by $\frac{N!}{n!(N-n)!}$. However, since the different configurations are periodic, all rotations, translations and reflections yield equivalent configurations. Hence, at a p(2x2) cell for a coverage of 0.5 ML there are only 2 unique configurations instead of the 6 possible configurations.

[11] He deformation energy will always be positive since the clean slab is the minimum of the Fe (100) surface

The equivalence between various configurations is illustrated for a coverage of 2/9 on a p(3x3) cell in Figure 3-1. Therefore, only unique configurations should be considered.

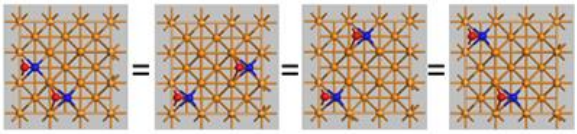

Figure 3-1: Equivalent configurations of a 2/9 ML coverage of CO on Fe (100) for a p(3x3) unit cell

By eliminating equivalent configurations, the total number of unique configurations in a particular unit cell size can be calculated[12]. This is shown in Figure 3-2. Note only adsorption in the hollow site was considered for this study. For the p(2x2) unit cells a total of 16 configurations are possible but only 6 are unique. For the p(3x3) unit cells a total of 512 configurations are possible but only 27 are unique. For the p(4x4) unit cells a total of 65536 configurations are possible but only 805 are unique. Note that this assumes that CO is only tilted in the hollow and does not consider different orientations at higher coverages, this will of course further increase the possible configurations.

Advancements in computing power have made calculations on larger unit cells feasible. For the purposes of this study the adsorption of CO on Fe (100) was investigated on p(4x4) unit cells.

[12] This is valid assuming a maximum coverage of one adsorbate per p(1x1) cell, which is the case for CO adsorption on Fe (100) [46]

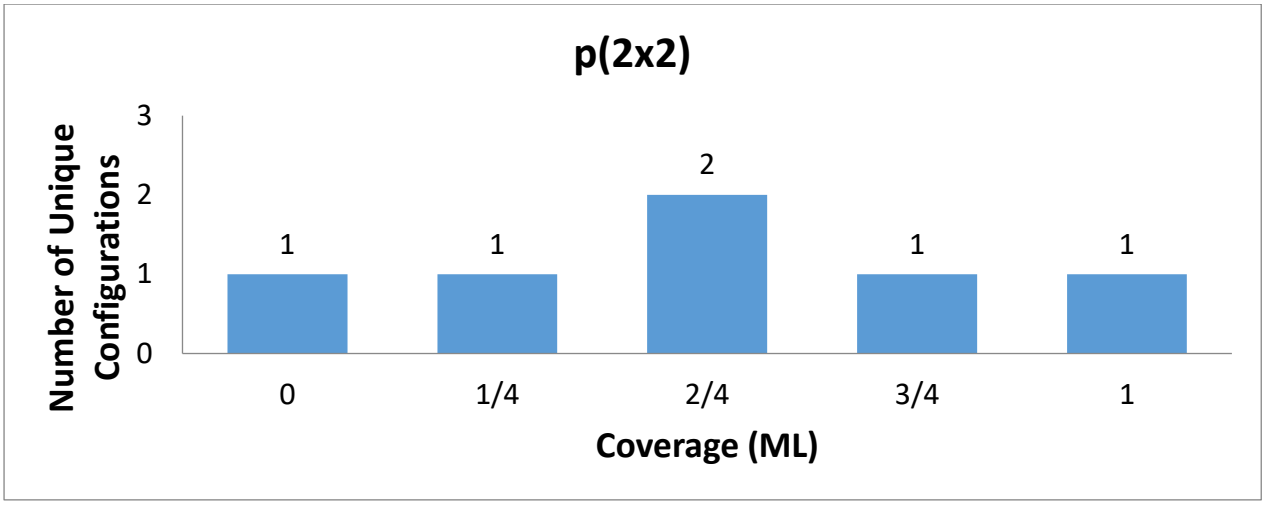

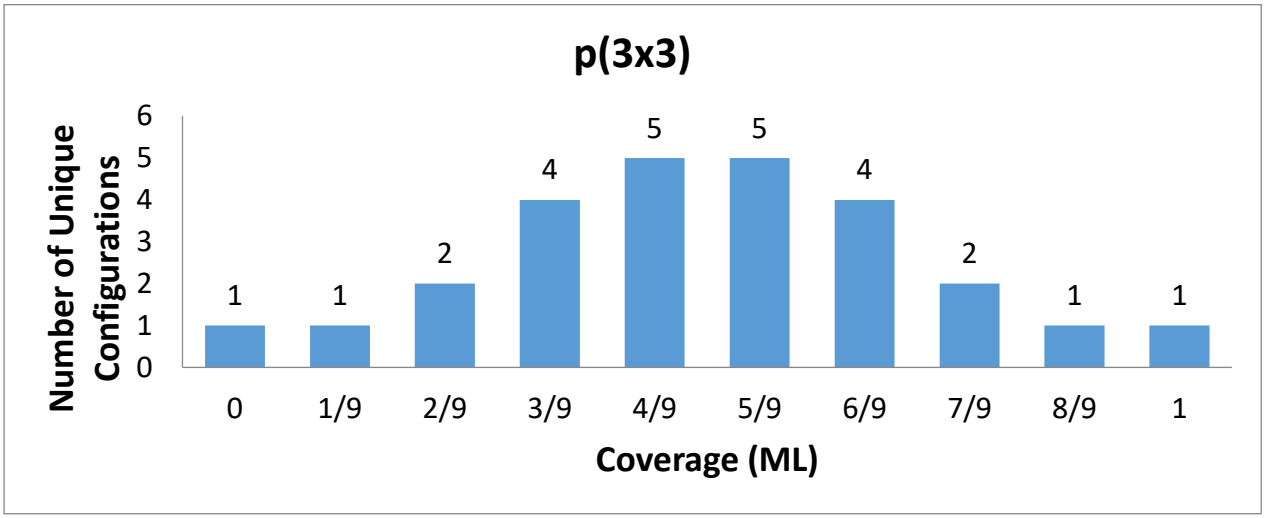

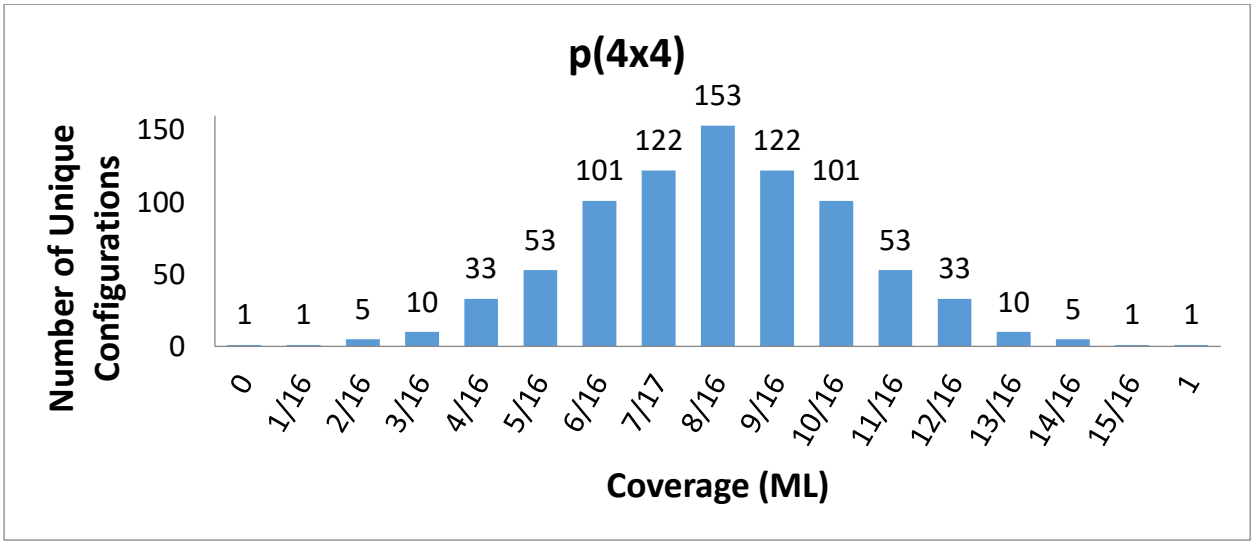

Figure 3-2: Unique configurations for CO adsorbed in the hollow site on Fe (100) for a) p(2x2) unit cells, b) p(3x3) unit cell and c) p(4x4) unit cell.

3.2.4 Vibrational frequencies and temperature corrections

A partial Hessian vibrational analysis was performed using density functional perturbation theory [44,45]. The vibrational analysis was performed using perturbations of 0.005 Å in the Cartesian space. From this analysis, we obtained the vibrational frequencies of the considered atoms.

Thermodynamic variables like the Gibbs free energy, enthalpy, entropy and pressure can be expressed in terms of the partition function or as a derivate of the partition function. The partition function differs with respect to the degrees of freedom. In this chapter only the stable adsorbed state of CO titled in the hollow site is considered, for which the partition functions correspond to 3N vibration degrees of freedom. The partition function for vibrations is written as:

$$p.f_{\cdot vibrational} = \sum_{n=0}^{\infty} e^{-\left(n+\frac{1}{2}\right)\cdot\frac{h\cdot\nu}{k_b\cdot T}} = \frac{e^{-\frac{1}{2}\cdot\frac{h\cdot\nu}{k_b\cdot T}}}{1-e^{-\frac{h\cdot\nu}{k_b\cdot T}}} \quad (3.\ 6)$$

where k_B is the Boltzmann constant, h is Planck constant, T is temperature and v is the vibrational frequency[13].

For adsorption and desorption, the translational and rotational degrees of freedom of the particles in the gas phase should also be considered.

$$p.f_{\cdot trans} = V \cdot \left(\frac{2\cdot m\cdot k_b\cdot T}{h^2}\right)^{\frac{3}{2}} \quad (3.\ 7)$$

The rotational partition function for linear molecules:

$$p.f_{\cdot rotational} = \frac{8\cdot\pi^2\cdot I}{\sigma\cdot h^2}\cdot k_b\cdot T \quad (3.\ 8)$$

The enthalpies and entropies and hence the Gibbs energy can be calculated from the partition functions

$$H = k_b\cdot T^2\cdot\frac{\partial ln(\,p.f_{\cdot x})}{\partial T} \quad (3.\ 9)$$

$$S = \frac{\delta}{\partial T}\ (k_b\cdot T\cdot ln(\,p.f_{\cdot x}\,)) \quad (3.\ 10)$$

The resulting Gibbs free energy is then

$$G = E_{Elec} + (H_{rot} + H_{trans} + H_{vib}) - T(S_{rot} + S_{trans} + S_{vib} - kTln\left(\frac{P}{P_0}\right)) \quad (3.\ 11)$$

[13] This derivation of the vibrational partition function includes the ZPE correction. If it the ZPE correction is calculated separately the partition function is of the form: $p.f_{\cdot vibrational} = 1/(1-e^{-\frac{h\cdot\nu}{k_b\cdot T}})$

3.3 Results

The lateral interactions in the adsorption of CO on Fe (100) at 0.25 ML was investigated by comparing six p(4x4) surface supercells. A 1/16 ML configuration was considered to have negligible lateral interactions in order to quantify the lateral interactions of the 0.25 ML configurations. Any deviations from this case were then considered a result of lateral interactions. For the rest of this chapter this configuration will be called the Single CO configuration.

For the Single CO configuration, the adsorption energy was found to be -1.91 eV/CO. The C-O bond length was found to be 1.304 Å, a tilt angle of 46.8° away from the normal and a stretching frequency of 1169 cm^{-1} was observed. This agrees with the experimental results [46–49] which show a tilt angle of 45° ± 10°, a stretching frequency of 1210 cm^{-1} and an elongated C-O bond length of 1.20 Å ± 0.02 Å. The experimental adsorption energy for CO is 1.14 eV at 440 K [46]. This will be explored in more detail in the section 3.3.2, regarding temperature corrections. The Mulliken charge on the C atoms was found to be -0.42 e, while the charge on the O atoms was -0.46 e.

As mentioned above the interaction between the CO molecules and the iron surface caused a shift in the position of the iron atoms. This shift in positions occurs mainly with the first Fe layer even though three layers are relaxed. The primary Fe atoms (see Figure 3-3) move in towards the CO and the hollow site. The deformed iron surface differed by 0.27 eV/CO from a clean relaxed surface.

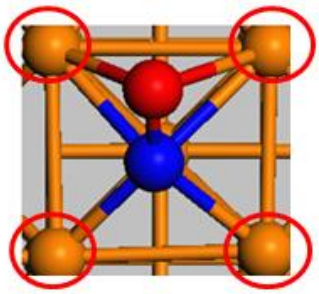

Figure 3-3: Fe atoms considered as "Primary" Fe atoms

In Figure 3-5, the density of states (DOS) for CO in the gas phase and the Single configuration is compared along with the orbitals associated with the respective peaks[14]. As seen in literature [3,15,40], the 2π* molecular orbital significantly broadens and shifts to below the Fermi level of Fe (-6.2 eV) allowing for back donation of electrons. The broadening of this orbital does not allow for clear identification and selection of peaks[15] and hence the orbital cannot be a visualized. The other orbitals also shift to lower energy levels. The shape of the orbitals, particularly the 4σ, 5σ and 1π orbitals, have changed, possibly due to additional hybridization with the Fe orbitals. Furthermore, for the adsorbed CO there are no discrete peaks for the 1π and 5σ molecular orbitals but rather one peak which can be interpreted as a hybridization of the 1π, 5σ and Fe orbitals.

The six unique geometries calculated at a coverage of 0.25 ML of CO adsorbed on p(4x4) unit cells of Fe (100) were optimized to demonstrate the effect of lateral interactions on the adsorption energy and can be seen in Figure 3-4. Table 3-1 summarizes some the results obtained for the configurations considered. In the "0 Share" configuration, CO is adsorbed on a p(1x1) subunit cell, which does not share an Fe-atom with another p(1x1) unit cell in which CO is adsorbed. For the "Diagonal", "Corner Share" and "2 Share" configurations, CO is adsorbed on a p(1x1) subunit cell which shares two Fe-atoms with other p(1x1) unit cells in which CO is adsorbed. For the "Cluster" configuration, CO is adsorbed on a p(1x1) subunit cell which shares three Fe-atoms with another p(1x1) unit cell in which

[14] The alpha spin states are shown here, but negligible difference was seen on the beta spin DOS

[15] A few thousand “peaks” corresponding to the energy range of the broadened 2π* molecular orbital some of which belong to the Fe atoms.

CO is adsorbed. Finally, for the "4 Share" configuration, CO is adsorbed on a p(1x1) subunit cell which shares four Fe-atoms with another p(1x1) unit cell in which CO is adsorbed.

The “0 Share” configuration is equivalent to the p(2x2) calculations completed in previous studies at 0.25 ML for CO adsorption on Fe (100). It is used in this study to compare the calculations completed here with the work completed in literature. For the "0 Share" configuration, the adsorption energy was found to be -1.88 eV/CO. The C-O bond length was found to be 1.304 Å and a tilt angle of 47.8° away from the normal was observed. These values are in good agreement with the work done by Sorescu[16] [8], who found a adsorption energy of -1.84 eV/CO, C-O bond length of 1.316 Å and tilt angle of 48° away from the normal, and van Helden[17] [43], who found a adsorption energy of -1.88 eV/CO, C-O bond length of 1.308 Å and tilt angle of 47.7° away from the normal. Again this agrees with the experimental results [46–49] which show a tilt angle of 45° ± 10°, a stretching frequency of 1210 cm^{-1} and an elongated C-O bond length of 1.20 Å ± 0.02 Å. The Mulliken charge on the C atoms was found to be -0.41 e, while the charge on the O atoms was -0.46 e, also in good agreement with that of van Helden[43].

The deformed iron surface differed by 0.098 eV/CO from a clean relaxed surface. It is interesting to note that the 1/16 ML configuration has a deformation energy of 0.27 eV/CO. This seems to indicate that the additional deformation energy for the additional three CO molecules does not increase the deformation energy as much. Much like we expect the differential adsorption energy to be less than the integral adsorption energy, the differential deformation energy will be less than the integral deformation energy. This could be a result of either CO 1/16 ML Fe (100) being more resistant to changes on the surface and/or the CO adsorbate shielding the surface from additional deviations.

For the "Diagonal” configuration, the adsorption energy was found to be -1.93 eV/CO. For this configuration, the lateral interactions seem to stabilize the CO adsorption. This is amplified by a lower contribution of the deformation energy i.e. removing the difference in the deformation energy, the stabilization seems to be even stronger. Sorescu [50] showed that C on Fe (100) shows a similar stabilizing effect if the adsorbates are in a c (2x2) patter, like the Diagonal pattern. This stabilization was seen for C-C interactions as well as C-O, C-H C-CH, C-CH_2 and C-CH_4 interactions.

The C-O bond length was found to be 1.304 Å and a tilt angle of 47.0° away from the normal was observed. The charge on the C atoms was found to be -0.42 e, while the charge on the O atoms was -0.45 e. The deformed iron surface differed by 0.098 eV/CO from a clean relaxed surface. Again, the deformation energy is less per CO than the 1/16 ML configuration.

[16] Calculations completed with VASP, GGA PW91

[17] Calculations completed with CASTEP, GGA RPBE

Table 3-1: Summary of some configurations for CO adsorption on Fe (100) at a coverage of 0.25 ML on a p(4x4) cell

Configuration	Heat of Ads. (eV/CO)	Fermi Energy (eV)	C-O Bond Length (Å)	C-Fe Distance (Å)	CO tilt Angle from normal	Fe Deform. (eV/CO)	Charge on C (e)	Charge on O (e)
Single CO	-1.91	-6.221	1.304	2.16	46.8°	0.270	-0.42	-0.46
0 Share	-1.88	-6.145	1.304	2.10	47.8°	0.098	-0.41	-0.46
2 Share	-1.79	-6.148	1.300	2.15; 2.10	47.7°; 44.4°	0.110	-0.39:-0.42	-0.45
Corner Share	-1.90	-6.146	1.301	2.10; 2.12	49.2°; 44.9°	0.096	-0.41:-0.44	-0.45
4 Share	-1.73	-6.134	1.285	2.21	50.2°	0.105	-0.34	-0.44
Cluster	-1.69	-6.130	1.291	2.11; 2.15	45.9°; 42.9°	0.119	-0.40	-0.44
Diagonal	-1.93	-6.150	1.304	2.11	47.0°	0.098	-0.42	-0.45

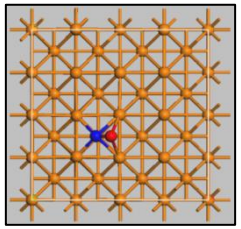

Single CO

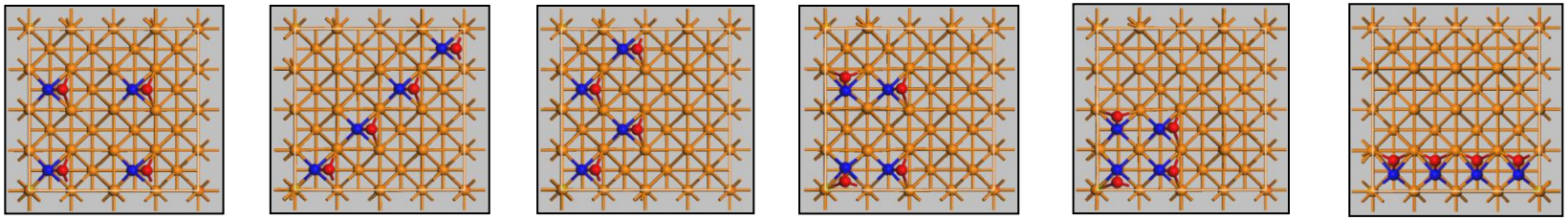

0 Share Diagonal Corner Share 2 Share Cluster 4 Share

Figure 3-4: Configurations studied at 0.25 ML

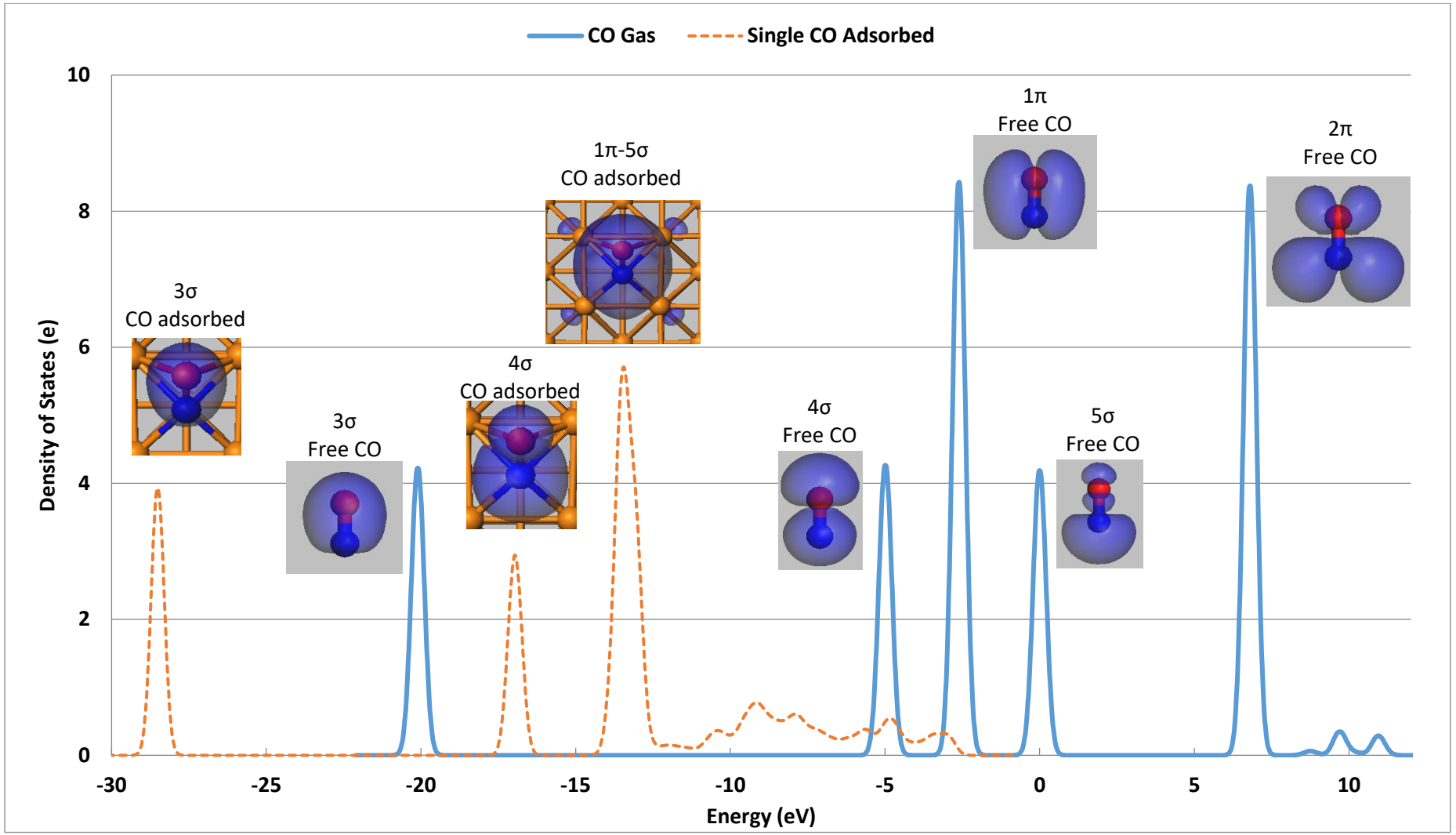

Figure **3-5:** Partial Density of States of CO in the Gas phase and CO in the "Single" configuration.

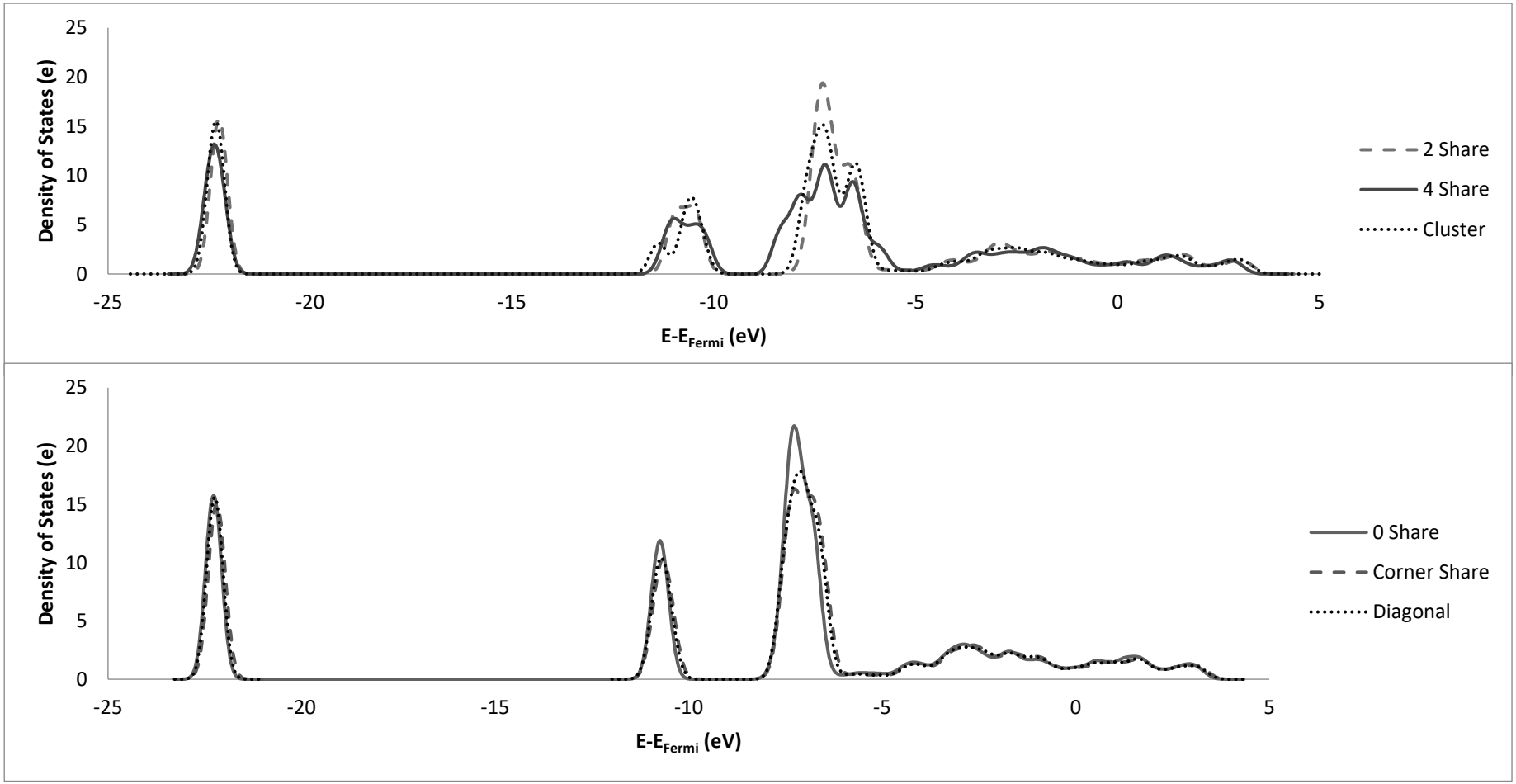

Figure 3-6: Partial Density of States of CO configurations on Fe (100) surface relative to the Fermi level. The Cluster and 4 share configurations also show a clear amount of orbital splitting.

For the "Corner Share" configuration, the integral adsorption energy was found to be -1.90 eV/CO. This is 0.01 eV less than the 1/16 ML configuration which is not significantly different. To conceptualize the differential adsorption energy we will need to consider four steps of CO adsorption. The first step will be the 1/16 ML configuration with an adsorption energy of -1.91 eV. The next 3 steps will involve interactions from the 0 Share and Diagonal configurations, with integral heats of adsorption of -1.88 eV and -1.94 eV. The CO adsorbates with the single space will slightly repel each other and the CO adsorbates that are next nearest neighbours will slightly attract each other.

Even though the differential adsorption energy will show a larger difference it is still not significantly lower. The C-O bond length was found to be 1.301 Å. Two unique CO adsorbate environments exist for this configuration. One with a tilt angle of 49.2° away from the normal and charge on the C atom of -0.41e and one with a tilt angle of 44.9° away from the normal and charge on the C atom of-0.44 e. The charge on all the O atoms was -0.45 e. The deformed iron surface differed by 0.096 eV/CO from a clean relaxed surface.

For the "2 Share" configuration, the adsorption energy was found to be -1.79 eV/CO. Allowing for geometry optimization, we see the adjacent CO adsorbates are perpendicular to one another. The adsorbate-adsorbate interaction may result in a re-orientation of the adsorbate structure as indicated by Nørskov [51]. The C-O bond length was found to be 1.300 Å. Two unique CO adsorbate environments exist for this configuration. One with a tilt angle of 47.7° away from the normal and charge on the C atom of-0.39 e and one with a tilt angle of 44.4° away from the normal and charge on the C atom of -0.42 e. The charge on all the O atoms was -0.45e. The deformed iron surface differed by 0.110 eV/CO from a clean relaxed surface.

For the "Cluster" configuration, the adsorption energy was found to be -1.69 eV/CO. For this configuration, each CO adsorbate has one CO nearest neighbour with the same orientation, one CO nearest neighbour that is perpendicular in orientation and one next nearest neighbour. The C-O bond length was found to be 1.291 Å. Two unique CO adsorbate environments exist for this configuration, one with a tilt angle of 45.9° away from the normal one with a tilt angle of 42.9° away from the normal. The charge on the C atoms was found to be -0.40 e, while the charge on the O atoms was -0.44 e. The deformed iron surface differed by 0.119 eV/CO from a clean relaxed surface.

For the "4 Share" configuration, the adsorption energy was found to be -1.73 eV/CO. In this configuration, the CO adsorbates are all in the same "row" on the surface and each CO adsorbates has two nearest neighbours. The C-O bond length was found to be 1.285 Å and a tilt angle of 50.2° away from the normal was observed. The charge on the C atoms was found to be -0.35 e, while the charge on the O atoms was -0.44 e. The deformed iron surface differed by 0.105 eV/CO from a clean relaxed surface.

Looking at the adsorption energy, we see that "Diagonal" configuration displays the highest adsorption energy at -1.93 eV, while the "Cluster" configuration displays the lowest adsorption energy at -1.69 eV. While most work on lateral interactions show a change in adsorption energy with increasing surface coverage [3,4,7,8,43], this work shows that the adsorption energy can differ by as much as 0.24 eV at 0.25 ML.

The deformation energy does appear to be a stronger function of coverage since the deformation energy is 0.270 eV/CO at 1/16 ML and 0.104 eV/CO ± 0.008 eV for the 0.25 ML configurations. While the deformation per CO adsorbed is lower for 0.25 ML coverages, the deformation energy per unit cell is larger i.e. at 1/16 ML it is 0.270 eV per unit cell and at 0.25 ML it is approximately 0.420 eV per unit cell. This means that even though the deformation energy per CO decreases on increasing coverage, sequential CO adsorption will continue to deform the surface.

Figure 3-6 displays the DOS of CO for the configurations studied relative to the respective Fermi levels. The same trends observed for the Single configuration are seen in these DOS. The $2\pi^*$ molecular

orbital significantly broadens and shifts to below the Fermi level of Fe (-6.2 eV) allowing for back donation of electrons. The other orbitals also shift to lower energy levels. Again, for the adsorbed CO there are no discrete peaks for the 1π and 5σ molecular orbitals but rather one peak which can be interpreted as a hybridization of the 1π, 5σ and Fe orbitals. Additionally, the 4 share and Cluster configurations show clear orbitals splitting.

If we consider the CO adsorbates themselves, Figure 3-7 below shows the subtle trend of increasing adsorption energy with decreasing C-O distance at 0.25 ML. We see that with configurations with low local coverage the C-O distance is longer than for configurations with high local coverage.

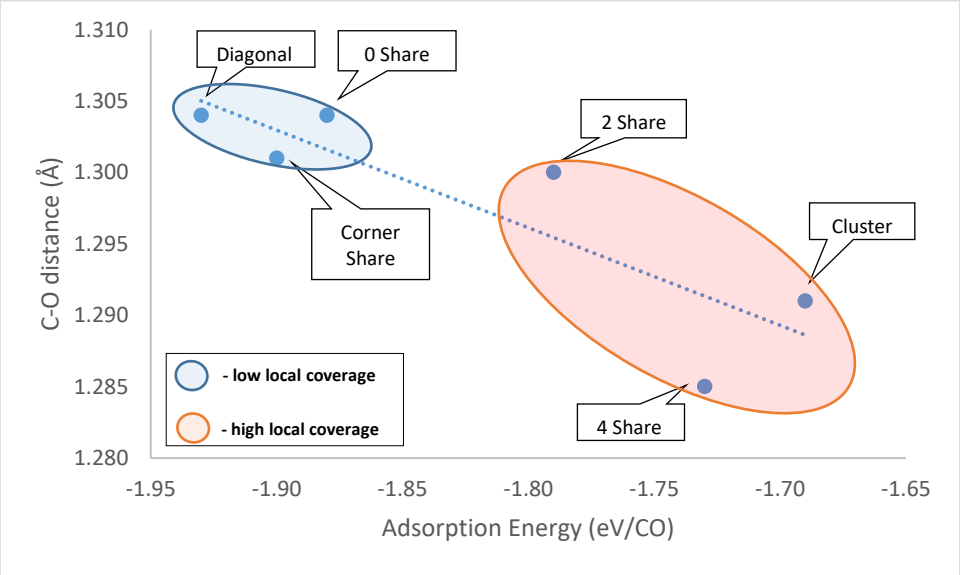

Figure 3-7: Adsorption energy of 0.25 ML of CO on Fe (100) for the coverages considered

All the 0.25 ML configurations besides that 4 Share configuration have a reduced Fe-C bond in comparison to single CO. This means the Fe-C bonding is stronger and the C=O bond is weaker. Considering the classical interpretation of molecular orbitals and bonding, this would imply less electrons in the anti-bonding orbital.

The orbitals of the CO adsorbate interact with the orbitals of the metal surface. The DOS of Free CO in Figure 3-5 compared to that of the Single CO configuration shows how the LUMO 2π* CO molecular orbital band is shifted below the fermi level upon adsorption. The fermi energy becomes less negative as we move from lower coverage to higher coverage. A change of 0.07-0.09 eV can be seen when comparing 0.0625 ML (Single CO) to 0.25 ML. This would mean less back donation between metal orbitals and 2π* CO molecular orbitals. In context to the models of Blyholder [15] and Föhlisch et al. [17] this would mean that the CO adsorbate will have less of the π-interactions stabilization. Van Helden and van Steen showed that the fermi level can change by as much as 0.5 eV when comparing CO coverages of 0.25 ML to 0.5 ML [34].

It is important to note that the fermi level as it is described here is a “global” representation of the interactions between CO and Fe. Hence, when considering only the 0.25 ML configurations, the differences in fermi levels are small, much as 0.02 eV. It would not be uncommon to dismiss such small changes as nothing but computational error. Figure 3-8 shows that a subtle trend of increasing adsorption energy with increasing Fermi energy at 0.25 ML. The configurations that show the 2 Share, 4 Share and Cluster configurations, configurations with higher local coverage, show a lower fermi energy and a lower fermi energy and lower adsorption energy. Similarly, the configurations that show the Diagonal, Corner Share and 0 Share configurations, configurations with lower local coverage, show a higher fermi energy and lower adsorption energy.

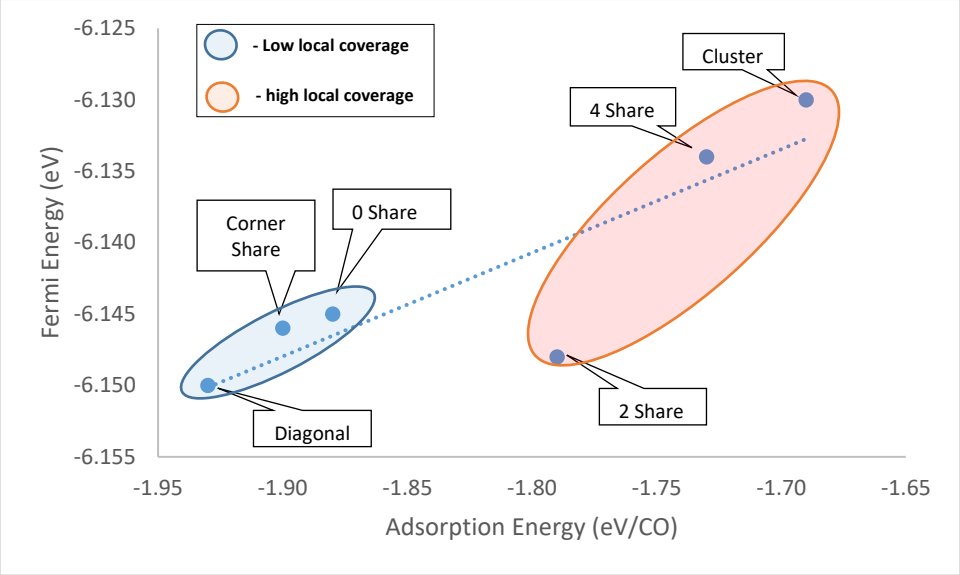

Figure 3-8: Adsorption energy with increasing fermi energy at 0.25 ML.

Charges associated with the atoms in the system as well as the change in electron density of the different configurations. The only significant changes for the Mulliken charges are for the 4 Share configuration. The electron density map in Figure 3-9 and the maps from Figure 3-10 onwards show how the presence of CO affects the electron density of the surface.

Figure 3-9 shows the electron density map in the plane running down the C-O bond for CO at 1/16 ML on Fe (100). Since the clean Fe electron density has been subtracted from the adsorption electron density, the change in colour from dark blue to teal indicates that electrons around the surface iron atoms have shifted. The change from dark blue to teal marked Fe_3 on the map shows the change in electrons around the Fe atom at the base of the hollow site. Figure 3-9 also shows the electron density map in the plane running along the first Fe layer for CO at 1/16 ML on Fe (100). Fe_1 on the map is the Fe atom closest to the O atom while Fe_2 is the Fe atom closest to the C atom. The electron density around Fe_2 appear to move towards C while the electron density around Fe_1 appear to move towards O.

This is in agreement with the Blyholder model [15] and the model proposed Föhlisch et al. [17] which postulates the dotation of electrons from metal. Furthermore, we see the Fe atoms at the base of the hollow site (Fe_3 in Figure 3-9) push electrons down away from the CO. This also both models which describe a back donation of electron, most likely with the π- orbitals.

Figure 3-10 shows the electron density maps for the 0 Share configuration. For each CO adsorbate in the 0 Share configuration the surrounding electron density is similar to that of the Single share configuration. The figure on the left shows the electrons of the Fe atom in the follow site move down and away from the CO adsorbate. The figure on the right shows the electrons of the Fe atoms in the first layer move towards the C and O atoms. In this case however, each Fe atom in the first layer forms part of a hollow site that has a CO chemisorbed to it. This means that each Fe atom in the first layer has its electrons either moved towards a C or O atom.

For the electron density maps of the 2 Share configuration, Figure 3-11 , the interactions with the Fe atom at the base of the hollow site looks similar to that of the Single CO configuration (figure on the left). The interactions with the Fe atoms in the first layer (figure on the right) does looks significantly different. There is no direct upwards movement of electron from a "Fe_1" type atom. Instead the electrons of the Fe atoms in the first layer all show some movement in this plain. The movement perpendicular to this plain will still be seen it is significantly different than when compared to the single CO configuration.

The 4 Share configuration electron density maps, Figure 3-12, again show the interactions with the Fe atom at the base of the follow site is similar to that of the Single CO configuration (figure on the left). Looking at the interactions with the first Fe layer, we do see a direct upwards movement of electron towards the O atoms from a "Fe_1" type atom but the accumulation of electrons on these atoms are significantly larger than for the Single CO. The Fe_2 type atoms also show a movement of electrons towards O, unlike in the Single CO configuration. The Fe atoms not part of the hollow site directly involved also show some unique electron densities. Looking at the proximity of the of the CO adsorbates and the larger charges on the primary Fe atoms, it is no surprise that this configuration shows a more repulsive electrostatic energy.

For the Cluster configuration, the electron density maps in Figure 3-13 shows interactions for both the electrons of the Fe atoms at the base of the follow site and the electrons if the Fe atoms in the fourth Fe layer. Furthermore, these electrons do not move away from the CO adsorbate, but to the side (in the same plain). For the figure on the right, we see that all the primary Fe atoms have significantly larger charges than that in of the Single configuration. The central Fe atom is shared by all four Co adsorbates and shows the largest charge. The electron densities around the CO adsorbates is significantly different from that of the single CO configuration.

Figure 3-14 shows the electron density maps for the Diagonal configuration. The figure on the left again shows electrons of the Fe atom at the base of the hollow site move down and away from the CO adsorbate. The figure on the right shows how the unshared Fe atoms behave like that of the Single CO configuration while the shared Fe atoms show some sort of hybrid effect of the Fe_1 and Fe_2 type atoms. The electron density of the Fe atoms shared between two CO adsorbates appear to move towards the C of the one adsorbate and towards the O of the other adsorbate. The Fe atoms in the first layer that are not part of the hollow sites of the CO adsorbates appear to also show some small repositioning of electrons.

Finally, the electron density maps of the Corner share configuration, Figure 3-15 , again shows electrons of the Fe atom at the base of the hollow site move down and away from the CO adsorbate (figure on the left). Like the Diagonal configuration, the figure on the right shows how the unshared Fe atoms behave like that of the Single CO. The shared atoms in this case behave very much like the Fe_1 atoms where the electrons move towards the O atom. The Fe atoms in the first layer that are not part of the hollow sites of the CO adsorbates appear to also show some small repositioning of electrons.

When CO adsorbates are close to one another, the charge on Fe_1 and Fe_2 (the primary Fe atoms in Figure 3-3) increase. While there is no question that electrostatics will be affected by magnitude of the electron densities of the different configurations, the changes in the shape of the electron density must also be considered, as this will affect the kinetic energy of the system.

The electron density maps shown in Figure 3-10 to Figure 3-15 show that the behaviour of primary Fe atoms that share CO adsorbates is different to that of Single CO configuration and other configurations which display no sharing of Fe atoms. This in in agreement with the work by Zeinalipour-Yazdi and van Santen[18] showed that the π back-donation is sensitive to the number of bonds connected to a metal atom.

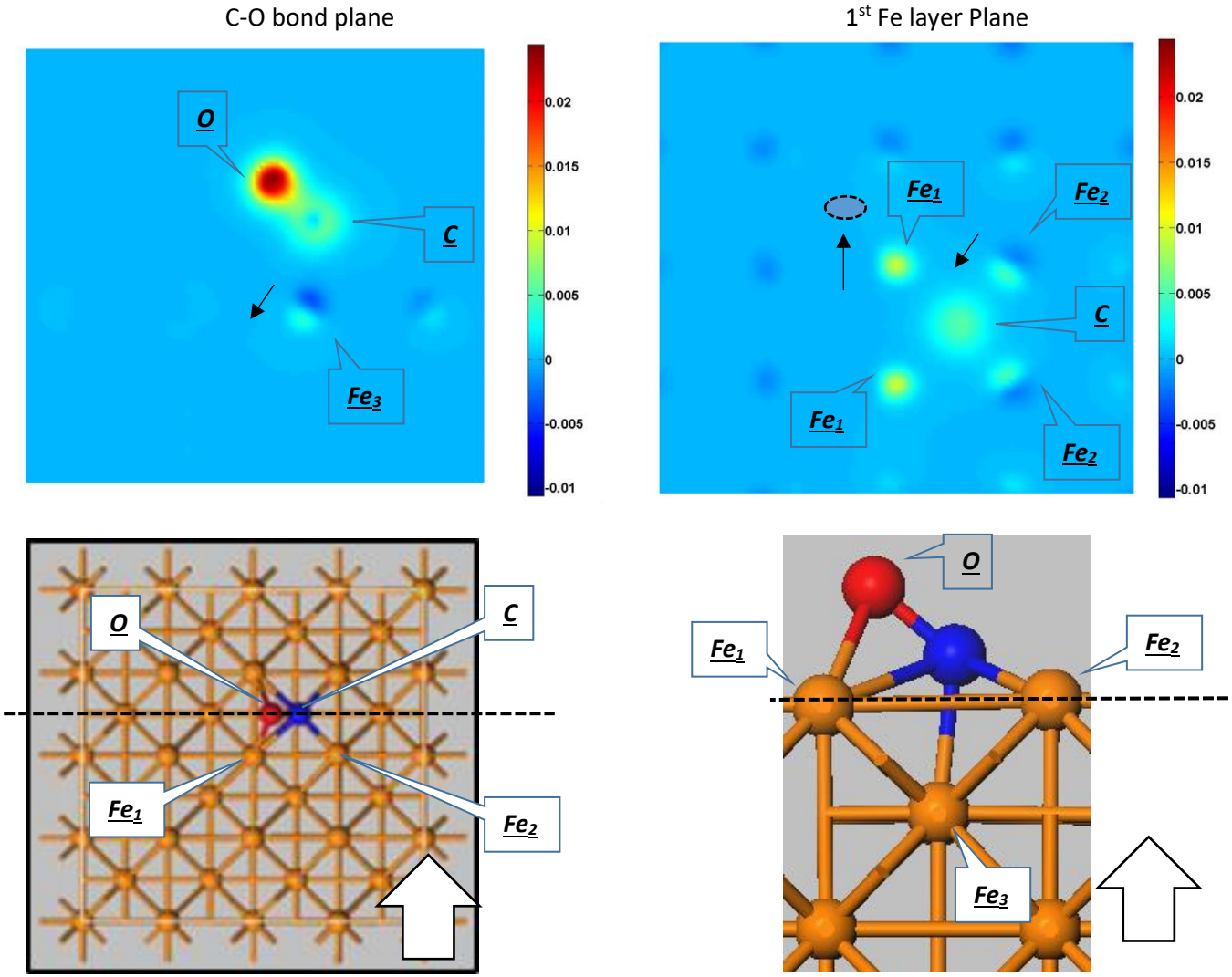

Figure 3-9: Electron density maps of Single CO configuration

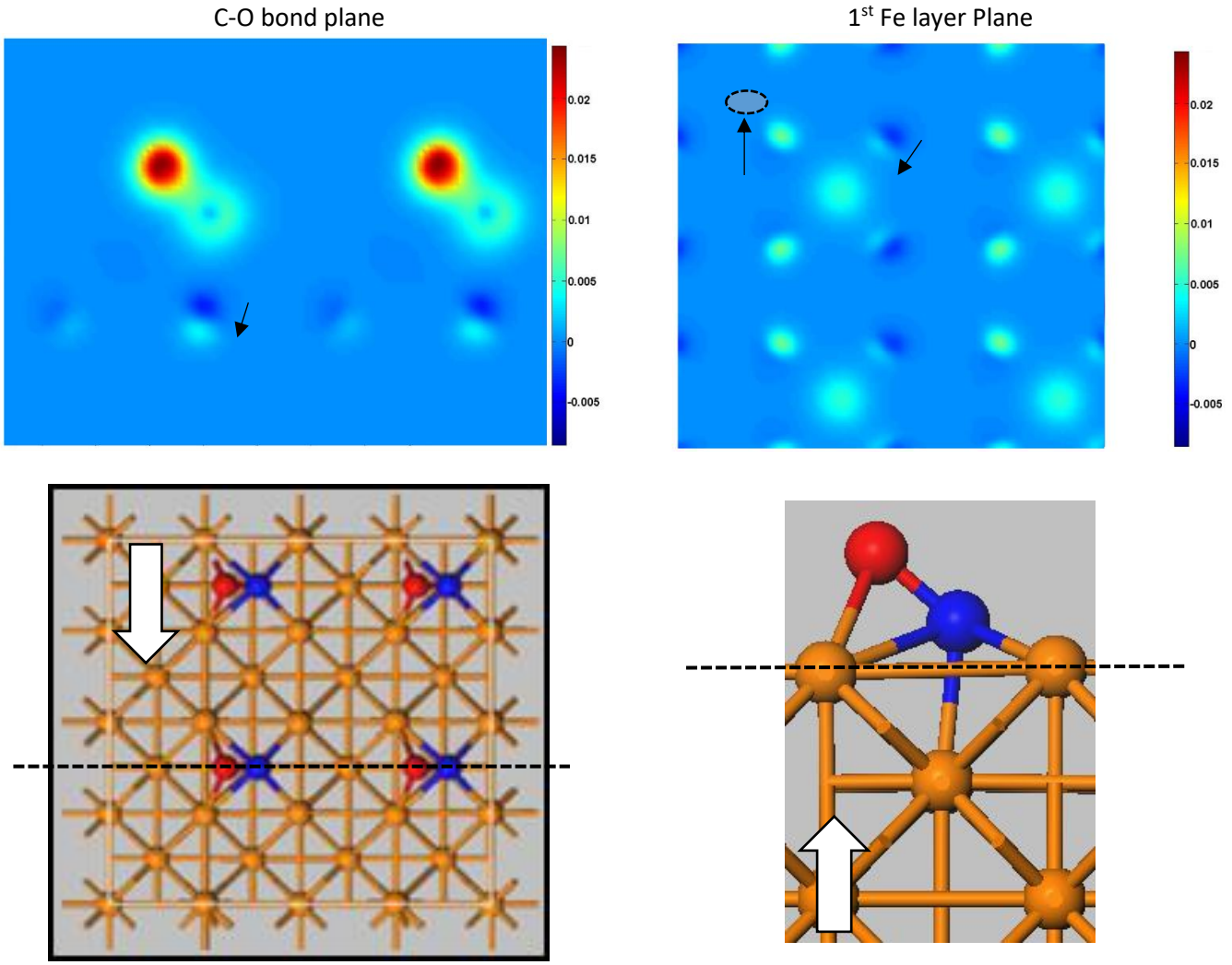

Figure 3-10: Electron density maps of 0 Share configuration

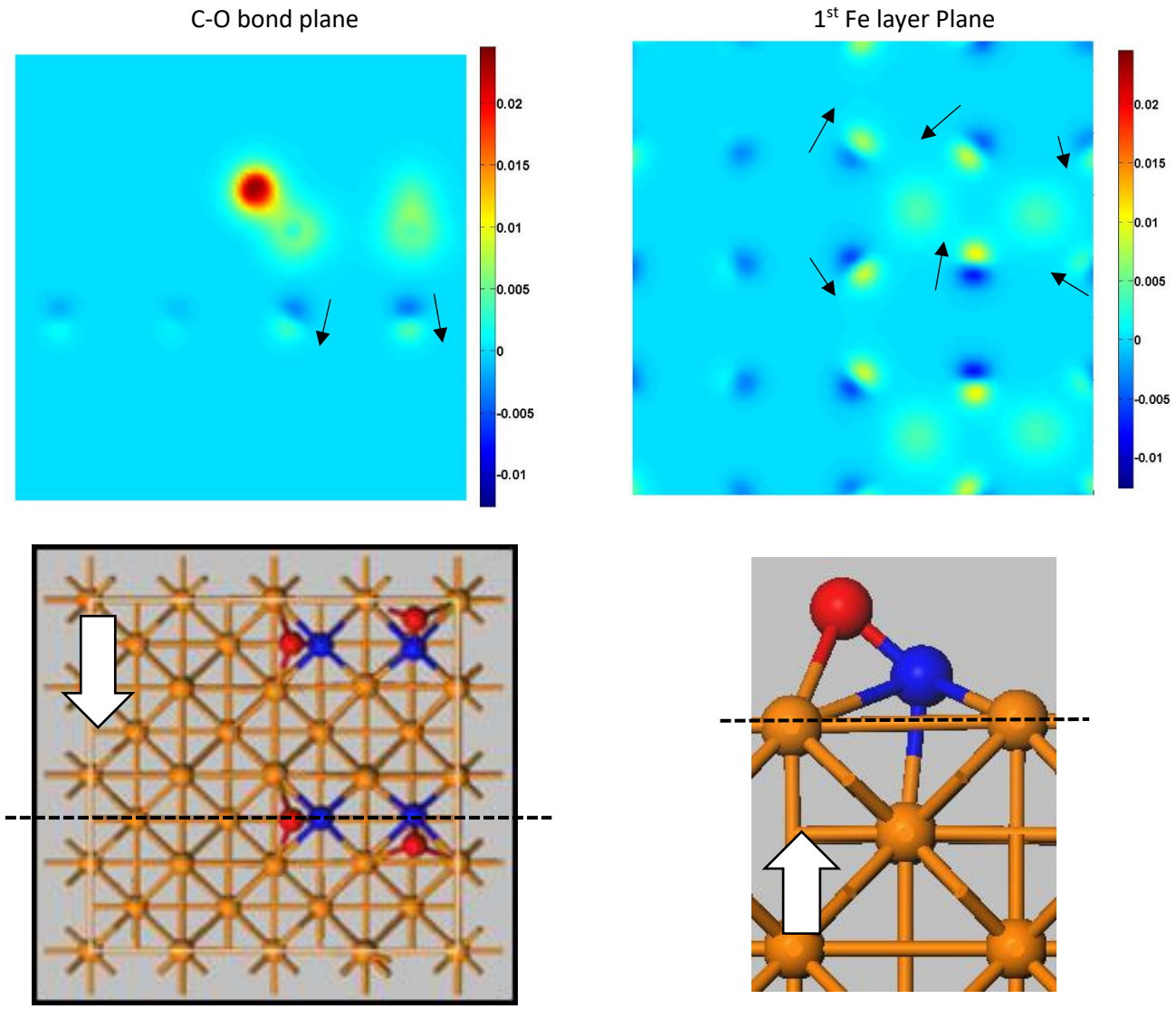

Figure 3-11: Electron density maps of 2 Share configuration

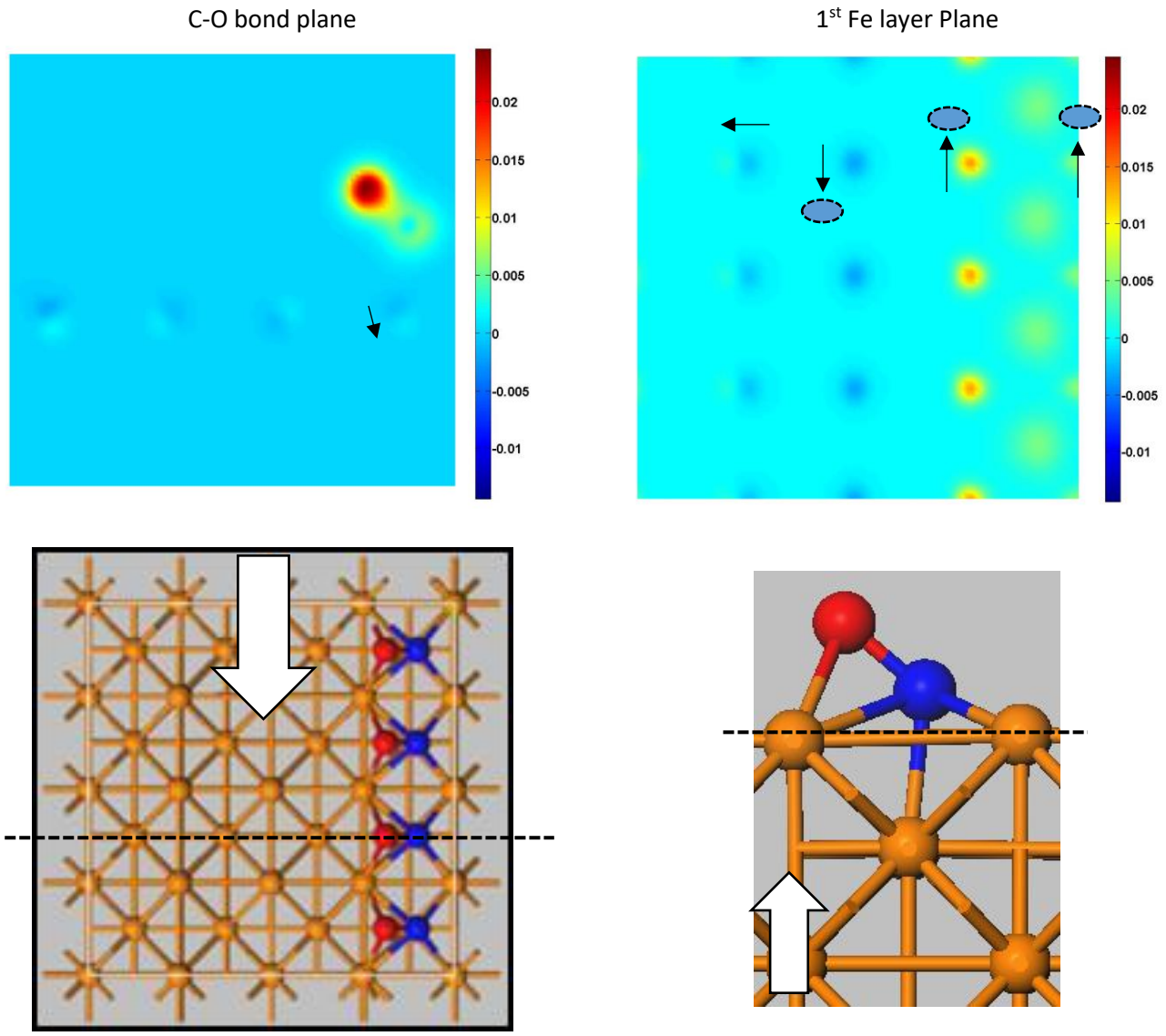

Figure 3-12: Electron density maps of 4 Share configuration

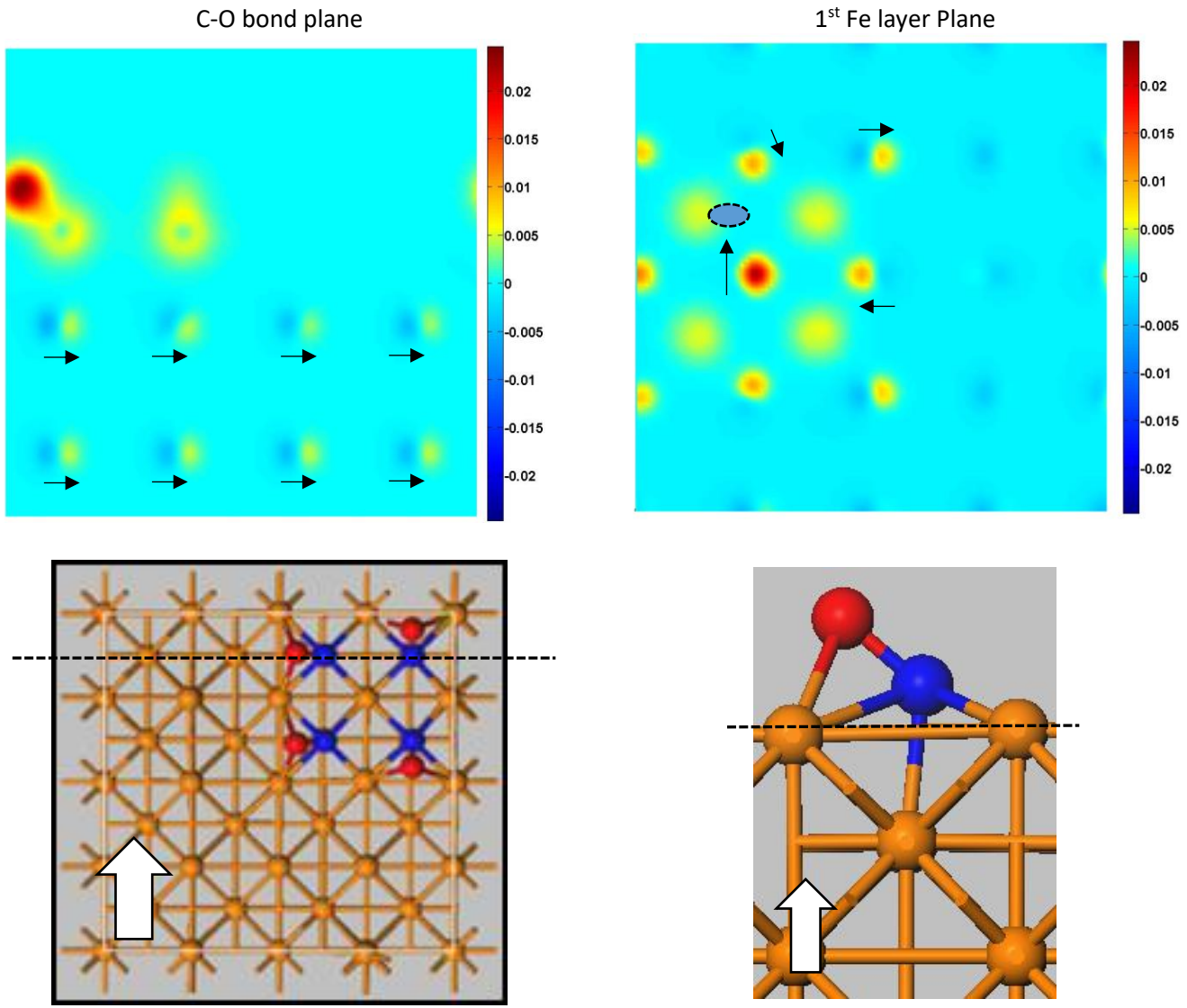

Figure 3-13: Electron density maps of the Cluster configuration

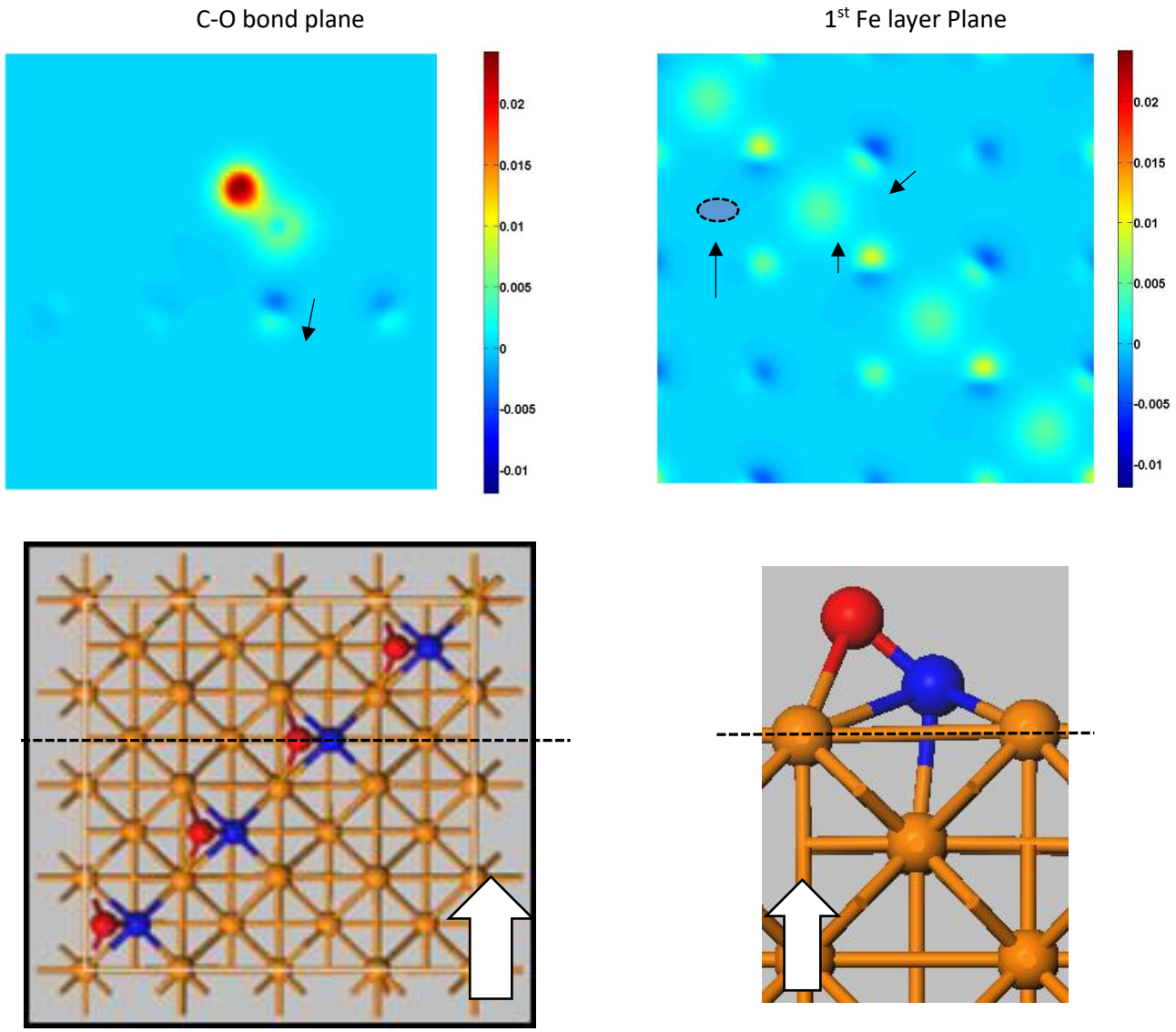

Figure 3-14: Electron density maps of the Diagonal configuration

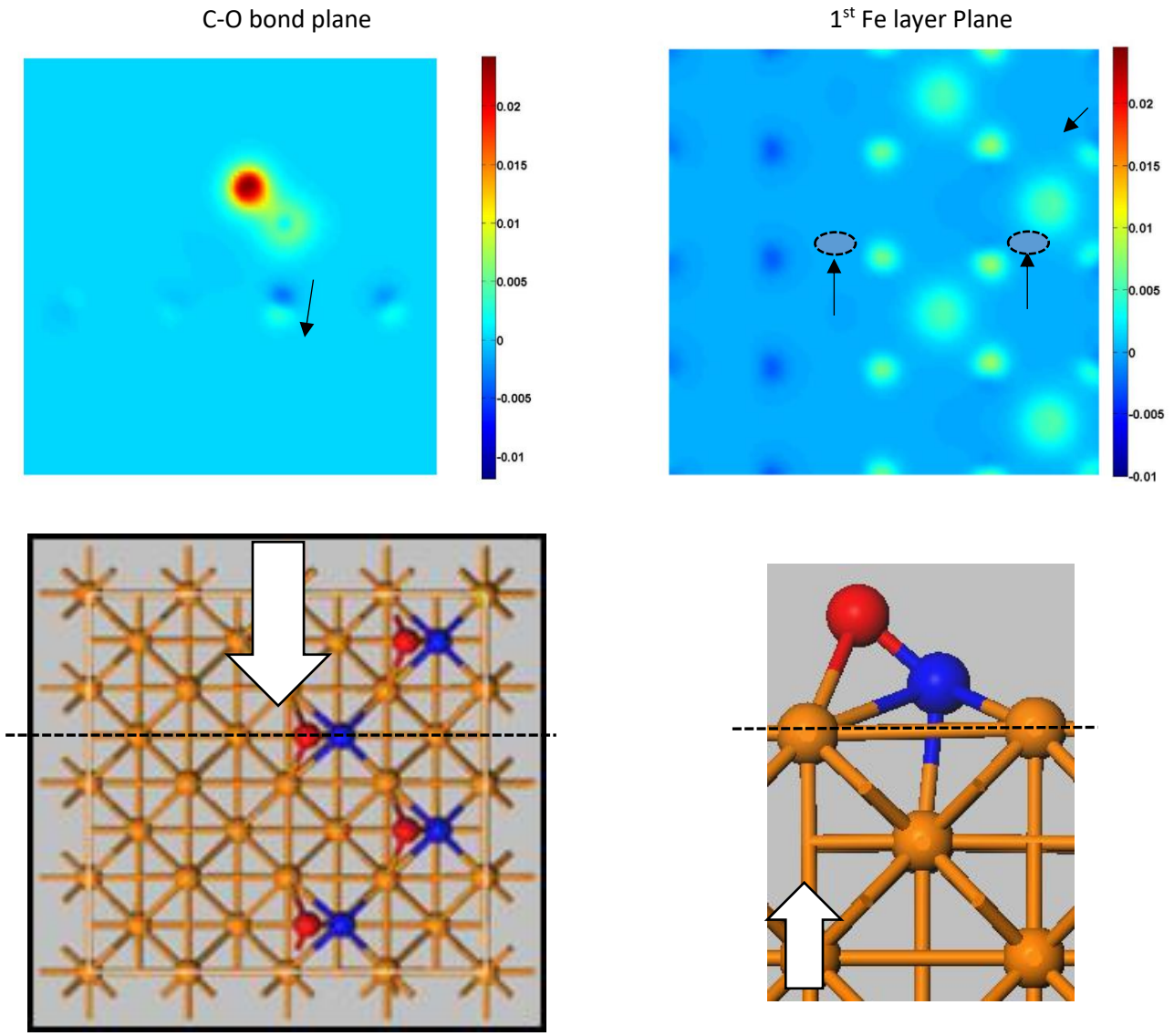

Figure 3-15: Electron density maps of the Corner Share configuration

3.3.1 Quantifying and describing CO lateral interactions

The lateral interactions can be analysed either by looking at the component energies of the system or by making some empirical observations.

3.3.1.1 Investigating component energies

The information in Table 3-2 summaries the different energetic contributions of the adsorption energy for the different configurations. As mentioned above these energies are calculated using equation 3.5, which uses the same procedure used to calculate the overall adsorption energy. The Hartree, Ewald, non-coulombic and pseudopotential energies were combined and used as one electrostatic contribution.

The electrostatic or coulombic potentials along with the exchange correlation potentials can be considered the laws we apply to our model. The kinetic energy is a magnitude of the curvature of electron density that changes as a result of the approximations enforced by the model.

If we combine the exchange–correlation energy with the electrostatic energy it can be considered a potential energy. The linear relationship between the kinetic and potential energy can be seen in Figure 3-16 and is reinforced by Figure 3-17 and the energies correlated well.

This "dependence" of kinetic and potential energy is interesting. It is seen in classical physics in countless examples (e.g. the swinging pendulum, the oscillating spring) and it is seen again here. The first law of thermodynamics states that for an isolated system energy is transformed and cannot be created or destroyed. A decrease in potential energy, and in this case, it is predominantly Coulombic potential energy, will result in an increase in kinetic energy. The linear equation in Figure 3-16 fits the data rather well in with and R^2 value of 0.9907. The gradient of the slope gives the relationship between the electrostatic energy and the kinetic energy with regard to adsorption. Thus, the adsorption energy can be written as:

$$E_{ads} = E_{Kin-Ads} + E_{Pot-Ads} = 0.123 \cdot E_{Pot-Ads} = -0.1403 E_{Kin-Ads}$$

If the change in potential energy is known and the relationship between the change in potential energy and kinetic energy is know the adsorption energy is can be determined. The lateral interaction is then not purely the difference between the electrostatic energies of two configurations but rather the change in kinetic energy in response to the change in the potential energy.

To use the kinetic or potential energy of adsorption to predict the adsorption energy it is important to note that the potential and kinetic energies are an order of magnitude larger than the adsorption energy. Thus, smaller errors are magnified as shown in Figure 3-18. It can be argued that the configurations that show the largest deviation from the prediction, the 4Share and Cluster configuration, have the lowest probability of existing per the Boltzmann distribution.

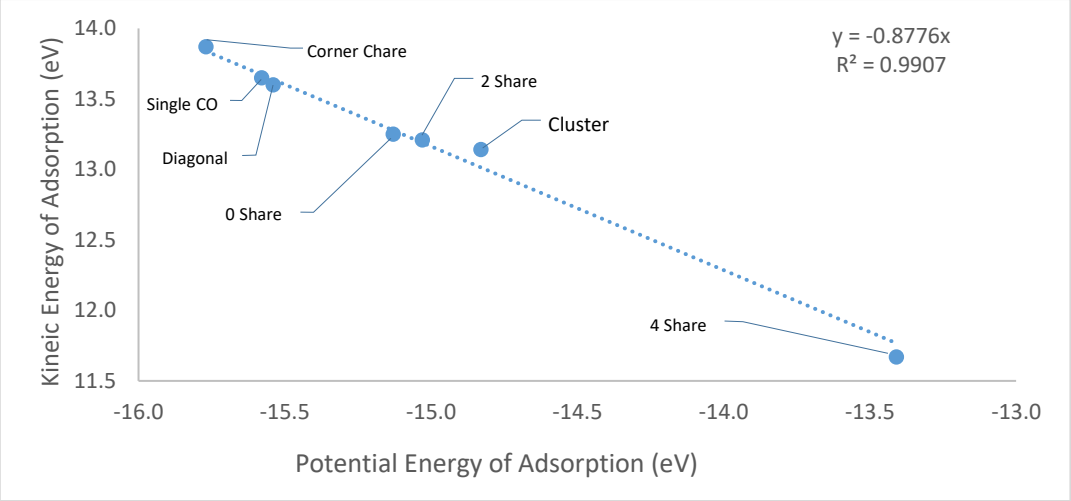

Figure 3-16: The relationship between the kinetic energy of adsorption and potential energy of adsorption appear to be linear

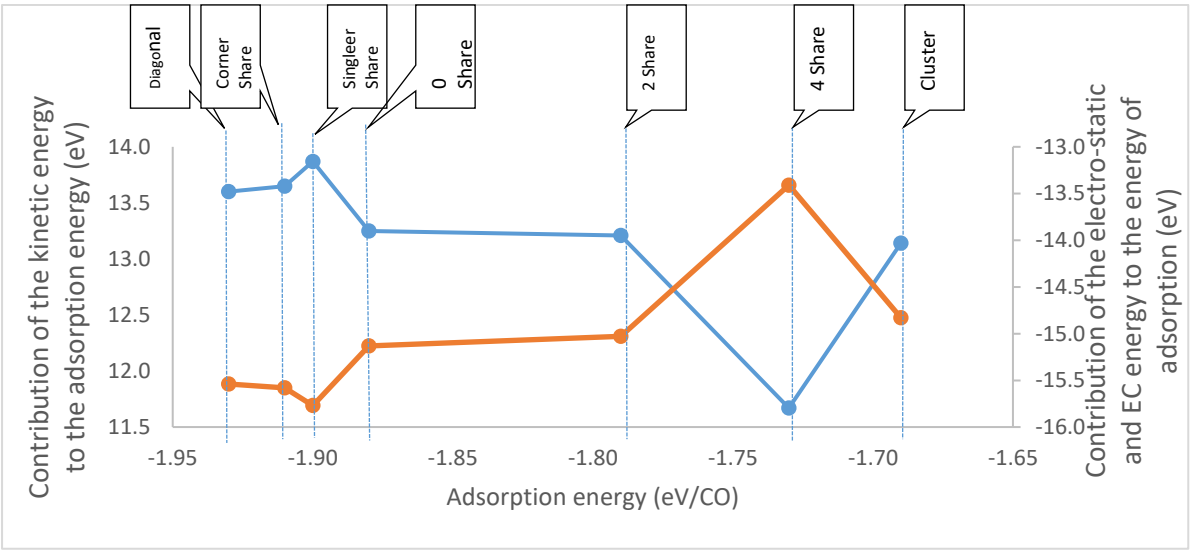

Figure 3-17: Here we see the relationship between the kinetic energy and electrostatic energy

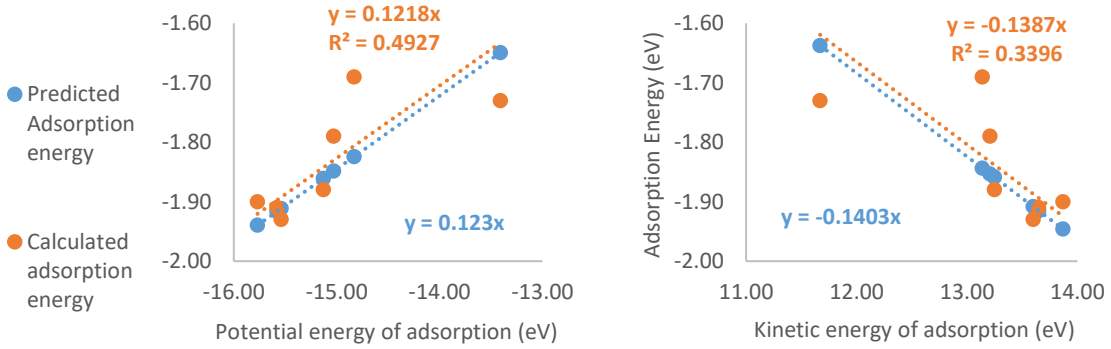

Figure 3-18: Kinetic or potential energy of adsorption used to predict the adsorption energy

In order to energetically break down the lateral interactions each energy for each 0.25 ML configuration was compared to that of the single configuration. This information is displayed in Figure 3-19. The exchange-correlation energy showed positive deviations for all the 0.25 ML configurations except the 4 Share configuration which displayed a negative deviation. The kinetic energy showed negative deviations for all 0.25 ML configurations except the Corner Share configuration which showed a positive deviation. The electrostatic energy showed negative deviations for the Corner share and Diagonal configurations and positive deviations for the 0 Share, 2 Share, 4 Share and Cluster configurations.

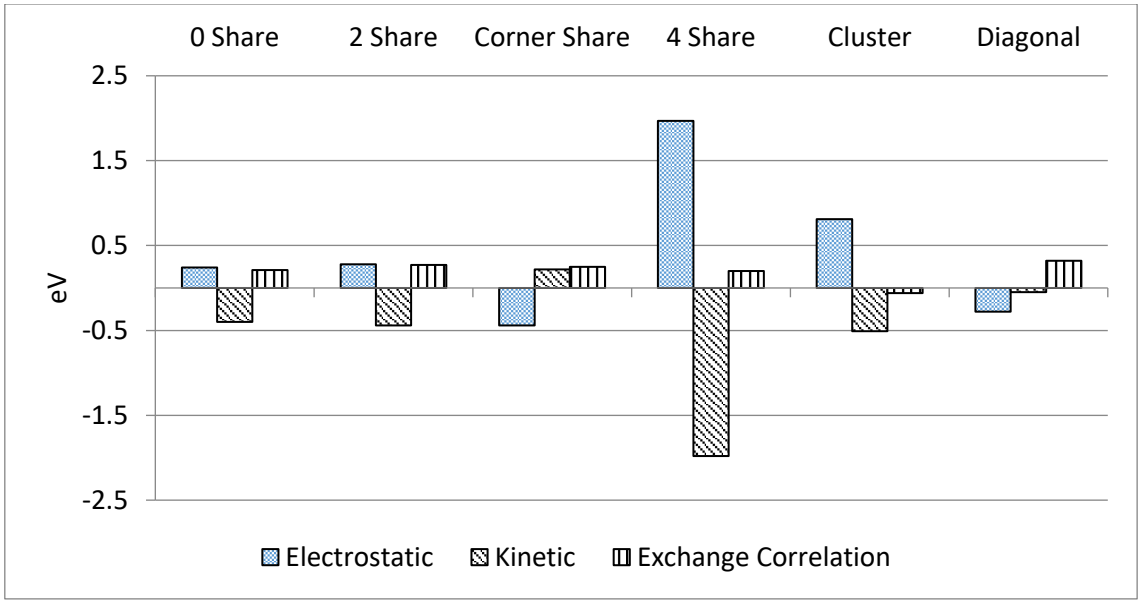

Figure 3-19: Deviations in component energies from Single CO configuration.

It is expected that the cluster and 4 share configurations to show large positive electrostatic deviations when compared to the Single CO configuration. The arrangement of the charges in Figure 3-12 and Figure 3-13 show this since the primary Fe atoms have significantly larger electron densities than that of the Single CO configuration. The smaller changes are harder to predict. The electrostatics alone are complex, since we need to consider all the CO-CO interaction and all the CO-Fe interactions. Furthermore, the system is periodic and expansions into all directions need to be considered.

It is interesting to note that Einstein [25] suggested that the lateral interactions are for the most part electrostatic. The results here indicate that while the electrostatics do make a significant contribution to the lateral interactions, the exchange-correlation energy and particularly the kinetic energy also play a significant role. Furthermore, even though some cases appear to display no lateral interactions like for the 0 Share, Diagonal and Corner Share configurations, deviations still existed from the Single configuration but cancel each other out.

Table 3-2: Energetic contributions to the adsorption energy

Configuration	Heat of Ads. (eV/CO)	Electrostatic					Total electrostatic energy (eV/CO)	Kinetic Energy (eV/CO)	Exchange-correlation energy (eV/CO)
		Hartree Energy (eV/CO)	Ewald Energy (eV/CO)	Local Pseudopotential Energy (eV/CO)	Non-Local Pseudopotential Energy (eV/CO)	Non-Coulombic Energy (eV/CO)			
Single CO	-1.91	-723.02	-844.71	1448.57	-4.45	113.08	-10.53	13.65	-5.05
0 Share	-1.88	-635.50	-756.20	1272.10	-4.16	113.47	-10.29	13.25	-4.84
2 Share	-1.79	-620.69	-740.44	1241.46	-4.05	113.47	-10.25	13.21	-4.78
Corner Share	-1.90	-598.19	-718.18	1197.81	-5.88	113.47	-10.97	13.87	-4.80
4 Share	-1.73	-637.28	-758.27	1275.21	-1.69	113.47	-8.56	11.67	-4.85
Cluster	-1.69	-669.84	-790.27	1341.28	-4.36	113.47	-9.72	13.14	-5.11
Diagonal	-1.93	-608.33	-729.31	1218.45	-5.09	113.47	-10.81	13.60	-4.73

3.3.1.2 Empirical Observation

When comparing the adsorption energy of the different configurations, a few empirical observations can be made. Once again, the 1/16 ML configuration was used as a reference point and deviations from this were attributed to lateral interactions. As shown in Table 3-4, three configurations caused a decrease in the adsorption energy and two configurations showed no change in the adsorption energy[18].

The configuration where CO adsorbates are in adjacent hollow sites and tilted away from each other causes a decrease in the adsorption energy by 0.09 eV/CO. The configuration where CO adsorbates are in adjacent hollow sites and lie perpendicular to each other causes a decrease in the adsorption energy by 0.12 eV/CO. The configuration where CO adsorbates are in adjacent hollow sites and lie parallel to each other causes a decrease in the adsorption energy by 0.15 eV/CO, the most significant change in adsorption energy.

For both the configurations where the CO adsorbates are separated by one hollow site and where the CO adsorbates are diagonal to each other, no significant change (<0.02 eV) in the adsorption energy was observed. Configurations which have the bridge interactions show a significant decrease in adsorption energy, whereas configurations which don't have bridge interactions display no significant change in adsorption energy. While previous studies have shown that the number of primary metal atoms involved can influence the adsorption energy and reaction energy [18], here we can see that adsorbate orientation with respect to neighbouring adsorbates is another component which needs to be considered. Furthermore, even though the empirical observations lead one to believe the non-bridge interactions show no lateral interactions, the results above show that the respective energies cancel each other out. Table 3-4 also shows the 3σ, 4σ and 1π-5σ orbitals associated with the configurations at ±0.01 e. $Å^{-3}$.

The validity of these empirical configurations was tested with four different configurations. Table 3-3 compares the predicted adsorption energy, calculated using the empirical observations, and the calculated adsorption energy. The predicted and calculated adsorption energies where in good agreement, with the largest error of 0.06 eV observed for the Test 4 configuration. Considering that the predicted adsorption energy took seconds to calculate while the calculated adsorption energy took days to calculate, this error may be considered acceptable. These results show that the observations are not limited to 0.25 ML coverage but can be applicable up to 0.5 ML.

If we assume that the empirical approximations can predict the adsorption energy for all coverages, then the number of unique configurations can be used to create an adsorption profile. Figure 3-20 compares the empirically approximated adsorption energy with the results of van Helden [43]. Where literature can only provide 3 data points at 0.25, 0.5 and 1 ML, the empirical approximations can yield 805 data points for a 4x4 system.

[18] The lateral interactions were attractive for the diagonal configuration but relative to the repulsive interactions and considering the DFT calculation error is approximately 0.05 eV the attractive interactions can be considered negligible

Table 3-3: Comparison of calculated adsorption energy and predicted adsorption energy

Configuration	Calculated Adsorption energy	Predicted Adsorption energy	Fermi Energy
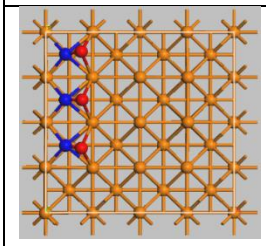 Test 1	**-1.81 eV**	**-1.79 eV**	**-6.166 eV**
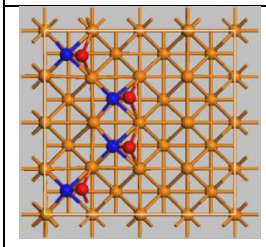 Test 2	**-1.85 eV**	**-1.82 eV**	**-6.146 eV**
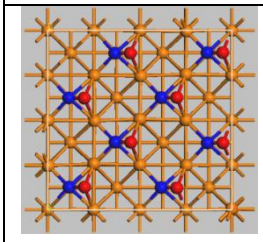 Test 3	**-1.90 eV**	**-1.91 eV**	**-5.985 eV**
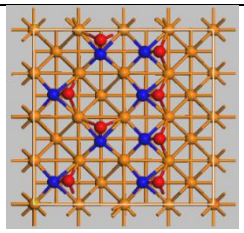 Test 4	**-1.69 eV**	**-1.75 eV**	**-5.977 eV**

Table 3-4: Empirical observations on the change in adsorption energy

CO Orientation	Change in Adsorption energy	Orbitals		
		3σ	4σ	1π-5σ
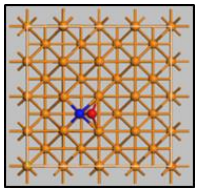	-	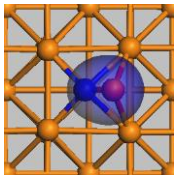	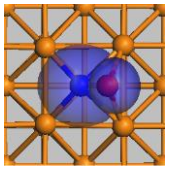	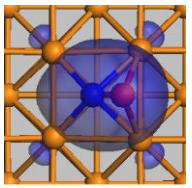
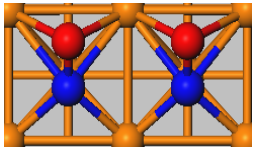	↓ E_{ads} = 0.15 eV /CO	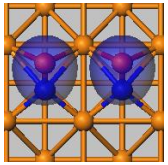	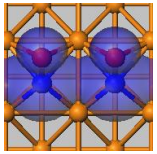	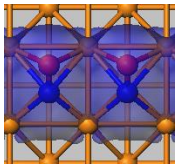
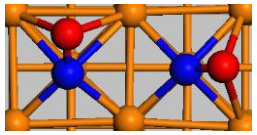	↓ E_{ads} = 0.12 eV /CO	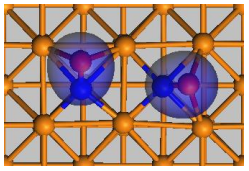	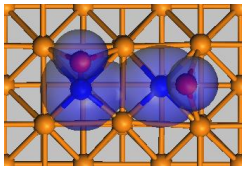	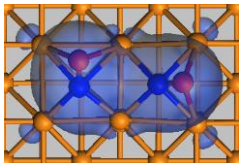
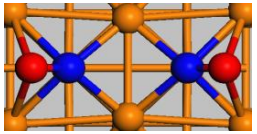	↓ E_{ads} = 0.09 eV /CO	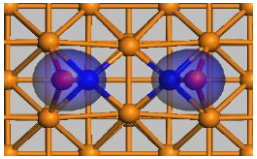	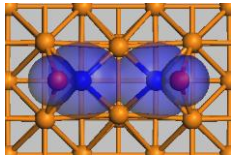	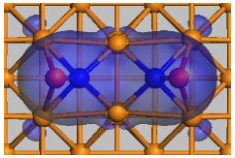
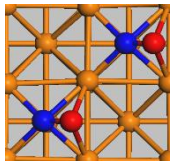	No Change	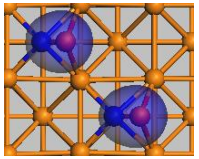	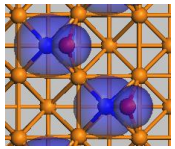	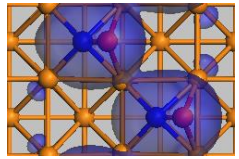
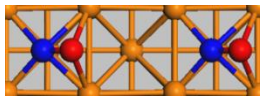	No Change	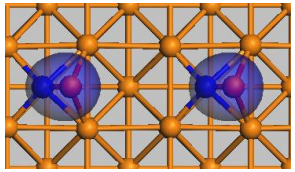	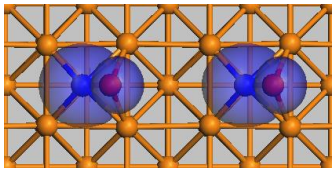	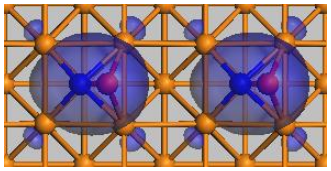

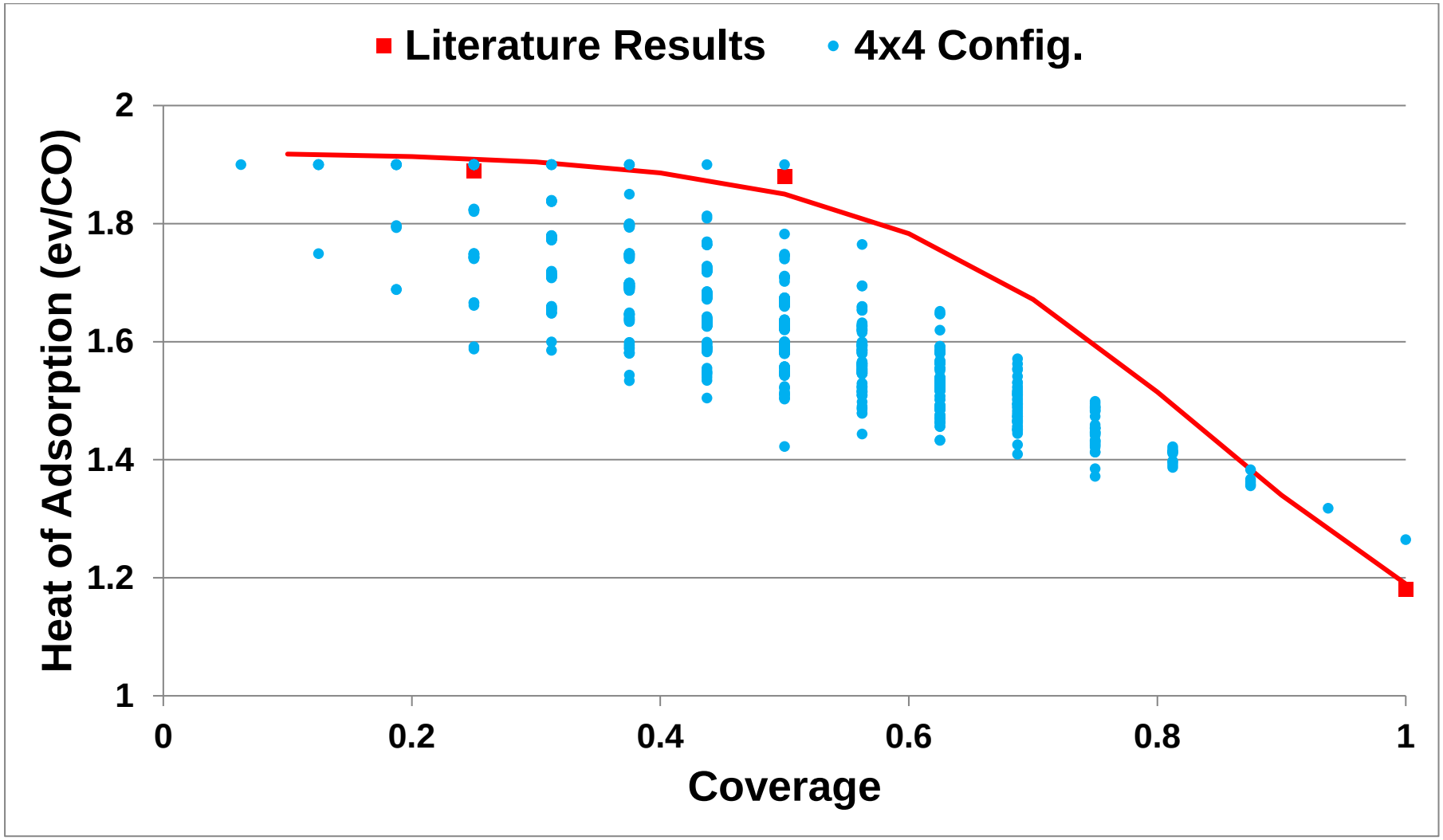

Figure 3-20: The adsorption energy of all the unique p(4x4) configurations compared to the results of van Helden[43].

3.3.2 Temperature Corrections

All the results so far have been for systems at 0 K. CO adsorption as part of the Fischer-Tropsch catalytic reaction takes place at approximately 150–300 °C or 420 – 570 K. To account for the temperature corrections the partition functions for CO in the gas phase and CO on the surface can be used to determine the vibrational, translational, and rotational entropy and enthalpy contributions.

The vibrational frequencies for CO in the gas phase and CO on the surface is given in Table 3-1. It is well know that upon adsorption the C-O bond length increases and the C-O stretching frequency decrease [4,8,47]

Table 3-5: Vibrational frequencies of CO in the gas phase and CO adsorbed on the surface

CO Gas

Species	**r(C-O)**	**v_1**
Present Work (USPP-rPBE)	1.13	2158
Experimental	***1,128***	***2170***

CO Adsorbed

Configuration	**r(C-O)**	**v_1**	**v_2**	**v_3**	**v_4**	**v_5**	**v_6**
0 Share	2.10	182	226	314	333	357	1177
2 Share	2.15; 2.10	215	228	292	375	396	1207
		221	230	298	388	398	1207

Considering the vibrational frequencies and the rotations and translations in the gas phase the entropic, enthalpic and Gibbs free energy of adsorption corrections of CO on Fe (100) can be seen in in Figure 3-21.

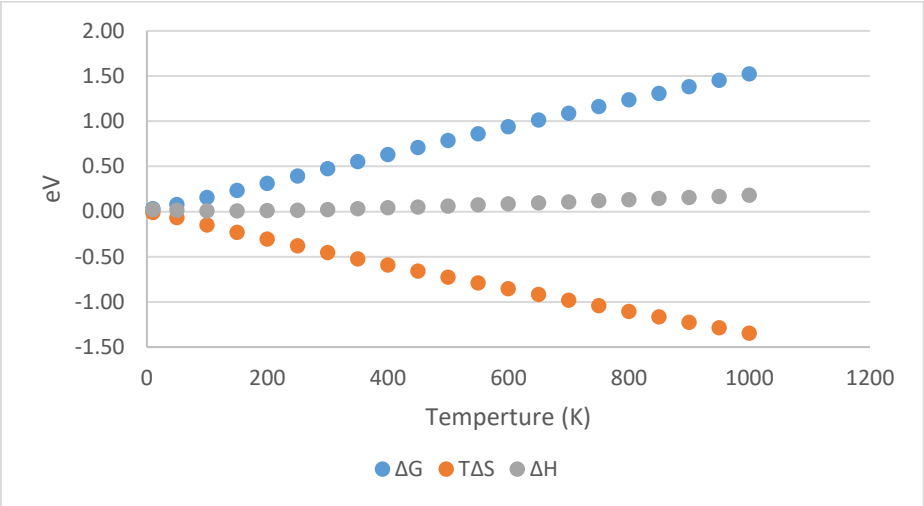

Figure 3-21: The temperature corrections for entropy, enthalpy and Gibbs free energy corrections for the adsorption energy of CO

Table 3-6: The change in heat of adsorption with Coverage, using the grand canonical distribution of lateral interactions model, and change in temperature using standard partition functions

Coverage (Θ)	Heat of Adsorption (eV/CO)	Temperature (K)										
		10	100	200	300	400	500	600	700	800	900	1000
	0.00	1.85	1.74	1.60	1.45	1.31	1.17	1.04	0.90	0.77	0.64	0.51
	0.05	1.85	1.74	1.60	1.45	1.31	1.17	1.04	0.90	0.77	0.64	0.51
	0.10	1.85	1.74	1.60	1.45	1.31	1.17	1.04	0.90	0.77	0.64	0.51
	0.15	1.85	1.74	1.60	1.45	1.31	1.17	1.04	0.90	0.77	0.64	0.51
	0.20	1.85	1.74	1.60	1.45	1.31	1.17	1.04	0.90	0.77	0.64	0.51
	0.25	1.85	1.74	1.60	1.45	1.31	1.17	1.03	0.90	0.76	0.63	0.50
	0.30	1.85	1.74	1.60	1.45	1.31	1.17	1.03	0.89	0.76	0.63	0.50
	0.35	1.85	1.74	1.60	1.45	1.31	1.17	1.03	0.89	0.75	0.62	0.49
	0.40	1.85	1.74	1.60	1.45	1.31	1.16	1.02	0.88	0.74	0.61	0.47
	0.45	1.85	1.74	1.60	1.45	1.30	1.15	1.00	0.86	0.72	0.59	0.45
	0.50	1.85	1.74	1.59	1.44	1.28	1.13	0.98	0.84	0.70	0.56	0.43
	0.55	1.79	1.68	1.54	1.39	1.24	1.09	0.94	0.80	0.66	0.53	0.39
	0.60	1.73	1.62	1.48	1.33	1.19	1.04	0.90	0.76	0.62	0.49	0.35
	0.65	1.67	1.56	1.42	1.27	1.13	0.99	0.85	0.71	0.57	0.44	0.31
	0.70	1.61	1.50	1.36	1.21	1.07	0.93	0.79	0.65	0.52	0.39	0.26
	0.75	1.55	1.44	1.30	1.15	1.01	0.87	0.73	0.60	0.46	0.33	0.20
	0.80	1.49	1.38	1.24	1.09	0.95	0.81	0.68	0.54	0.41	0.28	0.15
	0.85	1.43	1.32	1.18	1.03	0.89	0.75	0.62	0.48	0.35	0.22	0.09
	0.90	1.37	1.26	1.12	0.97	0.83	0.69	0.56	0.42	0.29	0.16	0.03
	0.95	1.31	1.20	1.06	0.91	0.77	0.63	0.50	0.36	0.23	0.10	-0.03
	1.00	1.25	1.14	1.00	0.85	0.71	0.57	0.44	0.30	0.17	0.04	-0.09

3.4 Conclusions

This study has shown that the change in adsorption energy is not only coverage dependant but also dependant on adsorbate configurations. A breakdown of the lateral interactions for CO on Fe (100) was made. The lateral interactions were not only due to electrostatic energy but also kinetic and exchange-correlations energy. Both positive and negative deviations from the adsorption energy were seen.

Geometric changes induced by CO adsorption are seen as a shift in Fe atoms resulting in deviations of 0.1 eV. An elongation of the adsorbed C-O bond length relative to that in the gas phase was also seen.

Electronic changes induced by CO adsorption showed are seen with a change in Fermi energy and change in electron density. The electron density map showed how the different configurations effect the movement of electrons of the metal surface.

The lateral interactions stem from both geometric and electron changes in the system. The lateral interactions have been quantified here with electrostatic, kinetic and exchange-correlation components. The kinetic and electrostatic interactions appear to a balancing relationship. While changes in electrostatic can be explained for highly perturbed systems, the subtler changes are hard to predict.

Empirical observations with respect to adsorbate orientation allowed us to predict the adsorption energy at different coverages. These observations allow for a quick estimate of the adsorption energy within reasonable accuracy. The empirical observations also displayed a distinct difference in “bridge” and “non-bridge” interactions. The empirical approximations allow us to look at the adsorption spectrum in greater detail.

3.5 References

[1] Van Santen, R.A., De Koster, A., Koerts, T., *Catal. Letters* **1990**, 7, 1–14.

[2] van der Laan, G.P., Beenackers, A.A.C.M., *Catal. Rev.* **1999**, 41, 255–318.

[3] van Helden, P., van Steen, E., *J. Phys. Chem. C* **2008**, 112, 16505–16513.

[4] Bromfield, T.C., Ferré, D.C., Niemantsverdriet, J.W., *Chemphyschem* **2005**, 6, 254–60.

[5] Chen, Y., Cao, D., Jun, Y., Li, Y., Wang, J., Jiao, H., *Chem. Phys. Lett.* **2004**, 400, 35–41.

[6] Jiang, D.E., Carter, E. a., *Surf. Sci.* **2004**, 570, 167–177.

[7] Nayak, S.K., Nooijen, M., Bernasek, S.L., Blaha, P., *J. Phys. Chem. B* **2001**, 105, 164–172.

[8] Sorescu, D., Thompson, D., Hurley, M., Chabalowski, C., *Phys. Rev. B* **2002**, 66, 35416.

[9] Morales, F., de Smit, E., de Groot, F.M.F., Visser, T., Weckhuysen, B.M., *J. Catal.* **2007**, 246, 91–99.

[10] Zhuo, M., Borgna, A., Saeys, M., *J. Catal.* **2013**, 297, 217–226.

[11] Ciobica, I.M., Kleyn, a. W., van Santen, R. a., *J. Phys. Chem. B* **2003**, 107, 164–172.

[12] Qin, Z.-H., Lewandowski, M., Sun, Y.-N., Shaikhutdinov, S., Freund, H.-J., *J. Phys. Condens. Matter* **2009**, 21, 134019.

[13] Lebedeva, N.P., Rodes, A., Feliu, J.M., Koper, M.T.M., van Santen, R.A., *J. Phys. Chem. B* **2002**, 106, 9863–9872.

[14] Farias, M.J.S., Herrero, E., Feliu, J.M., *J. Phys. Chem. C* **2013**, 117, 2903–2913.

[15] Blyholder, G., *J. Phys. Chem.* **1964**, 68, 2772–2777.

[16] Cao, D., Zhang, F., Li, Y., Jiao, H., *J. Phys. Chem. B* **2004**, 108, 9094–9104.

[17] Föhlisch, a., Nyberg, M., Bennich, P., Triguero, L., Hasselström, J., Karis, O., Pettersson, L.G.M., Nilsson, A., *J. Chem. Phys.* **2000**, 112, 1946.

[18] Zeinalipour-Yazdi, C.D., van Santen, R. a., *J. Phys. Chem. C* **2012**, 116, 8721–8730.

[19] Govender, A., Ferré, D.C., Niemantsverdriet, J.W., *Chemphyschem* **2012**, 13, 1583–90.

[20] Curulla-Ferré, D., Govender, A., Bromfield, T.C., Niemantsverdriet, J.W.H., *J. Phys. Chem. B* **2006**, 110, 13897–904.

[21] Stibor, A., Kresse, G., Eichler, A., Hafner, J., *Surf. Sci.* **2002**, 507–510, 99–102.

[22] van Bavel, A.P., Hermse, C.G.M., Hopstaken, M.J.P., Jansen, A.P.J., Lukkien, J.J., Hilbers, P.A.J., Niemantsverdriet, J.W., *Phys. Chem. Chem. Phys.* **2004**, 6, 1830.

[23] Borthwick, D., Fiorin, V., Jenkins, S.J., King, D. a., *Surf. Sci.* **2008**, 602, 2325–2332.

[24] Ma, Z.-Y., Huo, C.-F., Liao, X.-Y., Li, Y.-W., Wang, J., Jiao, H., *J. Phys. Chem. C* **2007**, 111, 4305–4314.

[25] Einstein, T.L., *Handb. Surf. Sci.* **2005**, 4111, 1-43.

[26] Mhadeshwar, A.B., Kitchin, J.R., Barteau, M.A., Vlachos, D.G., *Catal. Letters* **2004**, 96, 13–22.

[27] Trost, J., Zambelli, T., Wintterlin, J., Ertl, G., *Phys. Rev. B* **1996**, 54, 17850–17857.

[28] Hellman, A., Honkala, K., *J. Chem. Phys.* **2007**, 127, 194704: 1-6.

[29] Chen, J., Liu, Z.-P., *J. Am. Chem. Soc.* **2008**, 130, 7929–37.

[30] Yeo, Y.Y., Vattuone, L., King, D.A., *J. Chem. Phys.* **1996**, 104, 3810.

[31] Plata, J.J., Collico, V., Márquez, A.M., Sanz, J.F., *Theor. Chem. Acc.* **2012**, 132, 1311.

[32] Neurock, M., An Ab Initio Approach towards Engineering Fischer-Tropsch Surface Chemistry. University of Viginia, **2006**.

[33] Kokalj, A., *Phys. Rev. B* **2011**, 84, 45418.

[34] van Steen, E., van Helden, P., *J. Phys. Chem. C* **2010**, 114, 5932–5940.

[35] Clark, S.J., Segall, M.D., Pickard, C.J., Hasnip, P.J., Probert, M.I.J., Refson, K., Payne, M.C., *Zeitschrift für Krist.* **2005**, 220, 567–570.

[36] Accelrys Software Inc., Material Studio Modeling Environment, San Diego: Accelrys Software Inc., **2010**.

[37] Hammer, B., Hansen, L., Nørskov, J., *Phys. Rev. B* **1999**, 59, 7413–7421.

[38] Monkhorst, H.J., Pack, J.D., *Phys. Rev. B* **1976**, 13, 5188–5192.

[39] Hoffmann, R., *Angew. Chemie Int. Ed. English* **1987**, 26, 846–878.

[40] Sung, S.S., Hoffmann, R., *J. Am. Chem. Soc.* **1985**, 107, 578–584.

[41] Karmazyn, A. D., Fiorin, V., Jenkins, S.J., King, D. a., *Surf. Sci.* **2003**, 538, 171–183.

[42] Payne, M.C., Arias, T. A., Joannopoulos, J.D., *Rev. Mod. Phys.* **1992**, 64, 1045–1097.

[43] Van Helden, P., Initial Steps of the Fischer-Tropsch Synthesis on Fe(100): The Role of Hydrogen. University of Cape Town, **2010**.

[44] Baroni, S., Giannozzi, P., Testa, A., *Phys. Rev. Lett.* **1987**, 58, 1861.

[45] Gonze, X., *Phys. Rev. A* **1995**, 52, 1086.

[46] Moon, D.W., Dwyer, D.J., Bernasek, S.L., *Surf. Sci.* **1985**, 163, 215–229.

[47] Moon, D.W., Bernasek, S.L., Dwyer, D.J., Gland, J.L., *J. Am. Chem. Soc.* **1985**, 107, 4363–4364.

[48] Saiki, R.S., Herman, G.S., Yamada, M., Osterwalder, J., Fadley, C.S., *Phys. Rev. Lett.* **1989**, 63, 283–286.

[49] Moon, D.W., Cameron, S., Zaera, F., Eberhardt, W., Carr, R., Bernasek, S.L., Gland, J.L., Dwyer, D.J., *Surf. Sci.* **1987**, 180, L123–L128.

[50] Sorescu, D., *Phys. Rev. B* **2006**, 73, 155420.

[51] Nørskov, J.K., *Prog. Surf. Sci.* **1991**, 38, 103–144.

4 Stability of syngas methanation species on Fe (100)

4.1 Introduction

Several mechanisms have been proposed for methanation, the more popular approaches are via the alkyl mechanism and alkenyl mechanisms [1–3]. These mechanisms involve successive hydrogenation of atomic carbon to methane as well as dissociation of CO and formation of H_2O. Studies [4,5] have shown direct dissociation and assisted dissociation can occur, with assisted dissociation being more prevalent at higher coverages.

A simple methanation model will include CO, C, O, H, CH_x (x=1-4), OH and H_2O. First principle studies can be used to determine the preferred adsorption sites and geometries of specific adsorbates on the surface and the energy changes associated with moving between different sites (surface diffusion).

Several studies have been conducted on the chemisorption of CH_x species on Fe (100) [5–11], Fe (110) [12–14] and several Fe_5C_2 Hagg iron carbide surfaces [15–17]. The studies on Fe (100) imply that the four-fold hollow site is the stable adsorption site for C, CH and CH_2, while the CH_3 and OH species are stable on the two-fold bridge site. CH_4 only displays weak physisorption.

The stability of each species on the different Fe (100) sites (H –four fold hollow site, Br – bridge site, T – top site) are well defined in literature [5–11,18,19] and follows for the various adsorbed species in the following order:

C	**O**	**H**	**CH**
H>Br>T	H>Br>T	H≈Br>T	H>Br>T

CH_2	**CH_3**	**OH**
H>Br>T	Br>H>T	Br>H>T

Numerous studies have documented the change in energy with the change in coverage for single species [9,20–22]. The inter-species lateral interactions can be used to explain the change in the adsorption energy/binding energy as well as changes in geometry with change in coverage i.e. *"Coverage Effects"*.

While the coverage effects are well observed, they are not entirely understood. Theoretical studies [6–11,23] and experimental studies [24,25] have shown that atomic C adsorbed on Fe (100) is most stable in a c(2x2) configuration at 0.5 ML. The c(2x2) configuration at 0.5 ML also resulted in a more stable situation than for the 0.25 ML coverage. The stabilization from next nearest neighbour interactions was also seen in the previous chapter with CO adsorption on Fe (100). This means that a surface covered with 0.25 ML C or CO will split into vacant areas and areas which maximize next nearest neighbours when coverage increases to 0.5 ML.

The following chapter will investigate the methanation species individually at 0.25 ML, 0.33 ML, 0.5 ML and 1 ML with different configurations emphasizing nearest neighbour and next-nearest neighbour interactions. The changes in geometry, vibrations and energies will be considered.

4.2 DFT Calculations

The DFT calculations were performed using the CASTEP [26] and the RPBE functional [28]. A Gaussian smearing width of σ = 0.1 eV was utilized in all calculations. The ion-electron interactions were approximated using ultrasoft pseudopotentials (usPP) with core corrections, calculations allowed for spin-polarized orbitals and a cut-off energy of 400 eV was set.

A five-layer slab with three layers relaxed was used with an optimized vacuum spacing of 12 Å between surfaces. K-point sampling was generated using the Monkhorst-Pack [29] procedure with a k-point spacing of <0.03 $Å^{-1}$.

In order to determine if the converged energy was a minimum and not saddle point, a vibrational analysis was completed using a partial Hessian analysis [30] on the adsorbates in question. This is a valid approximation as the Fe atoms are significantly heavier than those of C, H and O. The atoms were perturbed by 0.005 Å in Cartesian space.

Adsorption energy was calculated as follows:

$$E_{ads} = \frac{E_{(Fe+nX)} - E_{(Fe\ Slab)}}{n} - E_X \quad (4.1)$$

Where $E_{(Fe+nX)}$ is the energy of *n* X adsorbates on an iron surface, $E_{(Fe\ Slab)}$ is the energy of a clean iron surface and E_X is the energy of the adsorbate in the gas phase. It should be noted that for hydrogen the binding energy and adsorption energies are slightly difference since it involves dissociative adsorption.

Adsorption energy for hydrogen and oxygen was calculated as follows:

$$E_{ads} = \frac{E_{(Fe+nX)} - E_{(Fe\ Slab)}}{n} - E_{X_2} \quad (4.2)$$

Where $E_{(Fe+nH)}$ is the energy of *n* X adsorbates on an iron surface, $E_{(Fe\ Slab)}$ is the energy of a clean iron surface and E_{H2} is the energy of X_2 in the gas phase.

Binding energy for hydrogen and oxygen was calculated as follows:

$$E_{bind} = \frac{E_{(Fe+nX)} - E_{(Fe\ Slab)}}{n} - E_X \quad (4.3)$$

Where $E_{(Fe+nH)}$ is the energy of *n* X adsorbates on an iron surface, $E_{(Fe\ Slab)}$ is the energy of a clean iron surface and E_H is the energy of the X adsorbate in the gas phase.

The interaction between the adsorbates and the iron surface causes a shift in the iron atoms. The deformation of the iron surface was then calculated as follows:

$$E_{deform} = E_{[(Fe+nX)-nX]} - E_{(Fe\ Slab)} \quad (4.4)$$

Where $E_{[(Fe+nX)-nX]}$ is the single point energy of the geometry optimized iron/adsorbate surface with adsorbates removed and $E_{(Fe\ Slab)}$ is the energy of a clean geometry optimized iron surface.

The results from this study were compared to those from Lo and Ziegler [6], Sorescu [7] and Govender [10,31]. It is important to note the difference in code and pseudopotential may yield different results. The accuracy of the different models can be seen by the calculation of bulk properties of Fe in Table 2-1. The computational methods used in these studies are summarized in Table 4-1.

The approximation of molecules in the gas phase can also give insight to the accuracy of the different models. In chapter 2, table 2-2 the bond angles, bond lengths and vibrational analysis of the molecules

calculated in a 10 Å x 10 Å x 10 Å box are compared with experimental gas phase molecules. We see that our results are accurate within 0.001 Å for bond lengths and 0.1° for bond length for CH, CH_2 and CH_4, while CH_2 is accurate within 0.001 Å for bond lengths and 4 ° for bond length. The same trend is seen for literature values.

Table 4-1: Details of computational methods used in studies by Lo and Ziegler[6], Govender[10,31], Bromfield et al. [9] and Sorescu[7].[19]

	Lo and Ziegler [2]	Govender et al. [6]/ Bromfield et al. [5]	Sorescu [3]
Electron-ion interaction	Ultrasoft pseudo-potentials (usPP)	Projector-augmented waves (PAW)	PAW and USPP
Code	VASP	VASP	VASP
Functional	PW91	PW91	PW91 and PBE
Kinetic energy cut off	400 eV	400 eV	495 eV (usPP) 400 eV (PAW)
Exchange correlation energy	GGA	GGA	GGA
k-point setting	7x7x1 for p(2x2)	5x5x1 for p(2x2)	4x4x2 for p(2x2)
Smearing width	σ = 0.2 eV	$\sigma \leq$ 0.1 eV	σ = 0.1 eV
Vacuum thickness	10 Å	10 Å	10 Å
Spin polarized	✓	✓	✓
Slab approximations	5-layer slab (2 relaxed)	4-layer slab (1 relaxed)	7-layer slab (2 relaxed)
Vibrational analysis	✓	✓	✓

[19] The model used in this study was as follows: USSP, CASTEP, RPBE, KE cut-off of 400 eV, GGA, 5x5x1 for p(2x2), $\sigma \leq$ 0.1 eV, vacuum thickness of 12 Å, spin polarized, 5-layer slab (2 relaxed), vibrational analysis was completed

4.2.1 Energetic breakdown

The energetic breakdown for the lateral interactions includes all the terms included in the Hamiltonian. For CASTEP [26] the resulting energies are the kinetic energy, Hartree energy, local and non-local pseudopotential energies, exchange-correlation energy, Ewald energy and non-Coulombic energy.

Hartree, Ewald, pseudopotential and Non-Coulombic energies combined will give an overall electrostatic interaction. The exchange-correlation potential includes the effects of the Pauli Exclusion Principle and long range dipole interactions not described by the classical electrostatic interactions.

The kinetic energy gives us an idea of the shape of the electron density. A system with sharper changes in concavity will have a higher kinetic energy.

The energy contribution to the total electronic energy of each of the terms was considered and the change in each energy on adsorption was considered. This was calculated using the same procedure to calculate the integral adsorption energy was calculated. This means:

$$E_{i,ads} = \frac{E_{i,(Fe+nX)} - E_{i,(Fe\ Slab)} - n \cdot E_{i,X}}{n} \qquad (4.5)$$

Where i is either the kinetic energy, Hartree energy, local and non-local pseudopotential energies, exchange-correlation energy, Ewald energy or non-Coulombic energy.

4.2.2 The Fermi Energy

An important factor regarding the interactions of an electronic system is the position of the Fermi level of the system. The interactions of an adsorbates molecular orbitals with transition metal electron bands are dependent on the Fermi level. The classical molecular orbital theory can still be used to describe the interactions. Typically, we see that anti-bonding orbitals are higher in energy than bonding orbitals due to repulsions. In cases where metal bands are close to or intersected by the Fermi level, the anti-bonding orbitals can be higher than the Fermi level. Electrons can then be transferred to the metal and the repulsive forces diminished [23,34–36]. Van Steen and van Helden [23] showed that for CO and C on Fe (100) the Fermi level decreases with increasing coverage. Furthermore, the centre of the d-band is in the same position relative to the Fermi level, i.e. the overall energy of the d-band is lowered. As a result, the energy difference between the frontier orbitals (HOMO and LUMO) of the adsorbate changes. If these frontier orbitals are fully occupied, the Pauli repulsion would then increase.

4.2.3 Bader analysis

The Bader analysis was completed by reconstructing the algorithm proposed by Henkelman et al. [37] for Bader decomposition of charge density. The algorithm was reconstructed in Matlab and was built to receive the formatted density file (.den_fmt) which needs to be requested in the parameters file of the CASTEP setup.

4.3 Adsorption of atomic carbon (C) on Fe (100)

The study of C on Fe surfaces has been approached from several perspectives including CO dissociation [8,9,23], catalyst deactivation [38] and surface transformation [39]. Theoretical studies [6–11,23] and low-energy electron diffraction (LEED) experimental studies[24,25] have shown that the most stable adsorption configuration for C on Fe (100) is in the four-fold hollow site. Table 4-2 shows the configurations considered in this study, along with a summary of the results obtained.

Table 4-2: Representation of the configurations used to study C adsorption on Fe (100)

	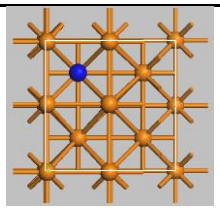	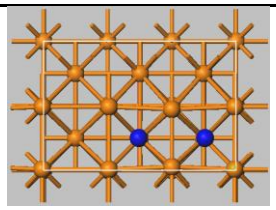	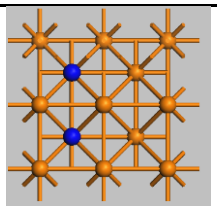	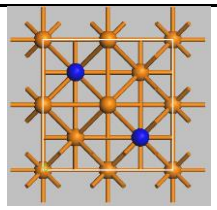	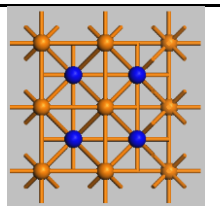
Coverage	**0.25 ML**	**0.33 ML**	**0.5 ML "adjacent"**	**0.5 ML "diagonal"**	**1 ML**
E_{ads} (eV/C)	-8.00	-8.01	-7.93	-8.05	-7.33
d C-Fe (Å)	1.961	1.955	1.931	1.898	1.835
E_{Deform} (eV/C)	0.11	0.12	0.15	0.10	0.17
E_{Fermi} (eV)	-6.271	-6.276	- 6.193	-6.267	-5.828
q_C	-1.60 e	-1.53 e	-1.42 e	-1.58 e	-1.31
$q_{Fe\ Prim.}$	+0.42 e	+0.41 e (Unshared) +0.65 e (Shared)	+0.61 e	+0.69 e	+0.98 e

Several studies [6,7,31] concur that the four fold hollow site is the most stable adsorption site for C adsorption on Fe (100) (see Table 4-4 for a summary of the results). In this work at the lowest studied coverage of 0.25ML, the C-Fe distance was found to be 1.961 Å. This distance is in good agreement with the study completed by Sorescu [8], who reported a C-Fe distances of 1.969 Å for a PAW-PBE model and 1.958 Å for a USPP-PW91 model. The PAW-PW91 model by Govender [31] resulted in a slightly larger C-Fe distance of 1.980 Å and the USPP-PW91 model by Ziegler and Lo [6] resulted in a significantly larger C-Fe distance of 2.048 Å. Experimental studies [24,25,39] indicate that the four-fold hollow site is the most stable site for C adsorption on Fe (100).

For the 0.25 ML configuration, the adsorption energy was found to be -8.00 eV/C relative to atomic carbon in the gas phase. These values are in good agreement with the values reported by Sorescu [7,8], who found a adsorption energy of –8.08 eV/C and –8.26 eV/C for the PW91 and PBE calculations respectively, Jiang & Carter [11] reported an adsorption energy of –8.24 eV/C for a PAW-PBE system, Govender [10,31], who found a adsorption energy of –8.28 eV/C , and Ziegler and Lo [6], who found a adsorption energy of –7.94 eV/C.

Table 4-3: Adsorption energy, geometry and vibrational frequency of C at 0.25 ML on Fe (100) with studies by Lo and Ziegler[6], Govender[10,31] and Sorescu[7]

	Author	Site	d_{Fe-C} (Å)	E_{ads} (eV)	v_1	v_2	v_3
					cm^{-1}		
C (0.25 ML)	Ziegler & Lo (USPP-PW91)	Four-fold hollow	2.048	-7.94			
	Govender (PAW-PW91)	Four-fold hollow	1.980	-8.28	470	482	483
	Sorescu (USPP-PW91)	Four-fold hollow	1.958	-8.08			
	Sorescu (PAW-PBE)	Four-fold hollow	1.969	-8.26	413	453	534
	Jiang & Carter (PAW-PBE)	Four-fold hollow	-	-8.24			
	Present Work (USPP-rPBE)	Four-fold hollow	1.961	-8.00	494	525	526

A summary of the changes in geometry, binding energy and vibrational frequencies can be seen in Table 4-4. For 0.33 ML, the C-Fe distance was found to be 1.955 Å which is a slight decrease from the 1.961 Å distance found for the 0.25 ML configuration. Carbon adsorbed in the 0.5 ML "adjacent" configuration has a shorter C-Fe distance of 1.931 Å and carbon adsorbed in the "Diagonal" configuration an even shorter C-Fe distance of 1.898 Å. The 1 ML configuration displays the shortest C-Fe distance 1.835 Å. The bond lengths appear to be in good agreement with studies by Lo and Ziegler[6], Govender[10,31] and Sorescu[7]. A shorter C-Fe distance indicates stronger bonding with the metal surface as C-Fe distance typically relates to the C-Fe bond strength. This mean the 0.5 ML "Diagonal" diagonal configuration has stronger C-Fe bonding than the 0.5 ML "Adjacent" configuration.

For the 0.33 ML configuration considered, each C atom has one nearest-neighbour for the configuration considered here. The adsorption energy was found to be -8.01 eV/C which is almost the same as the adsorption energy at 0.25 ML.

At a coverage of 0.5 ML, two configurations are considered. For the 0.5 ML "adjacent" configuration each C atom has two nearest-neighbours. The adsorption energy was found to be -7.93 eV/C, which is a slight decrease of 0.07 eV/C when compared to the 0.25 ML configuration adsorption energy. Sorescu [3,4] did a study on the same configuration and found an adsorption energy of –8.07 eV/C, a decrease of only 0.01 eV/C when compared 0.25 ML.

The other 0.5 ML configuration considered was the 0.5 ML "diagonal" configuration, where each C atom has four next nearest neighbours. The LEED studies[24,25] indicate that at a coverage of 0.5 ML, this type of configuration is prevalent. The adsorption energy was found to be -8.05 eV/C which is an increase of 0.05 eV when compared to the 0.25 ML configuration adsorption energy. Again these values are in good agreement with the work done by Sorescu [7,8] on a similar configuration, who found a adsorption energy of –8.12 eV/C and –8.31 eV/C for the PW91 and PBE calculations respectively, and Jiang & Carter [11] reported an adsorption energy of –8.28 eV/C for a PAW-PBE system.

For the 1 ML configuration, each C atom has four nearest-neighbours and four next-nearest-neighbours. The adsorption energy was found to be -7.33 eV/C which is a significant decrease of 0.68 eV when

compared to the 0.25 ML configuration adsorption energy. Again these values are in good agreement with the work done by Sorescu [7,8] on a similar configuration, who found an adsorption energy of –7.54 eV/C and –7.64 eV/C for the PW91 and PBE calculations respectively, and Jiang & Carter [11], who found an adsorption energy of –7.58 eV/C. Both Sorescu [7,8] and Jiang & Carter [11] report that the 1 ML configuration is preferred over graphite formation.

Both Sorescu [7,8] and Jiang & Carter [11] report an increase in the adsorption energy of atomic carbon of 0.05 eV/C, as in this study, and believe that this subtle increase will result in this diagonal configuration being prevalent at this coverage, agreeing with the LEED studies[24,25]. The differences in vibrational frequencies between 0.25 ML and 0.5 ML results in a further increase in lateral interaction. For this instance the differences in the vibrational enthalpic and entropic contributions between the 0.25 ML configuration and the 0.5 ML diagonal configuration show a further increase of 0.05 eV per/C at 400 K.

When looking at the Bader charge associated with the metal atoms, the charge is not equally distributed, but majority of the charge associated with the metal is assigned to the Fe atoms closest to the adsorbed atomic C, as shown in Figure 4-1. From here onwards these Fe atoms will be called "Primary" Fe atoms. For the 0.25 ML configuration, the charge on C is -1.6 e while the charge on each of the four primary atoms in this configuration is 0.42 e. The charge on the remaining Fe atoms are between -0.1 e and 0.1 e. At a coverage of 0.33 ML the charge on all of the C atoms is slightly reduced to -1.53 e. For this configuration two primary Fe atoms are shared between the adsorbates. The charges on these two shared Fe atoms are 0.65 e while the remaining primary atoms had charges of 0.41 e, and the remaining Fe atoms having charges between 0.12 and -0.12 e. For atomic carbon adsorbed in the 0.5 ML “diagonal” configuration the charge on C is -1.58 e. For this configuration, each primary Fe atom is shared between two adsorbates and each primary Fe atom has a charge of 0.69 e. Additionally for this configuration we see that the Fe atom at the base of the hollow site as a charge of -0.25 e. The remaining Fe atoms have charges between 0.12 and -0.12 e. Atomic carbon adsorbed in the 0.5 ML “Adjacent“ configuration has a charge of -1.42 e. Again, for this configuration each primary Fe atom is shared between two adsorbates and has a charge of 0.61 e, with the remaining Fe atoms having a charge between 0.12 and -0.12 e. Finally, for the 1 ML configuration, each primary atom is shared amongst four C atoms. The charge on the C atom is -1.31 e while the charge on the primary Fe atoms is 0.98 e. From these configurations, we see that the Bader charge associated with the C atom decreases with increasing coverage, and more specifically with more nearest-neighbour interactions, while the charge on the primary Fe atoms increases with increasing coverage.

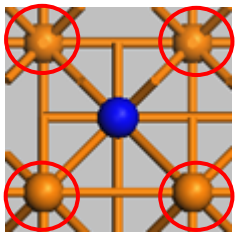

Figure 4-1: Fe atoms considered as "Primary" Fe atoms surrounding a species adsorbed in a hollow site

Table 4-4: Adsorption energy, geometry and vibrational frequencies of C of Fe (100) with coverage

	Author	Site	d_{Fe-X} (Å)	E_{ads} (eV)	v_1	v_2	v_3
					cm^{-1}		
C (0.33 ML)	Present Work (USPP-rPBE)	Four-fold hollow	1.955	-8.01	494 514	533 548	557 607
C (0.5 ML) adj.	Sorescu (USPP-PW91)	Four-fold hollow	1.923	-8.07			
	Present Work (USPP-rPBE)	Four-fold hollow	1.931	-7.93	536	538	574
C (0.5 ML) Diag.	Jiang & Carter (PAW-PBE)	Four-fold hollow	1.890	-8.29			
	Sorescu (PAW-PBE)	Four-fold hollow	1.894	-8.31			
	Sorescu (USPP-PW91)	Four-fold hollow	1.865	-8.12			
	Present Work (USPP-rPBE)	Four-fold hollow	1.898	-8.05	402 423	442 463	530 539
C (1 ML)	Jiang & Carter (PAW-PBE)	Four-fold hollow	-	-7.64			
	Sorescu (USPP-PW91)	Four-fold hollow	1.833	-7.54			
	Sorescu (PAW-PBE)	Four-fold hollow	1.828	-7.64			
	Present Work (USPP-rPBE)	Four-fold hollow	1.835	-7.33	364	393	520

The adsorption of carbon on Fe (100) results in some deformation of the Fe-atoms, particular the first layer of Fe atoms. This was seen in Chapter 2 with CO adsorption as well. When looking at the deformation energy (Table 4-4), nearest-neighbour interactions appear to result in a larger contribution of the deformation energy. The deformation energy also appears to increase with nearest neighbour interactions.

Figure 4-2 shows an energetic breakdown of the lateral interactions upon adsorption of carbon on Fe (100) taking a coverage at 0.25 ML as the baseline, i.e. no lateral interactions. Overall, there appears to be no correlations between the change in coverage and the change in the electro-static, kinetic energy and exchange correlation energies.

When the adsorption energy of the 0.33 ML configuration is broken down into its different components, the electrostatic energy is more repulsive by 2.91 eV while the changes in kinetic energy and exchange-correlation energy negates this with -2.02 and -0.90 respectively.

The energetic breakdown of the adsorption energy for the 0.5 ML “adjacent” configuration show increases in the electrostatic and kinetic of 0.18 eV and 0.64 eV respectively, while a decrease in the exchange-correlation energy of 0.75 eV is observed.

The energetic breakdown of the adsorption energy for the 0.5 ML “diagonal” configuration show increases in the electrostatic and exchange correlation energy of 0.92 eV and 0.34 eV respectively, while a decrease in the kinetic energy of 1.30 eV is observed.

The energetic breakdown of the adsorption energy for the 1 ML configuration show increases in the electrostatic and kinetic energy of 0.97 eV and 0.79 eV respectively, while a decrease in the exchange correlation energy of 1.07 eV is observed.

It is interesting to note that the component interaction energies can show large deviations but once combined the overall lateral interaction is considered negligible, as is the case for the 0.33 ML configuration. In each case, there are electrostatic repulsions as well as deviations in kinetic and exchange-correlation energies, the summation of these energies cancelling each other out. While changes in the adsorption energy are seen when comparing the 0.25, 0.33 and 0.5 ML coverages, these changes are small enough to be considered within the DFT calculation error.

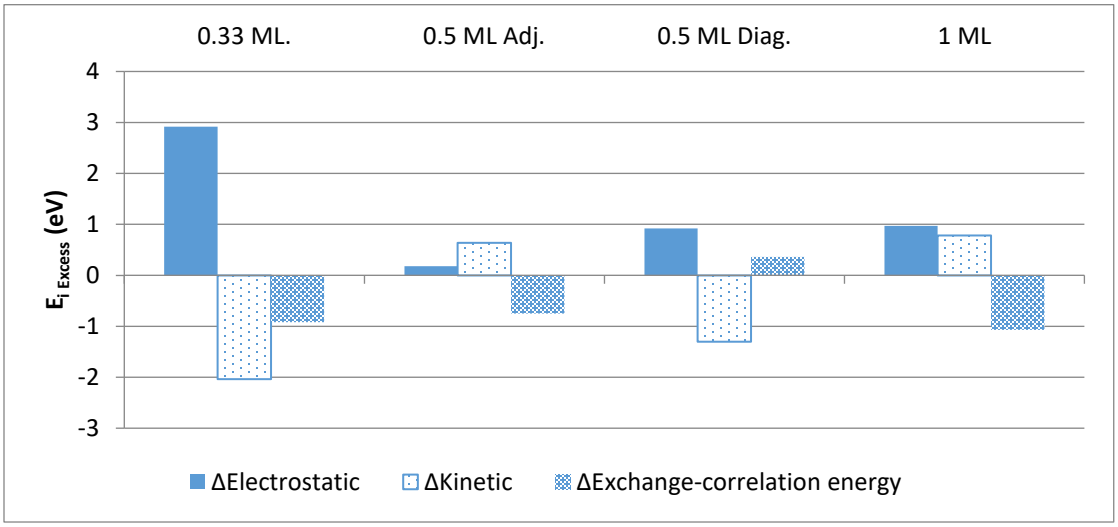

Figure 4-2: Energetic breakdown of lateral interactions between adsorbed atomic C relative to 0.25 ML coverage.

4.4 Adsorption of atomic oxygen (O) on Fe (100)

Theoretical studies[6,8,18] have shown that O can adsorb stably in the hollow site, bridge site and on-top site. The configuration with the lowest adsorption energy is the hollow site. Hence at lower coverages of atomic O on Fe (100), this configuration will be the dominant adsorption geometry. In the scope of this study, only the effect of the lateral interactions on the hollow site will be considered. The configurations considered as well as a summary of the results is available in Table 4-5. A direct comparison of our results and the results of Sorescu [7], Govender [10,31] and Ziegler and Lo [6] is given in Table 4-6.

Table 4-5: Configurations considered for the adsorption of O on Fe (100)

	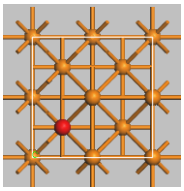	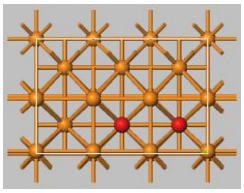	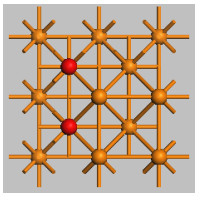	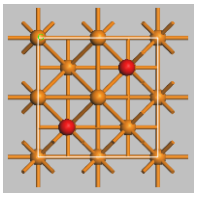	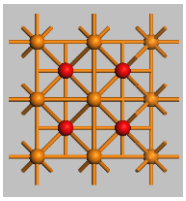
	0.25 ML	**0.33 ML**	**0.5 ML "adjacent"**	**0.5 ML "diagonal"**	**1 ML**
$E_{bind.}$ (eV/O)	-5.88	-5.89	-5.68	-5.88	-5.42
d O-Fe (Å)	2.138	2.000	2.122	2.079	2.088
E_{Defor} (eV/O)	0.04	0.04	0.04	0.06	0.09
E_{Fermi} (eV)	-6.15	-6.04	-6.09	-5.96	-5.77
q_O	-1.31	-1.31	-1.31	-1.30	-1.32
$q_{Fe\ Prim.}$	0.42	0.47	0.67	0.65	1.1

For the 0.25 ML configuration considered the O-Fe distance calculated in this study is the longest, 2.138 Å, while Lo and Ziegler[6] reported 2.101 Å and Sorescu [7] reported 2.096 Å for a PAW-PBE model and 2.095 Å usPP-PW91 model. The vibrational frequencies in Table 4-6 are for O at 0.25ML in the hollow site and confirm that it is indeed a minimum. The frequencies calculated in this study are in agreement with the results from literature.

Ziegler and Lo [6] have reported an adsorption energy of atomic O on Fe (100) at 0.25 ML of -3.434 eV/O, relative to O_2 in the gas phase. The results from this study show an adsorption energy of -3.77 eV/O. Sorescu [7] and Govender [10,31] have reported the adsorption energy relative to atomic O in the gas phase. Sorescu [7] reported binding energies of -6.38 eV/O for a PAW-PBE model and -6.07 eV/O usPP-PW91 model while Govender [10,31] reported a binding energy of -6.54 eV/O. Here, we report a binding energy of O on Fe (100) at 0.25 ML of -5.88 eV/O. The variation in binding energy between the different theoretical studies is larger for the O adsorption than for the other species considered in this study, as can be seen in Table 4-6. The study by Nørskov et al. [28] suggest that this is a result of the poor description of isolated O with DFT-GGA but this problem is typically seen for O_2. This study used a usPP-RPBE approach which should give a lower adsorption energy than usPP-PW91 approach [40].

Table 4-6: Adsorption of O on Fe (100) at a coverage of 0.25 ML compared with studies by Lo and Ziegler [6], Govender [10,31] and Sorescu [7]

	Author	Site	d_{O-Fe} (Å)	E_{ads} (eV)	E_{Bind} (eV)	v1	v2	v3
							cm^{-1}	
O (0.25 ML)	Ziegler & Lo	Four-fold hollow	2.101	-3.43	-			
	Govender	Four-fold hollow	-	-	-6.54	215	216	368
	Sorescu (USPP-PW91)	Four-fold hollow	2.095	-	-6.07			
	Sorescu (PAW-PBE)	Four-fold hollow	2.096	-	-6.38			
	Present Work	Four-fold hollow	2.138	-3.77	-5.88	320	320	335

A summary of the changes in geometry, binding energy and vibrational frequencies can be seen in Table 4-7. For 0.33 ML the O-Fe distance was found to be 2.000 Å which is an increase from the 1.961 Å distance found for the 0.25 ML configuration. The 0.5 ML "adjacent" and diagonal configuration has a shorter O-Fe distance of 2.122 Å and the "Diagonal" configuration a shorter O-Fe distance of 2.079 Å. The 1 ML configuration displays the shortest C-Fe distance 2.088 Å.

A 0.33 ML configuration was considered where each O atom has one nearest neighbour. The binding energy was found to be -5.89 eV/O. The difference in binding energy is negligible when compared to the 0.25 ML configuration.

The first 0.5 ML configuration considered was the "Adjacent" configuration, where each O atoms has two nearest neighbours. The binding energy was found to be -5.68 eV/O. A decrease in binding energy by 0.21 eV is observed when compared to the 0.25 ML configuration.

The next 0.5 ML configuration considered was the "Diagonal" configuration, where each O atom has four next-nearest neighbours. The binding energy was found to be -5.88 eV/O. The difference in binding energy is negligible when compared to the 0.25 ML configuration.

The 1 ML configuration considered has four nearest neighbours and four next-nearest neighbours for each O adsorbate. The binding energy was found to be -5.42 eV/O. A decrease in binding energy of 0.46 eV is observed when compared to the 0.25 ML configuration.

For coverages less than 0.5 ML, it appears that nearest neighbour interactions lowers the adsorption energy by about 0.11 eV while next-nearest neighbour interactions appear to be negligible. The electrostatic and kinetic energy of these systems show both negative and positive deviations from the 0.25 ML configuration while exchange-correlation energy decreases with increasing coverage. For atomic O adsorption on Fe (100), the lateral interaction with a destabilization of 0.11 eV per nearest neighbour can predict a binding energy at a coverage of 1 ML of -5.45 eV/O, in close agreement with the DFT-determined binding energy of -5.42 eV/O , unlike the C adsorption.

Looking at the Bader analysis, we see that majority of the charge associated with the metal is once again assigned to the "primary" Fe atoms (Figure 4-1). For the 0.25 ML configuration, the Bader charge on O is -1.31 e and on the primary Fe atoms is 0.42 e. The charge on the remaining Fe atoms are between -0.12

e and 0.12 e. For the 0.33 ML coverage, the charges on the O atoms were -1.31 e. For this configuration two primary atoms are shared between the adsorbates. The charges on these two shared Fe atoms were 0.47 e while the remaining primary atoms had charges of 0.4 e, and the remaining Fe atoms having charges between 0.12 and -0.12 e. For the 0.5 ML "diagonal" configuration the charge on O is -1.30 e. For this configuration, each primary Fe atom is shared between two adsorbates and has a charge of 0.65 e. The remaining Fe atoms have charges between 0.12 and -0.12 e. For the 0.5 ML "adjacent" configuration H has a charge of -1.31 e. Again, for this configuration each primary Fe atom is shared between two adsorbates and has a charge of 0.67 e, with the remaining Fe atoms having a charge between 0.12 and -0.12 e. Finally, for the 1 ML configuration, each primary atom is shared amongst four O atoms. The charge on the C atoms is -1.32 e while the charge on the primary Fe atoms is 1.1 e. The charge on the O atom remains relatively constant with increasing coverage while the charge on the primary Fe atoms increases with increasing coverage.

Table 4-7: Binding energy, geometry and vibrational frequencies of O of Fe (100) with coverage

	Author	Site	d_{Fe-O} (Å)	E_{ads} (eV)	E_{Bind} (eV)	v1	v2 cm^{-1}	v3
O (0.33 ML)	Present Work	Four-fold hollow	2.000	-3.79	-5.89	331	335	365
O (0.5 ML) adj.	Present Work	Four-fold hollow	2.122	-3.58	-5.68	265	361	368
O (0.5 ML) Diag.	Present Work	Four-fold hollow	2.079	-3.77	-5.88	306	322	354
O (1 ML)	Present Work	Four-fold hollow	2.088	-3.32	-5.42	352	382	383

The deformation energy appears to increase with increasing next-nearest-neighbour interactions. This is opposite to the deformation of atomic C on the surface which showed increase in deformation energy with increasing nearest-neighbour interactions. The deformation energy associated with the adsorption of C is larger than the deformation energy associated with the adsorption of O. This implies that the adsorption of C results in larger variation in the position of the Fe atoms in the structure compared to the adsorption of O.

The deviations in components of the adsorption energy from the 0.25 ML configuration can be seen in Table 4-5. There appears to be no correlations between the change in coverage and the change in the electro-static, kinetic energy and exchange correlation energies.

For 0.33 ML configuration, the difference in binding energy is negligible when compared to the 0.25 ML configuration, however when broken down into its different components, the electrostatic energy is more repulsive (increase in energy) by 1.80 eV while the attractive (decrease in energy) changes in kinetic energy and exchange-correlation energy negates this with -1.10 and -0.73 respectively. This was also observed in the adsorption of atomic carbon in an adjacent position at a coverage of 0.33 ML.

The 0.5 ML "Adjacent" configuration shows that the electrostatic energy is more repulsive by 2.12 eV while the changes in kinetic energy and exchange-correlation energy negates this with -0.92 and -1.00 respectively.

The 0.5 ML "Diagonal" configuration also shows a negligible difference in binding energy when compared to the 0.25 ML configuration, however when broken down into its different components, the electrostatic

and exchange correlation energies attractive with -1.38 eV and -0.91 eV respectively while the changes in kinetic energy is repulsive by 2.30 eV.

The 1 ML configuration shows a decrease in binding energy of 0.46 eV is observed when compared to the 0.25 ML configuration. When looking at the energetic breakdown of this change in binding energy we see that the electrostatic and kinetic energy are more repulsive by 1.51 eV and 0.81 eV while the changes in exchange-correlation energy is more attractive by 1.88 eV. Again, we see the component interaction energies show large deviations but once combined the overall lateral interaction is much smaller. In each case, there are electrostatic repulsions as well as deviations in kinetic and exchange-correlation energies, the summation of these energies cancelling each other out.

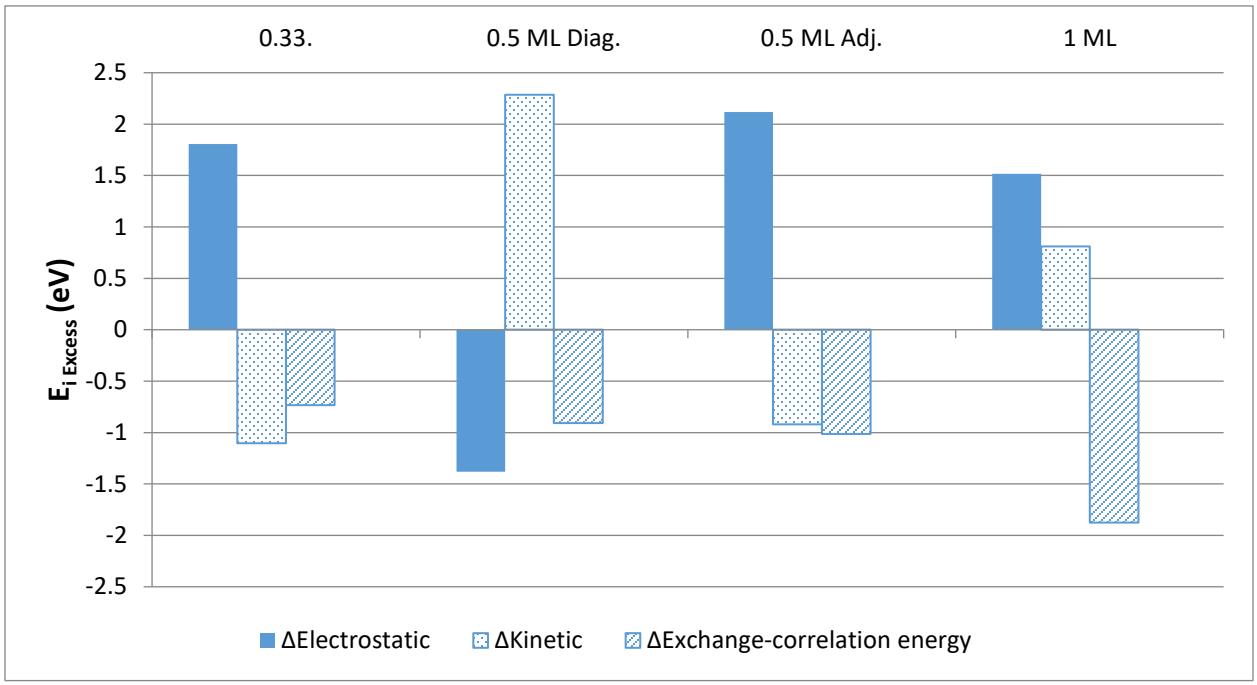

Figure 4-3: Energetic breakdown of lateral interactions of adsorbed atomic O on Fe (100) relative to 0.25 ML coverage.

4.5 Adsorption of atomic hydrogen (H) on Fe (100).

The interaction of hydrogen with metallic surfaces has been the subject of several experimental investigations including LEED [41], XPS and TPD [42] and HREELS [43]. These studies confirm that adsorption of H_2 takes place dissociative. Theoretical studies on low-index Fe surfaces have been used to predict the stability and sire preference of the adsorption of hydrogen [44–46]. Several theoretical studies [22,32,47] have shown that the most stable adsorption configuration for H on Fe (100) is in the four-fold hollow site. Table 4-8 shows the configurations considered in this study, along with a summary of the results obtained. While the hydrogen is stable on the bridge and on top sites, in the scope of this study, only the effect of the lateral interactions on the hollow site will be considered.

Table 4-8: Representation of the configurations used to study H adsorption on Fe (100)

	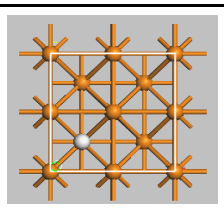	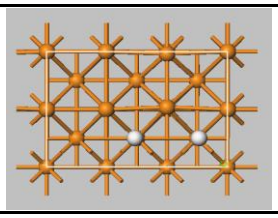	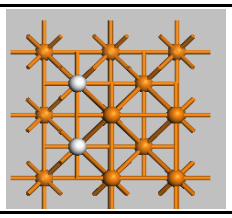	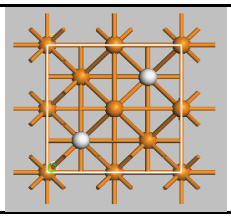	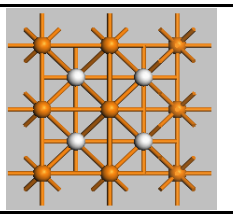
Coverage	**0.25 ML**	**0.33 ML**	**0.5 ML "adjacent"**	**0.5 ML "diagonal"**	**1 ML**
E_{Ads} (eV/H)	-0.25	-0.25	-0.28	-0.24	-0.25
d $_{H-Fe}$ (Å)	2.005	1.995	1.982	1.992	1.991
$E_{Deform.}$ (eV/H)	0.01	0.05	0.01	0.01	0.01
E_{Fermi} (eV)	-6.272	-6.276	- 6.263	-6.267	-6.228
q_H	-0.45 e	-0.43 e	-0.42 e	-0.44 e	-0.45
$q_{Fe\ Prim.}$	+0.12 e	+0.11 e	+0.15 e	+0.10 e	+0.28 e

Starting with the lowest coverage configuration, 0.25 ML, the H-Fe distance was found to be 2.005 Å. This distance is slightly less than the USPP-PW91 models by Ziegler and Lo [6], which showed a H-Fe distance of 2.048 Å ,and Sorescu[22], who found an H-Fe distances of 2.088 Å.

For the 0.25 ML configuration, the adsorption energy was found to be -0.25 eV/H relative to H_2 in the gas phase. These values are in good agreement with the work done by Sorescu [22], who reported an adsorption energy of –0.35 eV/H and Ziegler and Lo [6], who found a adsorption energy of –0.31 eV/H.

The vibrational frequencies in Table 4-10 are for H at 0.25ML in the hollow site and confirm that it is indeed a minimum. The frequencies calculated in this study are in agreement with the results from literature.

Table 4-9: Comparison of adsorption of H on Fe (100) with studies by Lo and Ziegler[6] and Sorescu[22]

	Author	Site	d_{H-Fe} (Å)	E ads (eV)	v1	v2	v3
					cm^{-1}		
H (0.25 ML)	Ziegler & Lo (USPP-PW91)	Four-fold hollow	2.048	-0.31			
	Sorescu (USPP-PW91)	Four-fold hollow	2.088	-0.35	209	227	1146
	Present Work (USPP-rPBE)	Four-fold hollow	2.005	-0.25	407	415	1170

A summary of the changes in geometry, adsorption energy and vibrational frequencies is given in Table 4-10. For 0.33 ML the H-Fe distance was found to be 1.995 Å which is not significantly different from the 2.005 Å distance found for the 0.25 ML configuration. The 0.5 ML "Adjacent" configuration has the shortest H-Fe distance of 1.982 Å and the "Diagonal" configuration a shorter H-Fe distance of 1.993 Å. The 1 ML configuration displays a H-Fe distance 1.991 Å. The bond lengths are in good agreement with studies by Lo and Ziegler [6] and Sorescu [22].

For the 0.33 ML configuration considered, each H atom has one nearest-neighbour for the configuration considered here. The adsorption energy was found to be -0.25 eV/H which is similar to the adsorption energy at 0.25 ML.

At a coverage of 0.5 ML, two configurations are considered. For the 0.5 ML "adjacent" configuration each H atom has two nearest-neighbours. The adsorption energy was found to be -0.28 eV/H, which is a slight decrease of 0.03 eV/H when compared to the 0.25 ML configuration adsorption energy. These values are in agreement with the work done by Sorescu [22] on a similar configuration, who found a adsorption energy of –0.37 eV/H which is a decrease of 0.02 eV/H when compared to the 0.25 ML configuration adsorption energy. This is different from the study by Ziegler and Lo [6] who reported an adsorption energy of –0.28 eV/H which is an increase of 0.03 eV/H when compared to the 0.25 ML configuration adsorption energy.

The other 0.5 ML configuration considered was the 0.5 ML "diagonal" configuration, where each H atom has four next-nearest-neighbours. The adsorption energy was found to be -0.24 eV/H which is similar compared to the 0.25 ML configuration adsorption energy.

For the 1 ML configuration, each H atom has four nearest-neighbours and four next-nearest-neighbours. The adsorption energy was found to be -0.25 eV/H which is a similar when compared to the 0.25 ML configuration adsorption energy. Again these values are in good agreement with the work done by Sorescu [22] on a similar configuration, who found a adsorption energy of –0.39 eV/H and Ziegler and Lo [6], who found a adsorption energy of –0.31 eV/H.

Table 4-10: Binding energy, geometry and vibrational frequencies of H of Fe (100) with coverage

	Author	Site	d_{Fe-H} (Å)	E_{ads} (eV)	v1	v2	v3
						cm^{-1}	
H (0.33 ML)	Present Work (USPP-rPBE)	Four-fold hollow	1.995	-0.25	380	426	1141
H (0.5 ML) adj.	Present Work (USPP-rPBE)	Four-fold hollow	1.982	-0.28	304	422	1150
	Sorescu (PAW-PBE)	Four-fold hollow	2.039	-0.36			
	Ziegler & Lo (USPP-PW91)	Four-fold hollow	2.048	-0.28			
H (0.5 ML) Diag.	Present Work (USPP-rPBE)	Four-fold hollow	1.993	-0.24	375	620	1215
H (1 ML)	Sorescu (USPP-PW91)	Four-fold hollow	2.034	-0.36	222	226	1127
	Ziegler & Lo (USPP-PW91)	Four-fold hollow	2.048	-0.31			
	Present Work (USPP-rPBE)	Four-fold hollow	1.991	-0.25	449	491	1153

Looking at the Bader analysis, we see that majority of the charge associated with the metal is assigned to the "primary" Fe atoms (Figure 4-1) once again. For the 0.25 ML configuration, the Bader charge on H is -0.45 e and on the primary Fe atoms is 0.12 e. The charge on the remaining Fe atoms are between -0.05 e and 0.05 e. For the 0.33 ML coverage, the charges on the H atoms were -0.43 e. For this configuration two primary atoms are shared between the adsorbates. Unlike the O and C configurations the charge on the shared and unshared Fe atoms is 0.11 e. For the 0.5 ML "diagonal" configuration the charge on H is -0.44 e. the charge on the primary Fe atoms is 0.10 e. For the 0.5 ML "adjacent" configuration H has a charge of -0.42 e. The charge on the primary Fe atoms is 0.15 e. Finally, for the 1 ML configuration, each primary atom is shared amongst four H atoms. The charge on the H atoms is -0.45 e while the charge on the primary Fe atoms is 0.28 e. The charge on the H atoms remain fairly constant with increasing coverage while the charge on the primary Fe atoms increases with the number of adsorbates adjacent to the primary Fe atom.

The deformation energy for hydrogen on Fe (100) is small and does not change much with coverage. Hydrogen adsorption has little to no effect on the positions of the Fe atoms.

The deviations in components of the adsorption energy from the 0.25 ML configuration can be seen in Figure 4-4. Overall, there appears to be no correlations between the change in coverage and the change in the electro-static, kinetic energy and exchange correlation energies. There does however appear to be a correlation between the kinetic energy and the sum of the electrostatic and exchange correlation energy, potential energy.

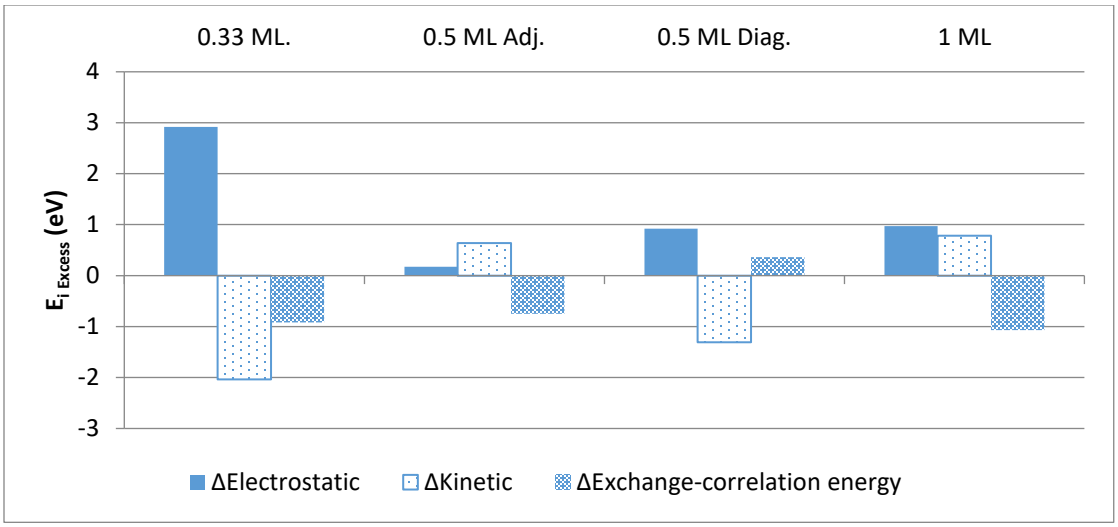

Figure 4-4: Energetic breakdown of lateral interactions between adsorbed atomic H relative to 0.25 ML coverage.

4.6 Adsorption of methylidyne (CH) on Fe (100)

Theoretical studies by Sorescu [7], Govender [10,31] and Ziegler and Lo [6] have shown that the most stable adsorption configuration for CH on Fe (100) is in the four-fold hollow site. Table 4-11 shows the configurations considered in this study, along with a summary of the results obtained. A direct comparison of our results and the results of Sorescu [7], Govender [10,31] and Ziegler and Lo [6] is available in Table 4-12.

Table 4-11: Representation of the configurations used to study CH adsorption on Fe (100)

	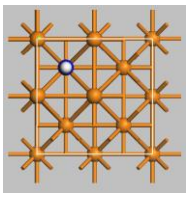	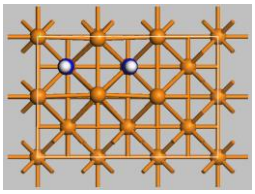	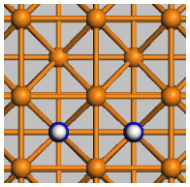	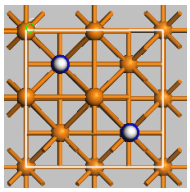	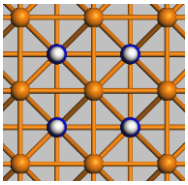
Coverage	**0.25 ML**	**0.33 ML**	**0.5 ML "adjacent"**	**0.5 ML "diagonal"**	**1 ML**
E_{Ads} (eV/CH)	-6.89	-6.81	-6.63	-7.00	-6.32
d C-Fe (Å)	2.072	2.077	2.067	2.067	2.086
d C-H (Å)	1.104	1.104	1.103	1.103	1.089
E_{Defo} (eV/CH)	0.02	0.03	0.03	0.03	0.04
E_{Fermi} (eV)	-6.09 eV	-6.03 eV	-5.86 eV	-5.89 eV	-5.28 eV
q_C	-1.35 e	-1.26 e	-1.38 e	-1.20 e	-1.21 e
q_H	0.05 e	0.05 e	0.06 e	0.06 e	0.11 e
$q_{Fe\ Prim.}$	0.33 e	0.33 e (Unshared) 0.50 e (Shared)	0.55 e	0.50 e	0.86 e

The Fe-C and C-H distances for adsorption of methylidene on Fe (100) at a coverage of 0.25 ML were found to be2.072 Å and 1.104 Å respectively, with the C-H bond is perpendicular to the surface. These distances are in good agreement with the literature results, as shown in Table 4-12. The vibrational frequencies for CH at 0.25ML in the hollow site and confirm that it is indeed a minimum. The frequencies calculated in this study are in agreement with the results from literature. The stretching frequency of C-H was found to be 2949 cm^{-1}, which is in reasonable agreement with Hung and Bernasek [48] who used HREELS measure a stretching frequency of 3010 cm^{-1}.

The 0.25 ML configuration has an adsorption energy of -6.89 eV/CH. These values are in good agreement with the work done by Sorescu [7], who reported an adsorption energy of –6.87 eV/CH and –7.00 eV/CH for the PW91 and PBE calculations respectively, Govender [10,31], who reported an adsorption energy of

–7.66 eV/CH, and Ziegler and Lo [6], who found a adsorption energy of –7.09 eV/CH. Other theoretical studies have not investigated configurations above 0.25 ML.

Table 4-12: Adsorption of CH on Fe (100) with studies by Lo and Ziegler[6], Govender[10,31] and Sorescu[7]

	Author	Site	d_{Fe-X} (Å)	d_{C-H} (Å)	E ads. (eV)	v1	v2	v3	v4	v5	v6
						cm^{-1}					
CH (0.25 ML)	Ziegler & Lo	Four-fold hollow	2.095	1.017	-7.09						
	Govender	Four-fold hollow	-	1.11	-7.66						
	Sorescu (USPP-PW91)	Four-fold hollow	2.075	1.109	-6.87	373	374	447	457	460	2919
	Sorescu (PAW-PBE)	Four-fold hollow	2.041	1.113	-7.00						
	Present Work	Four-fold hollow	2.072	1.104	-6.89	264	264	427	427	466	2949

A summary of the changes in geometry, binding energy and vibrational frequencies can be seen in Table 4-13. For 0.33 ML configuration the C-Fe and C-H distances are 2.077 Å and 1.104 Å respectively which is not significantly different from the geometry obtained for the 0.25 ML configuration. The 0.5 ML "adjacent" and "diagonal" configuration have identical C-Fe and C-H distances of 2.067 Å and 1.103 Å respectively. The 1 ML configuration displays C-Fe and C-H distances of 2.086 Å and 1.098 Å respectively. The bond lengths appear to be in good agreement with studies by Lo and Ziegler[6], Govender[10,31] and Sorescu[7]. The C-H bond is perpendicular to the surface for all cases except the 0.33 ML configuration which displays a slight tilt of 5^{o}.

A 0.33 ML configuration where CH has only one nearest neighbour was investigated. The adsorption energy was found to be -6.82 eV/CH, an increase of 0.08 eV, in the adsorption energy is observed when compared to the 0.25 ML configuration.

Two different configurations at 0.5 ML were investigated. With the 0.5 ML "adjacent" configuration, each CH has two nearest neighbours with which it interacts. The adsorption energy was found to be -6.61 eV/CH. This is an increase in the adsorption energy of 0.25 eV/CH, when compared to the adsorption energy obtained CH adsorbed in the 0.25 ML configuration

The other 0.5 ML configuration was the "diagonal" configuration, where each CH has four next-nearest neighbour interactions. The adsorption energy was found to be -7.00 eV/CH. This corresponds to a decrease in the adsorption energy of 0.12 eV/CH compared to the adsorption energy obtained for the adsorption of CH at a coverage of 0.25 ML. From this we can conclude that the next-nearest neighbour interaction has a stabilizing effect on the adsorption energy of CH.

A 1 ML configuration was investigated where each CH has four nearest and four next nearest neighbours. The adsorption energy was found to be -6.32 eV/CH. This represents a significant increase in the adsorption energy by 0.56 eV/CH in comparison to the adsorption energy obtained for the adsorption of CH at a coverage of 0.25 ML

From the configurations at 0.25, 0.33 and 0.5 ML it appears that nearest-neighbour interactions have a destabilizing interaction of about 0.15 eV/CH while next nearest neighbours have a stabilizing interaction of 0.06 eV/CH on the adsorption energy.

As seen with C adsorption, a large decrease in the adsorption energy of CH at a coverage of 1 ML is observed when compared to coverages at 0.5 and below. The approximation of a 0.15 eV/CH destabilization per nearest neighbour and stabilization of 0.03 eV/CH per next nearest neighbour would predict a decrease in adsorption energy of only 0.44 eV/CH. The 1 ML configuration shows stronger destabilization than the lower coverage species. This is further concluded by the longer C-Fe length and the shorter C-H bond length.

Table 4-13: Change in binding energy, geometry and vibrational frequencies of CH of Fe (100) with coverage

	Author	Site	d_{Fe-C} (Å)	d_{C-H} (Å)	$E_{ads.}$ (eV)	v1	v2	v3	v4	v5	v6
						cm^{-1}					
CH (0.25 ML)	Present Work	Four-fold hollow	2.072	1.104	-6.89	264	264	427	427	466	2949
CH (0.33 ML)	Present Work	Four-fold hollow	2.077	1.104	-6.81	275	366	447	453	480	2943
CH (0.5 ML) adj.	Present Work	Four-fold hollow	2.067	1.103	-6.63	243	443	445	459	548	2946
CH (0.5 ML) Diag.	Present Work	Four-fold hollow	2.067	1.103	-7.00	271	325	432	460	503	2960
CH (1 ML)	Present Work	Four-fold hollow	2.086	1.098	-6.32	353	360	497	545	546	2995

A Bader charge analysis showed that majority of the charge associated with the metal is assigned to the "primary" Fe atoms (Figure 4-1. For the 0.25 ML configuration, the Bader charge on C is -1.35 e, on H is 0.05 e and on the four primary Fe atoms is 0.33 e. The charges on the remaining surface Fe atoms are between -0.12 e and 0.12 e. With the 0.33 ML coverage, the charges on the C atoms are -1.26 e and the charges on the H atoms are 0.05 e. For this configuration two primary atoms are shared between the adsorbates. The charge on each of these two shared Fe atoms was 0.50 e while the remaining primary atoms had charges of 0.33 e; the remaining surface Fe atoms have charges between 0.12 and -0.12 e. For the 0.5 ML "diagonal" configuration the charge on C is -1.20 e and the charge on H is 0.06 e. Here each primary Fe atom is shared between two adsorbates and has a charge of 0.50 e and the remaining Fe atoms have charges between 0.12 and -0.12 e. For the 0.5 ML "adjacent" configuration C has a charge of -1.38 e and the charge on H of 0.06 e. Again, each primary Fe atom is shared between two adsorbates and has a charge of 0.55 e, with the remaining Fe atoms having a charge between 0.12 and -0.12 e. Finally, for the 1 ML configuration, each primary atom is shared amongst four CH atoms. The charge on the C atoms is -1.21 e, the Charge on H atoms 0.11 e while the charge on the primary Fe atoms is 0.86 e.

When looking at the deformation energy there appeared to very littler deviation with increasing coverage. The deviations from the 0.25 ML configuration in components of the adsorption energy can be seen in Figure 4-5. Overall, there appears to be no correlations between the change in coverage and the change in the electro-static, kinetic energy and exchange correlation energies.

For the 0.33 ML configuration, the energetic breakdown of the adsorption energy shows an increase in the electrostatic energy by 1.76 eV and a decrease in both the kinetic and exchange-correlation energy by 1.06 eV and 0.66 eV respectively.

For the 0.5 ML "Adjacent" configuration the energetic breakdown of the adsorption energy shows an increase in the kinetic energy of 0.85 eV, while a decreases the exchange-correlation energy 0.62 eV is observed. Negligible change in the electrostatic energy is observed.

For the 0.5 ML "Diagonal" configuration the energetic breakdown of the adsorption energy shows increases in the kinetic and electrostatic energy by 0.17 eV and 0.07 eV respectively, while the exchange-correlation energy decreases by 0.35 eV is observed.

For the 1 ML configuration, the energetic breakdown of the adsorption energy shows an increase in the electrostatic energy of 2.90 eV and a decrease in the kinetic and exchange-correlation energy of 0.91 eV and 1.42 eV respectively.

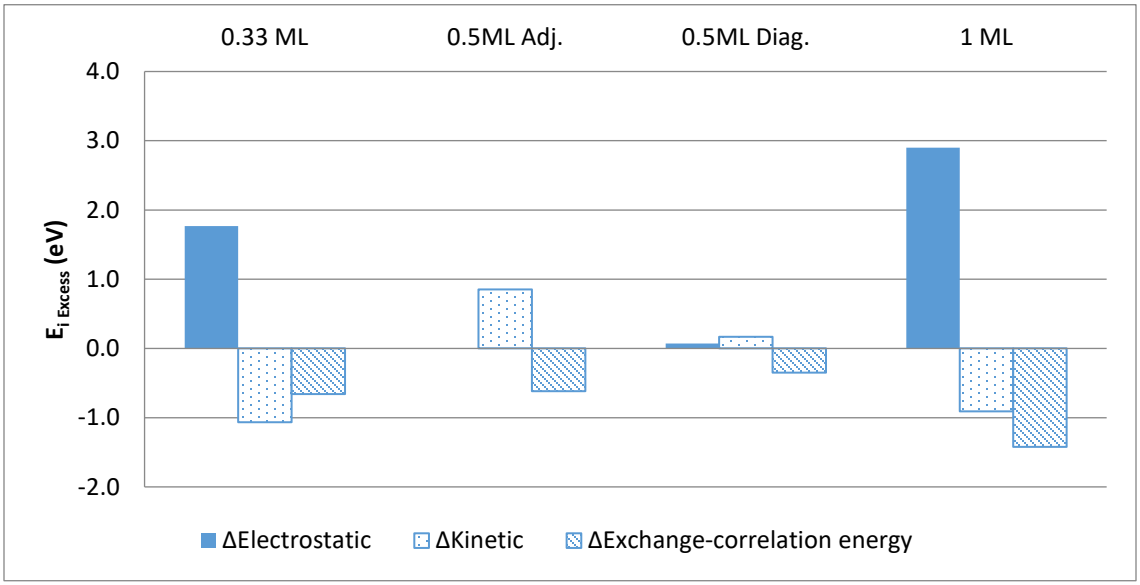

Figure 4-5: Energetic breakdown of lateral interactions between adsorbed CH-species relative to 0.25 ML coverage.

4.7 Adsorption of methylene (CH_2) on Fe (100)

Theoretical studies [6,7,10] have shown that the most stable adsorption configuration for CH_2 on Fe (100) is in the four-fold hollow site. The configurations considered as well as a summary of the results is available in Table 4-14. A direct comparison of our results and the results of Sorescu [7], Govender [10,31] and Ziegler and Lo [6] is available in Table 4-15.

Table 4-14: Configurations considered for the adsorption of CH_2 on Fe (100)

	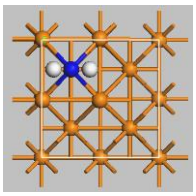	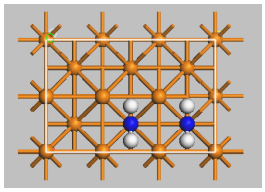	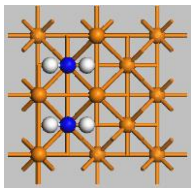	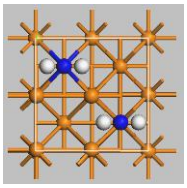	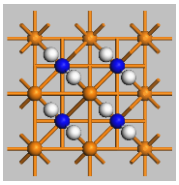
Coverage	**0.25 ML**	**0.33 ML**	**0.5 ML "adjacent"**	**0.5 ML "diagonal"**	**1 ML**
E_{Ads} (eV/CH_2)	-4.43	-4.48	-4.29	-4.42	-3.41
d C-Fe (Å)	2.133	2.145	2.145	2.131	2.143
d C-H (Å)	1.131	1.139	1.139	1.131	1.134
E_{Defo} (eV/CH_2)	0.05	0.01	0.01	0.01	0.01
E_{Fermi} (eV)	-6.01	-5.91	-5.60	-5.71	-5.05
q_C	-1.32 e	-1.36 e	-1.142 e	-1.28 e	-1.05 e
q_H	0.11 e	0.11 e	0.10	0.05 e	0.05 e
$q_{Fe\ Prim.}$	0.36 e	0.25 e(Unshared) 0.37 e(Shared)	0.45 e	0.52 e	0.72 e

Starting with the lowest coverage configuration, 0.25 ML, C-Fe and C-H distances of 2.133 Å and 1.131 Å respectively and a H-C-H angle of 101.1°. These values are in good agreement with the work done by Sorescu [7], C-Fe and C-H distances of 2.174 Å and 1.134 Å respectively and a H-C-H angle of 101.3° for a USPP-PW91 model and C-Fe and C-H distances of 2.174 Å and 1.139 Å respectively and a H-C-H angle of 101.4° for a PAW-PBE model. The PAW-PW91 model by Govender[31] resulted in a C-H distance of 1.140 Å and the USPP-PW91 model by Ziegler and Lo showed C-Fe and C-H distances of 2.144 Å and 1.139 Å respectively and a H-C-H angle of 101.2°

The adsorption energy of the 0.25 ML configuration was found to be -4.43 eV/CH_2. Sorescu [7] who reported an adsorption energy of –4.32 eV/CH_2 and –4.36 eV/CH_2 for the PW91 and PBE calculations

respectively, Govender [10,31], who found a adsorption energy of –4.55 eV/CH_2, and Ziegler and Lo [6], who found a adsorption energy of –4.36 eV/CH_2.

Table 4-15: Adsorption of CH_2 on Fe (100) with studies by Lo and Ziegler[6], Govender[10,31] and Sorescu[7]

	Author	Site	d_{Fe-C} (Å)	d_{C-H} (Å)	Θ(H-C-H) (°)	$E_{ads.}$ (eV)	v1	v2	v3	v4	v5	v6	v7	v8	v9
							cm^{-1}								
CH_2 (0.25 ML)	Ziegler & Lo	Four-fold hollow	2.144	1.139	101.2	-4.36	262	315	355	395	502	685	1202	2565	2578
	Govender	Four-fold hollow	-	1.14	-	-4.55									
	Sorescu (USPP-PW91)	Four-fold hollow	2.174	1.134	101.3	-4.32	285	328	362	367	481	687	1212	2615	2633
	Sorescu (PAW-PBE)	Four-fold hollow	2.174	1.139	101.4	-4.36									
	Present Work	Four-fold hollow	2.133	1.131	101.1	-4.43	345	366	372	401	417	635	1193	2619	2677

A summary of the changes in geometry, binding energy and vibrational frequencies can be seen in Table 4-16. For the 0.33 ML configuration C-Fe and C-H distances of 2.145 Å and 1.139 Å respectively and a H-C-H angle of 99.5°. This structure is similar to that of the 0.25 ML configuration.

At a coverage of 0.5 ML, two configurations are considered. The first considered is the 0.5 ML "adjacent" configuration where each CH_2 adsorbate has two nearest neighbour adsorbate. C-Fe and C-H distances of 2.145 Å and 1.139 Å respectively and a H-C-H angle of 99.4°. This configuration, the 0.33 ML and the 0.25 ML configurations have almost identical geometries.

The next 0.5 ML configuration is the "diagonal" configuration where each CH_2 adsorbate has four next-nearest neighbour adsorbates. C-Fe and C-H distances were found to be 2.134 Å and 1.131 Å respectively and a H-C-H angle of 101.1°.

The geometry optimization of the 0.33 ML and the 0.5 ML configurations results in the interesting orientations of the hydrogen atoms. For neighbouring adsorbates, the H-H plane of a particular CH_2 adsorbate is parallel to the H-H plane of the neighbouring CH_2 adsorbate. This is the case for both nearest neighbour and next nearest neighbour interactions. The phenomenon of adsorbate-adsorbate interaction resulting in a re-orientation of the adsorbate structure has been observed by Nørskov [49]. This reorientation leads one to believe that perpendicular and co-linear H-H planes of neighbouring CH_2 adsorbates result in a destabilization.

A 1 ML configuration was considered, where each CH_2 adsorbate has 4 nearest neighbours and 4 next-nearest neighbours. The adsorption energy was found to be -3.41 eV/CH_2, C-Fe and C-H distances of 2.143 Å and 1.134 Å respectively and a H-C-H angle of 92.8°. Again, we see an interesting change in the orientation of the H atoms. Firstly, the H-H planes of the CH_2 adsorbates are diagonal with regard to the surface Fe atoms. This allows for all the H-H planes of the nearest neighbour CH_2 adsorbates to be parallel

and two next nearest neighbour H-H planes to be co-linear and two next nearest neighbour adsorbates to be parallel.

In the 0.33 ML configuration, each CH_2 adsorbate has one nearest neighbour adsorbate. We find an adsorption energy of -4.28 eV/CH_2, the adsorption energy has decreased by 0.15 eV when compared to the 0.25 ML configuration. The energetic breakdown of the adsorption energy show increases in the electrostatic and kinetic energy of 0.81 eV and 0.37 eV respectively, while a decrease in the exchange-correlation energy of 1.05 eV is observed.

We look at two 0.50 ML configurations. The first considered is the 0.5 ML "adjacent" configuration where each CH_2 adsorbate has two nearest neighbour adsorbate. The adsorption energy was found to be -4.09 eV/CH_2. This represents a decrease of 0.34 eV in the adsorption energy is observed when compared to the 0.25 ML configuration. The energetic breakdown of the adsorption energy shows an increase in the kinetic energy of 1.99 eV, while decreases in the electrostatic and exchange-correlation energy of 0.55 eV and 1.10 eV are observed.

The next 0.50 ML configuration is the "diagonal" configuration where each CH_2 adsorbate has four next-nearest neighbour adsorbates. The adsorption energy was found to be -4.42 eV/CH_2. This represents a negligible change in the adsorption energy for the adsorption of methylidene at a coverage of 0.25 ML. The energetic breakdown of the adsorption energy shows an increase in the kinetic energy of 1.39 eV, while decreases in the electrostatic and exchange-correlation energy of 0.06 eV and 1.31 eV are observed.

For the 1 ML configuration the adsorption energy of CH_2 was found to be -3.41 eV/CH_2. This represents a large decrease of 1.02 eV in the adsorption energy compared to the adsorption of methylidene at a coverage of 0.25 ML. The energetic breakdown of the adsorption energy show increases in the kinetic energy and non-Coulombic of 2.70 eV and 0.60 eV respectively, while decreases in the electrostatic and exchange-correlation energy of 0.56 eV and 1.72 eV is observed.

For 0.5 ML and below it appears that nearest neighbour interactions lower the adsorption energy by approximately 0.15 eV while next nearest neighbour interactions appear to be negligible. The electrostatic energy of these systems varies while the kinetic energy is largely increased and exchange-correlation energy is largely decreased.

As seen with C and CH adsorption, there is a large decrease in the adsorption energy at 1 ML when compared to coverages at 0.5 and below. The approximation of a 0.15 eV/CH_2 destabilization per nearest neighbour will be an underestimate. Again, we suspect that the interactions are more complex at higher coverages and additional adsorbate-metal interactions need to be considered.

The Bader analysis again reveals the majority of charge on the metal is assigned to the "primary" Fe atoms. For the 0.25 ML configuration, the Bader charge on C is -1.32 e, on H is 0.11 e and on the primary Fe atoms is 0.32e. The charge on the remaining Fe atoms are between -0.12 e and 0.12 e. Increasing the coverage to 0.33 ML, the charges on the C atoms were -1.36 e and the charges on the H atoms were 0.11 e. This configuration has two primary atoms shared between the adsorbates. The charges on these two shared Fe atoms were 0.36 e with the unshared primary atoms having charges of 0.25 e, and the remaining Fe atoms having charges between 0.15e and -0.15 e. For the 0.5 ML "adjacent" configuration C has charges of -1.14 e and the charges on H of 0.10 e. For this configuration, each primary Fe atom is shared between two adsorbates and has a charge of 0.45 e, with the remaining Fe atoms having a charge between 0.12 and -0.12 e. The 0.5 ML "diagonal" configuration has charges on C of -1.28 e and charges on H of 0.05. Again, the configuration shares each primary Fe atom between two adsorbates and these have charges of 0.52 e. The remaining Fe atoms have charges between 0.12 and -0.12 e. Finally, for the 1 ML

configuration, each primary atom is shared amongst four C atoms. The charge on the C atom is -1.05 e, the charge on the H atom is -0.11 e while the charge on the primary Fe atoms is 0.72 e. Nearest neighbour interactions appear to increase the charge on the C atom while next nearest neighbour interactions appear to decrease the charge on the C atom.

Table 4-16: Adsorption energy, geometry, and vibrational frequencies of CH_2 of Fe (100) as a function of coverage

	Author	Site	d_{Fe-C} (Å)	d_{C-H} (Å)	Θ_{H-C-H} (°)	E ads. (eV)	v1	v2	v3	v4	v5	v6	v7	v8	v9
							cm^{-1}								
CH_2 (0.25 ML)	Present Work	Four-fold hollow	2.133	1.131	101.1	-4.43	345	366	372	401	417	635	1193	2619	2677
CH_2 (0.33 ML)	Present Work	Four-fold hollow	2.145	1.139	99.5	-4.28	108	349	372	384	418	643	1172	2564	2667
CH_2 (0.5 ML) adj.	Present Work	Four-fold hollow	2.145	1.139	99.4	-4.09	288	352	392	430	441	734	1206	2516	2599
CH_2 (0.5 ML) Diag.	Present Work	Four-fold hollow	2.134	1.131	101.1	-4.42	289	353	403	414	429	642	1184	2619	2671
CH_2 (1 ML)	Present Work	Four-fold hollow	2.143	1.134	92.8	-3.41	216	283	438	627	775	882	1375	2498	2581

The deformation energy was the lowest of all the C based species and showed very little deviation with increasing coverage or interaction.

The deviations from the 0.25 ML configuration in components of the adsorption energy can be seen in Figure 4-6. Overall, there appears to be no correlations between the change in coverage and the change in the electro-static, kinetic energy and exchange correlation energies.

For the 0.33 ML configuration, the adsorption energy has decreased by 0.15 eV when compared to the 0.25 ML configuration. The energetic breakdown of the adsorption energy show increases in the electrostatic and kinetic energy of 0.81 eV and 0.37 eV respectively, while a decrease in the exchange-correlation energy of 1.05 eV is observed.

The 0.5 ML “Adjacent” configuration displays a decrease of 0.34 eV in the adsorption energy when compared to the 0.25 ML configuration. The energetic breakdown of the adsorption energy shows an increase in the kinetic energy of 1.99 eV, while decreases in the electrostatic and exchange-correlation energy of 0.55 eV and 1.10 eV are observed.

The 0.50 ML “Diagonal” configuration shows negligible change in the adsorption energy is observed when compared to the 0.25 ML configuration. The energetic breakdown of the adsorption energy shows an increase in the kinetic energy of 1.39 eV, while decreases in the electrostatic and exchange-correlation energy of 0.06 eV and 1.31 eV are observed.

For the 1 ML configuration, a large decrease of 1.02 eV in the adsorption energy is observed when compared to the 0.25 ML configuration. The energetic breakdown of the adsorption energy show

increases in the kinetic energy and non-Coulombic of 2.70 eV and 0.60 eV respectively, while decreases in the electrostatic and exchange-correlation energy of 0.56 eV and 1.72 eV is observed.

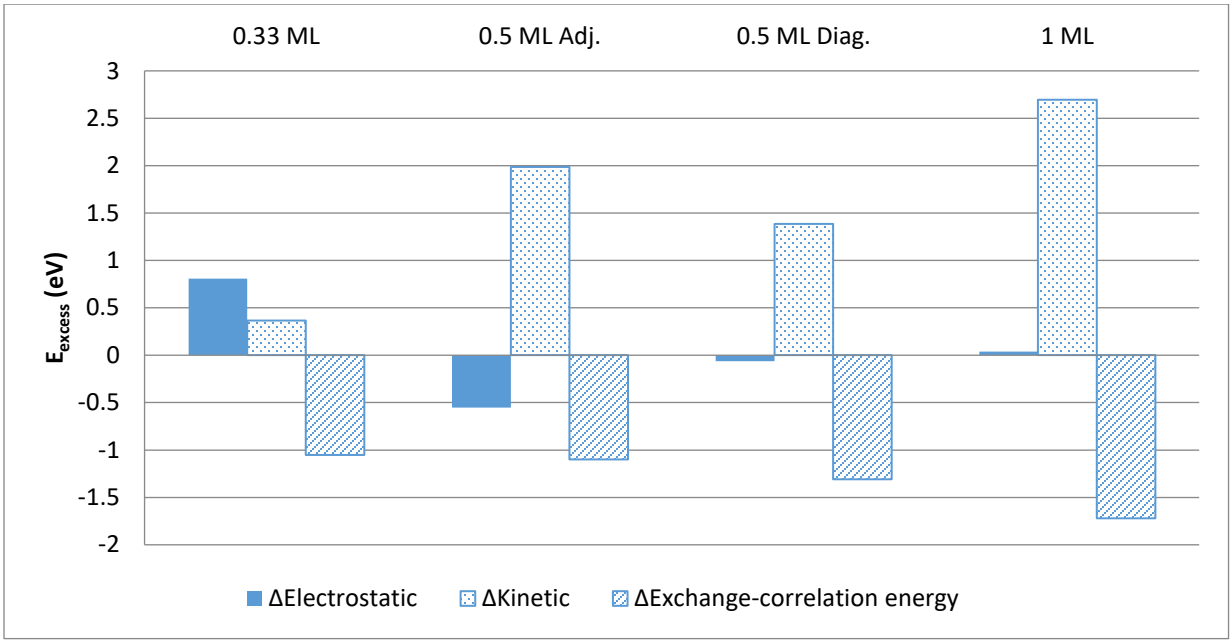

Figure 4-6: Energetic breakdown of lateral interactions between CH_2 species relative to 0.25 ML coverage.

4.8 Adsorption of methyl (CH_3) on Fe (100)

Theoretical studies [6,7,10] have shown that have shown that the most stable adsorption configuration for CH_3 on Fe (100) is 0n the bridge site. The configurations considered as well as a summary of the results is available in Table 4-17. A direct comparison of our results and the results of Sorescu [7], Govender [10,31] and Ziegler and Lo [6] is available in Table 4-18.

Table 4-17: Configurations considered for the adsorption of CH_3 on Fe (100)

	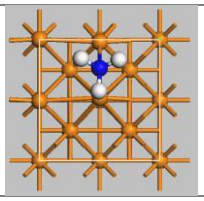	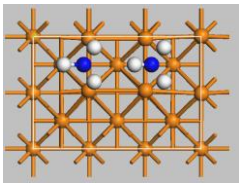	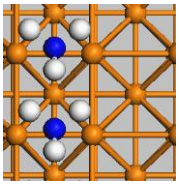	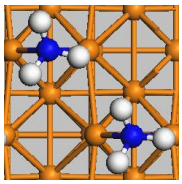	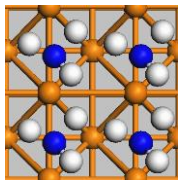
Coverage	**0.25 ML**	**0.33 ML**	**0.5 ML "adjacent"**	**0.5 ML "diagonal"**	**1 ML**
E_{Ads} (eV/CH_3)	-1.63	-1.53	-0.99	-1.59	-0.10
d C-Fe (Å)	2.134 2.249	2.184	2.156	2.142 2.241	2.048 2.340
d C-H (Å)	1.093 1.107	1.089 1.102	1.077 1.096	1.093 1.104	1.071 1.080
$E_{Deform.}$ (eV/CH_3)	0.12	0.10	0.05	0.08	0.03
E_{Fermi}	-5.96 eV	-5.85 eV	-5.70 eV	-5.67 eV	-5.27 eV
q_C	-0.81 e	-0.78	-0.85 e	-0.78 e	-0.60 e
q_H	0.11 e	0.11 e	0.11 e	0.11 e	0.07 e
$q_{Fe\ Prim.}$	0.35 e	0.35 e	0.35 e	0.35 e	0.44 e

Starting with a 0.25 ML configuration the C-Fe distances were found to be 2.134 Å and 2.249 Å, C-H distances of 1.10 ± 0.007 Å and a H-C-H angle of 106± 2.5°. One H atom appears to be co-planar to the Fe atoms of the involved bridge site. These values are in good agreement with the values reported by Sorescu [7], who found C-Fe distances of 2.174 Å, C-H distances of 1.03 ± 0.007 Å and a H-C-H angle of 105± 2.5° for PW91, C-Fe distances of 2.161 Å, C-H distances of 1.107 ± 0.007 Å and a H-C-H angle of 106± 2.5° for PBE calculations and Ziegler and Lo [6], who found C-Fe distances of 2.167 Å, C-H distances of 1.104 ± 0.008 Å and a H-C-H angle of 105± 2.5°

The adsorption energy of the 0.25 ML configuration was found to be -1.63 eV/CH_3. Sorescu [7] found a adsorption energy of –1.90 eV/CH_3 and –1.87 eV/CH_3 for the PW91 and PBE calculations respectively, Govender [10,31], who found a adsorption energy of –2.00 eV/CH_2, and Ziegler and Lo [6], who found a adsorption energy of –1.82 eV/CH_2.

Table 4-18: Adsorption of CH_3 on Fe (100) at a coverage of 0.25 ML compared with studies by Lo and Ziegler[6], Govender[10,31] and Sorescu[7]

	Author	Site	d_{Fe-CH3} (Å)	d_{C-H} (Å)	Θ_{H-C-H} (°)	E_{ads} (eV)
CH_3 (0.25 ML)	Ziegler & Lo	Bridge site	2.167	1.096 1.112	102.70 108.43	-1.815
	Govender	Bridge site	-	1.10 1.12	-	-2.00 (-2.07)
	Sorescu (USPP-PW91)	Bridge site	2.174	1.110 1.096	108.1 107.7 103.1	-1.90
	Sorescu (PAW-PBE)	Bridge site	2.161	1.100 1.114	107.9 103.2	-1.87
	Present Work	Bridge site	2.134 2.249	1.093 1.107	104.5 108.8	-1.63

Author	v1	v2	v3	v4	v5	v6	v7	v8	v9	v10	v11	v12
						cm^{-1}						
Present Work	198	244	332	352	540	598	1027	1311	1402	2902	2998	3178

A summary of the changes in geometry, binding energy and vibrational frequencies can be seen in Table 4-19. For the 0.33 ML configuration considered the geometry showed a C-Fe distance of 2.184 Å, C-H distances of 1.095 ± 0.007 Å and a H-C-H angle of 105± 2.5°. The carbon atom appears to be off centre of the bridge site and on H atoms appears to lie perpendicular to the bridge site.

For the 0.5 ML "adjacent" configuration the geometry showed a C-Fe distance of 2.156 Å, C-H distances of 1.085 ± 0.011 Å and H-C-H angles of ca. 104± 1°. One H atom appears to be co-planar to the Fe atoms of the involved bridge site.

The other 0.5 ML configuration considered was the 0.5 ML "diagonal" configuration. Here each CH_3 adsorbate has two nearest neighbours. with C-Fe distances of 2.142 Å and 2.241 Å, C-H distances of 1.10 ± 0.007 Å and an H-C-H angle of 106± 2.5°.

Finally, for the 1 ML configuration considered, each CH_3 adsorbate has four nearest neighbours and four next-neighbours. The adsorption energy was found to be -0.1 eV/CH_3 with C-Fe distances of 2.048 Å and 2.340 Å, C-H distances of 1.075 ± 0.005 Å and a H-C-H angle of 105± 3°. The hydrogen atoms appear to be in a very different configuration than the other configurations considered, most likely due to steric interactions.

For the 0.33 ML configuration considered each CH_3 adsorbate has one neighbouring CH_3 adsorbate on an adjacent bridge site. The adsorption energy was found to be -1.53 eV/CH_3 A decrease of 0.10 eV in the adsorption energy is observed when compared to the 0.25 ML configuration.

For the 0.5 ML “adjacent” configuration, each CH_3 adsorbate has two neighbouring CH_3 adsorbates on adjacent bridge sites. The adsorption energy was found to be -0.99 eV/CH_3 A significant decrease of 0.64 eV in the adsorption energy is observed when compared to the 0.25 ML configuration.

The other 0.5 ML configuration considered was the 0.5 ML “diagonal” configuration. Here each CH_3 adsorbate has four nearest neighbours. The adsorption energy was found to be -1.59 eV/CH_3 negligible change in the adsorption energy is observed when compared to the 0.25 ML configuration.

Finally, for the 1 ML configuration considered, each CH_3 adsorbate has four nearest neighbours and four next-neighbours. The adsorption energy was found to be -0.1 eV/CH_3, a large decrease in the adsorption energy of 1.53 eV is observed when compared to the 0.25 ML configuration. The energetic breakdown of the adsorption energy shows an increase in the kinetic energy of 7.18 eV, while decreases in the electrostatic and exchange-correlation energy of 3.75 eV and 1.87 eV were observed.

With 0.5 ML and below it appears that nearest neighbour interactions lower the adsorption energy by about 0.10 to 0.30 eV/CH_3 while next-nearest neighbour interactions appear to be negligible. As seen with the other CH_x species, a large decrease in the adsorption energy at 1 ML when compared to coverages at 0.5 and below. The approximation of about 0.2 eV/CH_3 destabilization per nearest neighbour will be an under estimate. Again, we suspect that the interactions are more complex at higher coverages and additional adsorbate-metal interactions need to be considered. The Fermi level, -5.28 eV, is again much lower than the lower coverage configurations. Again, this will change the interactions between the d-band and frontier orbitals. Once again, we recommend that the lateral interaction approximations should only be used for low to moderate coverages as it would under estimate at higher coverages.

Looking at the Bader analysis, as with the C, CH and CH_2 adsorbates majority of the charge associated with the metal is not evenly distributed but assigned to the atoms directly involved in the bond. For the bridge adsorption site the primary atoms are indicated in Figure 4-7. On a BCC (100) surface when adsorbates are adsorbed on the bridge sites, the sharing of primary metal atoms is reduced. For the 0.25 ML configuration, the Bader charge on C is -0.81 e, on H is 0.11 e and on the primary Fe atoms is 0.35 e. The charge on the remaining Fe atoms are between -0.12 e and 0.12 e. For the 0.33 ML coverage, the charges on the C atoms were -0.78 e and the charges on the H atoms were 0.11 e. The charges on the two primary Fe atoms are 0.35 e and the remaining Fe atoms having charges between 0.15and -0.15 e. For the 0.5 ML “diagonal” configuration the charge on C is -0.78 e and the charge on H is 0.11. For this configuration, each primary Fe atom is shared between two adsorbates and has a charge of 0.35 e. The remaining Fe atoms have charges between 0.12 and -0.12 e. For the 0.5 ML “adjacent” configuration C has a charge of -0.85 e and the charge on H of 0.11 e. Each primary Fe atom has a charge of 0.35 e, with the remaining Fe atoms having a charge between 0.12 and -0.12 e. Finally, for the 1 ML configuration the charge on the C atom is -0.60 e, the charge on the H atom is 0.07 e while the charge on the primary Fe atoms is 0.44 e.

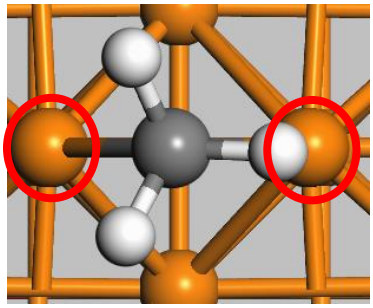

Figure 4-7: Fe atoms considered as "Primary" Fe atoms for a bridge site

Table 4-19: Adsorption energy, geometry and vibrational frequencies of CH_3 of Fe (100) with coverage

	Author	Site	d_{Fe-C} (Å)	d_{C-H} (Å)	Θ_{H-C-H} (°)	E_{ads} (eV)
CH_3 (0.25 ML)	Present Work	Bridge site	2.134 2.249	1.093 1.107	104.5 108.8	-1.63
CH_3 (0.33 ML)	Present Work	Bridge site	2.184	1.089 1.102	103.5 107.5	-1.53
CH_3 (0.5 ML) adj.	Present Work	Bridge site	2.156	1.077 1.096	105.2 106.0	-0.99
CH_3 (0.5 ML) Diag.	Present Work	Bridge site	2.142 2.241	1.093 1.104	103.5 105.5 108.5	-1.59
CH_3 (1 ML)	Present Work	Bridge site	2.048 2.340	1.071 1.080	102.0 104.0 108.5	-0.10

Coverage	**v1**	**v2**	**v3**	**v4**	**v5**	**v6**	**v7**	**v8**	**v9**	**v10**	**v11**	**v12**
						cm^{-1}						
0.25	198	244	332	352	540	598	1027	1311	1402	2902	2998	3178
0.33	110	236	316	362	505	615	1189	1355	1387	2957	3012	3190
0.50 (adj.)	200	266	346	360	529	606	1093	1362	1393	2933	3025	3182
0.50 (diag)	212	220	322	354	578	667	1030	1322	1395	2893	3092	3201
1	143	221	354	404	467	616	1087	1338	1553	3033	3114	3228

The deformation energy decreases with increasing coverage and the effect appears more sever with nearest neighbour interactions.

The deviations from the 0.25 ML configuration in components of the adsorption energy can be seen in Figure 4-8. Overall, there appears to be no correlations between the change in coverage and the change in the electro-static, kinetic energy and exchange correlation energies.

A 0.33 ML configuration shows a decrease of 0.10 eV in the adsorption energy when compared to the 0.25 ML configuration. The energetic breakdown of the adsorption energy show increases in the electrostatic and kinetic energy of 0.29 eV and 0.16 eV respectively, while a decrease in the exchange-correlation energy of 0.55 eV.

For the 0.5 ML "adjacent" configuration shows significant decrease of 0.64 eV in the adsorption energy when compared to the 0.25 ML configuration. The energetic breakdown of the adsorption energy shows an increase in the kinetic energy of 3.59 eV, while decreases in the electrostatic and exchange-correlation energy of 1.88 eV and 1.12 eV were observed.

The 0.5 ML "diagonal" configuration has negligible change in the adsorption energy when compared to the 0.25 ML configuration. The energetic breakdown of the adsorption energy shows an increase in the kinetic energy of 1.39 eV, while decreases in the electrostatic and exchange-correlation energy of 0.91 eV and 0.46 eV were observed.

The 1 ML configuration displays a large decrease in the adsorption energy of 1.53 eV when compared to the 0.25 ML configuration. The energetic breakdown of the adsorption energy shows an increase in the kinetic energy of 7.18 eV, while decreases in the electrostatic and exchange-correlation energy of 3.75 eV and 1.87 eV were observed.

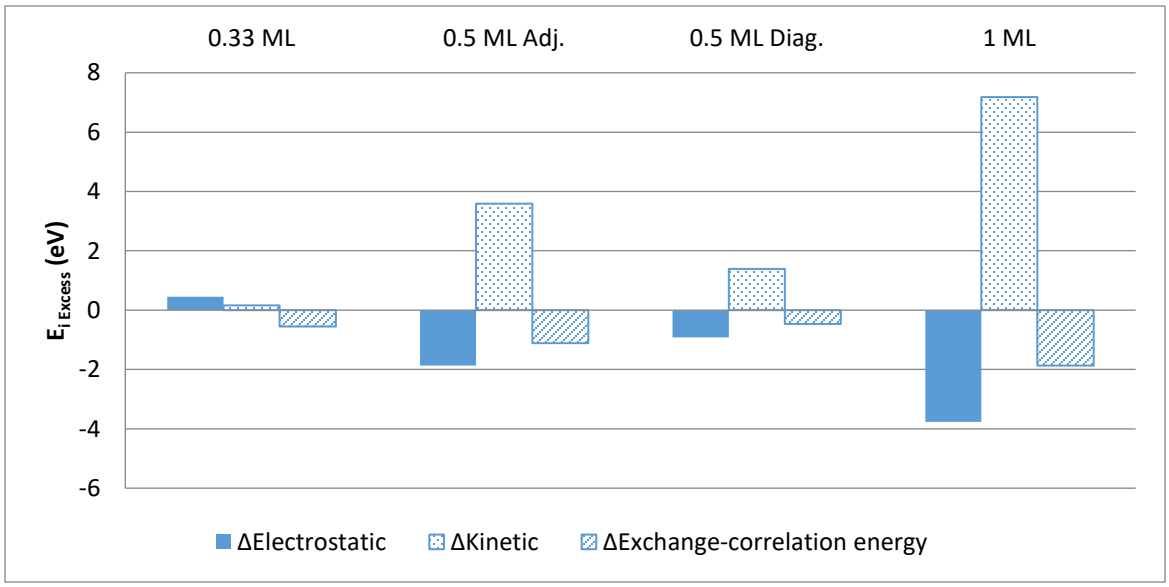

Figure 4-8: Energetic breakdown of lateral interactions of CH_3 on Fe (100) relative to 0.25 ML coverage.

4.9 Adsorption of OH on Fe (100)

As with O, theoretical studies[18,19] have shown that OH absorption on Fe (100) is stable at multiple sites, viz. the hollow site, tilted on the bridge site and on the on-top site. The configuration with the lowest adsorption energy is the bridge site. Using the same rational as with the O adsorption this configuration will be the dominant adsorption geometry, at lower coverages. In the scope of this study, only the effect of the lateral interactions on the bridge site will be considered. The configurations considered as well as a summary of the results is available in Table 4-21. A direct comparison of our results and the results of Eder & Terakura [19] and Govender[18,31] is available in Table 4-21.

Table 4-20: Configurations considered for the adsorption of OH on Fe (100)

	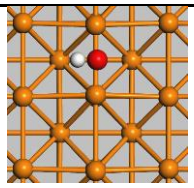	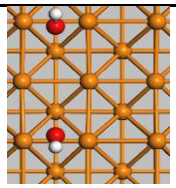	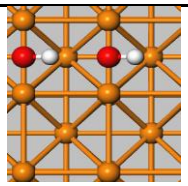	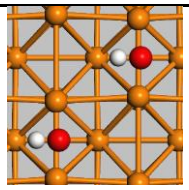	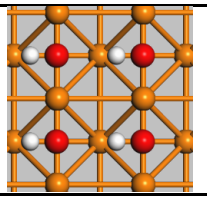
Coverage	**0.25 ML**	**0.33 ML**	**0.5 ML "adjacent"**	**0.5 ML "diagonal"**	**1 ML**
E_{Ads} (eV/OH)	-4.33	-4.31	-4.50	-4.36	-4.14
d O-Fe (Å)	2.012	2.016	2.015	2.015	2.006
d O-H (Å)	0.97	0.97	0.98	0.98	0.98
Tilt angle	63°	56°	60°	63°	65°
E_{Defo} (eV/OH)	0.06	0.06	0.08	0.09	0.10
E_{Fermi} (eV)	-6.09	-5.98	-6.00	-5.89	-5.84
q_O	-1.59	-1.58	-1.56	-1.57	-1.57
q_H	1.01	1.00	1.00	1.01	1.00
$q_{Fe\ Prim.}$	0.60	0.69	0.68	0.65	0.65

Starting with the 0.25 ML configuration the O-Fe and O-H distances were found to be 2.012 Å and 0.97 Å respectively and a title angle of 63° away from the normal. This is comparable to the results by Eder & Terakura [19] who found an OH distance of 0.98 Å and tilt angle of 53°, and Govender[18,31] who found an OH distance of 0.98 Å and tilt angle of 63° away from the normal.

For the 0.25 ML configuration the adsorption energy was found to be -4.33 eV/OH. The adsorption energy is slightly higher but still in agreement with the results of Eder & Terakura [19], who found a adsorption energy of -4.13 eV/OH, OH distance of 0.98 and tilt angle of 53°, and Govender[18,31] who found a adsorption energy of -4.12 eV/OH. The other theoretical studies have not investigated configurations above 0.25 ML.

Table 4-21: Adsorption of OH on Fe (100) with studies by Eder & Terakura [19] and Govender[18,31].

	Author	Site	Tilt Angle	d_{Fe-O} (Å)	d_{O-H} (Å)	E_{Ads} (eV)	v1	v2	v3	v4	v5	v6
							cm^{-1}					
OH (0.25 ML)	Eder & Terakura	Bridge Site	64°		0.98	-4.12						
	Govender	Bridge Site	53°		0.98	-4.13						
	Present Work	Bridge Site	63°	2.012	0.97	-4.33	245	274	389	415	566	3688

A summary of the changes in geometry, binding energy and vibrational frequencies is given in Table 4-22. For the 0.33 ML configuration considered the O-Fe and O-H distances were found to be 2.016 Å and 0.97 Å and a title angle of 56° away from the normal. The two OH adsorbates are tilted away from each other.

The first 0.5 ML configuration considered is the “adjacent” configuration, where O-Fe and O-H distances were found to be 2.015 Å and 0.98 Å and a title angle of 60° away from the normal. The OH adsorbates are tilted in the same direction.

The next 0.5 ML configuration considered is the “diagonal” configuration, with O-Fe and O-H distances of 2.015 Å and 0.98 Å and a title angle of 63° away from the normal. The OH adsorbates are tilted in the same direction.

The 1 ML configuration considered has O-Fe and O-H distances of 2.006 Å and 0.98 Å and a title angle of 65° away from the normal. The OH adsorbates are tilted in the same direction.

Looking at the 0.33 ML configuration considered, each OH adsorbate has one nearest neighbour. The adsorption energy was found to be -4.31 eV/OH. Negligible change in the adsorption energy is observed when compared to the 0.25 ML configuration.

The first 0.5 ML configuration considered is the “adjacent” configuration, where each OH adsorbate has two nearest neighbour. The adsorption energy was found to be -4.50 eV/OH. The adsorption energy is increased by 0.17 eV when compared to the 0.25 ML configuration.

The next 0.5 ML configuration considered is the “diagonal” configuration, where each OH adsorbate has four next nearest neighbours. The adsorption energy was found to be -4.36 eV/OH. Negligible change in the adsorption energy is observed when compared to the 0.25 ML configuration.

Finally, the 1 ML configuration considered has four nearest neighbour and four next nearest neighbours. The adsorption energy was found to be -4.13 eV/OH. The adsorption energy is decreased by 0.20 eV when compared to the 0.25 ML configuration.

With 0.5 ML and below it appears that nearest neighbour interactions stabilizes the adsorption energy by about 0.08 eV/OH while next nearest neighbour interactions appear to be negligible. When the 1 ML configuration is compared to the 0.5 ML and below configurations it appears that the interactions are more complex at higher coverages and additional adsorbate-metal interactions need to be considered. The Fermi level, -5.84 eV, is again much lower than the lower coverage configurations. Again, this will change the interactions between the d-band and frontier orbitals. Once again, we recommend that the lateral interaction approximations should only be used for low to moderate coverages as it would under estimate at higher coverages.

As with all the other species investigated, the Bader analysis reveals that majority of the charge associated with the metal is assigned to the "primary" Fe atoms (Figure 4-7) once again. As mentioned with the CH_3 adsorption, the number of shared primary atoms is much lower for adsorbates adsorbed on bridge sites than on hollow sites. For the 0.25 ML configuration, the Bader charge on O is -1.59 e, on H is 1.01 e and on the primary Fe atoms is 0.60 e. The charge on the remaining Fe atoms are between -0.12 e and 0.12 e. With the 0.33 ML configuration, the charge on the O was -1.58 e while the charge on the H was 1.00 e. The charges on the two primary Fe atoms are 0.69 e and the remaining Fe atoms having charges between 0.15and -0.15 e. For the 0.5 ML "diagonal" configuration the charge on O is -1.57 e and the charge on H is 1.01 e. For this configuration, each primary Fe atom is shared between two adsorbates and has a charge of 0.65 e. The remaining Fe atoms have charges between 0.12 and -0.12 e. For the 0.5 ML "adjacent" configuration O has a charge of -1.56 e and the charge on H of 1.00 e. Each primary Fe atom has a charge of 0.68 e, with the remaining Fe atoms having a charge between 0.12 and -0.12 e. Finally, for the 1 ML configuration the charge on the O atom is -1.57 e, the charge on the H atom is 1.00 e while the charge on the primary Fe atoms is 0.65 e.

Table 4-22: Adsorption energy, geometry and vibrational frequencies of OH of Fe (100) with coverage

	Author	Site	Tilt Angle	d_{Fe-O} (Å)	d_{O-H} (Å)	E_{Ads} (eV)	v1	v2	v3	v4	v5	v6
							cm^{-1}					
OH (0.25 ML)	Present Work	Bridge Site	63°	2.012	0.97	-4.33	245	274	389	415	566	3688
OH (0.33 ML)	Present Work	Bridge Site	56°	2.016	0.97	-4.31	275	280	421	433	610	3690
OH (0.5 ML) adj.	Present Work	Bridge Site	60°	2.015	0.98	-4.50	236	241	423	425	588	3720
OH (0.5 ML) Diag.	Present Work	Bridge Site	63°	2.015	0.98	-4.36	297	312	415	422	570	3650
OH (1 ML)	Present Work	Bridge Site	65°	2.006	0.98	-4.13	198	212	437	448	592	3730

The deformation energy increases with both increasing nearest neighbour and next nearest neighbour interactions.

The deviations from the 0.25 ML configuration in components of the adsorption energy can be seen in Figure 4-8. Overall, there appears to be no correlations between the change in coverage and the change in the electro-static, kinetic energy and exchange correlation energies.

Looking at the 0.33 ML configuration negligible change in the adsorption energy is observed when compared to the 0.25 ML configuration. The energetic breakdown of the adsorption energy shows an increase in the electrostatic energy of 1.23 eV, while decreases in the kinetic and exchange-correlation energy of 0.59 eV and 0.64 eV were observed.

The 0.5 ML "Adjacent" configuration the adsorption energy is increased by 0.17 eV when compared to the 0.25 ML configuration. The energetic breakdown of the adsorption energy shows increases in electrostatic and kinetic energy of 0.15 eV and 0.10 eV respectively, while a decrease exchange-correlation energy of 0.40 eV were observed.

The 0.5 ML configuration has negligible change in the adsorption energy is observed when compared to the 0.25 ML configuration. The energetic breakdown of the adsorption energy shows an increase in kinetic energy of 0.96 eV, while decreases in electrostatic and exchange-correlation energy of 0.81 eV and 0.17 eV were observed.

Finally, the 1 ML configuration shows the adsorption energy is decreased by 0.20 eV when compared to the 0.25 ML configuration. The energetic breakdown of the adsorption energy shows an increase in kinetic energy of 0.40 eV, while decreases in electrostatic and exchange-correlation energy of 0.18 eV and 0.03 eV were observed.

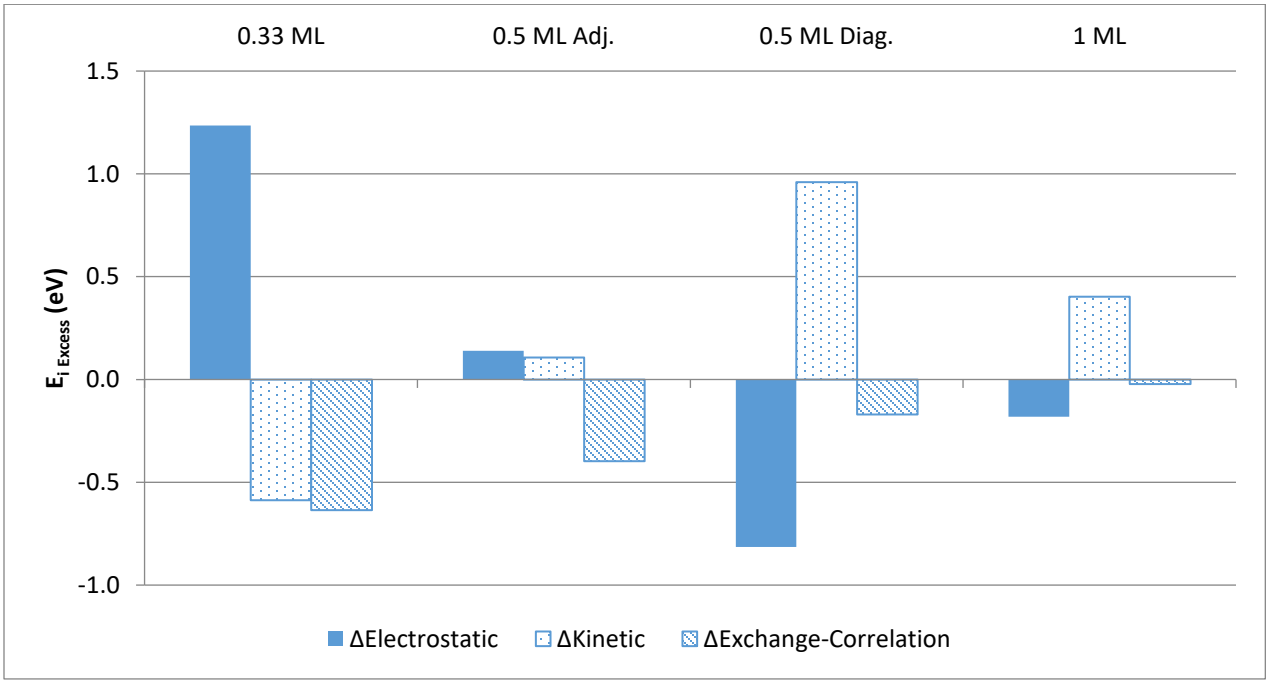

Figure 4-9: Energetic breakdown of lateral interactions of OH on Fe (100) relative to 0.25 ML coverage.

4.10 General intra-species interaction trends

For the species and configurations considered we see that the overall nearest neighbour interactions are typically repulsive, with the exception of OH, and the overall next nearest neighbour interactions small enough to be considered negligible (i.e. within our DFT calculation error). When these interactions are broken down into their electrostatic, kinetic and exchange-correlation components we see that even when the overall lateral interactions are small or negligible, large deviations of the individual components can exist.

While we typically see the adsorption energy/binding energy of the species decrease with increasing coverage, the same systematic decrease in electrostatic, kinetic and exchange correlation energy is not seen. Instead we see large fluctuations in both magnitude and sign for the electrostatic and kinetic interactions, while the exchange-correlation interactions are always negative.

We also see that as the size of the adsorbate increases, the magnitude of the later interaction increases. Of the three largest adsorbates, CH_2, CH_3 and OH, the lateral interactions of the adsorbates on the bridge site, OH and CH_3, have the largest magnitude.

The Bader analysis reveals that a large amount of the charge associated with the metal is located around what was called “Primary” Fe atoms. The definition of the primary Fe atom is dependent of the adsorption site geometry (See Figure 4-1 and Figure 4-7). If these primary Fe atoms are shared amongst adsorbates the magnitude of the charge on these atoms is even higher. As for the adsorbates, themselves we see that the variation in charge on the adsorbate atoms is relatively small when compared the variation in primary Fe atom charge. One would think that magnitude of Bader charge would form a simple relationship with the change in electrostatic energy but this is not the case. This because the electrostatic energy encompasses the Ewald sum of ionic - ionic interactions and periodic integrals of electron density - electron density interactions and ionic - electron density interactions.

The Bader charge on the C atom is lowered as we move from atomic C to CH_3. The atomic C having charges in the region of -1.5 e, dropping to -1.3 e from CH and CH_2 and dropping further to -0.75 e for CH_3. The O atoms experience the opposite as atomic O as a charge of about -1.3 e while the O in OH has a charge of -1.55 e.

Figure 4-10 shows the relationship between the coverage of a single species and the Fermi level. The intercept with y axis on the graph would be the Fermi energy of the Fe clean surface, -6.2714 eV. The linear relationship agrees well for the species concern except for atomic C and OH. Second order polynomial provide a better fit for C and OH and it should be noted that the C trend has a minimum while the OH trend has a maximum. The average deviations in Fermi level from largest to smallest are as follows:

$$CH_2 > CH_3 > CH > OH > O > C > H$$

At 0.25 ML the sequence is as follows:

$$CH_3 > CH_2 > CH = OH > O > C = H$$

The DOS of the different configurations show that the centre of the d-band is un-shifted relative to the Fermi level, as seen by van Helden and van Steen[23]. We also see that for all the species considered we see that the Fermi level decreases with increasing coverage. This lowering in the Fermi level relates lowering in the absolute energy of the d-band. The Fermi level of the 1 ML configurations is significantly lower than when compared to the relevant 0.25 ML configuration. This will alter the attractive and

repulsive interactions between the d-band and frontier orbitals of the adsorbate. The magnitude of the change these interactions is encapsulated in the exchange-correlation energy. We also see that the Fermi level is lower for heavier adsorbates.

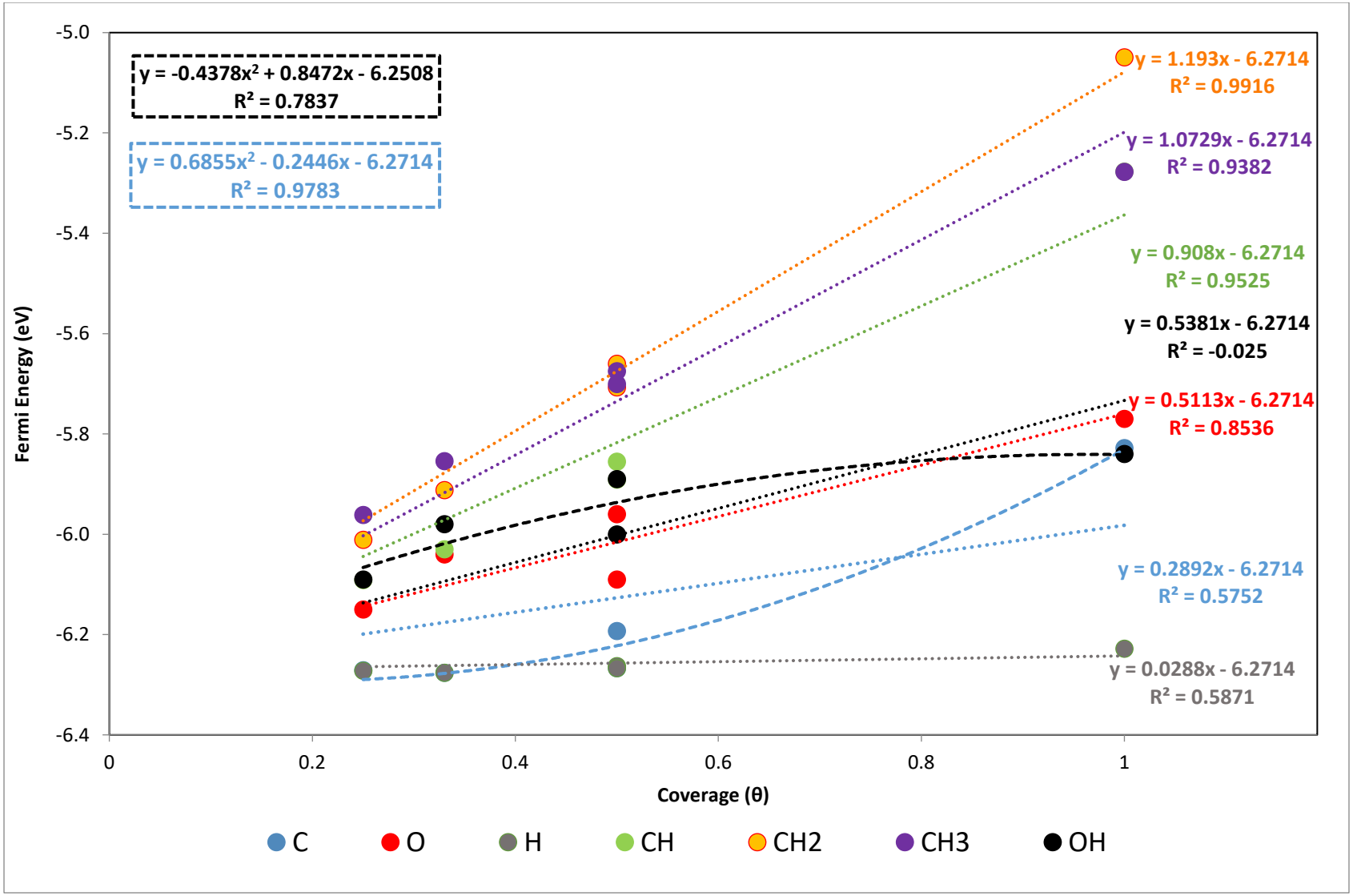

Figure 4-10: A linear relationship that exists between coverage and Fermi energy

4.11 References

[1] Fischer, F., Tropsch, H., *Brennstoff-Chemie* **1926**, 7, 97–104.

[2] Craxford, S.R., Rideal, E.K., *J. Chem. Soc.* **1939**, 1604–1614.

[3] Claeys, M., Van Steen, E., *Stud. Surf. Sci. Catal.* **2004**, 152, 601–680.

[4] Elahifard, M., Fazeli, E., Joshani, A., Gholami, M., *Surf. Interface Anal.* **2013**.

[5] Van Helden, P., Initial Steps of the Fischer-Tropsch Synthesis on Fe(100): The Role of Hydrogen. University of Cape Town, **2010**.

[6] Lo, J.M.H., Ziegler, T., *J. Phys. Chem. C* **2007**, 111, 11012–11025.

[7] Sorescu, D., *Phys. Rev. B* **2006**, 73, 155420.

[8] Sorescu, D., Thompson, D., Hurley, M., Chabalowski, C., *Phys. Rev. B* **2002**, 66, 35416.

[9] Bromfield, T.C., Ferré, D.C., Niemantsverdriet, J.W., *Chemphyschem* **2005**, 6, 254–60.

[10] Govender, A., Ferré, D.C., Niemantsverdriet, J.W.H., **2009**.

[11] Jiang, D., Carter, E., *Phys. Rev. B* **2005**, 71, 45402.

[12] Mavrikakis, M., Gokhale, A.A., *Am. Chem. Soc.* **2005**, 229, 861–865.

[13] Erley, W., McBreen, P.H., Ibach, H., *J. Catal.* **1983**, 84, 229–234.

[14] McBreen, P.H., Erley, W., Ibach, H., *Surf. Sci.* **1984**, 148, 292–310.

[15] Zhao, S., Liu, X.-W., Huo, C.-F., Li, Y.-W., Wang, J., Jiao, H., *J. Catal.* **2012**, 294, 47–53.

[16] Cao, D.-B., Li, Y.-W., Wang, J., Jiao, H., *J. Mol. Catal. A Chem.* **2011**, 346, 55–69.

[17] Gracia, J.M., Prinsloo, F.F., Niemantsverdriet, J.W., *Catal. Letters* **2009**, 133, 257–261.

[18] Govender, A., Ferré, D.C., Niemantsverdriet, J.W., *Chemphyschem* **2012**, 13, 1583–90.

[19] Eder, M., Terakura, K., Hafner, J., *Phys. Rev. B* **2001**, 64, 115426.

[20] Moon, D.W., Dwyer, D.J., Bernasek, S.L., *Surf. Sci.* **1985**, 163, 215–229.

[21] Zeinalipour-Yazdi, C.D., van Santen, R. A., *J. Phys. Chem. C* **2012**, 116, 8721–8730.

[22] Sorescu, D.C., *Catal. Today* **2005**, 105, 44–65.

[23] van Steen, E., van Helden, P., *J. Phys. Chem. C* **2010**, 114, 5932–5940.

[24] Blum, V., Schmidt, A., Meier, W., Hammer, L., Heinz, K., *J. Phys. Condens. Matter* **2003**, 15, 3517–3529.

[25] Grabke, H.J., Tauber, G., Viefhaus, H., *Scr. Metall.* **1975**, 9, 1181–1184.

[26] Clark, S.J., Segall, M.D., Pickard, C.J., Hasnip, P.J., Probert, M.I.J., Refson, K., Payne, M.C., *Zeitschrift für Krist.* **2005**, 220, 567–570.

[27] Accelrys Software Inc., Material Studio Modeling Environment, San Diego: Accelrys Software Inc., **2010**.

[28] Hammer, B., Hansen, L., Nørskov, J., *Phys. Rev. B* **1999**, 59, 7413–7421.

[29] Monkhorst, H.J., Pack, J.D., *Phys. Rev. B* **1976**, 13, 5188–5192.

[30] Li, H., Jensen, J.H., *Theor. Chem. Accounts Theory, Comput. Model. (Theoretica Chim. Acta)* **2002**, 107, 211–219.

[31] Govender, A., Towards a Mechanism for the Fischer-Tropsch Synthesis on Fe(100) Using Density Functional Theory. Eindhoven University of Technology, **2010**.

[32] van Helden, P., van Steen, E., *J. Phys. Chem. C* **2008**, 112, 16505–16513.

[33] Kittel, C., *Introduction to Solid State*, Wiley, New York **1996**.

[34] Van Santen, R.A., De Koster, A., Koerts, T., *Catal. Letters* **1990**, 7, 1–14.

[35] Sung, S.S., Hoffmann, R., *J. Am. Chem. Soc.* **1985**, 107, 578–584.

[36] Hammer, B., Nørskov, J.K., *Adv. Catal.* **2000**, 45, 71–129.

[37] Henkelman, G., Arnaldsson, A., Jónsson, H., *Comput. Mater. Sci.* **2006**, 36, 354–360.

[38] Swart, J.C.W., Ciobîcă, I.M., van Santen, R.A., van Steen, E., *J. Phys. Chem. C* **2008**, 112, 12899–12904.

[39] Eliason, S.A., Bartholomew, C.H., *Stud. Surf. Sci. Catal.* **1997**, 111, 517–526.

[40] Yang, K., Zheng, J., Zhao, Y., Truhlar, D.G., *J. Chem. Phys.* **2010**, 132, 164117.

[41] Bozso, F., Ertl, G., Grunze, M., Weiss, M., *Appl. Surf. Sci.* **1977**, 1, 103–119.

[42] Burke, M.L., Madix, R.J., *Surf. Sci.* **1990**, 237, 20–34.

[43] Merrill, P.B., Madix, R.J., *Surf. Sci.* **1996**, 347, 249–264.

[44] Blyholder, G., Head, J., Ruette, F., *Surf. Sci.* **1983**, 131, 403–418.

[45] Walch, S.P., *Surf. Sci.* **1984**, 143, 188–203.

[46] Raeker, T.J., DePristo, A.E., *Surf. Sci.* **1990**, 235, 84–106.

[47] Govender, A., Ferré, D.C., Niemantsverdriet, J.W.H., *Chemphyschem* **2012**, 13, 1591–6.

[48] Hung, W.-H., Bernasek, S.L., *Surf. Sci.* **1995**, 339, 272–290.

[49] Nørskov, J.K., *Prog. Surf. Sci.* **1991**, 38, 103–144.

5 Interactions between species of interest in the methanation of syngas on Fe (100)

The investigation of interactions between CH_X (x = 0-4) species as well as C, O, OH and CO on Fe surfaces can yield great insight into the initial steps of Fischer-Tropsch synthesis. The steps proposed by the alkyl mechanism, as represented in Figure 5-1 a) , alkenyl mechanism, as represented in Figure 5-1 b), and related mechanisms [1–3] are of particular interest. Furthermore, the interactions of methanation species, can also help understand mechanisms proposed for the higher alcohol synthesis [4] , as represented in Figure 5-1 c).

a) Alkyl mechanism

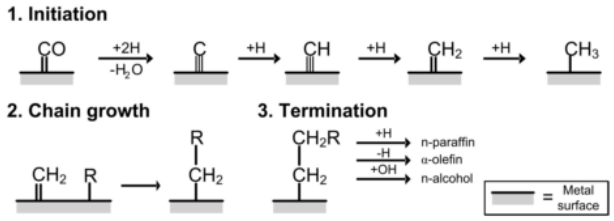

b) Alkenyl mechanism

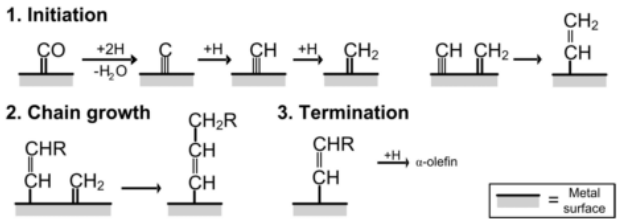

c) Higher alcohol synthesis

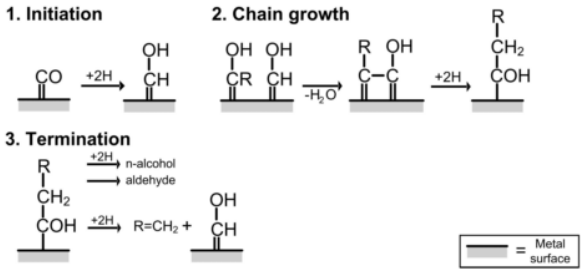

Figure 5-1: Representation on **a)** Alkyl, **b)** Alkenyl and **c)** Higher alcohol synthesis (adapted from Claeys & Van Steen [3] and Van Helden [5])

The hydrogenation of carbon monoxide can yield a whole zoo of species. When considering only the species involved in methanation, there are at least 10 different species on the surface (CO, H, CH_x (x=0-4), O, OH, H_2O) all reacting and interacting with each other. Methanol and ethanol synthesis is beyond the scope of this project, but the interactions between the species listed above are also relevant for the formation of

these alcohols from synthesis gas. Much is known about the reactions between these species[6–12], while little is known about the interactions between the species.

Ciobica et al. [11] showed significant changes in the energy diagram for methanation over Ru(0001) between 0.11 ML and 0.25 ML. They showed that repulsions between species exist for configurations where species were close together. When comparing adsorption energies at 0.11 ML and 0.25 ML, the adsorption energies increased significantly for C and CH and moderately for CH_2 and CH_3 at the lower coverage. Furthermore, the exothermicity for elementary reactions $CH_{x+1} \rightarrow CH_x + H$ (x=1-3) increases with decreasing coverage.

Van Helden et al. [5,13] concluded that the adsorption of hydrogen on Fe(100) is hardly affected by H-H, H-CO and H-C lateral interactions below 1 ML, since the adsorption energy of hydrogen hardly changes; The energy associated with adsorption of H in the hollow site does decreases with increasing coverage above 1 ML[t]. This is also seen on other Fe surfaces [5,14–18] and other transition metal surfaces [11,12].

In the previous chapters, we saw that strong repulsions can exists between neighbouring adsorbates of the same species on the surface. The analysis showed that adsorbates in the "Nearest-Neighbour" position (see Figure 5-2) are typically repulsive, while adsorbates in the "Next Nearest-Neighbour" position may be even slightly attractive in nature.

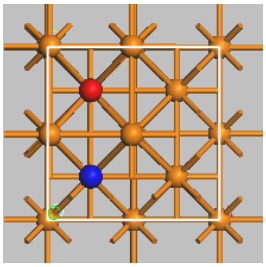

a) Nearest-Neighbour

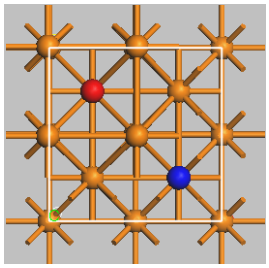

b) Next-Nearest-Neighbour

Figure 5-2: Demonstration of a) Nearest-Neighbour and b) Next-Nearest-Neighbour configurations

For the single species adsorption of CO and its dissociation to C and O on Fe (100) the adsorption energy decrease with increasing coverage from 0.25 to 1 ML [5,6,9,19,20]. Previous studies also give some sort of indication of the intraspecies interactions for CO, C and O, which are repulsive in this case.

Van Steen and van Helden conducted a DFT study on the adsorption of H on C and CO precovered Fe(100) [21] and coadsorption of H and CO on Fe(100) [13]. They concluded that repulsions between C and H and CO and H exist on Fe (100), when the species are in close proximity. They also showed that the barrier for the dissociative adsorption of hydrogen increases when coverage of C and CO increases on the surface.

Sorescu [9] investigated the effects of co-adsorption of C with H, O, CH_x (x = 1-4) and CO. Only next-nearest-neighbour interactions for a c(2x2) configuration were considered. For all the species considered, except for CH_3, a stabilization (attraction) was observed. This was attributed to an expansion of the local surface environment, stemming from another study of his [19] which showed that the binding energy of CO increases with lattice expansion.

[t] H is adsorbed in both the bridge and the hollow sites above 1 ML. The heat of adsorption was measured for the hollow site.

While lateral interactions are more popularly studied theoretically, they are observed experimentally as well. Burke and Madix [22] observed through TPD experiments that the binding energy of H on Fe is lowered in the presence of coadsorbed CO, implying repulsive interaction between adsorbed H and adsorbed CO. The same conclusions were drawn by Madix and Merril [23] using EELS on the same system.

The lateral interactions can be observed over large distances [24,25], but as a first approximation one can consider nearest-neighbour and next-nearest-neighbour interactions as demonstrated in Figure 5-2. Interactions beyond this can be considered negligible as the literature suggests that the lateral interactions decrease exponentially with an increase in distance [25][u].

The binding energies of CH_x (1-4) has only been studied at 0.25 ML on p(2x2) unit cells making it difficult to give any insight into the lateral interactions. Here we investigate lateral interactions between species involved in the methanation over Fe (100) on a larger unit cell to get insight in the nearest neighbour interactions and the next nearest neighbour interaction. The lateral interactions for the surface species CH_4 and H_2O have not been included in this study since in the context of a microkinetic model it is assumed that these species will desorb almost instantaneously. Furthermore literature shows weak adsorption of CH_4 on Fe(100) [9,26], less than 0.1 eV, which can be significantly influenced by the error expected in this model. The heat of adsorption of water of Fe (100) was found to be 0.53 eV by Govender [7] and 0.35 eV by Eder and Terakura [27].

In this chapter the interactions of CO, H, CH_x (x=0-3), O and OH with each other will be investigated at coverages of 0.5 ML and below. For each A-B interaction three configurations will be considered to probe the nearest and next nearest neighbour interactions.

5.1 DFT Calculations

The CASTEP [28] code along with the RPBE functional [30] was used for the DFT calculations and a Gaussian smearing width of σ = 0.1 eV was utilized. The ion-electron interactions were approximated using ultrasoft pseudopotentials with core corrections, calculations allowed for spin-polarized orbitals and a cut-off energy of 400 eV was set.

A five-layer slab with three layers relaxed was used with an optimized vacuum spacing of 12 Å between surfaces. K-point sampling was generated using the Monkhorst-Pack[31] procedure with a k-point spacing of <0.03 $Å^{-1}$.

In order to determine if the converged energy was a minimum and not a saddle point, a vibrational analysis was completed. A partial Hessian analysis [32] was conducted for the adsorbates in question. This is a valid approximation as the Fe atoms are significantly heavier than those of C, H and O. The atoms were perturbed by 0.005 Å in Cartesian space. All reported configurations represent minima on the potential energy surface (PES) as indicated by the positive, real vibrational frequencies obtained (see **Appendix B**).

[u] The components of the lateral interactions, like electrostatic interactions, decrease sharply with increasing distance

5.1.1 Co-Adsorption of Methanation intermediates

For the interspecies interactions, co-adsorption studies were conducted. Only the sites that were regarded as the most stable for the same species interactions were considered. As mentioned in the introduction, only a few of the co-adsorption configurations have been investigated in literature and where possible, comparisons will be made.

Like the single species interactions, only nearest neighbour and next nearest neighbour interactions were considered. In order to investigate these "A-B" interactions, three configurations are considered; two configurations a 0.5 ML p(2x2) cell (again called the "Diagonal" and "Adjacent" configurations) and a 0.33 ML on a p(3x2) cell configuration. Each configuration has equal amounts of species A and B. For 0.33 ML configuration, each adsorbate only has one nearest neighbour while for the 0.5 ML "Adjacent" configuration, each adsorbate has two nearest neighbours. Although most species present during methanation are stable in the hollow site on Fe (100), some species such as OH and CH_3 are stable on the bridge site. For these species, the configurations in Figure 5-3 d)-f) are used to investigate interactions with the other methanation species.

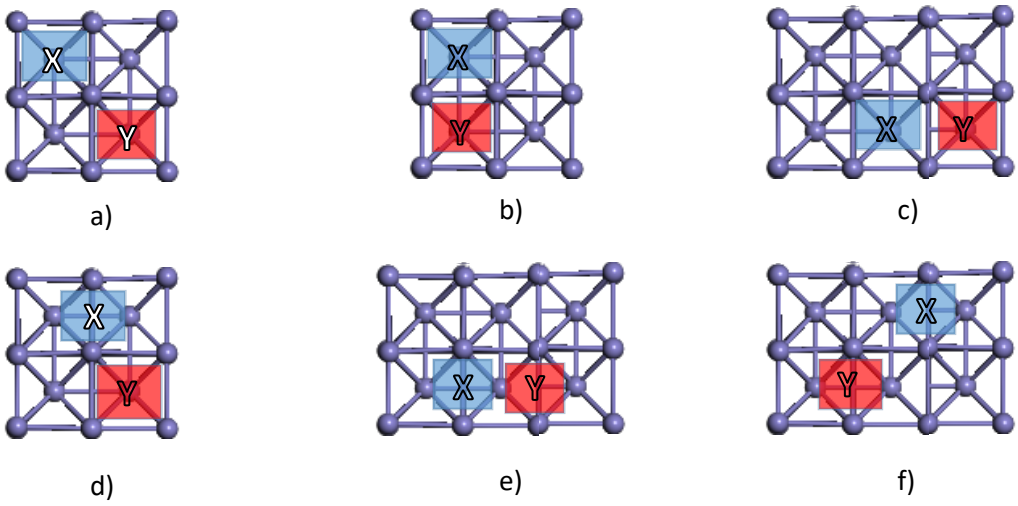

Figure 5-3: Configurations for two species in the hollow site at a) 0.5 ML next nearest neighbours (Diagonal), b) 0.5ML nearest neighbours (Adjacent) and c) 0.33 ML nearest neighbours. The figure d) shows one bridge (X) and one hollow species (Y) as 0.5 ML nearest neighbours e) two bridge species as 0.33 ML nearest neighbours and f) two bridge species as 0.33 ML next nearest neighbours.

The lateral interactions are quantified here by calculating the excess energy of the configuration, defined as

$$E_{Excess} = E_{AB} - E_{A,0.25ML} - E_{B,0.25ML} + E_{xFe} \qquad (5.1)$$

Where E_{AB} is the total coadsorption system energy, $E_{A,\ 0.25\ ML}$ and $E_{B,\ 0.25\ ML}$ are the total energies of the individual species at 0.25 ML[v] and E_{xFe} is the total energy of a clean Fe surface. The number of Fe atoms used in the E_{xFe} surface is determined by balancing the total number of Fe atoms of the co-adsorbed

[v] While chapter 3 investigated lateral interactions as deviations from a 0.0625 ML configuration, the 0.25 ML configuration with no nearest and next nearest neighbour interactions had deviation is total energy of <0.01 eV. Furthermore, nearest, and next nearest neighbour interactions are of importance at higher coverages and the deviation from a 0.25 ML p(2x2) unit cells are enough to show this.

configuration with the 0.25 ML configurations (i.e. if the co-adsorption configuration was calculated on a 2x2 unit cells and the two 0.25 ML individual configurations are always 2x2 unit cells, a clean Fe 2x2 unit cell will be used to balance the system).

The interaction between the adsorbates and the iron surface causes a shift in the iron atoms. The deformation of the iron surface was then calculated as follows:

$$E_{deform} = E_{[(Fe+nX)-nX]} - E_{(Fe\ Slab)} \qquad (5.2)$$

Where $E_{[(Fe+nX)-nX]}$ is the single point energy of the geometry optimized iron/adsorbate surface with adsorbates removed and $E_{(Fe\ Slab)}$ is the energy of a clean geometry optimized iron surface.

The interaction energy is again broken down into electrostatic, kinetic and exchange-correlation energy. In this case, the components are broken down into ***Excess*** electrostatic, kinetic and exchange correlations energies much like equation 5.1 (See **Appendix C**)

As discussed in section 4.2.2 (*The Fermi Energy*), the centre of the d-band is in the same position relative to the Fermi level. As a result, the energy difference between the frontier orbitals (HOMO and LUMO) of the adsorbate changes. If these frontier orbitals are fully occupied, the Pauli repulsion would then increase. Changes Fermi energy gives an idea of changes in Pauli repulsion.

Using the vibrational frequencies, the enthalpic and entropic (and hence Gibbs Free energy) vibrational contributions can be estimated at a given temperature. A similar formulation to equation 5.1 is applied:

$$G_{Excess} = G_{AB,T} - G_{A,0.25ML,T} - G_{B,0.25ML,T} \qquad (5.3)$$

Where G_{AB} is the Gibbs free vibrational energy of coadasorption system, $G_{A,\ 0.25\ ML}$ and $G_{B,\ 0.25\ ML}$ are the Gibbs Free Vibrational energies of the individual species at 0.25 ML. Since the partial Hessian approximation was made, only the frequencies of the adsorbates are captured and Fe correction term, as in Equation 5.1, is not needed.

5.2 Lateral Interactions between CO – Methanation species

The literature for the single species adsorption of CO and its dissociation to C and O on Fe(100) [5,6,9,19,20] shows the adsorption energy of CO decrease in the presence of CO, C and O with increasing coverage from 0.25 to 1 ML. This means that repulsive lateral interactions must exist between CO, C and O.

Van Steen and van Helden conducted a DFT study on the adsorption of H on C and CO pre-covered Fe(100) [21] and co-adsorption of H and CO on Fe(100)[13]. They concluded that repulsions between C and H and CO and H exist on Fe (100), when the species are in close proximity. They also showed that the barrier for the dissociative adsorption of hydrogen increases with coverage of C and CO increases on the surface.

The results in Table 5-1 summaries the bond lengths, Fermi energies, deformation energy, excess energies and Bader charges for CO – methanation species interactions. Repulsive interactions result in a longer Fe-C distance for adsorbed CO and a shorter C-O bond length, and vice versa for the attractive interactions. This is often interpreted as, the Fe-C interaction has decreased and the C-O bond is stronger for repulsive interactions.

Table 5-1 also shows that the nearest neighbour interactions are all repulsive and the interactions increases with increasing coverage and number of nearest neighbours. The next nearest neighbour interactions are all attractive but much lower in magnitude than the repulsive nearest neighbour interaction. It is interesting to note that in chapter 4 for the intra-species interactions, the interaction at 0.33 ML coverage is typically non-existing or even attractive, but at 0.5ML in the adjacent configuration you have signification lateral interaction. For the inter-species interaction, significant repulsions are observed for both 0.33 ML and 0.5 ML Adjacent configurations with the magnitude of the repulsion for the 0.5 ML being double or more than the 0.33 ML. A major contributor of this is the deformation energy which shows larger deviations at 0.33 ML than at 0.5 ML. This indicates that the same species configurations deform the surface less than mixed species configurations.

The 0.5 ML configurations have two nearest-neighbours while the 0.33 ML configuration has one nearest neighbour. For all the species, except H and CH, the repulsion of the 0.5 ML adjacent configuration is more than double the repulsion of the 0.33 ML configuration. The repulsions for CO-H are negligible (<0.5 ML) and hence at higher coverages CO-H nearest neighbours will be favoured over other species. CO dissociation is then still possible via hydrogen assisted dissociation.

The repulsive interactions also result in an increase charge on the C and O atoms, while the charge on the primary Fe atoms appears to be a function of how many adsorbates it is shared between, as shown in the previous chapters.

The Fermi energy increases with increasing coverage and configurations with larger adsorbates like CH_2 and CH_3 have further increased Fermi energies. A decrease in Fermi level relates to a subsequent lowering in the absolute energy of the d-band, altering the interactions with the frontier orbitals upon further adsorption.

The temperature corrections for CO-X nearest-neighbour interactions and CO-X next-nearest neighbour interactions can be seen in Figure 5-4. The nearest neighbour interactions all show increases in repulsion with increasing temperature, with the exception of CO-O and CO-H, which displays a subtle decrease.

For the next-nearest neighbour interactions the CO-C, CO-O, CO-CH and CO-H show increases in attraction with increasing temperature while the attraction decreases for CO-CO and CO-CH_2.

Recalling equation 5.3, the change in temperature accounts for the difference in the co-adsorption system Gibbs free energy (G_{AB}) and the systems with no lateral interactions ($G_{X\ 0.25ML}$) Gibbs free energy. For all systems, the Gibbs free energy decreases with increasing temperature since the entropic contributions dominate at higher temperatures. If the interaction energy increases with temperature, the Gibbs free energy of coadsorption system decreases slower than the no lateral interaction systems. This is indeed the case of CO-CH_3 nearest neighbours and is demonstrated in Figure 5-1. Alternatively, if the interaction energy decreases with temperature, the Gibbs free energy of coadsorption system decreases faster than the no lateral interaction systems, as is the case for CO-H nearest neighbours. The interaction energy at 0 K must be added to the G_{excess} term to get the overall Gibbs free energy of interaction at a specific temperature. The nature of the decrease in Gibbs energy with temperature is a result of the vibrational frequencies, which is given in Table 5-2.

Table 5-1: Co-adsorption of CO with other species present during methanation on Fe (100)

Species		$d_{Fe-C(O)}$ (Å)	d_{C-O} (Å)	E_{Fermi} (eV)	E_{Deform} (eV)	E_{Excess} (eV)	Bader charge		
							C(O)	O	Primary Fe
CO-C	0.33 ML Adj.	2.109	1.317	-6.181	0.45	0.15	0.26	-1.83	0.64 shared 0.42 unshared
	0.5 ML Adj.	2.151	1.287	-6.129	0.17	0.35	0.65	-1.95	0.6
	0.5 ML Diag.	2.015	1.317	-6.128	0.22	-0.14	0.41	-1.88	0.65
CO-O	0.33 ML Adj.	2.127	1.299	-6.127	0.09	0.15	0.44	-1.86	0.55 shared 0.38 unshared
	0.5 ML Adj.	2.134	1.286	-6.050	0.06	0.45	0.72	-2.03	0.62
	0.5 ML Diag.	2.031	1.319	-6.017	0.11	-0.07	0.40	-1.93	0.66
CO-H	0.33 ML Adj.	2.138	1.306	-6.120	0.06	0.02	0.45	-1.92	0.47 shared 0.22 unshared
	0.5 ML Adj.	2.127	1.301	-6.112	0.06	0.01	0.57	-2.01	0.30
	0.5 ML Diag.	2.108	1.309	-6.100	0.07	-0.08	0.41	-1.92	0.31
CO-CH	0.33 ML Adj.	2.125	1.300	-6.077	0.45	0.24	0.49	-1.89	0.55 shared 0.36 unshared
	0.5 ML Adj.	2.129	1.289	-5.964	0.06	0.47	0.68	-2.01	0.55
	0.5 ML Diag.	2.030	1.312	-5.971	0.08	-0.04	0.43	-1.92	0.58
$CO-CH_2$	0.33 ML Adj.	2.157	1.299	-6.011	0.45	0.14	0.50	-1.89	0.50 shared 0.35 unshared
	0.5 ML Adj.	2.197	1.291	-5.859	0.04	0.42	0.64	-1.95	0.52
	0.5 ML Diag.	2.060	1.311	-5.884	0.05	-0.14	0.47	-1.95	0.58
$CO-CH_3$	0.33 ML Adj.	2.110	1.317	-5.990	0.45	0.14	0.50	-1.94	0.52 shared 0.38 unshared
	0.5 ML Adj.	2.087	1.318	-5.95	0.25	0.29	0.45	-1.91	0.45
CO-OH	0.33 ML Adj.	2.110	1.311	-5.99	0.37	0.14	0.50	-1.95	0.62 shared 0.32 unshared
	0.5 ML Adj.	2.087	1.322	-5.95	0.22	0.29	0.55	-1.99	0.45

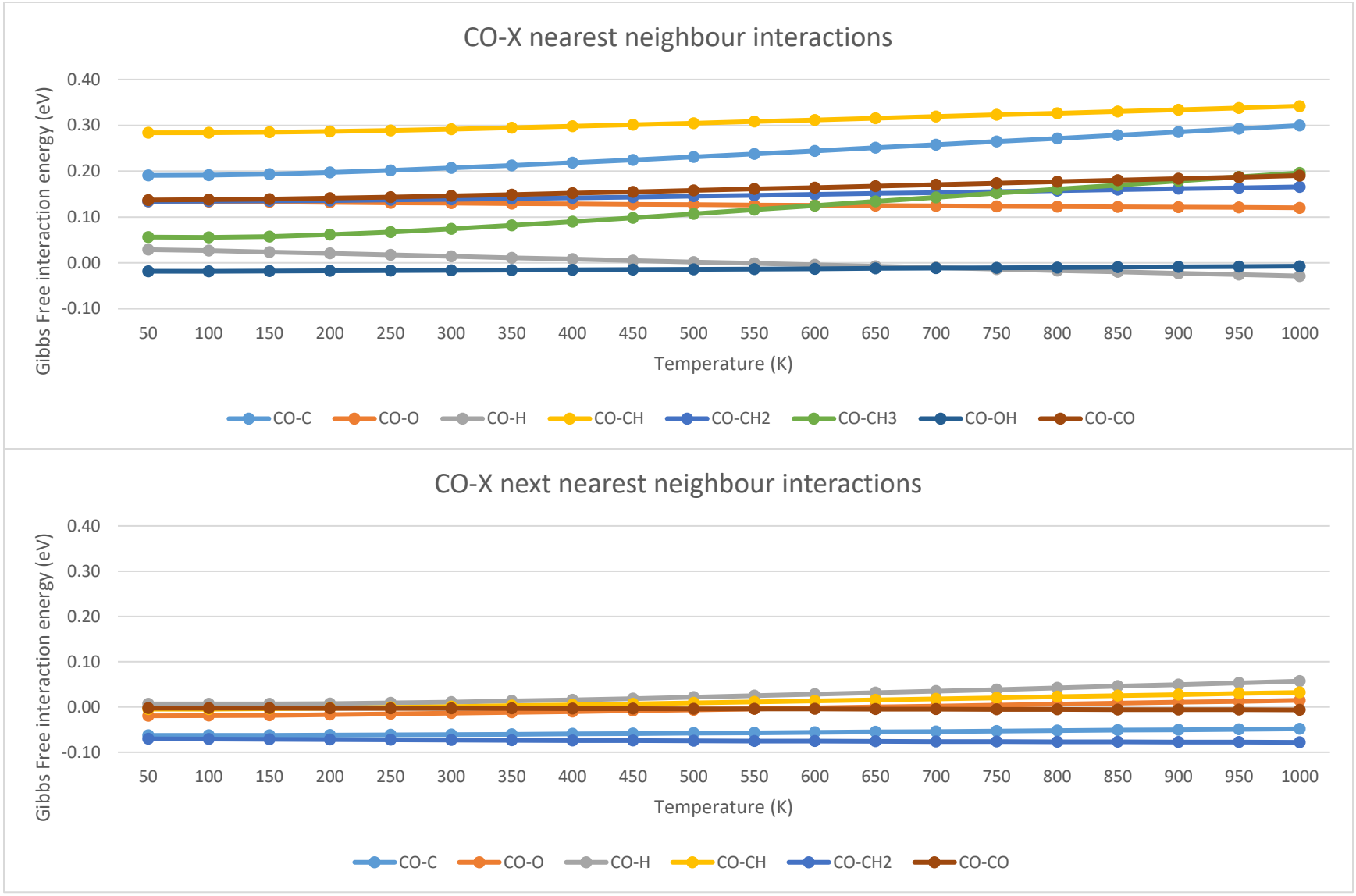

Figure 5-4: Temperature corrected Gibbs free interaction energies for CO-X nearest and next-nearest neighbour interactions

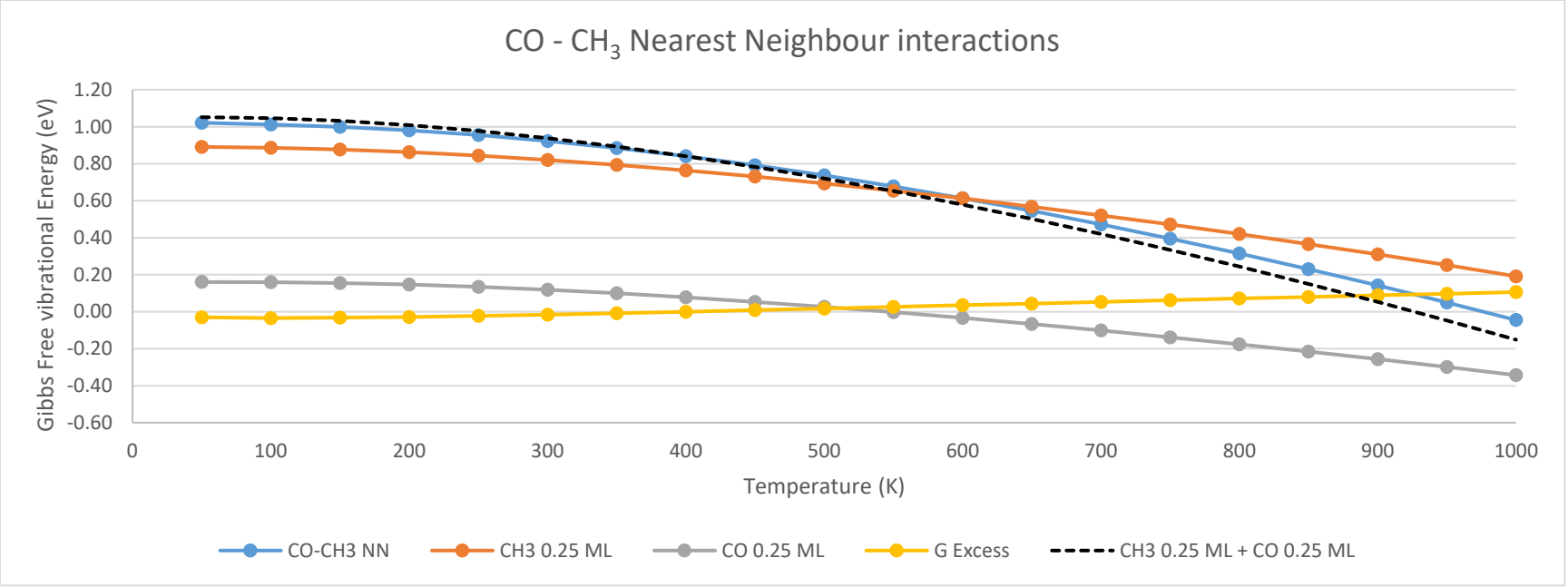

Figure 5-5: Gibbs free vibrational energies for CO-CH_3 nearest neighbours, CH_3 at 0.25 ML and CO at 0.25 ML configurations

Table 5-2: Co-adsorption of CO-CH_3 in the nearest neighbour position on Fe (100)

Species	v1	v2	v3	v4	v5	v6	v7	v8	v9	v10	v11	v12	v13	v14	v15	v16	v17	v18
CO-CH3 NN	46	177	239	258	326	371	425	484	585	602	738	1169	1225	1282	1389	1850	2158	3114
CH3 0.25 ML	102	110	192	336	525	531	1161	1324	1371	2758	2962	3007						
CO 0.25 ML	182	226	314	333	357	1177												

5.3 Lateral Interactions between C – Methanation species

The C-X interspecies interactions studied by Sorescu[9] can be compared with the 0.5 ML "Diagonal" configuration in this study. Sorescu [9] investigated the effects of co-adsorption of C with H, O, CH_x (x = 1-4) and CO for next-nearest-neighbour interactions on a c(2x2). For all the species considered, except for CH_3, a stabilization was observed.

The results in Table 5-3 summaries the bond lengths, Fermi energy, deformation energy, excess energy and Bader charge for C – methanation species interactions. The Fe-C distance is longer for repulsive interactions and shorter for attractive interactions. This can be interpreted as the attractive interaction result in stronger binding between C and the metal surface and vice versa.

Table 5-3 also shows that the next-nearest neighbour interactions are all attractive, except C-CH_3 and C-OH, which is in agreement with the work done by Sorescu [9]. There are some subtle differences in the magnitude of the attractive next-nearest neighbour interaction between adsorbed atomic C on Fe(100) and other species as calculated in this study compared to the results reported by Sorescu [9], which may be attributed to the difference in the used exchange-correlation functional (PW91 vs. RPBE in this study).

Interestingly, for the C-H interactions all configurations show attractive interactions with the "Diagonal" configuration showing the largest and most attractive lateral interactions. For the other species, the next-nearest-neighbour interactions yield attractive lateral interactions whilst nearest-neighbour interactions yield repulsive lateral interactions, much like the CO-X interactions. Another similarity with the CO-X interactions is that of the adjacent interactions, O, CH and CH_2 all have repulsive lateral interactions larger than 0.4 eV for the 0.5 ML Adj. The deformation energies of the 0.33 ML configurations are also larger than the 0.5 ML configurations.

The diagonal configurations also yield slightly larger charges on the C atomic for all interactions except the C-CO interaction. This configuration has the smallest charge on the C atom, -1.41 e. The larger charges on the atomic C may be a contributing factor to attractive interaction energies. This is also a key difference between the CO-X interactions, which showed larger charges on the C and O atoms for the repulsive interactions

The Fermi energy increases with increasing coverage and configurations with larger adsorbates like CH_2 and CH_3 have further increased Fermi energies. A decrease in Fermi level relates to a subsequent lowering in the absolute energy of the d-band, altering the interactions with the frontier orbitals upon further adsorption.

The corrections for C-X nearest-neighbour interactions and C-X next-nearest neighbour interactions can be seen in Figure 5-6. The nearest neighbour interactions all show increases in repulsion with increasing temperature, with the exception of C-OH, which displays a subtle decrease. For the next-nearest neighbour interactions the C-C, C-CH, C-CH_2 and C-H show increases in attraction with increasing temperature while the attraction decreases for C-CO and C-O.

Table 5-3: Co-adsorption of atomic C with other species present during methanation on Fe (100)

Species		d_{Fe-C} (Å)	E_{Fermi} (eV)	E_{Deform} (eV)	E_{Excess} (eV)	Sorescu [9] E_{Excess} (eV)	Bader Charge	
							C	Primary Fe
C-CO	0.33 ML Adj.	1.931	-6.181	0.45	0.15	-	-1.52	0.64 Shared 0.42 Unshared
	0.5 ML Adj.	1.962	-6.129	0.17	0.35	-	-1.57	0.6
	0.5 ML Diag.	1.937	-6.128	0.22	-0.14	-0.24	-1.41	0.65
C-H	0.33 ML Adj.	1.931	-6.257	0.45	-0.04	-	-1.55	0.48 Shared 0.35 Unshared
	0.5 ML Adj.	1.960	-6.228	0.17	-0.05	-	-1.54	0.49
	0.5 ML Diag.	1.966	-6.197	0.22	-0.13	-0.13	-1.63	0.48
C-O	0.33 ML Adj.	1.931	-6.198	0.45	0.19	-	-1.55	0.62 Shared 0.39 Unshared
	0.5 ML Adj.	1.917	-6.110	0.12	0.64	-	-1.43	0.61
	0.5 ML Diag.	1.931	-6.105	0.12	-0.19	-0.17	-1.64	0.66
C-CH	0.33 ML Adj.	1.931	-6.148	0.45	0.22	-	-1.52	0.58 Shared 0.34 Unshared
	0.5 ML Adj.	2.184	-6.025	0.11	0.43	-	-1.49	0.53
	0.5 ML Diag.	1.926	-6.072	0.11	-0.04	-0.20	-1.59	0.59
C –CH_2	0.33 ML Adj.	1.970	-6.076	0.18	0.11	-	-1.53	0.55 Shared 0.35 Unshared
	0.5 ML Adj.	1.954	-5.931	0.14	0.47	-	-1.49	0.55
	0.5 ML Diag.	1.932	-5.965	0.14	-0.18	-0.24	-1.59	0.57
C –CH_3	0.33 ML Adj.	1.977	-6.071	0.19	0.05	-	-1.56	0.60 Shared 0.33 Unshared
	0.5 ML Adj.	1.977	-5.928	0.19	0.05	0.05	-1.55	0.58 Shared 0.35 Unshared
C –OH	0.33 ML Adj.	1.967	-6.086	0.22	0.09	-	-1.52	0.60 Shared 0.34 Unshared
	0.5 ML Adj.	1.937	-6.153	0.23	0.17	-	-1.53	0.55 Shared 0.34 Unshared

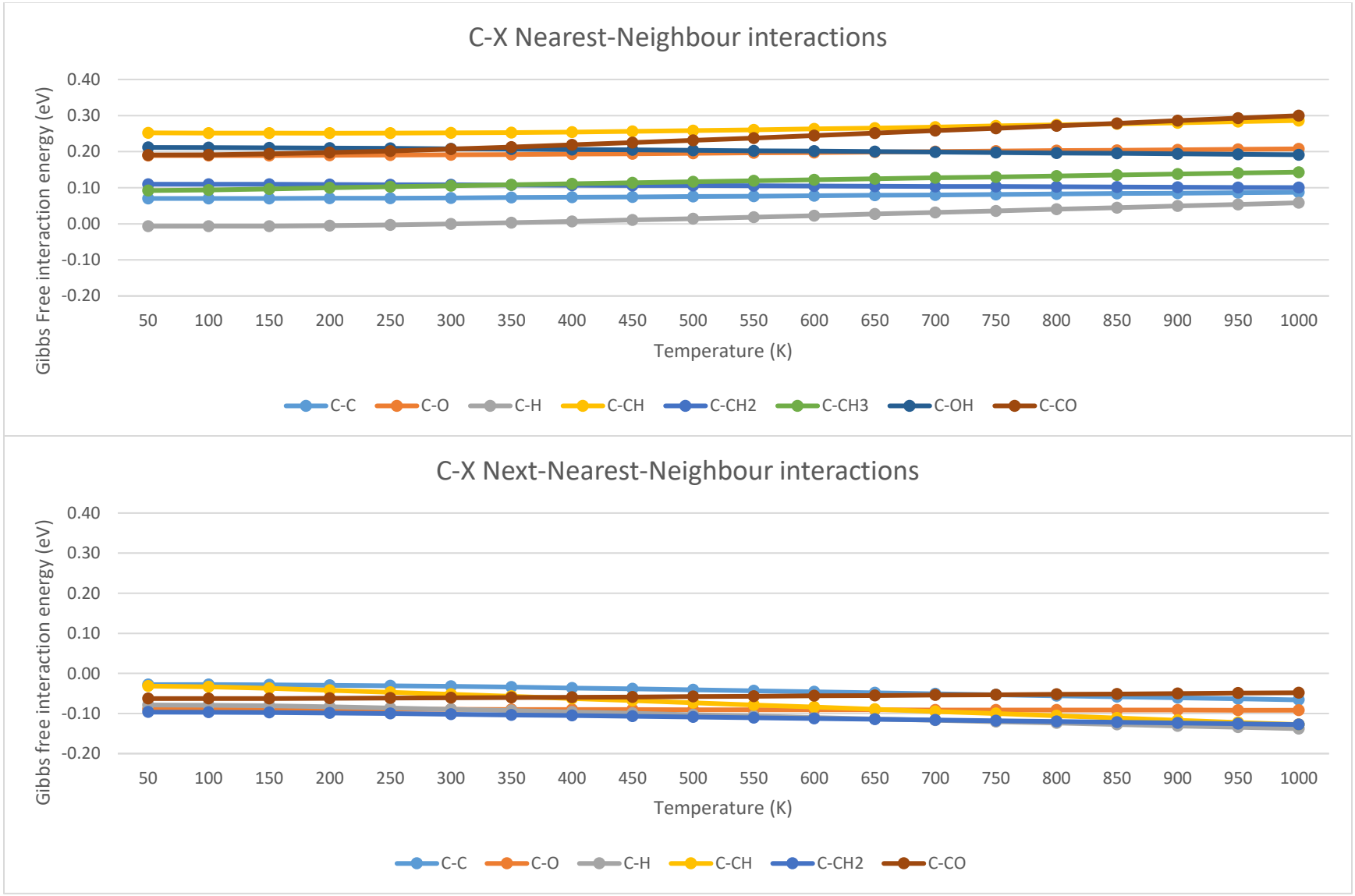

Figure 5-6: Temperature corrected Gibbs free interaction energies for C-X nearest and next-nearest neighbour interactions

5.4 Lateral Interactions between O – Methanation species

The literature focussing on CO dissociation to C and O on Fe(100) [5,6,9,19,20] gives a brief insight to O-CO and O-C lateral interactions. The studies suggest that these are all repulsive. The interactions between oxygen and other methanation species are of importance to several mechanisms. O-CH_x interactions give insights into formation of oxygen containing organic compounds such as alcohols, aldehydes, acids and ketones.

The results in Table 5-4 summaries the bond lengths, Fermi energy, deformation energy, excess energy and Bader charge for C – methanation species interactions. The atomic distances show no clear trend in bond energy and bond length unlike what was seen for CO-X and C-X interactions. This indicates that bond length is not always synonymous with bond strength.

The excess energies in Table 5-4 show that, with the exception of O-H interactions, the next-nearest neighbour interactions are attractive while the nearest neighbour interactions are repulsive. For O-H interactions all configurations show repulsive lateral interactions. The repulsive interactions of O-CO, O-C, O-CH and O-CH_2 are all larger than 0.4 eV, with the O-C, O-CH and O-CH_2 interactions all above 0.6 eV. As mentioned in Chapter 2, in the context of kinetics, these changes will have significant consequences on the rate of reaction. Large attractive interactions are seen for the O-C and O-CH_2 on the "Diagonal" configuration.

The 0.5 ML diagonal configurations also yield slightly larger charges on the O atom for all interactions except the O-H interaction. Large charges are seen on the share primary Fe atoms, in excess of 0.5 e. The Fermi energy increases with increasing coverage and configurations with larger adsorbates like CH_2 and CH_3 have further increased Fermi energies.

The temperature corrections are calculated using the vibrational frequencies obtained. The temperature corrections for O-X nearest-neighbour interactions and O-X next-nearest neighbour interactions can be seen in Figure 5-7. For the nearest neighbour interactions O-CH_2, O-CO and O-OH display decreases in repulsion with increasing temperature while O-H, O-O, O-C, O-CH and O-CH_3 display increases in repulsion with increasing temperature.

For the next-nearest neighbour interactions all species show increased repulsions with increasing temperature with the exception of O-CH_2 which shows increasing attraction. It is interesting to note that the O-CO interaction is slightly attractive at lower temperatures but changes to slightly repulsive at higher temperatures.

Table 5-4: Co-adsorption of atomic O with other species present during methanation on Fe (100)

Species		d_{Fe-O} (Å)	E_{Fermi} (eV)	E_{Deform} (eV)	E_{Excess} (eV)	Bader Charge	
						O	Primary Fe
O-CO	0.33 ML Adj.	2.125	-6.127	0.09	0.15	-1.29	0.55 Shared 0.38 unshared
	0.5 ML Adj.	2.107	-6.050	0.06	0.45	-1.25	0.62
	0.5 ML Diag.	2.097	-6.017	0.11	-0.07	-1.30	0.66
O-H	0.33 ML Diag.	2.154	-6.160	0.07	0.01	-1.33	0.43 Shared 0.28 unshared
	0.5 ML Adj.	2.137	-6.110	0.05	0.06	-1.31	0.45
	0.5 ML Diag.	2.157	-6.087	0.05	0.05	-1.29	0.46
O-C	0.33 ML Adj.	2.160	-6.198	0.45	0.19	-1.35	0.62 shared 0.39 unshared
	0.5M Adj.	2.129	-6.110	0.12	0.64	-1.25	0.61
	0.5 ML Diag.	2.049	-6.105	0.12	-0.19	-1.35	0.66
O-CH	0.33 ML Adj.	2.141	-6.084	0.12	0.31	-1.28	0.54 shared 0.28 unshared
	0.5 ML Adj.	2.131	-5.954	0.08	0.73	-1.27	0.57
	0.5 ML Diag.	2.050	-5.934	0.11	-0.07	-1.31	0.64
$O-CH_2$	0.33 ML Adj.	2.158	-6.023	0.13	0.16	-1.30	0.50 shared 0.38 unshared
	0.5 ML Adj.	2.051	-5.911	0.10	0.70	-1.28	0.58
	0.5 ML Diag.	2.147	-5.830	0.09	-0.23	-1.31	0.57
$O-CH_3$	0.33 ML Adj.	2.127	-5.990	0.13	<0.01	-1.30	0.57 shared 0.33 unshared
	0.5 ML Adj.	2.138	-5.875	0.14	0.10	-1.30	0.55 shared 0.36 unshared
O-OH	0.33 ML Adj.	2.139	-6.090	0.11	0.05	-1.31	0.58 shared 0.37 unshared
	0.5 ML Adj.	2.130	-6.022	0.08	0.17	-1.30	0.54 shared 0.36 unshared

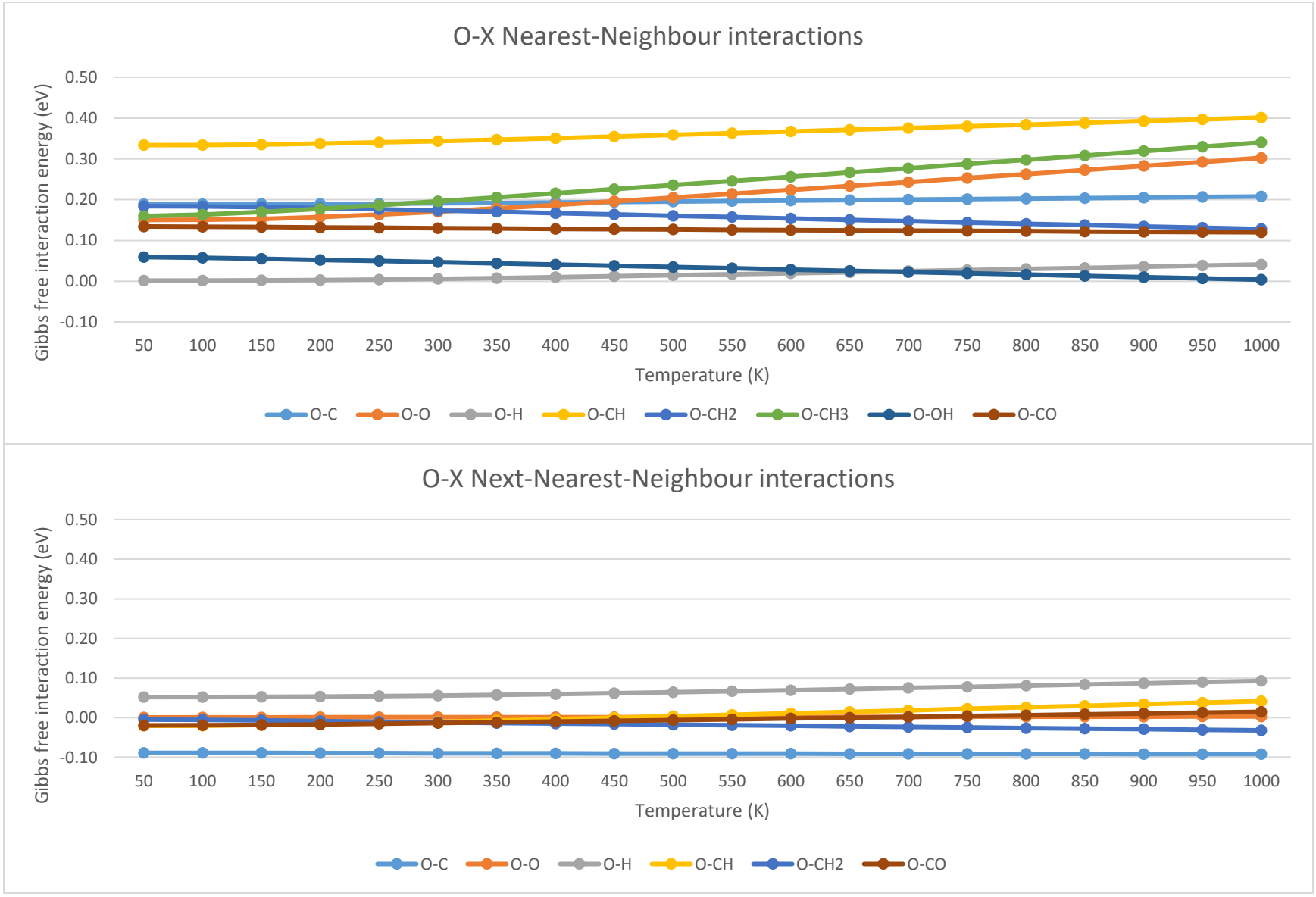

Figure 5-7: Temperature corrected Gibbs free interaction energies for O-X nearest and next-nearest neighbour interactions

5.5 Lateral Interactions between H – Methanation species

Configurations which consider H-CH_x interactions can be thought of as precursors to hydrogenation type reactions. Hydrogenation of CH_x species are of importance to several mechanisms and is one of the simplest mechanisms postulated for methanation.

The results in Table 5-5 summaries the bond lengths, Fermi energy, deformation energy and excess energy for C – methanation species interactions. The atomic distances show that Fe-H distance varied by less than 0.01 Å for all the configurations considered. This indicates that the Fe-H distance is not strongly influenced by the presence of neighbouring adsorbates, nearest-neighbour or next-nearest-neighbour. The results in Table 5-5 also show that the H-C interactions and the H-CO and H-CH_2 diagonal interactions are slightly attractive. All the other interactions are slight repulsive.

Very little variation is seen with the H-Fe distance and the Bader charge on the on the H. The OH-H 0.33 ML configurations results in the smallest charge of -0.41 e on H while the CO-H 0.5 ML adjacent and CH_3-H 0.33 ML configurations result in the largest charge of -0.48 e.

The Fermi energy increases with increasing coverage and configurations with larger adsorbates like CH_2 and CH_3 have further increased Fermi energies. The diagonal configurations display the largest fermi energies.

The temperature corrections for H-X nearest-neighbour interactions and H-X next-nearest neighbour interactions can be seen in Figure 5-8. For the nearest neighbour interactions H-H, H-CO and H-OH display decreases in repulsion with increasing temperature while H-O, H-C, H-CH, H-CH_2 and H-CH_3 display increases in repulsion with increasing temperature.

For the next-nearest neighbour interactions all species show increased repulsions with increasing temperature with the exception of H-CH_2 which shows increasing attraction.

Table 5-5: Co-adsorption of H with other species present during methanation on Fe (100)

Species		d_{Fe-H} (Å)	E_{Fermi} (eV)	E_{Deform} (eV)	E_{Excess} (eV)	Bader Charge	
						H	Primary Fe
H-CO	0.33 ML Adj.	1.989	-6.120	0.06	0.02	-0.42	0.47 Shared 0.22 Unshared
	0.5 ML Adj.	1.988	-6.112	0.06	0.01	-0.48	0.30
	0.5 ML Diag.	1.990	-6.100	0.07	-0.08	-0.43	0.31
H-C	0.33 ML Adj.	1.993	-6.257	0.45	-0.04	-0.45	0.48 Shared 0.35 Unshared
	0.5 ML Adj.	1.992	-6.228	0.17	-0.05	-0.44	0.49
	0.5 ML Diag.	1.996	-6.197	0.22	-0.13	-0.43	0.48
H-O	0.33 ML Diag.	1.988	-6.160	0.07	0.01	-0.45	0.43 S 0.28 US
	0.5 ML Adj.	1.992	-6.110	0.05	0.06	-0.41	0.45
	0.5 ML Diag.	1.987	-6.087	0.05	0.05	-0.42	0.46
H-CH	0.33 ML Adj.	1.989	-6.116	0.45	0.10	-0.45	0.38 Shared 0.3 Unshared
	0.5 ML Adj.	1.981	-6.033	0.04	0.10	-0.44	0.41
	0.5 ML Diag.	1.989	-6.027	0.04	0	-0.45	0.40
H –CH_2	0.33 ML Adj.	1.990	-6.066	0.45	0.01	-0.43	0.55 Shared 0.35 Unshared
	0.5 ML Adj.	1.991	-5.956	0.05	0.11	-0.43	0.55
	0.5 ML Diag.	1.992	-5.946	0.07	-0.08	-0.45	0.57
H –CH_3	0.33 ML Adj.	1.987	-6.024	0.15	0.02	-0.48	0.60 Shared 0.33 Unshared
	0.5 ML Adj.	1.987	-5.911	0.14	0.02	-0.44	0.58 Shared 0.35 Unshared
H –OH	0.33 ML Adj.	1.989	-6.09	0.19	0.03	-0.41	0.60 Shared 0.34 Unshared
	0.5 ML Adj.	1.987	-6.03	0.18	0.05	-0.43	0.55 Shared 0.34 Unshared

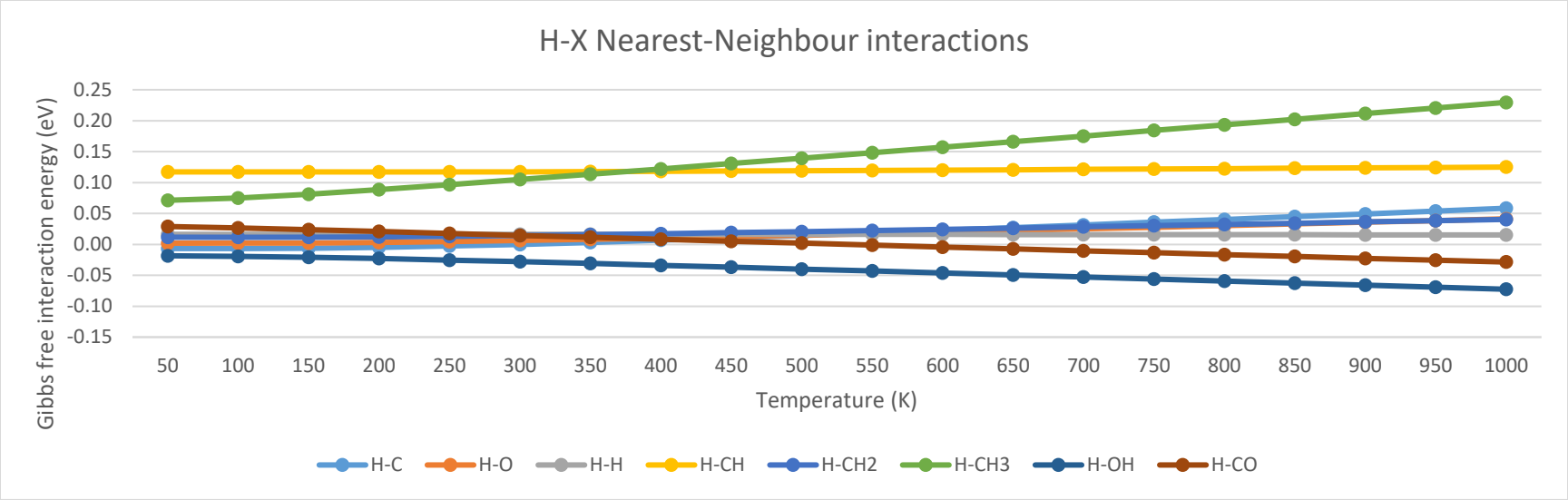

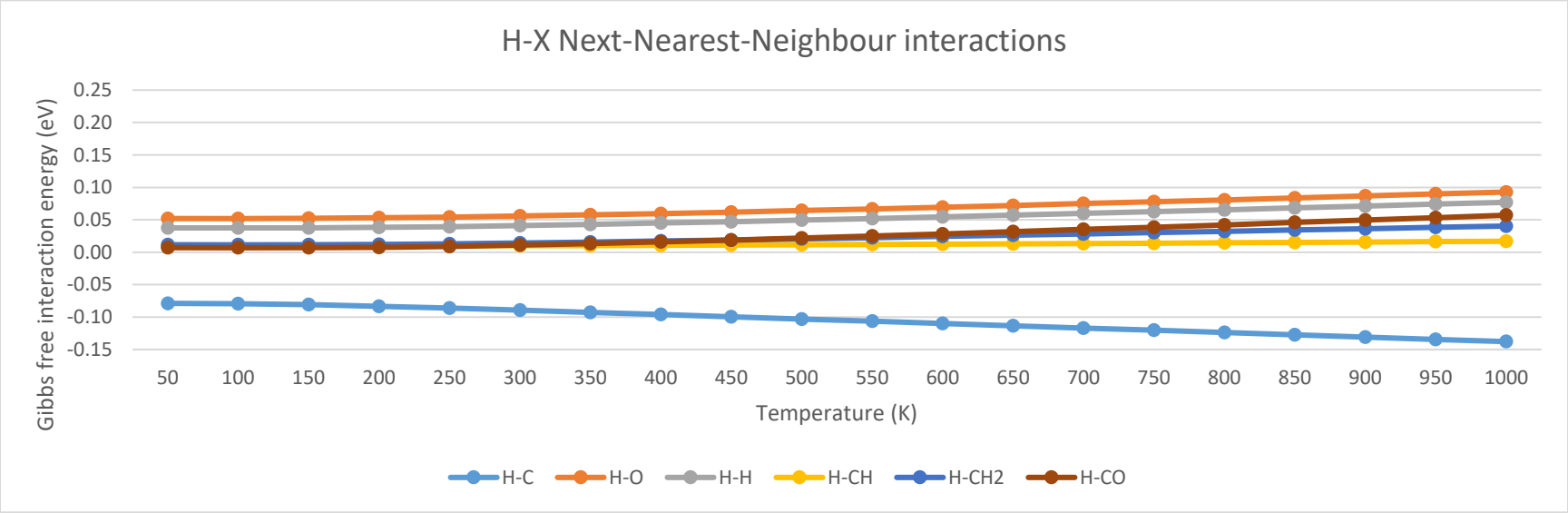

Figure 5-8: Temperature corrected Gibbs free interaction energies for H-X nearest and next-nearest neighbour interaction

5.6 Lateral Interactions between CH – Methanation species

The interactions between CH and other methanation species can give insights into various reaction precursors. CH hydrogenation is one of the proposed pathways to form methane from synthesis gas and in particular CH-CH_x interactions can give insights into adsorbate coupling and formation of larger organic compounds [1–3].

The results in Table 5-6 summaries the bond lengths, Fermi energy, deformation energy and excess energy for CH– methanation species interactions. The atomic distances show that Fe-C distances decrease with increasing coverage with diagonal configurations showing the shortest distances. This can be interpreted as the Fe-C bonds strength increases with increasing coverage and is even stronger for diagonal configurations. The results also show that the C-H distances vary by less than 0.01 Å for all configurations. This can be interpreted as the C-H bond strength is not strongly influenced by presence of neighbouring adsorbates.

The results from Table 5-6 show that the next-nearest-neighbour interactions yield attractive lateral interactions and nearest-neighbour interactions yield repulsive lateral interactions for all CO-X species. Of the adjacent interactions, CO, O, C and CH_2 all have repulsive lateral interactions larger than 0.4 eV for the 0.5 Adj. configurations, noting again the interaction energy of O-CH.

The diagonal configurations also yield slightly larger charges on the C atomic for all interactions except the CH-CH_2 and CH-O configuration. The charges on H show little deviation with coverage for all interactions with the exception of CH-O, which show the largest charge on H at 0.33 ML at 0.12 e.

The Fermi energy increases with increasing coverage and configurations with larger adsorbates like CH_2 and CH_3 have further increased Fermi energies. The 0.5 ML adjacent configurations display larger Fermi energies.

The corrections for CH-X nearest-neighbour interactions and CH-X next-nearest neighbour interactions can be seen in Figure 5-9. All interactions show increasing repulsion with increasing temperature with the exception of the next-nearest-neighbour CH-CH_2 interaction which shows an increase in attraction with increasing temperature.

Table 5-6: Co-adsorption of CH with other methanation species on Fe (100)

Species		d_{Fe-C} (Å)	d_{C-H} (Å)	E_{Fermi} (eV)	E_{Deform} (eV)	E_{Excess} (eV)	Bader Charge		
							C	H	Primary Fe
CH-CO	0.33 ML Adj.	2.117	1.102	-6.077	0.45	0.24	-1.27	0.06	0.55 shared 0.36 unshared
	0.5 ML Adj.	2.055	1.102	-5.964	0.06	0.47	-1.20	0.08	0.55
	0.5 ML Diag.	2.050	1.103	-5.971	0.08	-0.04	-1.39	0.08	0.58
CH-H	0.33 ML Adj.	2.101	1.101	-6.116	0.45	0.10	-1.27	0.05	0.38 shared 0.3 unshared
	0.5 ML Adj.	2.071	1.105	-6.033	0.04	0.10	-1.25	0.05	0.41
	0.5 ML Diag.	2.082	1.104	-6.027	0.04	0	-1.33	0.08	0.40
CH-O	0.33 ML Adj.	2.081	1.104	-6.084	0.31	0.31	-1.45	0.12	0.54 shared 0.28 unshared
	0.5 ML Adj.	2.077	1.104	-5.954	0.73	0.73	-1.21	0.04	0.57
	0.5 ML Diag.	2.045	1.104	-5.934	-0.07	-0.07	-1.42	0.06	0.64
CH-C	0.33 ML Adj.	2.101	1.101	-6.148	0.45	0.22	-1.27	0.04	0.58 shared 0.34 unshared
	0.5 ML Adj.	1.961	1.104	-6.025	0.11	0.43	-1.22	0.08	0.53
	0.5 ML Diag.	2.002	1.101	-6.072	0.11	-0.04	-1.33	0.09	0.59
$CH-CH_2$	0.33 ML Adj.	2.101	1.101	-5.972	0.45	0.24	-1.24	0.08	0.48 Shared 0.30 unshared
	0.5 ML Adj.	2.151	1.104	-5.781	0.08	0.55	-1.28	0.08	0.49
	0.5 ML Diag.	2.038	1.103	-5.796	0.05	-0.04	-1.26	0.06	0.55
$CH-CH_3$	0.33 ML Adj.	2.121	1.099	-5.953	0.45	0.20	-1.33	0.07	Shared 0.57 Unshared 0.40
	0.5 ML Adj.	2.140	1.101	-5.788	0.19	0.30	-1.30	0.08	Shared 0.53 Unshared 0.34
CH-OH	0.33 ML Adj.	2.114	1.106	6.039	0.22	0.13	-1.33	0.06	Shared 0.49 Unshared 0.35
	0.5 ML Adj.	2.046	1.102	-5.935	0.15	0.29	-1.32	0.09	Shared 0.52 Unshared 0.38

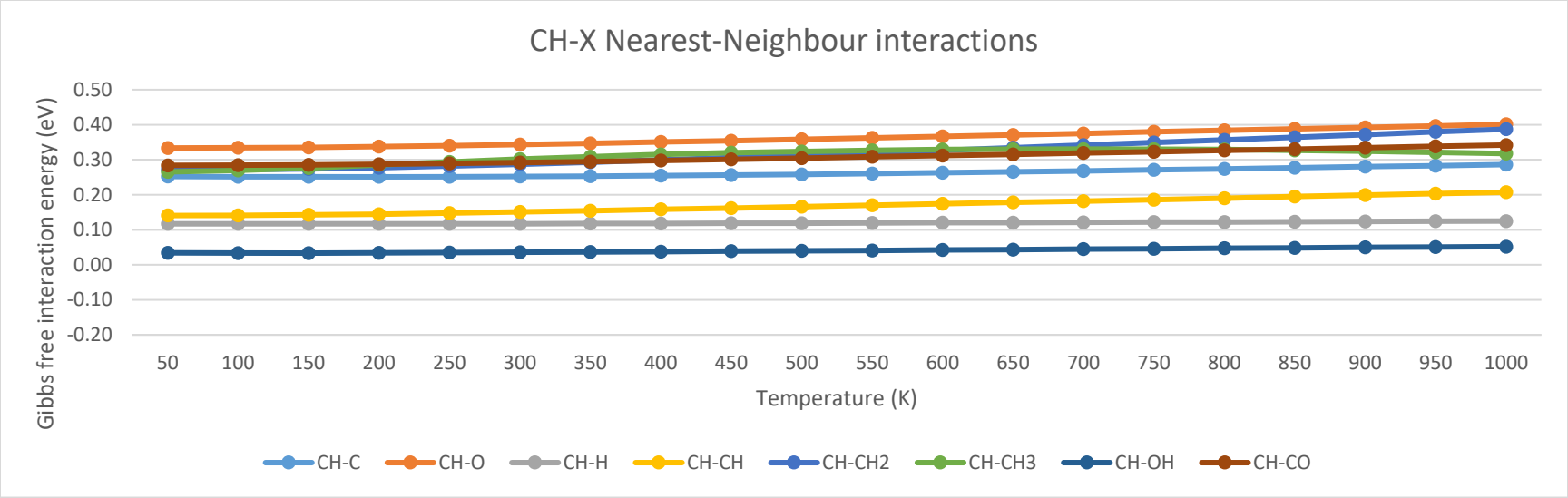

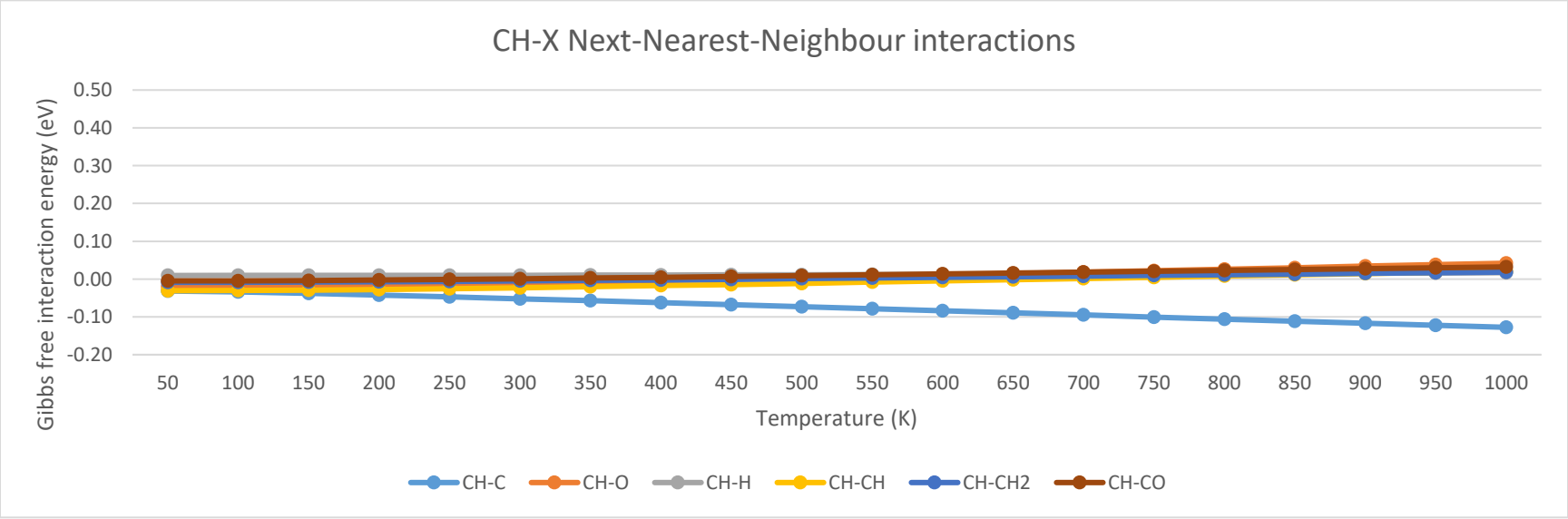

Figure 5-9: Temperature corrected Gibbs free interaction energies for CH-X nearest and next-nearest neighbour interactions

5.7 Lateral Interactions between CH_2 – Methanation species

Much like the CH, the interactions between CH_2 and other methanation species can give insights into various reaction precursors. CH_2 hydrogenation is one pathway to form methane and CH_2-CH_x interactions can give insights into adsorbate coupling and formation of larger organic compounds.

The results in Table 5-7 summaries the bond lengths, Fermi energy, deformation energy and excess energy for CH_2– methanation species interactions. The atomic distances show that Fe-C distances decrease with increasing coverage with diagonal configurations showing the shortest distances. This indicates that the Fe-C bonds strength increases with increasing coverage and is even stronger for diagonal configurations. The C-H distances are shorter for 0.5 ML adjacent configurations. This can be interpreted as the C-H bond strength is stronger for repulsive interactions.

The next-nearest neighbour interactions result in attractive interactions while nearest neighbour interactions display repulsive interactions. Large repulsive interactions are seen with the largest being the CH_2-O interactions, resulting in a 0.7 eV repulsion. Again, the C-H distances remain fairly constant, with the exception of the CH_2-CO 0.5 ML "Adjacent" and CH_2-O 0.5 ML "Diagonal" configurations.

As with the intraspecies interactions, the charge on the C atom for CH_2 adsorbates are fairly similar, in the region of -1.30 e.

The Fermi energy increases with increasing coverage and configurations with larger adsorbates like CH_2 and CH_3 have further increased Fermi energies. The 0.5 ML diagonal configurations display larger Fermi energies.

The temperature corrected Gibbs free interactions for CH_2-X nearest-neighbour interactions and CH_2-X next-nearest neighbour interactions can be seen in Figure 5-10. The nearest neighbour interactions all show increases in repulsion with increasing temperature, with the exception of CH_2-OH, CH_2-C, CH_2-CH_2 and CH_2-CH which displays a subtle decrease.

For the next-nearest neighbour interactions the configurations show increases in attraction with increasing temperature while the attraction decreases for CH_2-O, CH_2-CO and CH_2-CH_2.

Table 5-7: Co-adsorption of CH_2 with other methanation species on Fe (100)

Species		d_{Fe-X} (Å)	d_{C-H} (Å)	E_{Fermi} (eV)	E_{Deform} (eV)	E_{Excess} (eV)	Bader charge		
							C	H	Fe
	0.33 ML Adj.	2.212	1.137	-6.011	0.45	0.14	-1.30	0.08	0.50 shared 0.35 unshared
CH_2-CO	0.5 ML Adj.	1.961	1.193	-5.859	0.04	0.42	-1.32	0.05	0.52
	0.5 ML Diag.	2.122	1.137	-5.884	0.05	-0.14	-1.28	0.07	0.58
	0.33 ML Adj.	2.279	1.131	-6.066	0.45	0.01	-1.35	0.09	0.45 Shared 0.35 unshared
CH_2-H	0.5 ML Adj.	2.183	1.124	-5.956	0.05	0.11	-1.36	0.11	0.40
	0.5 ML Diag.	2.133	1.135	-5.946	0.07	-0.08	-1.38	0.09	0.39
	0.33 ML Adj.	2.279	1.131	-6.023	0.13	0.16	-1.33	0.11	0.43 Shared 0.28 unshared
CH_2-O	0.5 ML Adj.	2.298	1.103	-5.911	0.10	0.70	-1.30	0.12	0.45
	0.5 ML Diag.	2.238	1.238	-5.830	0.09	-0.23	-1.29	0.10	0.46
	0.33 ML Adj.	2.127	1.130	-6.076	0.18	0.11	-1.33	0.14	0.55 Shared 0.35 unshared
CH_2-C	0.5 ML Adj.	2.147	1.131	-5.931	0.14	0.47	-1.35	0.13	0.55
	0.5 ML Diag.	2.097	1.130	-5.965	0.14	-0.18	-1.33	0.10	0.57
	0.33 ML Adj.	2.279	1.131	-5.972	0.45	0.24	-1.31	0.12	0.48 Shared 0.30 unshared
CH_2-CH	0.5 ML Adj.	2.098	1.136	-5.781	0.08	0.55	-1.30	0.09	0.49
	0.5 ML Diag.	2.107	1.130	-5.796	0.05	-0.04	-1.32	0.11	0.55
	0.33 ML Adj.	2.116	1.132	-5.8907	0.25	0.05	-1.32	0.10	Shared 0.45 Unshared 0.28
CH_2-CH_3	0.5 ML Adj.	2.106	1.129	-5.705	0.17	0.29	-1.28	0.08	Shared 0.44 Unshared 0.33
	0.33 ML Adj.	2.127	1.133	-5.984	0.15	0.11	-1.31	0.11	Shared 0.40 Unshared 0.23
CH_2-OH	0.5 ML Adj.	2.111	1.131	-5.884	0.12	0.26	-1.33	0.14	Shared 0.41 Unshared 0.27

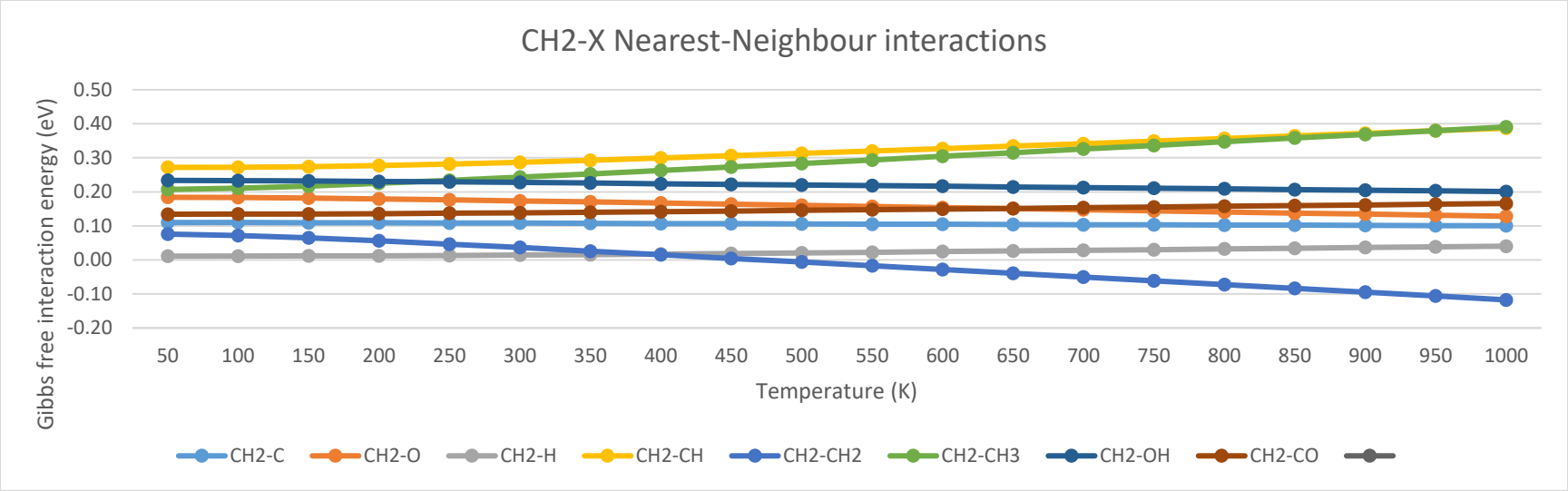

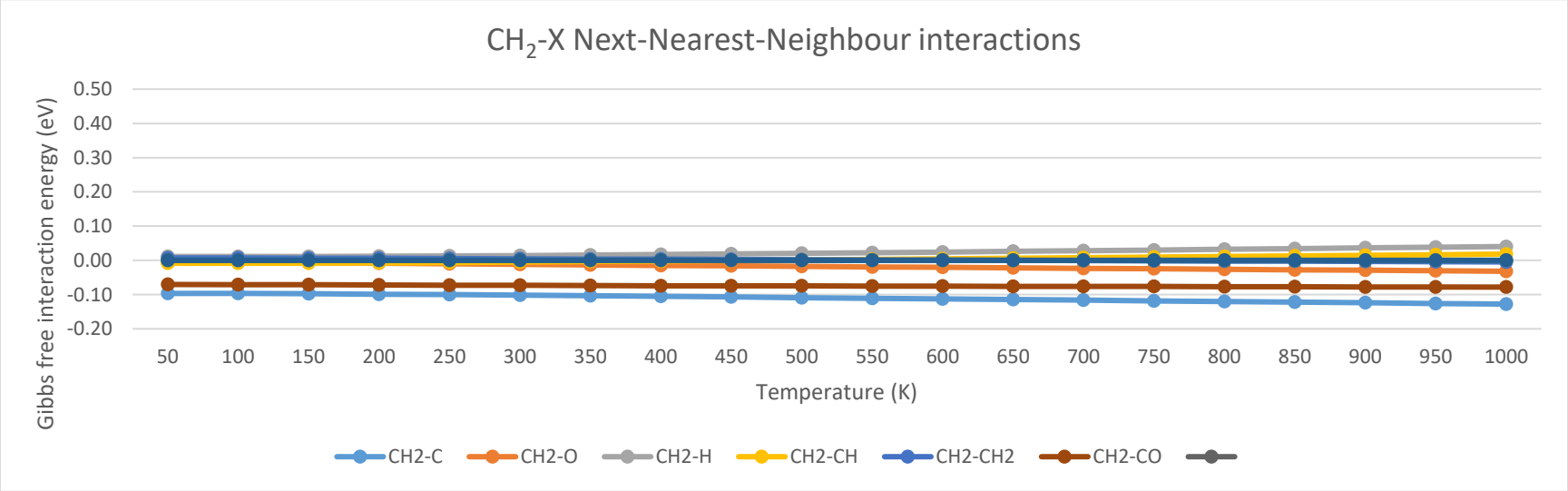

Figure 5-10: Temperature corrected Gibbs free interaction energies for CH_2-X nearest and next-nearest neighbour interactions

5.8 Lateral Interactions between CH_3 – Methanation species

CH_3 species are most stable on the bridge site, next nearest neighbour interactions with species in the hollow site are significantly further than hollow-hollow next nearest neighbour interactions. For this reason, only next nearest neighbour interactions with other bridge species was consider. The interactions between CH_3 and other methanation species are of importance to several mechanisms. While CH_3 hydrogenation is one pathway to form methane, CH_3-CH_x interactions give insights into adsorbate coupling and formation of larger organic compounds.

The results in Table 5-9 summaries the bond lengths, Fermi energy, deformation energy and excess energy for CH_3– methanation species interactions. Atomic distances indicate that Fe-C distances decrease with increasing coverage. This can be interpreted as the Fe-C bonds strength increases with increasing. The results also show that the C-H distances vary by less than 0.01 Å for all configurations. This indicates the C-H bond strength is not strongly influenced by presence of neighbouring adsorbates.

All of the CH_3-X interactions are repulsive, but all interactions are below 0.3 eV. The CH_3 adsorbate prefers the bridge site and as a result is typically closer to the other adsorbates. As with the intraspecies interactions, the charge on the C atom for CH_3 adsorbates are fairly similar, in the region of -0.80 e. The charge on H is also fairly stable.

The Fermi energy increases with increasing coverage and configurations with larger adsorbates like CH_2 and CH_3 have further increased Fermi energies.

The temperature corrected Gibbs free interactions for CH_3-X nearest-neighbour interactions and CH_2-X next-nearest neighbour interactions can be seen in Figure 5-11. The nearest neighbour interactions all show increases in repulsion with increasing temperature.

For the next-nearest neighbour interaction for CH_3-CH_3 show a decrease in repulsion with increasing temperature which CH_3-OH interactions show attractive interactions at low temperatures and repulsive interactions at high temperatures.

Table 5-8: Co-adsorption of CH_3 with other methanation species on Fe (100)

Species		d_{Fe-X} (Å)	d_{C-H} (Å)	E_{Fermi} (eV)	E_{Deform} (eV)	E_{Excess} (eV)	Bader charge		
							C	H	Fe
CH_3-CO	0.5 ML	2.156	1.091	-5.95	0.14	0.29	-0.80	0.10	0.45
	0.33 ML.	2.221	1.087	-5.990	0.29	0.14	-0.79	0.09	0.52 shared 0.38 unshared
CH_3-H	0.5 ML	2.140	1.103	-5.911	0.15	0.02	-0.74	0.10	0.38
	0.33 ML	2.210	1.089	-6.024	0.14	0.02	-0.75	0.10	0.36 shared 0.27 unshared
CH_3-O	0.5 ML	2.190	1.090	-5.875	0.13	0.10	-0.80	0.11	0.55 shared 0.36 unshared
	0.33 ML	2.183	1.089	-5.990	0.14	<0.01	-0.76	0.12	0.57 shared 0.33 unshared
CH_3-C	0.5 ML	2.167	1.087	-6.153	0.19	0.17	-0.77	0.10	0.58 shared 0.35 unshared
	0.33 ML	2.149	1.089	-6.086	0.19	0.09	-0.77	0.12	0.60 shared 0.33 unshared
CH_3-CH	0.5 ML	2.170	1.089	-5.788	0.45	0.30	-0.80	0.10	0.53 Shared 0.34 Unshared
	0.33 ML	2.217	1.089	-5.953	0.19	0.20	-0.79	0.10	0.57 Shared 0.40 Unshared
CH_3-CH_2	0.5 ML	2.197	1.089	-5.705	0.25	0.29	-0.75	0.11	0.44 Shared 0.33 Unshared
	0.33 ML	2.211	1.089	-5.8907	0.17	0.05	-0.79	0.12	0.45 Shared 0.28 Unshared
CH_3-OH	0.5 ML	2.225	1.098	-5.771	0.13	<0.01	-0.80	0.13	0.50 Shared 0.33 Unshared
	0.33 ML	2.222	1.101	-5.951	0.15	0.09	-0.81	0.12	0.52 Shared 0.34 Unshared

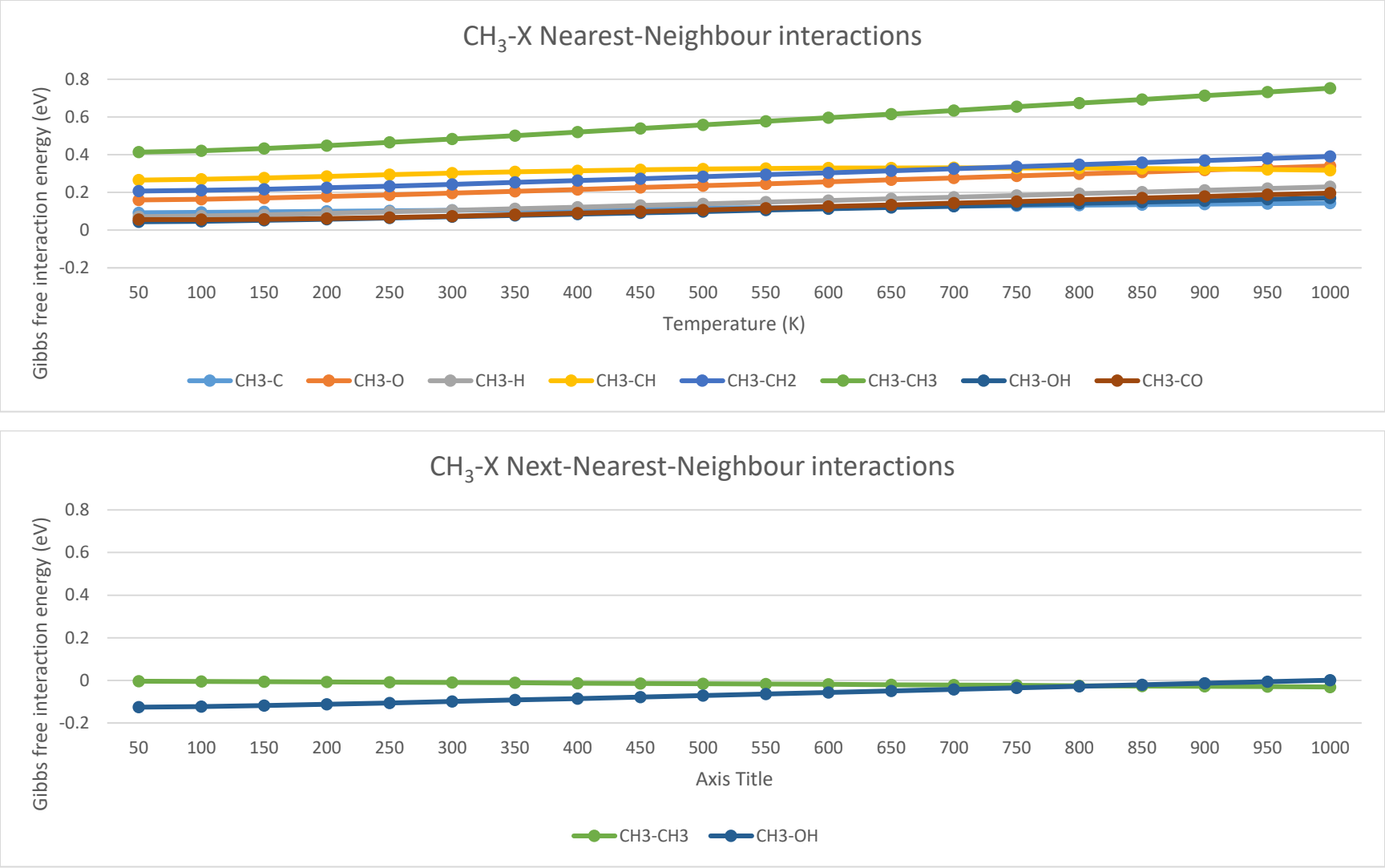

Figure 5-11: Temperature corrected Gibbs free interaction energies for CH_3-X nearest and next-nearest neighbour interactions

5.9 Lateral Interactions between OH – Methanation species

The interactions between OH and other methanation species can give insights into reaction precursors for to several mechanisms. OH hydrogenation is one pathway to form water, OH-CH_x interactions can give insights into adsorbate coupling and formation of larger oxygen containing organic compounds, particularly alcohols.

The results a in Table 5-9 summaries the bond lengths, Fermi energy, deformation energy and excess energy for OH– methanation species interactions. Atomic distances indicate that Fe-O distances decrease with increasing coverage. This can be interpreted as the Fe-O bonds strength increases with increasing. The results also show that the O-H distances vary by less than 0.01 Å for all configurations. This indicates the C-H bond strength is not strongly influenced by presence of neighbouring adsorbates.

As seen for the CH_3-X interactions, the OH-X interactions are all repulsive (Table 5-9). And again, the interactions energies are below 0.3 eV. As with CH_3, OH prefers the bridge site at lower coverages.

As with the intraspecies interactions, the charge on the O atom for OH adsorbates are fairly similar, in the region of -1.6 e. The charge on H is also fairly stable at 1.00 e.

The Fermi energy increases with increasing coverage and configurations with larger adsorbates like CH_2 and CH_3 have further increased Fermi energies with the exception of OH-C which shows a decrease in Fermi energy with coverage.

The corrected interactions for OH-X nearest-neighbour interactions and OH-X next-nearest neighbour interactions can be seen in Figure 5-12. The nearest neighbour interactions all show increases in repulsion with increasing temperature.

For the next-nearest neighbour interactions for OH-CH_3 and OH-OH both show an increase in repulsion with increasing temperature.

Table 5-9: Co-adsorption of OH with other methanation species on Fe (100)

Species		d_{Fe-X} (Å)	d_{O-H} (Å)	E_{Fermi} (eV)	E_{Deform} (eV)	E_{Excess} (eV)	Bader charge		
							O	H	Fe
OH-CO	0.5 ML	1.997	0.97	-5.95	0.37	0.29	-1.55	1.01	0.45
	0.33 ML.	2.005	0.97	-5.99	0.22	0.14	-1.56	1.02	0.62 shared 0.32 unshared
OH-H	0.5 ML	2.013	0.97	-6.03	0.19	0.05	-1.60	1.00	0.36
	0.33 ML	2.011	0.97	-6.09	0.18	0.03	-1.62	1.01	0.41 shared 0.24 unshared
OH-O	0.5 ML	2.020	0.97	-6.02	0.11	0.17	-1.59	0.99	0.55 shared 0.34 unshared
	0.33 ML	2.035	0.97	-6.09	0.08	0.05	-1.59	1.01	0.60 shared 0.34 unshared
OH-C	0.5 ML	2.006	0.97	-6.15	0.22	0.17	-1.60	1.03	0.58 shared 0.35 unshared
	0.33 ML	2.011	0.97	-6.09	0.23	0.09	-1.60	0.99	0.60 shared 0.33 unshared
OH-CH	0.5 ML	2.023	0.97	-5.94	0.22	0.29	-1.57	1.00	0.52 Shared 0.38 Unshared
	0.33 ML	2.081	0.97	-6.04	0.15	0.13	-1.58	1.00	Shared 0.49 Unshared 0.35
$OH-CH_2$	0.5 ML	2.031	0.97	-5.88	0.15	0.26	-1.60	1.01	0.50 Shared 0.33 Unshared
	0.33 ML	2.040	0.97	-5.98	0.12	0.11	-1.61	1.01	0.52 Shared 0.34 Unshared
$OH-CH_3$	0.5 ML	2.082	0.98	-5.77	0.13	<0.01	-1.58	1.00	0.50 Shared 0.33 Unshared
	0.33 ML	2.079	0.97	-5.95	0.15	0.09	-1.59	1.01	0.52 Shared 0.34 Unshared

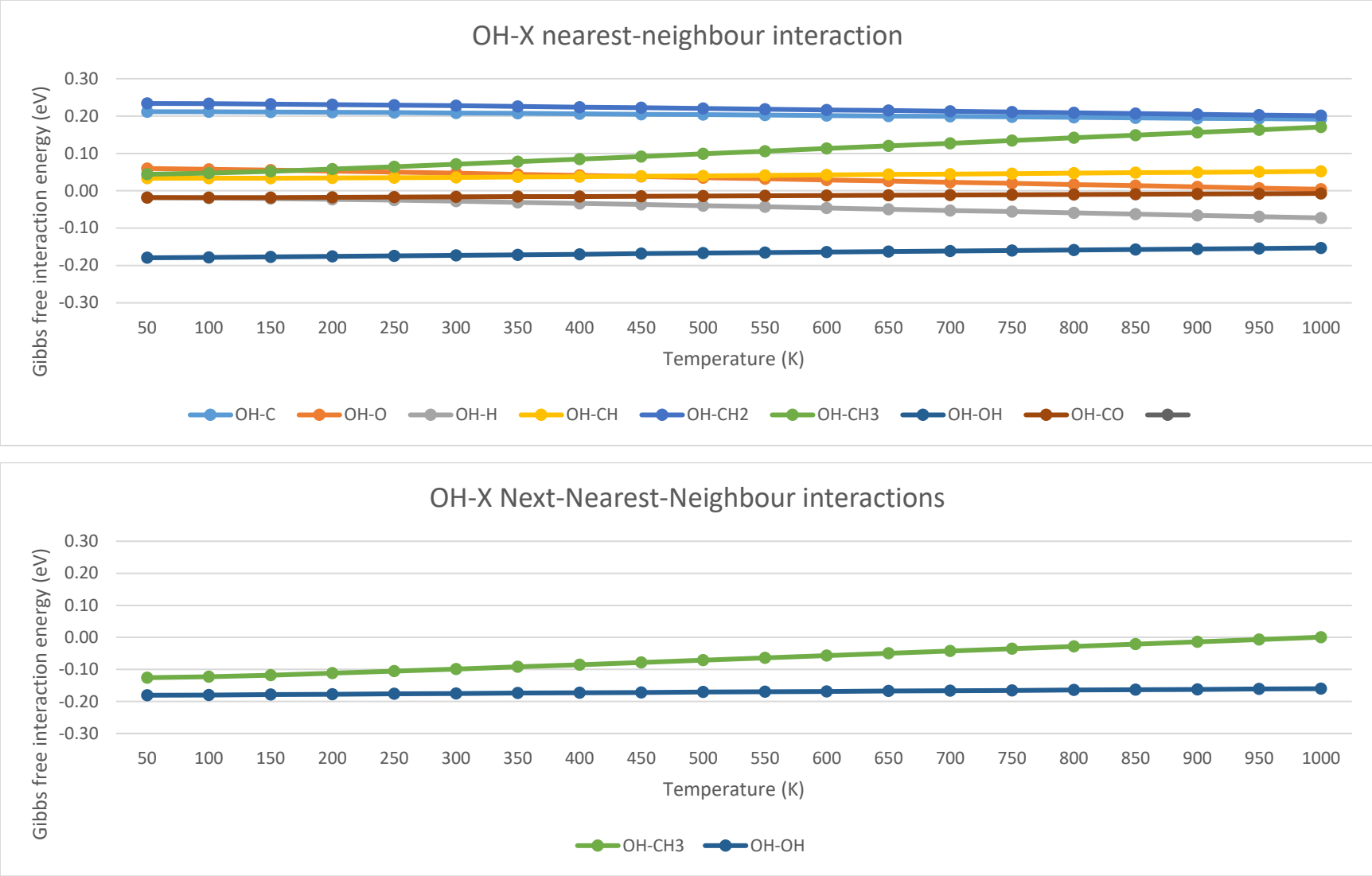

Figure 5-12: Temperature corrected Gibbs free interaction energies for OH-X nearest and next-nearest neighbour interactions

5.10 General trends for interspecies interactions

As with the interspecies interactions, the nearest neighbour interactions display repulsive interactions while the next-nearest neighbour interactions typically attractive or small enough to be considered negligible. Apart from the H-X interactions, the other species did how significant lateral interactions for the 0.5 “Adjacent” configurations. The largest interactions were the “Adjacent” C-O, CH-O and CH_2-O, all in excess of 0.64 eV.

Table 5-10 and Table 5-11 below show approximations of the nearest neighbour and next nearest neighbour interactions. The values in these tables show the average lateral interactions if one adsorbate were to sit in the corresponding neighbouring site. The values are calculated considering that adsorbates in the 0.33 ML configurations have one nearest neighbour, 0. 5 ML “adjacent” have two nearest neighbours and 0.5 ML “diagonal” have four next nearest neighbours. The highlighted values along the diagonal of these tables are interspecies interactions while all those off the diagonal are next nearest neighbour interactions. Also, since the interactions of X-Y are the same as Y-X, the tables are triangular in nature. These approximations could predict heats of adsorption and binding energies for coverages of 0.5 ML and below.

Table 5-13 and Table 5-14 below show approximations of the nearest neighbour and next nearest neighbour Gibbs free interaction energies at 600 K.

The energetic breakdown of the excess energies showed that the exchange-correlation excess energies were for the most part negative, while the electrostatic and kinetic energies vary largely in both magnitude and sign. This is similar to the interspecies interactions.

For the interspecies interactions, we saw that as the coverage increased, the Fermi level decreased. The same is seen for the interspecies interactions as the coverage is increased for a corresponding interaction.

Another interesting observation was the atomic distances of the adsorbate (i.e. C-H distances for CH_x species and O-H distances for OH) showed little variation even when the excess energy varied significantly.

Table 5-10: Approximation of nearest neighbour interactions at 0K + ZPE

Nearest Neighbour	CO	C	O	H	CH	CH2	CH3	OH
CO	0.12	0.17	0.13	0.01	0.20	0.18	0.13	0.15
C	0.17	0.03	0.25	-0.03	0.21	0.18	0.03	0.09
O	0.13	0.25	0.07	0.02	0.33	0.28	0.03	0.07
H	0.01	-0.03	0.02	0.02	0.07	0.03	0.01	0.03
CH	0.20	0.21	0.33	0.07	0.12	0.26	0.16	0.14
CH2	0.18	0.18	0.28	0.03	0.26	0.15	0.12	0.13
CH3	0.13	0.03	0.03	0.01	0.16	0.12	0.22	0.00
OH	0.15	0.09	0.07	0.03	0.14	0.13	0.00	0.02

Table 5-11: Approximation of next nearest neighbour interactions at 0K + ZPE

Next Nearest Neighbour	CO	C	O	H	CH	CH2	CH3	OH
CO	0.00	-0.04	-0.02	-0.01	-0.01	-0.03	-	-
C	-0.04	0.00	-0.05	-0.03	-0.01	-0.04	-	-
O	-0.02	-0.05	0.00	0.01	-0.02	-0.06	-	-
H	-0.01	-0.03	0.01	0.00	0.00	0.00	-	-
CH	-0.01	-0.01	-0.02	0.00	-0.03	-0.01	-	-
CH2	-0.03	-0.04	-0.06	-0.02	-0.01	0.00	-	-
CH3	-	-	-	-	-	-	0.00	-
OH	-	-	-	-	-	-	-	-0.01

Table 5-12: Approximation of nearest neighbour interactions at 600 K

Nearest Neighbour	CO	C	O	H	CH	CH2	CH3	OH
CO	0.16	0.24	0.13	0.00	0.31	0.15	0.12	-0.01
C	0.24	0.08	0.20	0.02	0.26	0.10	0.12	0.20
O	0.13	0.20	0.22	0.02	0.37	0.15	0.26	0.03
H	0.00	0.02	0.02	0.02	0.12	0.02	0.16	-0.05
CH	0.31	0.26	0.37	0.12	0.17	0.33	0.33	0.04
CH2	0.15	0.10	0.15	0.02	0.33	-0.03	0.30	0.22
CH3	0.12	0.12	0.26	0.16	0.33	0.30	0.60	0.11
OH	-0.01	0.20	0.03	-0.05	0.04	0.22	0.11	-0.16

Table 5-13: Approximation of next nearest neighbour interactions at 600 K

Next Nearest Neighbour	CO	C	O	H	CH	CH2	CH3	OH
CO	0.00	-0.06	0.00	0.03	0.01	-0.08	-	-
C	-0.06	-0.05	-0.09	-0.11	-0.08	-0.11	-	-
O	0.00	-0.09	0.00	0.07	0.01	-0.02	-	-
H	0.03	-0.11	0.07	0.05	0.01	0.02	-	-
CH	0.01	-0.08	0.01	0.01	0.00	0.00	-	-
CH2	-0.08	-0.11	-0.02	0.02	0.00	0.00	-	-
CH3	-	-	-	-	-	-	-0.02	-0.06
OH	-	-	-	-	-	-	-0.06	-0.17

5.11 References

[1] Fischer, F., Tropsch, H., *Brennstoff-Chemie* **1926**, 7, 97–104.

[2] Craxford, S.R., Rideal, E.K., *J. Chem. Soc.* **1939**, 1604–1614.

[3] Claeys, M., Van Steen, E., *Stud. Surf. Sci. Catal.* **2004**, 152, 601–680.

[4] Forzatti, P., Tronconi, E., Pasquon, I., *Catal. Rev.* **1991**, 33, 109–168.

[5] Van Helden, P., Initial Steps of the Fischer-Tropsch Synthesis on Fe(100): The Role of Hydrogen. University of Cape Town, **2010**.

[6] Lo, J.M.H., Ziegler, T., *J. Phys. Chem. C* **2007**, 111, 11012–11025.

[7] Govender, A., Ferré, D.C., Niemantsverdriet, J.W., *Chemphyschem* **2012**, 13, 1583–90.

[8] Govender, A., Ferré, D.C., Niemantsverdriet, J.W.H., *Chemphyschem* **2012**, 13, 1591–6.

[9] Sorescu, D., *Phys. Rev. B* **2006**, 73, 155420.

[10] Swart, J.C.W., Ciobîcă, I.M., van Santen, R.A., van Steen, E., *J. Phys. Chem. C* **2008**, 112, 12899–12904.

[11] Ciobîcă, I.M., Frechard, F., van Santen, R.A., Kleyn, A.W., Hafner, J., *Chem. Phys. Lett.* **1999**, 311, 185–192.

[12] Ciobica, I.M., Kleyn, a. W., Van Santen, R. a., *J. Phys. Chem. B* **2003**, 107, 164–172.

[13] van Helden, P., van Steen, E., *J. Phys. Chem. C* **2008**, 112, 16505–16513.

[14] Ciobîcă, I.M., Kramer, G.J., Ge, Q., Neurock, M., van Santen, R. a., *J. Catal.* **2002**, 212, 136–144.

[15] Błoński, P., Kiejna, A., Hafner, J., *Surf. Sci.* **2005**, 590, 88–100.

[16] Jiang, D., Carter, E., *Phys. Rev. B* **2005**, 71, 45402.

[17] Jiang, D.E., Carter, E. a., *Surf. Sci.* **2004**, 570, 167–177.

[18] Juan, A., Hoffmann, R., *Surf. Sci.* **1999**, 421, 1–16.

[19] Sorescu, D., Thompson, D., Hurley, M., Chabalowski, C., *Phys. Rev. B* **2002**, 66, 35416.

[20] Bromfield, T.C., Ferré, D.C., Niemantsverdriet, J.W., *Chemphyschem* **2005**, 6, 254–60.

[21] van Steen, E., van Helden, P., *J. Phys. Chem. C* **2010**, 114, 5932–5940.

[22] Burke, M.L., Madix, R.J., *Surf. Sci.* **1990**, 237, 20–34.

[23] Merrill, P.B., Madix, R.J., *Surf. Sci.* **1996**, 347, 249–264.

[24] Kokalj, A., *Phys. Rev. B* **2011**, 84, 45418.

[25] Einstein, T.L., *Handb. Surf. Sci.* **2005**, 4111, 1-43.

[26] Govender, A., Ferré, D.C., Niemantsverdriet, J.W.H., **2009**.

[27] Eder, M., Terakura, K., Hafner, J., *Phys. Rev. B* **2001**, 64, 115426.

[28] Clark, S.J., Segall, M.D., Pickard, C.J., Hasnip, P.J., Probert, M.I.J., Refson, K., Payne, M.C., *Zeitschrift für Krist.* **2005**, 220, 567–570.

[29] Accelrys Software Inc., Material Studio Modeling Environment, San Diego: Accelrys Software Inc., **2010**.

[30] Hammer, B., Hansen, L., Nørskov, J., *Phys. Rev. B* **1999**, 59, 7413–7421.

[31] Monkhorst, H.J., Pack, J.D., *Phys. Rev. B* **1976**, 13, 5188–5192.

[32] Li, H., Jensen, J.H., *Theor. Chem. Accounts Theory, Comput. Model. (Theoretica Chim. Acta)* **2002**, 107, 211–219.

[33] Govender, A., Towards a Mechanism for the Fischer-Tropsch Synthesis on Fe(100) Using Density Functional Theory. Eindhoven University of Technology, **2010**.

[34] Kittel, C., *Introduction to Solid State*, Wiley, New York **1996**.

[35] Payne, M.C., Arias, T. a., Joannopoulos, J.D., *Rev. Mod. Phys.* **1992**, 64, 1045–1097.

[36] Van Santen, R.A., De Koster, A., Koerts, T., *Catal. Letters* **1990**, 7, 1–14.

[37] Sung, S.S., Hoffmann, R., *J. Am. Chem. Soc.* **1985**, 107, 578–584.

[38] Hammer, B., Nørskov, J.K., *Adv. Catal.* **2000**, 45, 71–129.

6 Kinetic models on Fe (100) including interactions

Microkinetic modelling examines catalytic reactions in terms of elementary kinetic steps and their relation to each other during the catalytic process [1]. Micro-kinetic modelling is an important tool in understanding and developing the field of catalysis [2–5].

While macrokinetic modelling will always have practical applications (reactor design, understanding catalyst deactivation, catalyst quality control [2,5]) they reveal little information about the mechanistic steps involved in the process. Furthermore, Corma et al. [6] showed that different macrokinetic models with different mechanistic underpinnings can fit kinetic data equally well (or poorly), indicating that "the effect of distribution of site energies on the global kinetics is weak.". This is indeed the case for systems which have low to moderate variations with respect to site energies.

The thought of variations with respect to site energies can be extended to total energy as well. The previous three chapters have shown the variation of total energy, and therefore adsorption energies and excess Gibbs free energies, with change in neighbouring adsorbate. The interactions range from largely repulsive (CH_3-CH_3 nearest neighbours, repulsive interactions of 0.6 eV @ 600K) to negligible (H-H nearest neighbour, repulsive interaction of approx. 0.02 eV @ 600 K) and moderately attractive (C-O next nearest neighbour, attractive interaction of 0.16 eV @ 600K).

Monte Carlo simulations are the popular choice for microkinetic models but they are computationally expensive. Deterministic simulations are computationally less demanding [3] and should converge to the results obtained in a Monte-Carlo type method if all interactions are captured correctly. The energetics required to build a microkinetic model can be obtained experimentally, from single crystal studies [7–9], or theoretically, popularly with DFT studies or UBI-QEP studies [1–3,10].

The ammonia synthesis is one of the most studied catalytic processes. Hellman and Honkala [3,11] have used DFT studies to create several microkinetic models of ammonia synthesis on Ru(001) and Ru(101). The focus of the article was to determine the best method of incorporating lateral interactions into a deterministic kinetic model. They discussed three methods:

The site approximation method, which ignores the lateral interactions,

$$\bar{E}_x = E_x \qquad (6.1)$$

the mean-field approximation, which uses an average lateral interaction,

$$\bar{E}_x = E_x + N \sum^N \theta_i w_i \qquad (6.2)$$

and the quasi-chemical approximation, which uses a grand canonical distribution to approximate the effects of the lateral interactions.

$$\bar{E}_x = E_x + N \sum^N P(\theta_i) w_i \qquad (6.3)$$

Where E_x is the energy of species x without any lateral interactions, $\bar{E}_x$ is the apparent energy of species x, N is the number of neighbouring sites, w_i is the lateral interactions of species i, θ_i is the coverage of species i and P is the probability of species i being next to species x. The results were then compared to a Monte Carlo microkinetic model of the same system and it showed that the QCA method was in good agreement with this. It should be noted that equations 6.1 and 6.2 can be written as approximations of equation 6.3; for the mean-field approximation the probability of species i being next to species x is simply the coverage of species I and for the single site approximation and probability and the interaction energies are assumed to be zero.

An ammonia synthesis model on Fe surfaces was created by Nørskov and Stoltze [7,8] using both experimental results, Fe single crystal surfaces studies at ultrahigh vacuum conditions, to find the rate constants for adsorption and desorption steps, and quantum mechanical calculations, to determine other elementary steps. The studies showed that the kinetics of the ammonia synthesis at industrial conditions, 150-300 atm. @ 375-500°C, can be extrapolated from experimental ultrahigh-vacuum studies. Nørskov and Stoltze also mentioned that a possible reason for the kinetics of ammonia synthesis not being well described by a Langmuir-Hinshelwood expression is that the coverages of adsorbed NH, NH2, NH3, and H species are found to be larger than the coverage of empty sites i.e. the Langmuir-Hinshelwood falls short at higher coverages when lateral interactions are prevalent.

Ovesen et al. [9] created a microkinetic model of the low-temperature water–gas shift reaction over Cu catalysts using the surface redox mechanism. The study explored the kinetics over Cu single-crystal surfaces and was compared with results for Cu supported on Al_2O_3, SiO_2 and mixed ZnO/Al_2O_3. The study showed that interpreting results from metallic Cu is important in understanding the mechanism while the catalyst support has important secondary roles.

Grabow et al. [12] also used the surface redox mechanism with an additional COOH-mediated mechanism to create a microkinetic model for low-temperature water gas shift reaction but over Pt(111). The model was created in Athena Visual Workbench, which solves deterministic kinetic equations. The destabilizing effect of a high surface coverage of CO on the binding energy of neighbouring surface species was included in the micro-kinetic model. The study showed new mechanisms which potentially improve the understanding of the WGS reaction over a platinum catalyst.

Ciobica et al. [13] showed significant changes in the potential energy diagram for methanation on Ru(0001) upon increasing the coverage from 0.11ML to 0.25ML. They showed that repulsions between species exist for configurations where species were close together. When comparing adsorption energies at 0.11 ML and 0.25 ML, the adsorption energies increased largely for C and CH and moderately for CH_2 and CH_3 at the lower coverage. Furthermore, the exothermicy for elementary reactions $CH_{x+1} \rightarrow CH_x + H$ (x=1-3) is increased with decreasing coverage.

A simple methanation process will involve the adsorption of syngas followed by a series of hydrogenation steps and desorption of methane and water. Depending on the species involved the adsorption/dissociation and the hydrogenation kinetics have vastly different orders of magnitude [14,15]. For this reason, two kinetic models will be investigated, a simplified CO TPD model which will investigate the desorption and dissociation kinetics of CO on Fe (100) and a syngas methanation kinetic model which will investigate the CO dissociation and C and O hydrogenation kinetics on Fe (100).

6.1 Methodology

Using the results from Chapters 3-5 the Gibbs free energy of reaction of reactions involving methanation species can be calculated at a given temperature. The effect of lateral interactions on the Gibbs free energy of reaction is also approximated using pair-wise nearest neighbour and next nearest neighbour interactions at a given temperature. To model a complete reaction the activation barriers need to be known as well. In chemical kinetics, the stability of reaction intermediates is not the only important characteristic, but the activation energy is as important as well.

The activation energy for a variety of steps involved in the methanation over Fe(100) were determined by Govender [16–18]. As outlined before (see Chapter 4 and 5), the adsorption energy can be significantly affected by the presence of other adsorbates in the form of lateral interactions. In the same manner, the activation energy can be affected. It is proposed to use Hammonds's postulate [19] to account for the change in the activation barrier. Hammond’s postulate states that the transition state is similar in

structure to the reactant or product, whichever is closest in energy i.e. the structure of the reactants and the transitions state show a greater similarity, if the energy of the transition state closer to that of the reactants (and similarly products). One could also say if the forward barrier is smaller than the reverse barrier then the transitions state is similar to the reactants, and vice versa. If the reactants are similar to the transition state, the convention is to call it an early transition state, and similarly for products, a late transition state.

If we choose to accept this postulate then it would extend that the lateral interactions of the transition state are similar to the lateral interactions of the reactant or product, whichever is closest in energy. The figures below show how the barriers change when the reactants experience lateral interactions of α and the products experience lateral interactions of β. Figure 6-1 shows that for an early transition state the forward barrier would remain constant while the reverse barrier would vary. The opposite is seen for the late transition state in Figure 6-2, with the reverse barrier remaining constant and the forward varying.

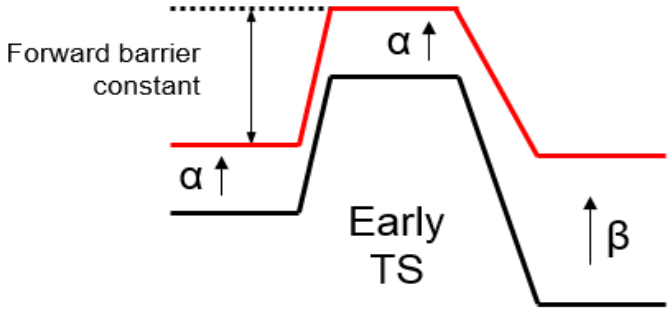

Figure 6-1: Accounting for lateral interactions for an early transition state (α: lateral interactions associated with reactants; β: lateral interactions associated with products)

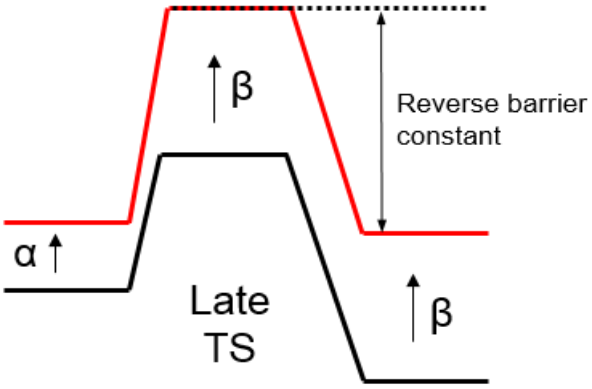

Figure 6-2: Accounting for lateral interactions for a late transition state (α: lateral interactions associated with reactants; β: lateral interactions associated with products)

To account for influence of lateral interactions on the barriers, the following equations ae proposed:

Early TS

$$eb^f = eb^{f0} \qquad (6.4)$$

$$eb^r = eb^{r0} + (LI_{React.} - LI_{Prod.}) \qquad (6.5)$$

Late TS

$$eb^f = eb^{f0} + (LI_{Prod.} - LI_{React.}) \qquad (6.6)$$

$$eb^r = eb^{r0} \qquad (6.7)$$

Where eb^f is the forward barrier, eb^r is the reverse barrier, eb^{x0} is a barrier with no lateral interactions, $LI_{React.}$ are the lateral interactions experienced by the reactants and $LI_{Prod.}$ are lateral interactions experienced by the products. LI will be determined by the method of implementation used, in this case single site approximation, mean field approximation (Equation 6.2) and the QC approximation (Equation 6.3). Following this convention, CO would then have an early transition state.

The equilibrium constant would then be:

$$K_{EQ} = e^{\frac{eb^r - eb^f}{RT}} = e^{\frac{-(\Delta G^0 - (LI_{Prod.} - LI_{React.}))}{RT}} \qquad (6.8)$$

This implies that the overall system becomes thermodynamically consistent and will result in a continuous reaction energy profile. Hammond's postulate is a wording of the Bronsted-Evans-Polanyi relationship. However, it is used here in terms of the Gibbs free energy to obtain thermodynamic correct relationships.

6.2 Microkinetic study on the lateral interactions of simulated CO TPD experiment

TPD studies can be used to investigate the binding energy on an adsorbate on a surface as well as kinetics involved in the system. *Fundamentals of Industrial Catalytic Processes* [20]: "temperature programmed desorption (TPD) was originally developed by surface scientists to quantitatively investigate the kinetics of desorption of molecules from well-defined single crystal (SC) surfaces in high vacuum".

Moon et al [21] conducted X-ray photoelectric Spectroscopy (XPS) and TPD studies with CO on Fe(100). The TPD results can be seen in Figure 6-3 below. They found that at higher coverages CO desorbs at 220 K, the α_1 peak and 306 K, the α_2 peak, and for all coverages CO desorbs at 440 K, corresponding to the α_3 peak. High temperature recombination and desorption of adsorbed CO occurs at 820 K, the β peak.

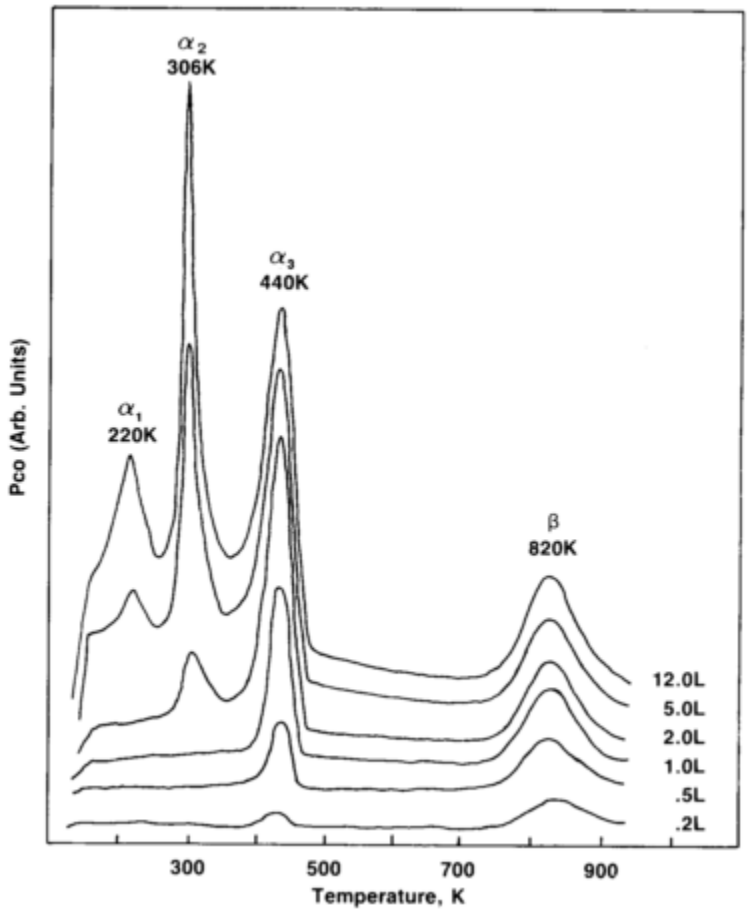

Figure 6-3: CO-TPD on Fe(100) as reported by Moon et al. [21] upon various dosages of CO in Langmuir (α peaks indicate desorption of associatively adsorbed CO, whereas the high temperature β peak represents desorption of dissociatively adsorbed CO)

Moon et al. [21] mentions that each α peak corresponds to a different state of associatively adsorbed CO. The CO state associated with the α_3 peak (440 K) is filled first, then the CO state associated with the α_2 peak (306 K) is filled, and then the CO states associated with the α_1 peak (220 K) are filled. The α_1 and α_2 peaks can be considered high coverage peaks as the α_2 peak is only visible upon exposure of more than 1.0 L of CO while the α_3 peak is visible after exposure to more than 2.0 L of CO. The surface was saturated after 12.0 L, this was evident when no appreciable increase in peak size was seen upon further increase of CO exposure. A later study Moon et al. [22] using high-resolution electron energy loss spectroscopy

(HREELS) confirmed that the α_3 state corresponds to CO adsorbed in the hollow site while the adsorption states of CO for α_2 and α_1 are postulated to be different from α_3.

Experimental procedures and its analysis [23] are well established. Becker et al. [24] mentions that creating a simulated TPD gives useful insight into understanding of the microscopic kinetic events involved in desorption. Several studies [25–30] have used Monte Carlo Simulations to reproduce TPD spectra in good agreement with experimental data. Some of these studies have considered methods of implementing lateral interactions.

Meng and Weinberg [27] used Monte Carlo simulations with quasichemical approximations for nearest-neighbours and mean-field approximations for next-nearest-neighbours. They tested various model reactions on different lattices with varying strength in lateral interactions. The results showed that for large repulsive lateral interactions, separations between peaks can occur and the difference in the peak temperatures is strongly dependent on the strength of the interaction. While small repulsive interactions result in single peak broadening rather than peak splitting.

A common challenge with using the Monte Carlo simulations is the slow computation of the diffusion steps. Makeev and Kevrekidis [28] took steps to solve this problem using a hybrid numerical approach that they referred to as Quasi-Equilibrium Kinetic Monte Carlo (QE-KMC) for modelling surface reactions. The approach uses classical Metropolis Monte Carlo simulations in combination with solving ODEs. The method was designed to more efficiently compute the much faster diffusion steps in the process.

As mentioned before Monte Carlo simulations are the popular choice but are computationally expensive. Deterministic simulations are computationally less demanding [3] and should converge to the results obtained in a Monte-Carlo type of method if all interactions are captured correctly. Van Helden et al. [31] used a deterministic approach for a simulated hydrogen TPD on Co(111) and Co(100). Lateral interactions were incorporated by a surface coverage dependent heat of adsorption. The simulated TPD was in good agreement with experimental TPD data for both surfaces.

In this section, a simplified CO adsorption model will be used investigate the effect of lateral interactions on the kinetics of the system. The model will consider adsorption of CO on the hollow site and dissociation of CO, hence we expect to see something resembling the α_2, α_3 and the β peak. The α_1 peak require additional studies around the binding states of CO at higher coverage and is beyond the scope of this project.

6.2.1 Model setup

The most stable adsorption geometry for CO on Fe (100) surface is with CO in the hollow site tilted at $\pm 45^0$ in the hollow site, shown in Figure 6-4 below. The figure shows that CO can have 4 nearest neighbours (the red squares) and 4 next nearest neighbours (the yellow squares). In Chapter 3 we have shown that CO-CO nearest neighbour interactions are strongly repulsive while next nearest neighbour interactions are negligible.

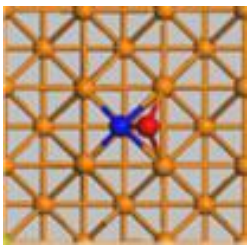

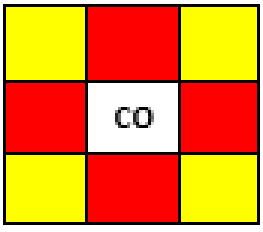

Figure 6-4: Representation of CO and its nearest-neighbour sites (in Red) and next-nearest-neighbour sites (in Yellow).

One of the most popular methods of incorporating lateral interactions into a deterministic microkinetic model is the mean field (MF) approximation [32]. The mean-field approximation uses an average lateral interaction and scales it according to the coverage. It assumes that the adsorbate distribution is completely random.

$$\overline{\mathrm{E}}_{\mathrm{x}} = \mathrm{E}_{\mathrm{x}} + \mathrm{N}_{nn} \sum \theta_{\mathrm{i}} \mathrm{E}_{\mathrm{nn}} + \mathrm{N}_{nnn} \sum \theta_{\mathrm{i}} \mathrm{E}_{\mathrm{nnn}} \qquad (6.9)$$

Here $\overline{\mathrm{E}}_{\mathrm{x}}$ is net energy of the system, E_{x} is the energy of the system without lateral interactions, N_{nn} is the number of nearest neighbours, N_{nnn} is the number of next nearest neighbours, Θ_i is the coverage of species i, E_{nn} is the interaction action energy for nearest neighbours and E_{nnn} is the interaction energy for next nearest neighbours.

Another solution is the quasi-chemical approximation (QCA) [32]. The quasi-chemical approximation best describes systems with non-random distributions. For the case of adsorbates on the surface of a metal, the non-random distribution is a function of the interaction energy. The model calculates the probability of a neighbouring site having an adsorbate with the probability being a function of the interaction energy.

An analytical solution exists for one species. The theory shows that if we consider two adjacent sites, three different scenarios exist; both sites occupied by species A, one site occupied by species A or both sites empty. The probability of each case is then calculated as:

$$\frac{P_{AA}P_{00}}{P_{A0}} = 0.25e^{\left(\frac{-E_{AA}}{k_b T}\right)} \qquad (6.10)$$

$$P_{AA} + P_{A0} + P_{00} = 1 \qquad (6.11)$$

$$2P_{AA} + P_{A0} = 2\theta_A \qquad (6.12)$$

Where P_{AA} is the probability of finding both sites occupied by species A, P_{AO} the probability of finding one site occupied by species A, P_{OO} the probability of finding both sites empty, E_{AA} the interaction energy of species A with and adjacent species A, Θ the coverage and T the temperature.

With an interaction energy of 0.12 eV, that of the CO-CO interaction, and a temperature of 600K the probabilities in Figure 6-5 are calculated. At a coverage below 0.5 ML the adsorbate will most likely have an empty site as a nearest neighbour. From 0.5 to 1 ML the probability of an adsorbate having a neighbouring adsorbate increases sharply.

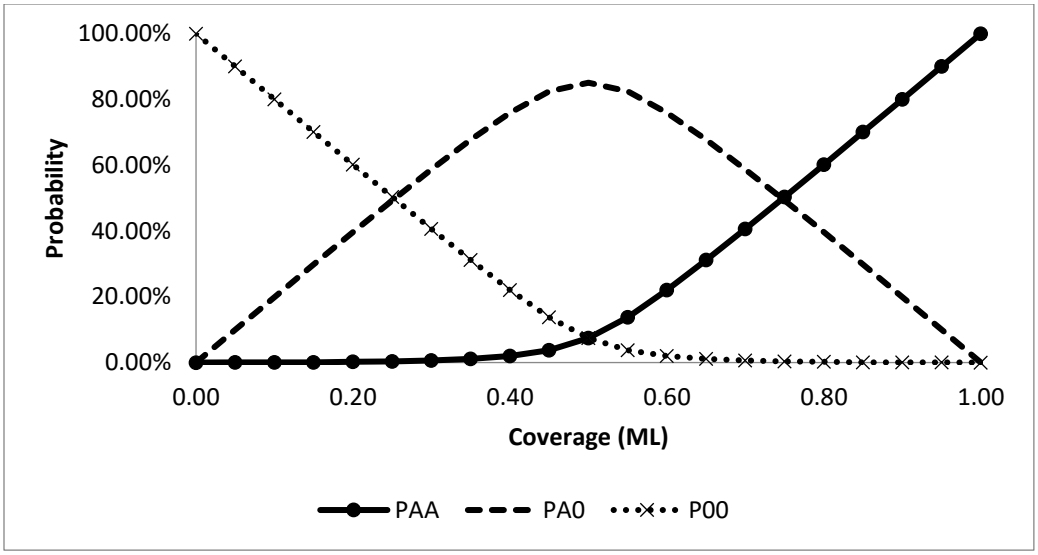

Figure 6-5: QCA for a single species adsorption showing the probability of the neighbouring site being empty or occupied.

The equation to describe the energy of the system then becomes:

$$\overline{\mathrm{E}}_{\mathrm{x}} = \mathrm{E}_{\mathrm{x}} + \mathrm{N}_{nn} \sum \mathrm{P}_{\mathrm{XYnn}} \mathrm{E}_{\mathrm{nn}} + \mathrm{N}_{nnn} \sum \mathrm{P}_{\mathrm{XYnnn}} \mathrm{E}_{\mathrm{nnn}} \qquad (6.13)$$

The nomenclature is similar to that of equation 6.9 above, with the substitution of P_{yxnn}, the probability of species being nearest neighbours and P_{yxnnn}, the probability of species being next nearest neighbours. Looking at this framework, the mean-field formulation is similar to QCA with the probability of having a species i as its neighbour or its next nearest neighbour given by the coverage of the species i.

Figure 6-6 shows the CO coverage profile for a single site approximation (No Lateral interactions), a mean field approximation and a quasichemical approximation. The mean field approximation shows a linear decrease in the heat of adsorption while the QCA approximation can be described as constant for 0 to 0.5 ML and a linear decrease from 0.5 to 1 ML.

Using the energetics from chapters 3, 4 and 5 and the methods described above, a simulated TPD model of CO on Fe (100) was created. The TPD was modelled two different ways, considering only the desorption of CO from the surface and considering both the dissociation and desorption of CO. For comparative purposes TDPs with no lateral interactions and TPDs using the mean field approximation and quasi chemical approximations were created.

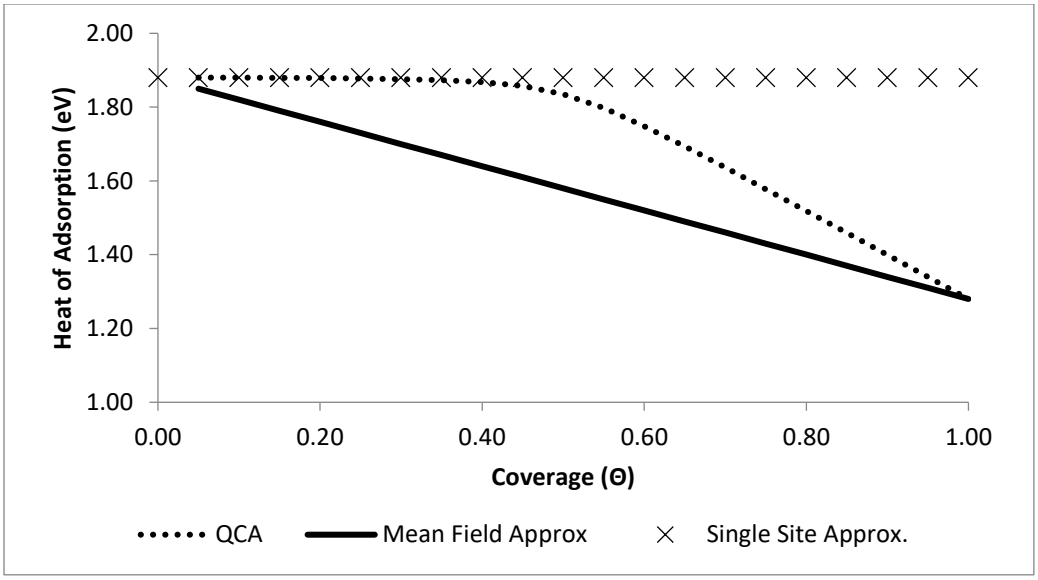

Figure 6-6: Profiles of CO adsorption energy with respect to coverage for not lateral interactions, MF and QCA.

For CO desorption only, the reaction is:

$$CO^* \rightarrow CO_{Gas} + *$$ Reaction 1

Where * is an empty site. The defining equations are then:

$$\frac{d[CO]}{dt} = r_{Deso} = k\theta_{CO} \quad (6.14)$$

$$k = \frac{k_B T}{h} e^{-\Delta G_{Rxn}(T, LI_{CO})/k_B T} \quad (6.15)$$

$$\frac{dT}{dt} = 10 \quad (6.16)$$

Equation 6.14 is the rate of desorption of CO and equation 6.15 is the rate constant for the desorption rate, where Θ_{CO} is the coverage of CO, k_B is the Boltzmann constant, h is Planck constant, LI_{CO} is the lateral interactions experience by CO adsorbates and ΔG_{Rxn} is the Gibbs free energy of reaction. Equation 6.16 is the rating rate for the experiment, 10 K/s, the same heating rate used by Moon et al. [21].

The ΔG_{Rxn} is affected by temperature (rotation, translation and vibration energies) and the lateral interactions between adsorbed CO species, which are also dependent on temperature

In order to include the dissociation of CO several additions need to be made. The first is the forward and reverse barrier for CO dissociation, Bromfield et al. [33] showed a forward barrier of 1.11 eV and a reverse barrier of 1.48 eV which is in agreement with both experimental results and other theoretical studies.

The next addition is the lateral interactions caused by the presence of C and O adsorbates. The results from the study in chapter 4 where used, with the relevant interaction data shown in Table 6-1 a) and b) below. The tables show that Nearest-neighbour interactions are large and repulsive while the Next-Nearest-Neighbour interactions vary between small and large attractive interactions.

Table 6-1: Interactions energy (eV) for species involved in a CO TPD model at 0 K + ZPE

Nearest neighbour interactions of C, O and CO

X → Y↓	CO	C	O
CO	0.12	0.15	0.13
C		0.06	0.18
O			0.09

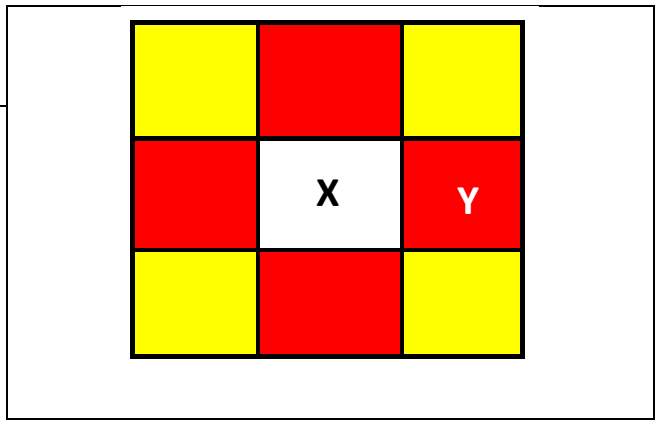

Next nearest neighbour interactions of C, O and CO

X → Z↓	CO	C	O
CO	0.00	-0.07	-0.03
C		-0.01	-0.09
O			0.00

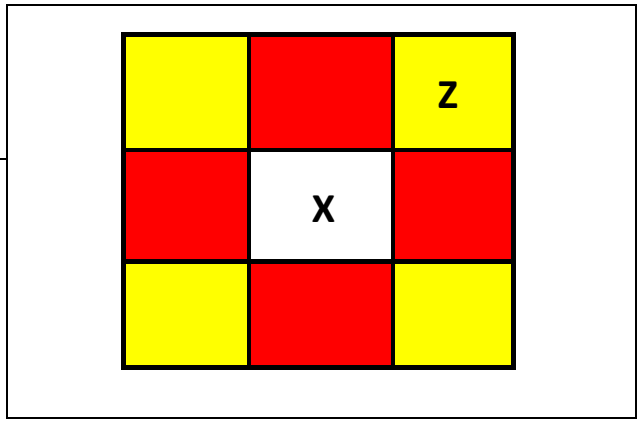

The last addition is to incorporate the effect of lateral interactions on the reaction barriers themselves. For this we will use an approximation aided by Hammond's postulate.

The reactions are then:

$$CO^* \rightarrow CO_{Gas} + *$$ Reaction 1

$$CO^* + * \rightarrow C^* + O^*$$ Reaction 2

Desorption kinetics

$$r_{Deso.} = k_1 \theta_{CO} \quad (6.17)$$

$$k_1 = \frac{k_B T}{h} e^{-\Delta G_{Rxn1}(T,LI)/k_B T} \quad (6.18)$$

Dissociation kinetics

$$r_{Diss} = k_2 (\theta_* \theta_{CO} - {}^{\theta_C \theta_C}/_{K_{e2}}) \quad (6.19)$$

$$k_2 = \frac{k_B T}{h} e^{-eb_2^f / k_B T} \quad (6.20)$$

$$Ke_2 = \prod Q_{v_i} Q_{T_i} Q_{R_i} \, e^{-(eb_2^f - eb_2^r)/k_B T} \quad (6.21)$$

$$eb^f = eb^{f0} \quad (6.22)$$

$$eb^r = eb^{r0} + (LI_{React.} - LI_{Prod.}) \quad (6.23)$$

Where * is an empty site. Then defining equations are then:

$$\frac{d\theta_{CO}}{dt} = r_{CO} = -(r_{Deso.} + r_{Diss.}) \quad (6.24)$$

$$\frac{d\theta_C}{dt} = \frac{d\theta_O}{dt} = r_{Diss} \quad (6.25)$$

$$\frac{dT}{dt} = 10 \quad (6.26)$$

Equation 6.24 is the reaction rate of CO formation, since both desorption and dissociation consume CO. Equation 6.17 is the rate of desorption of adsorbed CO and equation 6.18 is the rate constant for the desorption, where Θ_{CO} is the coverage of CO, k_B is the Boltzmann constant, h is Planck constant, LI is the lateral interaction and ΔG_{Rxn} is the Gibbs free energy of reaction. The ΔG_{Rxn} is affected by temperature (rotation, translation and vibration energies) and the lateral interactions of the reactants and products i.e. the change in the Gibbs free energy upon desorption. For this case, the reactant is CO adsorbed and the product is CO in the gas phase. There would be no lateral interactions for CO in the gas phase, thus the lateral interactions experienced by adsorbed CO is what influences the equation. Equation 6.26 is the heating rate for the experiment, 10 K/s.

To simulate the TPD we will record the rate of desorption as a function time. Differential equation for each surface species were setup for the different methods and different scenarios. The differential equations were then solved with ode23 solver [34], as recommended for stiff ode's as part of the MatLab [35] package. The initial temperature was set to 150 K which was increased linearly with a heating rate equal to 10K/s up to 950 K.

In addition to recording the rate at which CO is desorbing from the surface, the coverage profiles and the lateral interactions at each point were recorded. The lateral interactions in conjunction with temperature can be used to determine how the reaction energies are changing with time. The energy profiles are relative to CO adsorbed on the surface. The energy profile at 150 K in the absence of lateral interaction is shown in Figure 6-7.

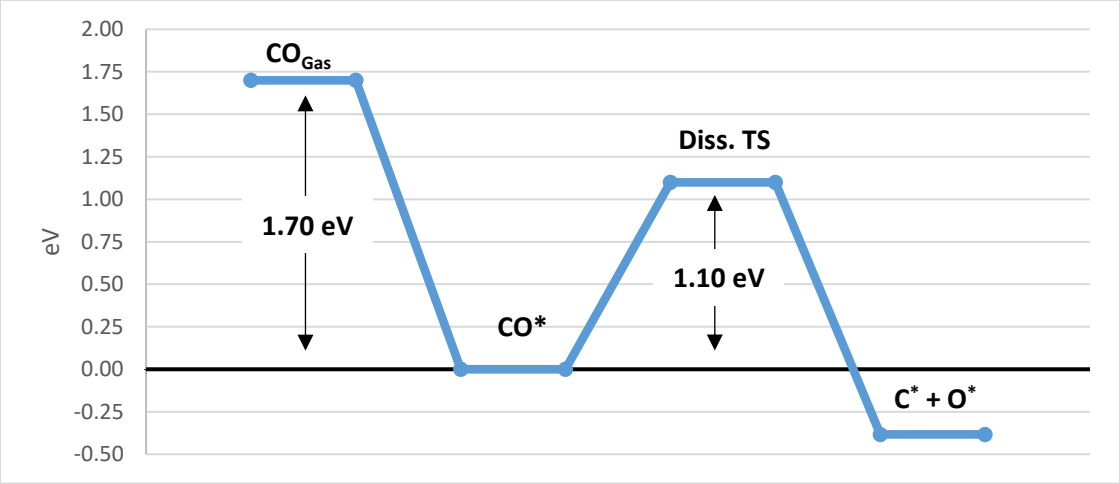

Figure 6-7: Energy profile of CO adsorption and Dissociation with no lateral interactions at 150 K

6.2.2 Results and discussion

This study will show how lateral interactions can allow for CO desorption at lower temperatures by comparing the obtained TPD-spectrum without any lateral interaction, the inclusion of lateral interaction in a mean-field model (see eq. 6.9) and using the quasi-chemical interaction (see eq. 6.13). The full Monte Carlo simulation was attempted using the Zacros package developed by Neilsen et al. [36], but was computationally very expensive in particular due to the low energy barrier for diffusion ($\Delta G_{Diff} \leq 0.3$ eV), which necessitated a large number of step in the Monte Carlo simulation. Hence, studies reporting Monte Carlo simulations often include an equilibration step to side-step the inclusion of the diffusion step [28].

The impact of lateral interaction will be first discussed considering only CO desorption (i.e. in the absence of CO dissociation). This will be followed by the TPD spectra obtained including the possibility of CO-dissociation

The coverages of CO, C, O and the empty sites for each starting coverage and each lateral interaction implementation method are shown. The change in the heat of adsorption and changes in ΔG_{Rxn} for CO dissociation with regard to time, and hence temperature is shown for each coverage and lateral interaction implementation method.

6.2.2.1 Desorption only

When only the desorption of CO is considered (i.e. in the absence of CO dissociation), the simulated TPD shows only one peak, the α_3 peak shown by Moon et al. [21], which has the highest intensity at 440 K. In this case, in the absence of lateral interactions and CO dissociation, the peak maximum is 500K.

As the coverage increases the lateral interactions increase and this affects the rates significantly. If the heat of adsorption[23] is decreased by 0.12 eV, the approximate lateral interaction of a CO-CO nearest neighbour interaction, the rate constant is approximately 50 times larger at 400K than when no interactions are considered. Similarly, at 1 ML the interaction energy is 0.48 eV and the rate constant is approximately 800 000 times larger than when no interactions are considered, see equations 6.17 and 6.18.

In the absence of lateral interactions, the TPD spectra shows the desorption peak in the CO-TPD spectrum, the α peak, at 500K, Figure 6-8. When analysing the spectrum the 'broadness' of the peaks is characterised

[23] The heat of adsorption is the activation energy for the desorption process (for a non-activated adsorption process).

in terms of the 2nd moment of the rate distribution (and skewness in terms of the 3rd moment). In Figure 6-8 the broadness of the peak is narrow and remains fairly constant while the intensity of the peak increases with increasing coverage. This is to be expected as the binding energy remains unchanged.

For the mean field approximation, the α peak broadens, from 320 to 500K, with increasing coverage and the intensity remains fairly constant, Figure 6-9. The broadness of the peak appears to change proportionally to the coverage. This is a result of the linear decrease in energy.

Finally, the quasi-chemical method (QCA) predicts an intense a peak at 500K with a pre-edge ranging down to 320K for the TPD-spectrum with an initial coverage of 1 ML, Figure 6-10. The distortion in the shape of the peak is a result of non-random distributions of CO on the Fe (100) surface. At lower coverages (below 0.5 ML), the CO adsorbates will prefer configurations with negligible lateral interactions. At higher coverages (above 0.5 ML) however, the lateral interactions are unavoidable. Hence, we see severe distortion in the 0.6, 0.8 and 1ML.

The change in the heat of adsorption is evident for the mean field approximation and the quasi-chemical approximation. The lateral interactions lower the binding energy of CO to the Fe (100) surface and hence show appreciable rates at lower temperatures.

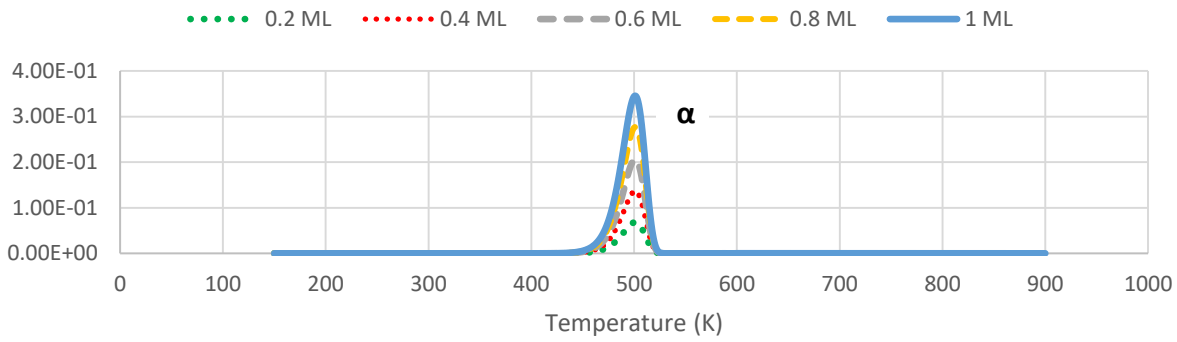

Figure 6-8: TPD spectrum for CO desorption only system with no lateral interaction.

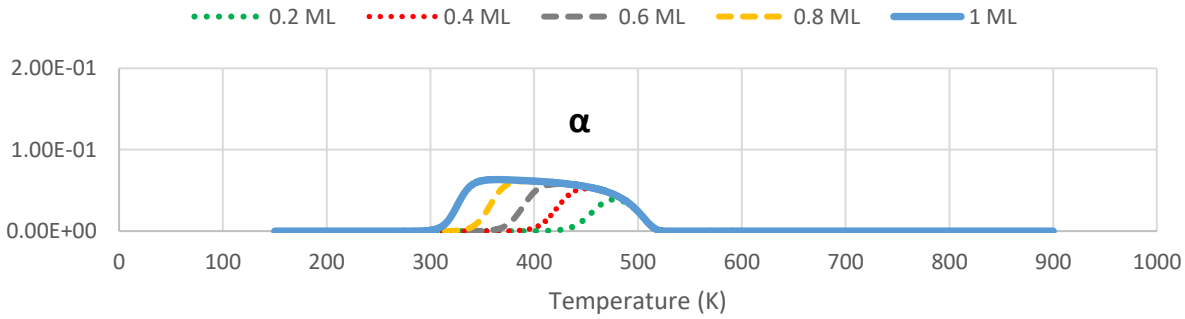

Figure 6-9: TPD spectrum for CO desorption only system with a mean field approximation for the lateral interactions.

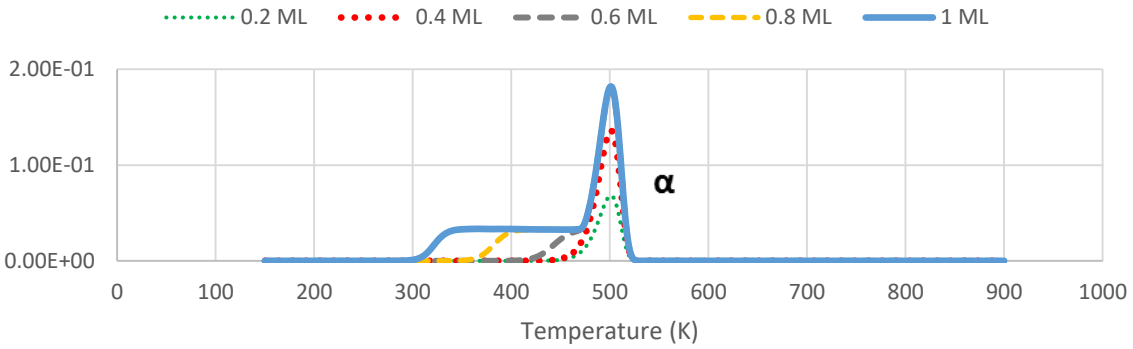

Figure 6-10: TPD spectrum for CO desorption only system with a quasi-chemical approximation for the lateral interactions.

Lateral interactions lower the binding energy of CO and CO is able to desorb at lower temperatures. Once the CO adsorbates start desorbing, the interaction energy will be reduced, since the interaction energy decreases with decreasing coverage, and the binding energy will increase. Furthermore. the vibrational, rotational and translational Gibbs free contributions (temperature corrections) decrease the heat of adsorption by approximately 0.12 eV/ 100K. It is almost as if the decrease in interaction energy is balanced by the temperature corrections. This is evident in the mean field TPD since the rate of desorption remains rather constant over a wide temperature range. For the QCA TPD, the lateral interactions cause a broad pre-shoulder for 0.6, 0.8 and 1ML which extends till 320 K for 1ML. The 0.4 ML and 0.2 ML spectra for the QCA system is almost identical to the no lateral interaction spectra for 0.4 ML and 0.2 ML.

The figures above have shown that lateral interactions can alter the appearance of the TPD spectra significantly. If little is understood about the lateral interactions of a system, TPD-data can be interpreted incorrectly. A pre-shoulder is indicative for the presence of strong lateral interactions and not necessarily due to presence of adsorbed species on different sites.

6.2.2.2 *Desorption and Dissociation*

When both CO desorption and CO dissociation are considered, it is expected that 2 peaks would be visible, the α_3 peak and β peak shown by Moon et al. [21]. The dissociation of CO has an early barrier, this means that, using the Hammond's postulate approximation, the reverse barrier is affected by the lateral interactions of the system. All the interactions for CO, C and O are considered, as shown in Table 6-1. The TPD spectra with all the coverages considered will be discussed first for each method. Each starting coverage with its coverage profiles and energy profiles will be discussed in subsections below.

For the system with no lateral interactions (NL) there is an α peak at 500 K and β peak at 630 K, Figure 6-11. For this scenario, the heat of adsorption and the barriers for the dissociation are unaffected by lateral interactions and only influenced by temperature. For both peaks the intensity of the peaks increase as the coverage increases, while the β peak broadens more than the α peak with increasing coverage, indicative of a reaction with a large barrier. The peak maximum of the β peak shifts from 650 K at 0.2 ML to 630 K at a CO coverage above 0.8 ML.

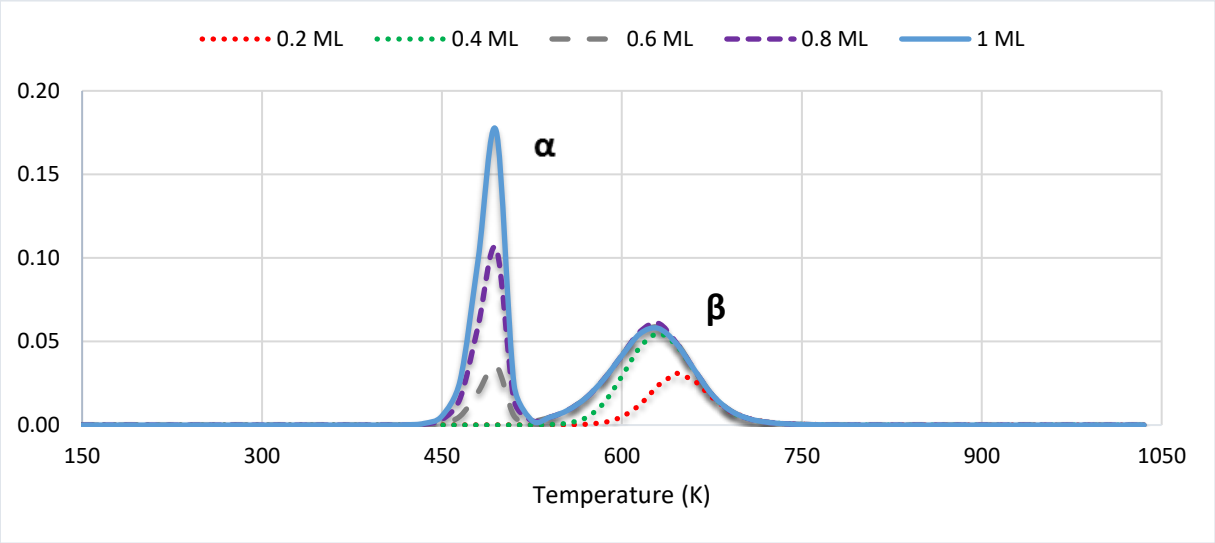

Figure 6-11: TPD spectrum for CO desorption and dissociation in the absence of lateral interaction.

Using the mean field (MF) approximations to incorporate lateral interactions, the α peak shifts to 390 K and β peak shifts to 640 K, Figure 6-12. For this scenario, the heat of adsorption and the reverse barrier of CO dissociation are influenced by lateral interactions. A small α peak is visible for 0.4 ML while larger α peaks can be seen for 0.6, 0.8 and 1 ML coverages. The maximum intensity shifts to a higher temperature for lower coverage i.e. at 0.6 ML the peak is most intense at 403K while for 1 ML the peak is most intense at 390 K. The α peak at 1 ML has a prominent early shoulder. As the coverage increases the lateral interactions are increased. Furthermore, CO dissociates to atomic C and O, each occupying a hollow site, further increasing the overall coverage and lateral interaction. The 0.2 ML system shows only a small β peak at 640 K. The β peak at 640 K increases in intensity with increasing coverage but the broadness remains constant for all coverages.

Using the quasi-chemical approximation (QCA) to incorporate lateral interactions there is an α peak at 420 K and β peak at 600 K, Figure 6-13. For this scenario, the heat of adsorption and the reverse barrier of CO dissociation are influenced by lateral interactions. The α peak appears for 0.6, 0.8 and 1 ML coverages each showing unique profiles, similar to the mean field approximation. The 1 ML spectra is most intense at 420K and has shoulders on both sides of the peak. For 0.8 ML spectra, the peak is most

intense at 420 K with a late shoulder while for 0.6 ML the peak is broad most intense at 470 K. Like the mean field approximation, the 0.2 ML system shows only a small β peak at 640 K. The β peak at 600 K increases in intensity with increasing coverage but the broadness remains constant for all coverages, except for 0.4 ML which shows an early peak at 590K.

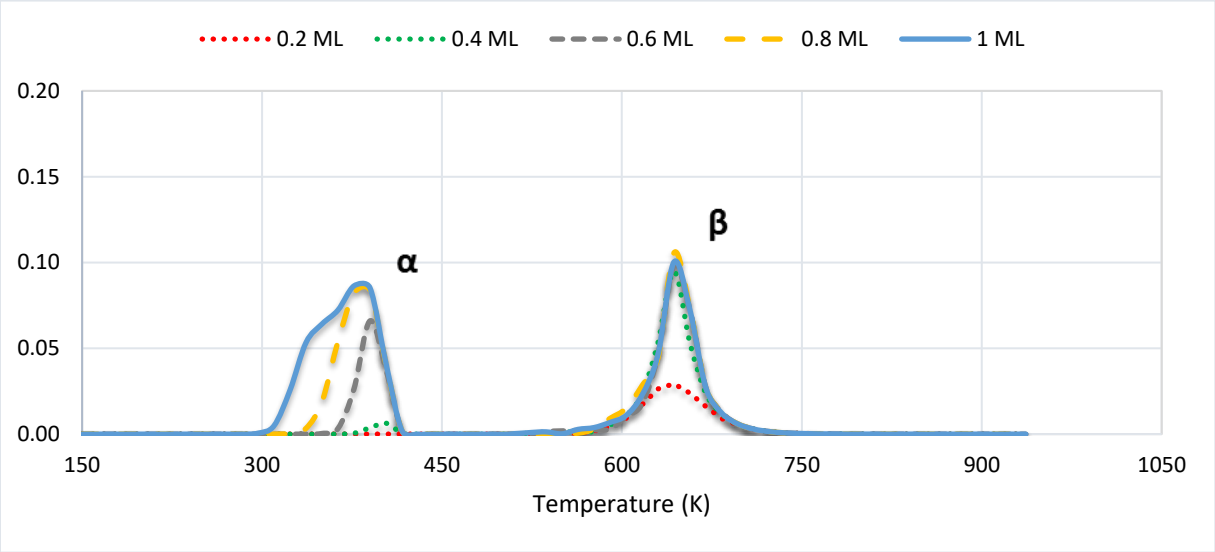

Figure 6-12: TPD spectrum for CO desorption and dissociation with a mean field approximation for the lateral interactions.

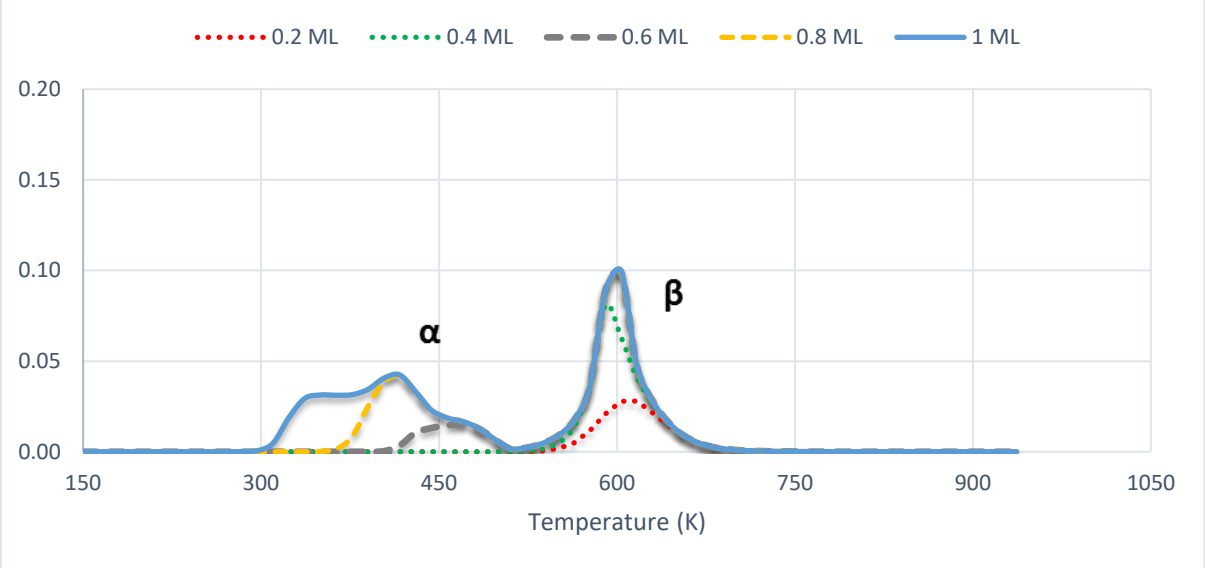

Figure 6-13: TPD spectrum for CO desorption and dissociation with a quasi-chemical approximation for the lateral interactions.

6.2.2.2.1 Starting coverage of 0.2ML

The 0.2 ML systems will have the lowest lateral interactions of all the scenarios considered. The coverage profiles in Figure 6-15 are very similar for all three systems. CO dissociates at about 350 K and CO is only desorbed later. Since all the CO dissociates, there is no α peak. Once all the CO dissociates, the maximum

coverage is 0.4 ML, 0.2 ML C and 0.2 ML O. The dissociation is favoured as it has a lower, and hence more favourable, reaction barrier.

The Gibbs free energy for the adsorption/desorption of CO and the subsequent dissociation energy profiles in Figure 6-15 show that the forward barrier of the dissociation reaction is smaller than the Gibbs free energy of desorption for 350K and 430 K, hence the dissociation reaction is favoured. For 630 K, the Gibbs free energy of desorption is less than the forward barrier of the dissociation reaction and hence the desorption reaction is favoured. The temperature is also large enough to overcome the recombination barrier.

The Gibbs free energy of adsorption profile, Figure 6-16, shows that the mean field approximation deviates positively about 0.2 eV from the NL system. The QCA approximation shows a negligible change in the heat of adsorption.

The Gibbs free energy of reaction for CO dissociation Figure 6-17, shows that the mean field approximation initially has a small deviation of 0.05 eV, but once the CO starts to dissociate, at about 350 K the deviation increases to 0.18 eV. The profile obtained using the quasi-chemical approach (QCA) is similar to the one obtained neglecting lateral interaction (NL) system until CO dissociates at 360 K, the profile deviates negatively by approximately 0.05 eV from the NL system. While this deviation for the QCA system appear small at first, the result of the lateral interactions is a lower β peak, 620K, than that of the mean field and NL systems, 640K. Figure 6-14 shows configurations with next nearest neighbour interactions are strongly favoured with QCA since they are attractive interactions while the nearest neighbour interactions are repulsive.

The deviations from the NL system are a result of C and O each occupying a hollow site, and thus increasing the lateral interactions of the system. The Gibbs free energy of reaction shows unique deviations since the difference between the interactions of the product and reacts are considered.

a) Attractive NNN interactions b) Repulsive NN interactions

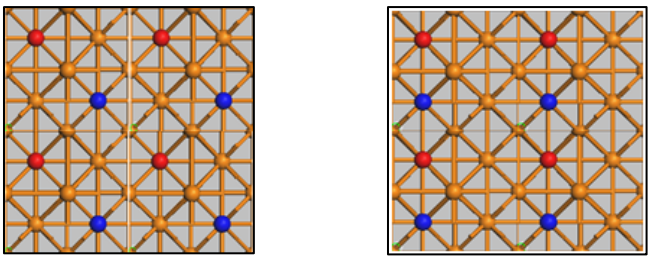

Figure 6-14: Attractive next nearest neighbour interactions and repulsive nearest neighbour interactions

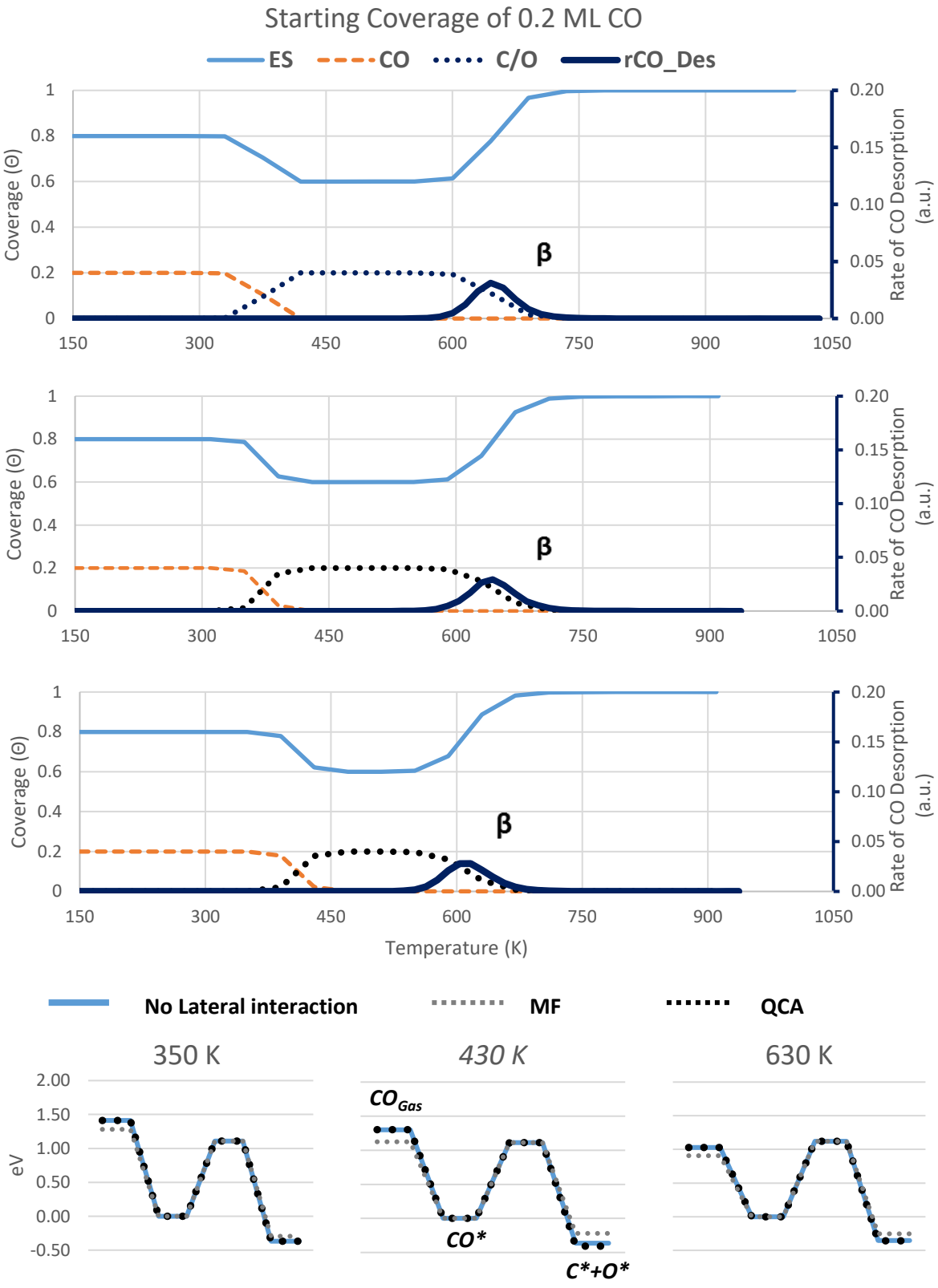

Figure 6-15: Coverage profiles, TPD spectrum and Gibbs free energy profiles for CO TPD with a starting coverage of 0.2 ML

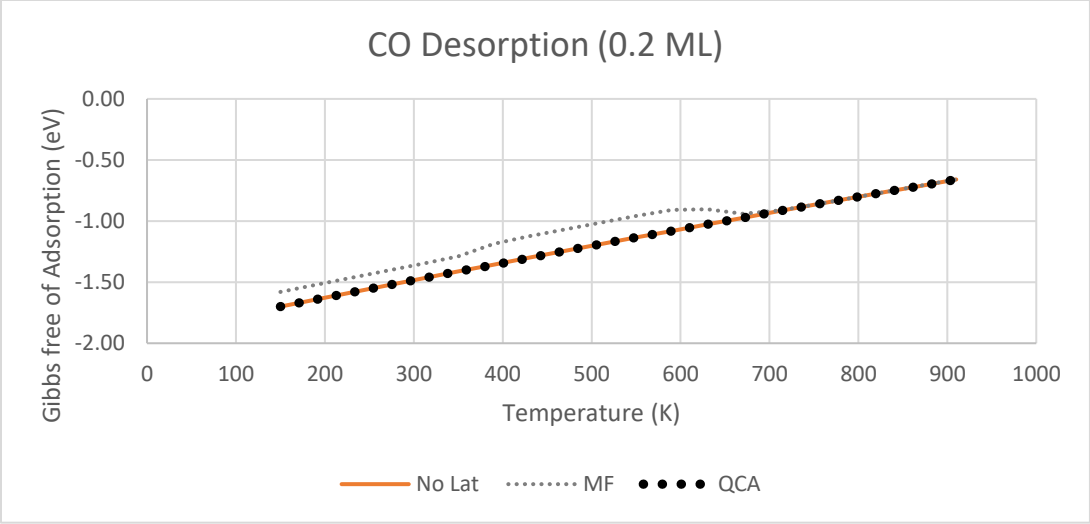

Figure 6-16: Heat of adsorption profiles for starting coverage of 0.2 ML

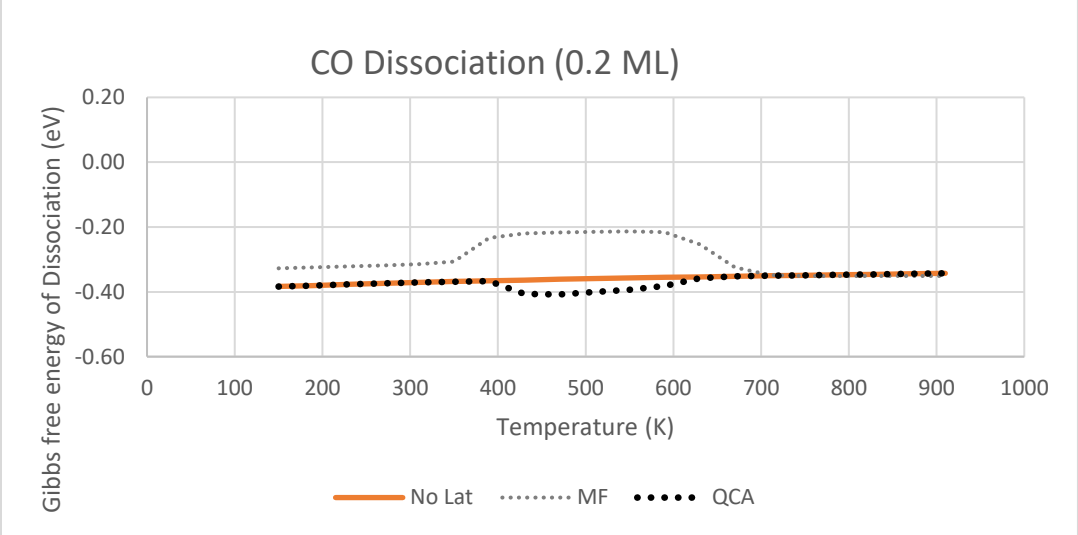

Figure 6-17: Gibbs free energy of CO Dissociation for starting coverage of 0.2 ML

6.2.2.2.2 Starting coverage of 0.4ML

The 0.4 ML systems will have the second lowest lateral interactions of all the scenarios considered. The coverage profiles in

Figure 6-18 are again very similar for all three systems. The NL has a β peak at 645 K, and mean field systems has a β peak at 630 K while the QCA system has a β peak at 590 K. For the QCA and NL systems, all the CO dissociates at about 350 K and CO is only desorbed later. The mean field system however shows a small α peak at 390 K.

The CO dissociates and for the QCA and NL systems, the C and O each reach a coverage of 0.4 ML, making the overall coverage 0.8 ML. The mean field system shows an overall coverage of 0.75 ML as a small amount of CO desorbed. The desorption is a result of mean field interactions being large enough to lower the binding energy of CO and increase the rate constant of desorption and create an appreciable rate, shown by the small α peak at 390 K.

Figure 6-18 show that the forward barrier of the dissociation reaction is smaller than the heat of desorption for 350K and 430 K, hence the dissociation reaction is favoured. For 630 K, the heat of desorption is less than the forward barrier of the dissociation reaction and hence the desorption reaction is favoured. The temperature is also large enough to overcome the recombination barrier. The mean field approximations significantly lower the heat of desorption, hence the small desorption displayed.

The Gibbs free energy of adsorption profile, Figure 6-19, shows that the mean field approximation deviates positively about 0.3 eV from the NL system. The QCA approximation again shows a negligible change in the heat of adsorption.

The Gibbs of reaction profile for CO dissociation, Figure 6-20, shows that the mean field approximation initially has a deviation of 0.12 eV, but once the CO starts to dissociate, at about 350 K the deviation increases to 0.3 eV. The QCA profile is similar to the NL system and only starts to deviate positively at 470 K, when the overall coverage is highest at 0.8ML.

The deviations for the QCA system again shows a lower β peak than the mean field and NL systems. The deviations were large enough to force early recombination desorption. This resulting from QCA favouring configurations with more NNN interactions than NN interactions. The mean field approximation assumes that there is an average split of NNN interactions and NN interactions. Since the NN interactions are larger and repulsive, the interactions energy will be repulsive.

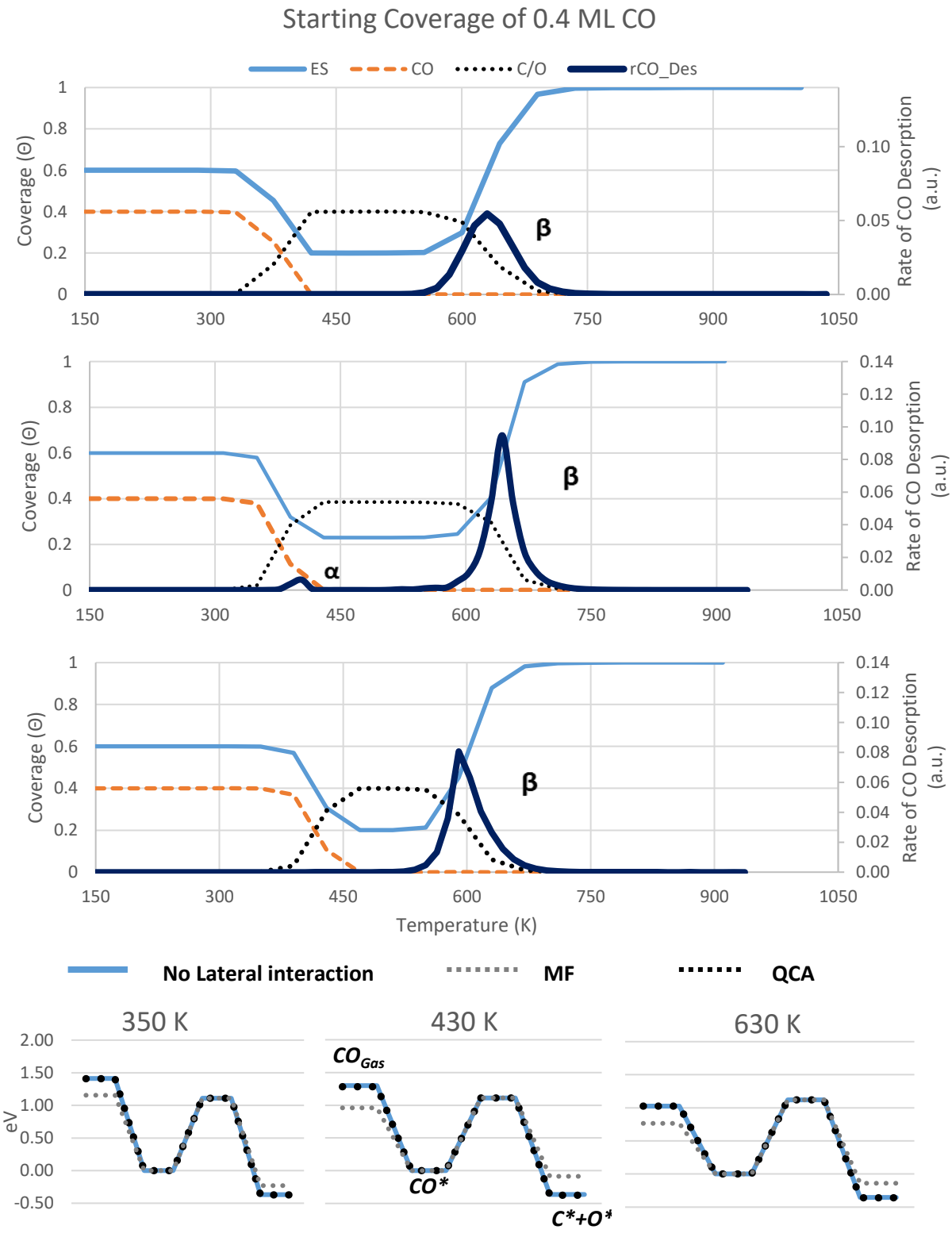

Figure 6-18: Coverage profiles, TPD spectrum and Gibbs free energy profiles for CO TPD with a starting coverage of 0.4 ML

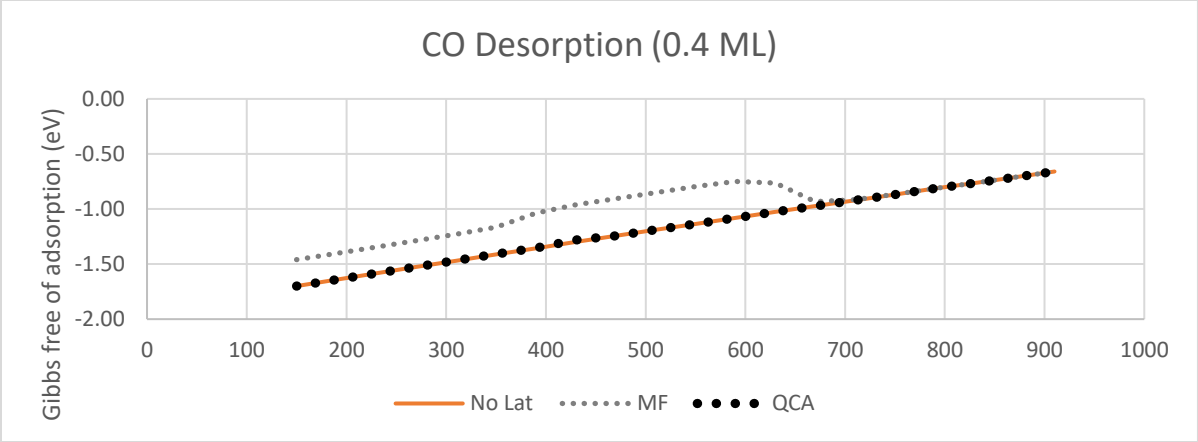

Figure 6-19: Gibbs free energy of adsorption profiles for starting coverage of 0.4 ML

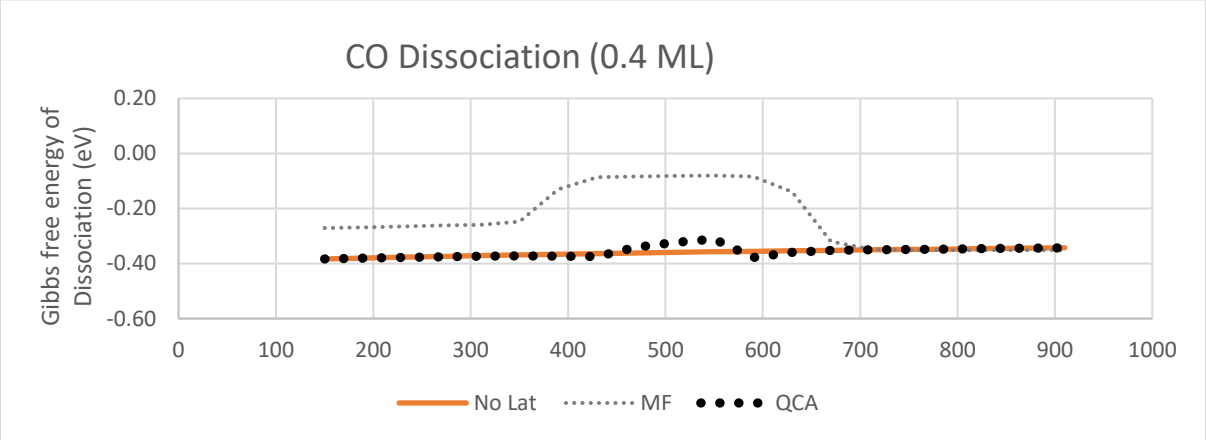

Figure 6-20: Gibbs free energy of CO Dissociation for starting coverage of 0.4 ML

6.2.2.2.3 Starting coverage of 0.6ML

The 0.6 ML systems can be considered as a midpoint of the coverages concerned. All three systems have an α and β peak. The profiles in Figure 6-21 show that the NL has a small but sharp α peak at 495 K and a broad β peak at 630 K. CO starts dissociating at 330 K until the surface is saturated at 1 ML at 400K. Only at 460 K does some of the remaining CO start desorbing while some dissociates to C and O. The maximum dissociation coverage reached is 0.5 ML for C and O

The mean field approximation has a sharp α peak at 390 K and a β peak at 643 K. CO starts dissociating at 350 K and soon after at 360 K also starts desorbing. The β starts showing a small shoulder at 500 K and starts growing fast at 590 K. The maximum dissociation coverage reached is 0.42 ML for C and O

The QCA has a small broad α peak at 470 K and a β peak at 603 K. Like the mean field approximation CO starts dissociating at 350 K and soon after at 400 K also starts desorbing. The result of desorption occurring later is a maximum dissociation coverage reached is 0.5 ML for C and O. The β starts immediately after the α peak at 530 K.

The Energy profiles in Figure 6-21 show that the forward barrier of the dissociation reaction is smaller than the heat of desorption for 350K and 430 K, hence the dissociation reaction is favoured. For 630 K, the heat of desorption is less than the forward barrier of the dissociation reaction and hence the desorption reaction is favoured. The mean field approximations show significant deviations for both the heat of adsorption and recombination barrier. The QCA approximation also shows deviations at 430 K.

The Gibbs free energy of adsorption profile, Figure 6-22, shows that the mean field approximation deviates positively approximately 0.35 eV from the NL system. The QCA approximation shows a gradual build to a positive deviation of 0.15 eV at 430 K.

The Gibbs of reaction profile for CO dissociation Figure 6-23, shows that the mean field approximation initially has a deviation of 0.15 eV, but once the CO starts to dissociate, at about 350 K the deviation increases to 0.35 eV. The QCA profile starts at the same point as the NL system and slowly starts decreasing to -0.10 eV at 470 K. The energy starts changing positively until a deviation of 0.1 eV at 550 K and moves back to the NL energy.

The deviations for the QCA system again shows a lower β peak than the mean field and NL systems. The deviations were large enough to force early recombination desorption. This resulting from QCA favouring configurations with more NNN interactions than NN interactions. The mean field approximation assumes that there is an average split of NNN interactions and NN interactions. Since the NN interactions are larger and repulsive, the interactions energy will be repulsive. The QCA method would also favour CO-O and CO-C NNN interactions as they are attractive interactions. For this reason, the β peak is earlier.

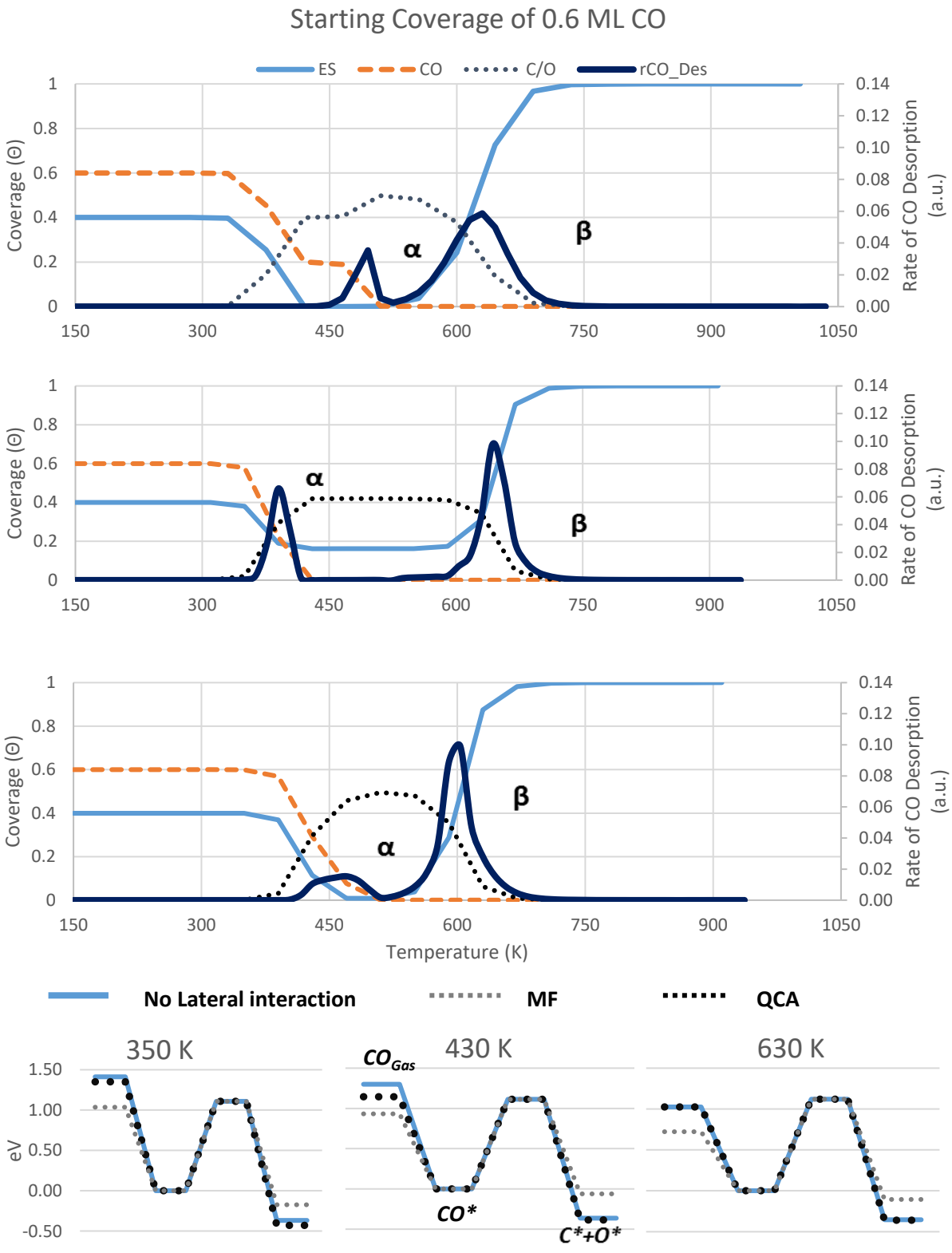

Figure 6-21: Coverage profiles, TPD spectrum and energy profiles for CO TPD with a starting coverage of 0.6 ML

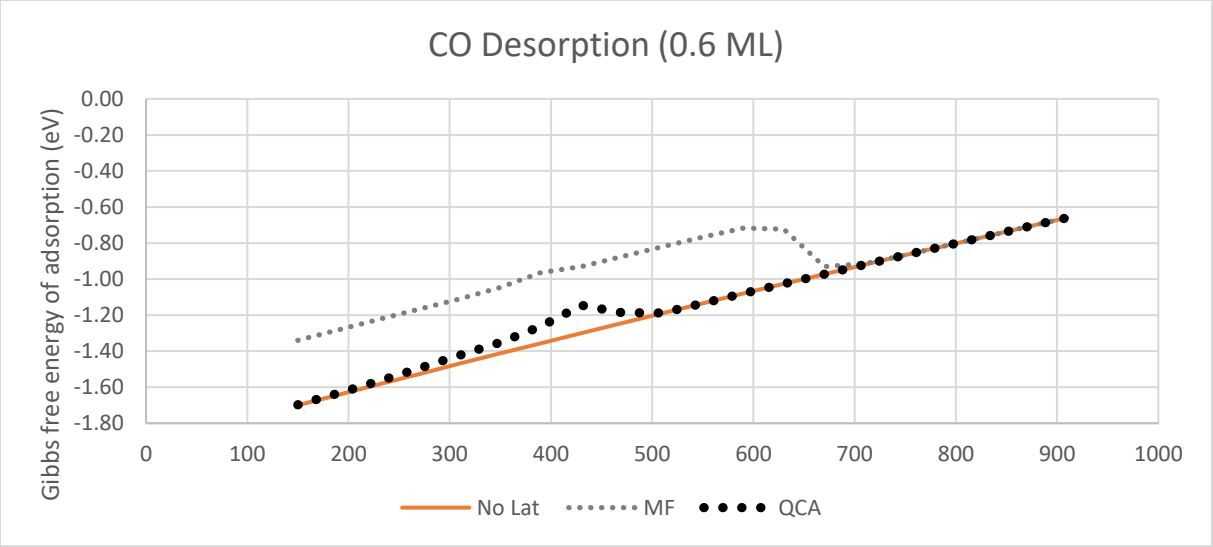

Figure 6-22: Gibbs free energy of adsorption for starting coverage of 0.6 ML

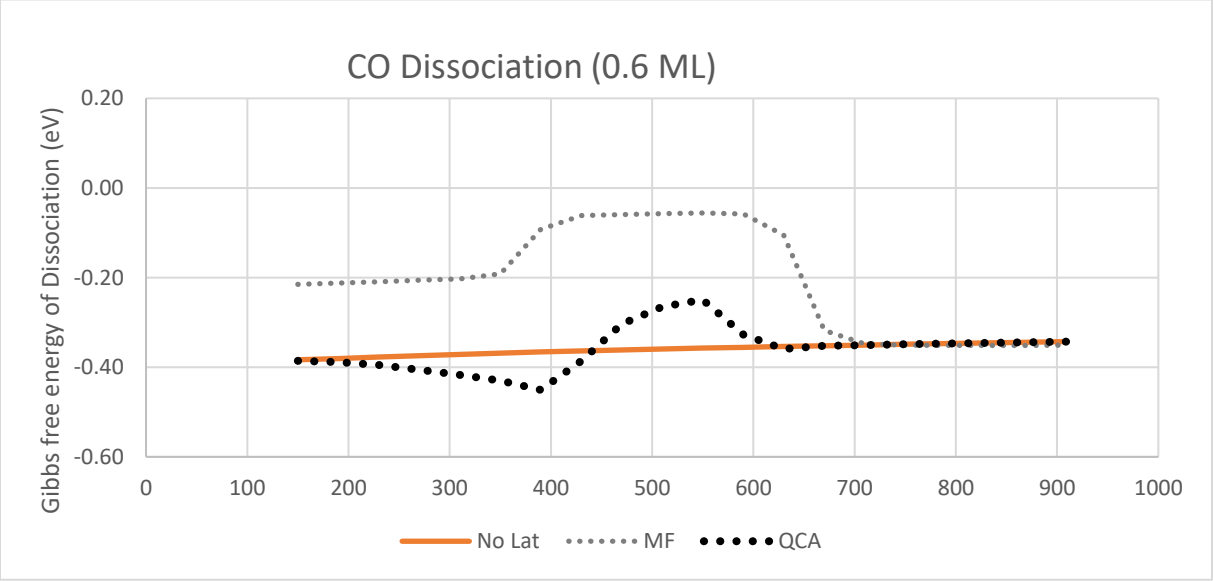

Figure 6-23: Gibbs free energy of CO Dissociation for starting coverage of 0.6 ML

6.2.2.2.4 Starting coverage of 0.8ML

The 0.8 ML systems have the 2nd most lateral interactions of the coverages considered. All three systems have an α and β peak. From the profiles in Figure 6-24 the NL has a large sharp α peak at 495 K and a broad β peak at 630 K. CO starts dissociating at 330 K and the rate of dissociation slows down as the maximum coverage of 1 ML is reach. CO starts desorbing at 430 K and more sites become available for CO dissociation. The β peak starts immediately after the α peak at 530 K.

The mean field approximation has a large α peak at 390 K and a β peak at 643 K. CO starts dissociating and desorbing at 350 K. The β peak starts showing a pronounced pre-shoulder at 550 K and starts growing fast at 610 K. The maximum dissociation coverage reached is 0.42 ML for C and O

The QCA has an α peak at 420 K with a trailing post-shoulder and a β peak at 603 K. Like the mean field approximation dissociating and desorbing at 350 K. The α peak is broader and allows the dissociation reaction to take preference hence the maximum dissociation coverage reached is 0.5 ML for C and O. The β peak starts immediately after the α peak at 530 K.

The for the NL Energy profiles in Figure 6-24 show that the forward barrier of the dissociation reaction is smaller than the heat of desorption for 350K and 430 K, hence the dissociation reaction is favoured. For 630 K, the feat of desorption is less than the forward barrier of the dissociation reaction and hence the desorption reaction is favoured. For the mean field energy profiles, the heat of adsorption is always less than the forward dissociation barrier. For this reason, both α and β peaks are large. For the QCA energy profiles, the heat of adsorption and the forward dissociation barrier are approximately of equal magnitude for all three instances. The reverse dissociation barrier is increased at 350 K and 430 K making it harder for C and O to recombine.

The Gibbs free energy of adsorption profile, Figure 6-25, shows that the mean field approximation deviates positively about 0.4 eV from the NL system. At 400 K, this deviation is deceased to 0.35 eV. The QCA starts with a positive deviation of 0.15 eV and begins to return to the NL profile after 400K.

The Gibbs of reaction profile for CO dissociation, Figure 6-26, shows that the mean field approximation initially has a deviation of 0.25 eV, but once the CO starts to dissociate, at about 350 K the deviation increases to 0.3 eV. The QCA profile shows an initial deviation of -0.12 eV and slowly starts decreasing till -0.30 eV at 370 K. The energy starts changing positively until a deviation of 0.1 eV at 550 K and moves back to the NL energy.

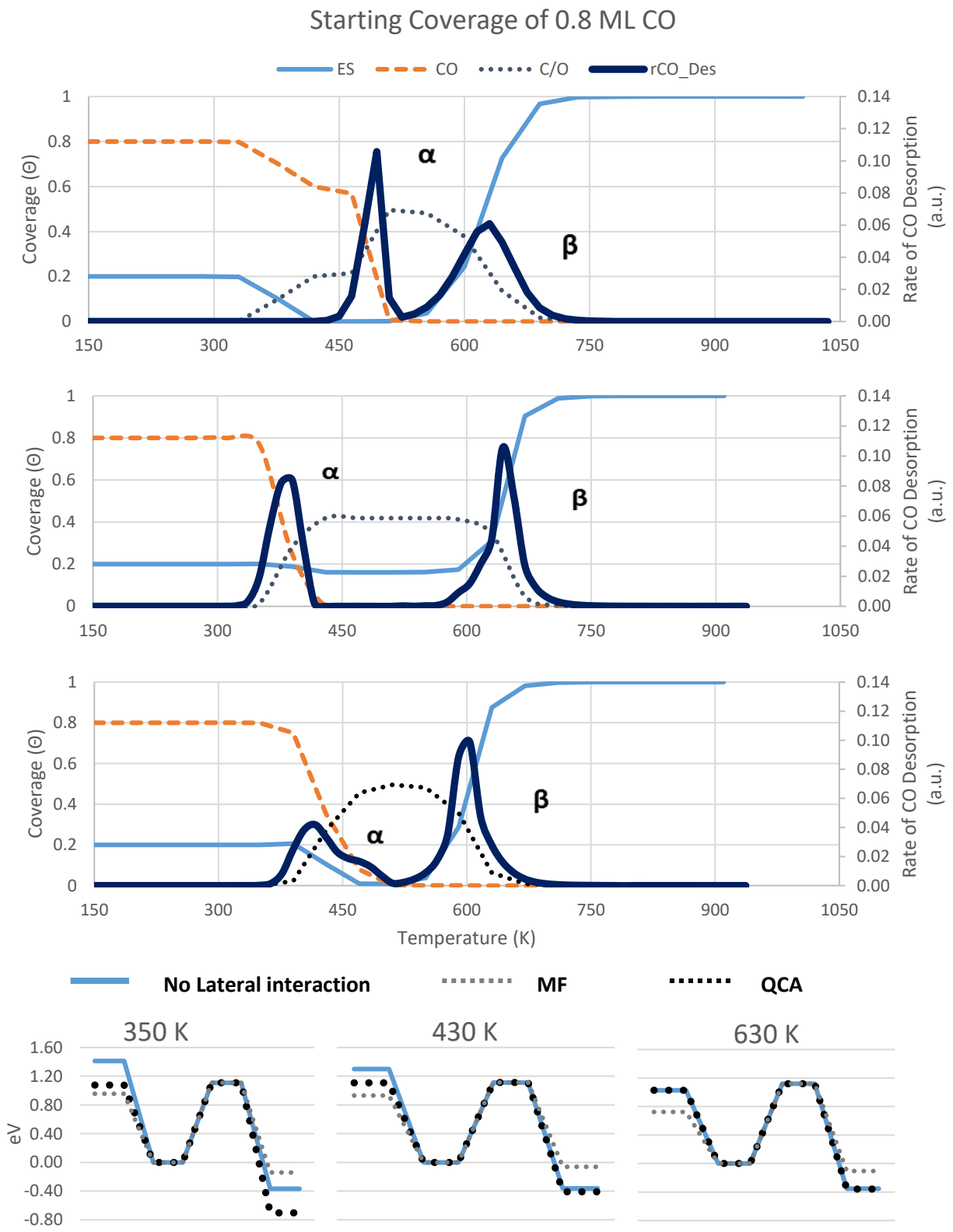

Figure 6-24: Coverage profiles, TPD spectrum and Gibbs free energy profiles for CO TPD with a starting coverage of 0.8 ML

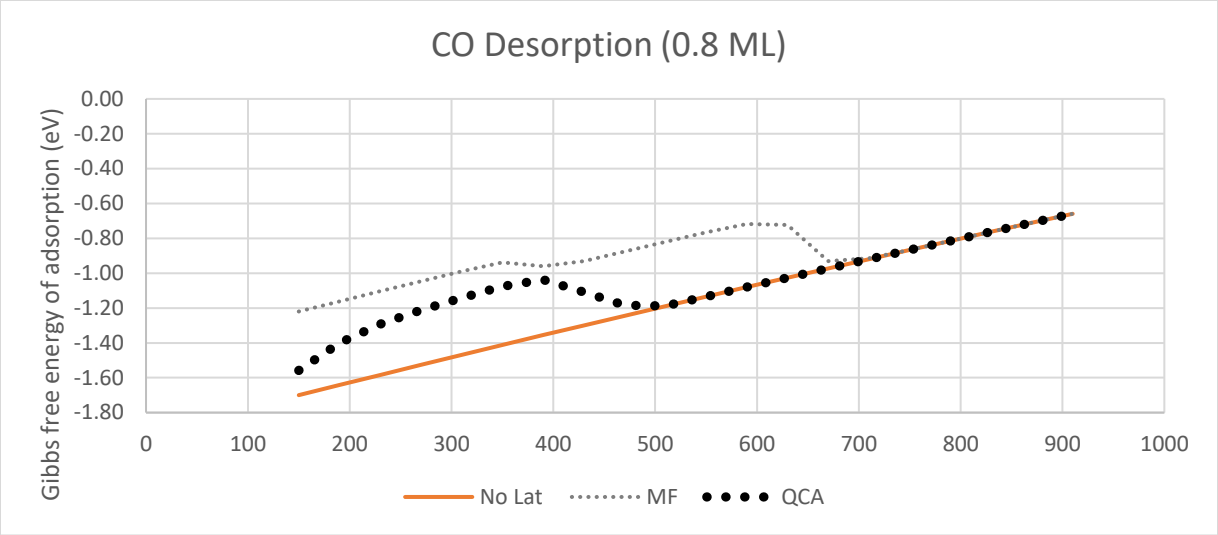

Figure 6-25: Gibbs free energy of adsorption profiles for starting coverage of 0.8 ML

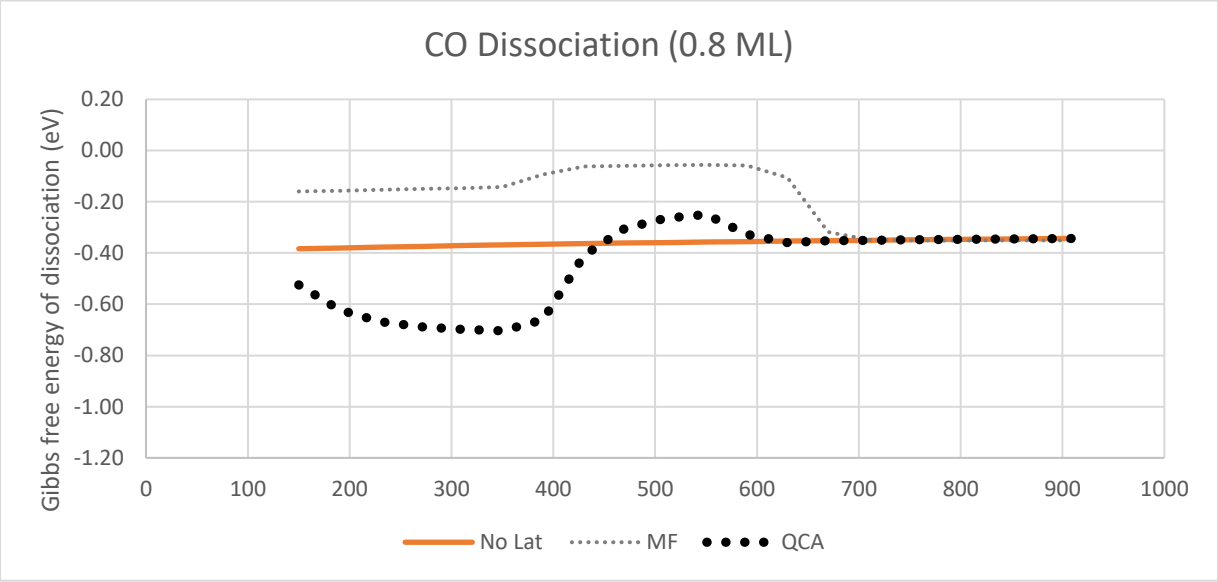

Figure 6-26: Gibbs free energy of CO Dissociation for starting coverage of 0.8 ML

6.2.2.2.5 Starting coverage of 1ML

The 1 ML systems have the most lateral interactions of the coverages considered. All three systems have an α and β peak. For all three systems CO only starts dissociating once some of the CO has desorbed and sites are available for dissociation. From the profiles in Figure 6-27 the NL has a large sharp α peak at 495 K and a broad β peak at 630 K. The initial CO desorption occurs at 440 K. The β peak starts immediately after the α peak at 530 K.

The mean field approximation has a large α peak at 390 K with a pre-shoulder and a β peak at 643 K. CO starts desorbing at 310 K. The initial CO dissociation occurs at 390 K and cause the α peak to increase further. The β peak starts showing a small appreciable rate at 550 K and starts growing fast at 610 K. The maximum dissociation coverage reached is 0.42 ML for C and O

The QCA has an α peak at 420 K with a significant pre-shoulder starting at 330 K and a trailing post-shoulder and a β peak at 603 K. The rate of desorption for the α peak pre-shoulder plateaus until dissociation starts at 390K. This like the mean field approximation, also increases the rate of desorption. The β peak starts immediately after the α peak at 530 K.

For the NL Energy profiles in Figure 6-27 show that the forward barrier of the dissociation reaction is smaller than the heat of desorption for 350K and 430 K, hence the dissociation reaction is favoured. For 630 K, the feat of desorption is less than the forward barrier of the dissociation reaction and hence the desorption reaction is favoured. For the mean field energy profiles, the heat of adsorption is always less than the forward dissociation barrier. For this reason, both α and β peaks are large. For the QCA energy profiles, the heat of adsorption and the forward dissociation barrier are approximately of equal magnitude for all three instances. The reverse dissociation barrier is increased at 350 K and 430 K making it harder for C and O to recombine.

The Gibbs free energy of adsorption profile, Figure 6-28, shows that the mean field approximation deviates positively about 0.5 eV from the NL system. At 400 K, this deviation is deceased to 0.35 eV. The QCA starts with a positive deviation of 0.5 eV and begins to return to the NL profile after 400K.

The Gibbs of reaction profile for CO dissociation Figure 6-29, shows that the mean field approximation initially has a deviation of 0.3 eV and remains at this deviation until the 600 K where it returns to the NL profile. The QCA profile shows an initial deviation of 0.6 eV and slowly starts to increase at 300 K to a deviation of 0.1 eV at 550 K and moves back to the NL energy.

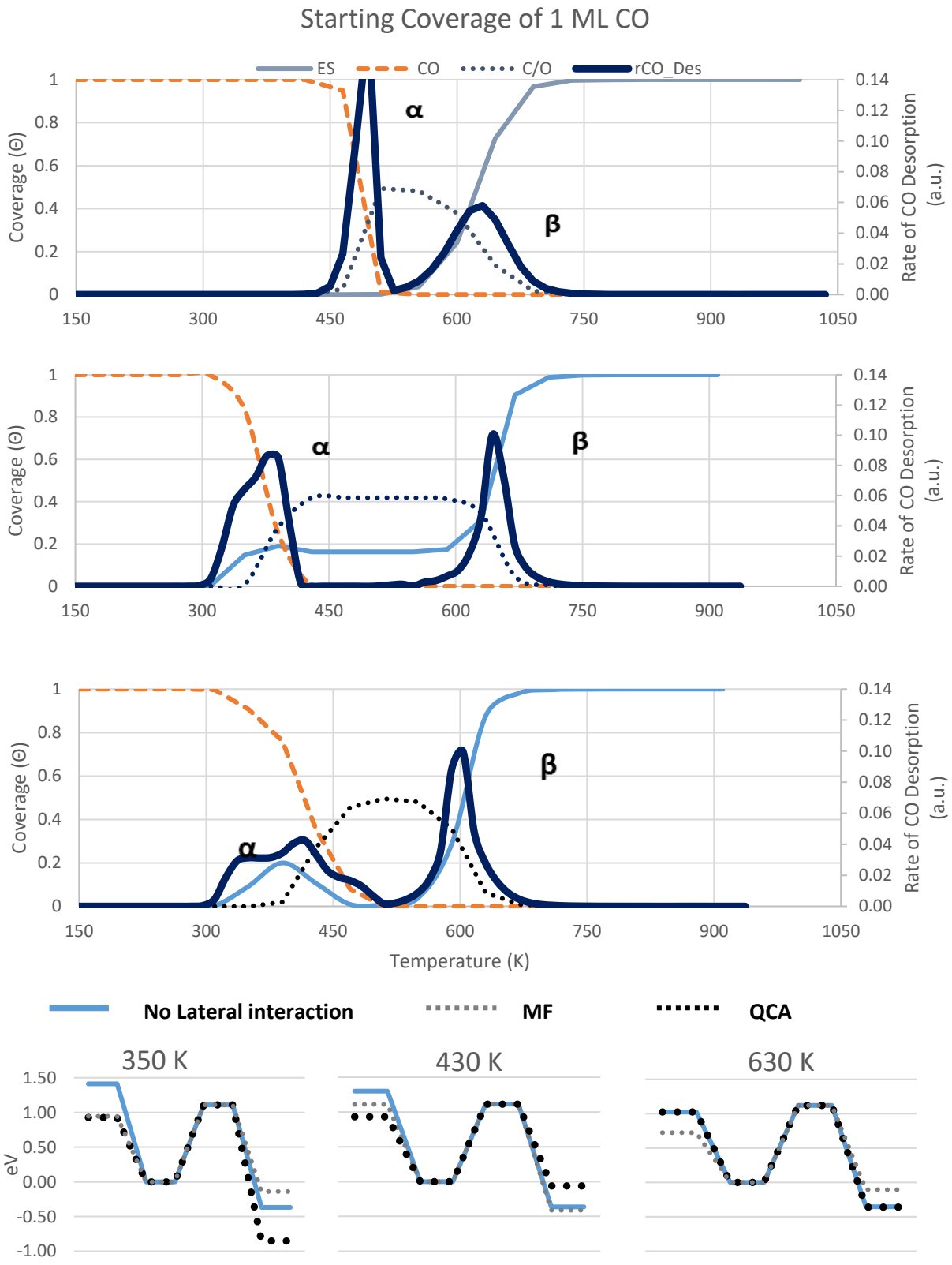

Figure 6-27: Coverage profiles, TPD spectrum and Gibbs free energy profiles for CO TPD with a starting coverage of 1 ML

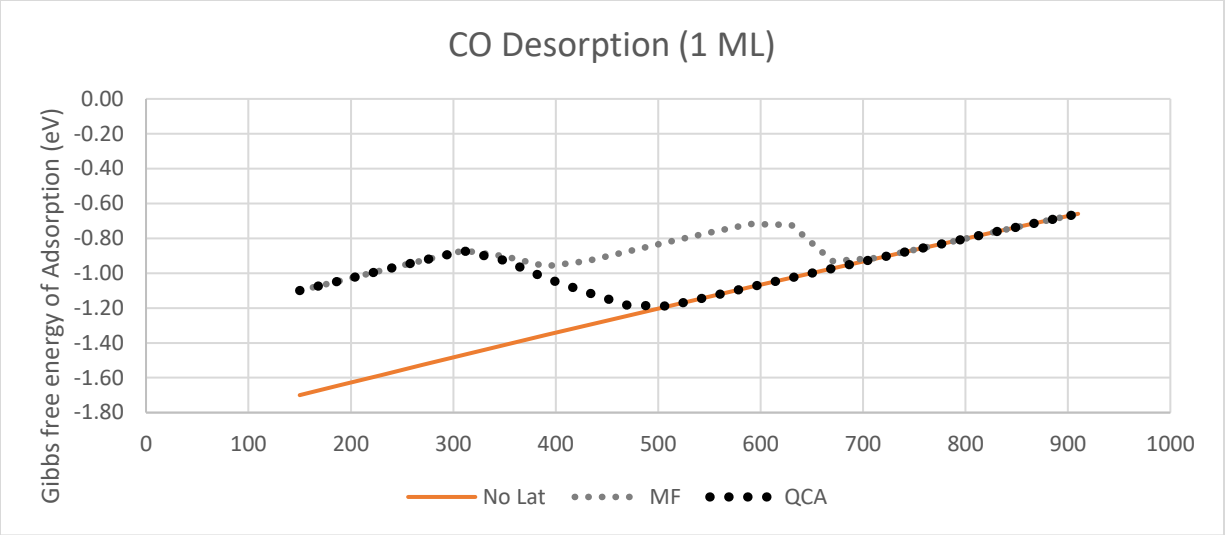

Figure 6-28: Gibbs free energy of adsorption for starting coverage of 1 ML

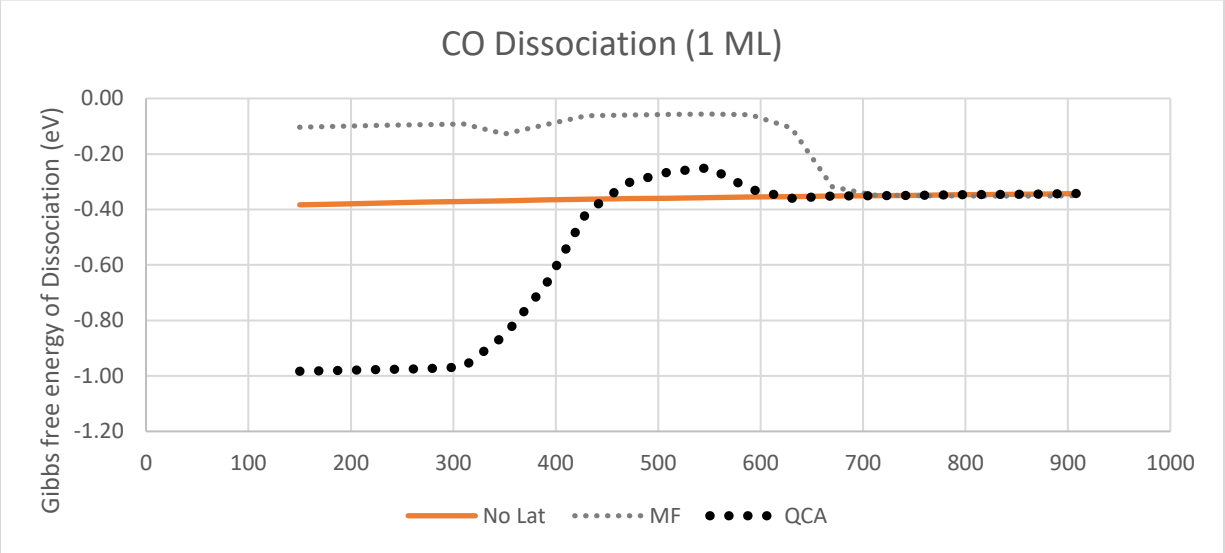

Figure 6-29: Gibbs free energy of reaction profiles for CO Dissociation for starting coverage of 1 ML

For all three methods and starting coverages, CO dissociation was preferential at temperatures below 400 K. For the NL system at 0.6 ML and above, CO would dissociate and the surface would become saturated. For the QCA and mean field systems the lateral interactions would significantly lower the binding energy of CO and CO would desorb faster, creating available sites for CO dissociation.

The α peaks showed significant deviations from the system where no interactions where included. Shoulders around the maxima of the α peaks can be seen for both the mean field and QCA methods, the QCA more distorted than the mean field. The broadness of the α peaks changes as coverage changes.

For all three methods, the β peaks were very similar, even though the maxima were at different temperatures. The peak broadness remains fairly constant as starting coverage increases. 0.6, 0.8 and 1

ML all show similar peaks, in both intensity and broadness. This is a result of the surface being saturated at 1 ML, for the QCA and NL methods, or a maximum C, O coverage of 0.42 ML for the mean field method.

The mean field and quasi-chemical approximations replicated the TPD spectrum by Moon et al. [21] rather well. Using the mean field approximation, the peaks shift to temperatures lower than those reported by Moon et al., possibly due to the choice in functional for this study. The quasi-chemical approximation shows one peak with a prominent pre-shoulder and post shoulder. If diffusion is incorporated correctly the splitting of this peak into three distinct three peaks could potentially occur as adsorbates could shift to different environments. The position of the β-peak appears too soon and could be shifted higher if both C and O diffusions in and on the bulk of Fe is correctly included in the model.

6.2.3 Conclusions

A simulated TPD was created looking at only the desorption of CO and both the dissociation and desorption of CO. The method used to incorporate the lateral interactions can have a significant effect on the overall TPD picture. Mean field and quasichemical approximation methods showed that lateral interactions lowered the binding energy of CO and allowed for an appreciable rate of desorption of CO at lower coverages. The interactions also affected the broadness of the breaks.

The TPD with no lateral interactions shows narrow peaks that appear at the same temperatures irrespective of coverage. For the mean field approximation, we see the α_3 peak is very narrow at about 400 K. The broadness is unaffected by an increase in coverage. An increase in intensity of the β peak is seen. The QCA TPD shows distortions in the broadness of the peaks, particularly the α_3 peaks. This can be attributed to the preference of ordered states.

The overall picture between dissociation and desorption and desorption only is also very different. The energy profiles relative to CO showed that at lower temperatures CO dissociation is preferred to CO desorption. The system with no lateral interaction even becomes saturated at an overall coverage of 1 ML as CO dissociation take place rapidly.

The mean field model does show an improvement from the model with no lateral interactions but when comparing it to the QCA model the additional refinement makes a significant difference. The QCA model appears to agree well with the experimental studies. The results here show that strong lateral interactions can create pre-shoulder and post-shoulders. It is important to distinguish between the effects of strong lateral interactions and the presence of adsorbed species on different sites.

From the desorption and dissociation\desorption TPDs we see that the inclusion of one additional reaction can have a significant effect on the overall picture. Including the C and O diffusions both in and on bulk Fe (100) could improve on the current model.

Computational studies will improve with time, the barriers for reactions will be more accurate but since the lateral interactions can have a significant effect on these barriers they cannot be ignored.

6.3 Methanation on Fe (100)

The methanation of synthesis gas on Fe surfaces is studied as a precursor for Fischer Tropsch synthesis on Fe-based catalysts. A basic potential energy surface with no interactions has been studied for Fe on lower Miller index surfaces [37–39]. Deviations from the potential energy surface as a result of lateral interactions are known to exist, but it's full effect on the kinetics is still being discovered.

Erley et al. [40] studied the methanation of syngas on Fe(110) with fixed a H_2/CO ratio at 300^o C, 1 atm. By conducting High resolution electron energy loss spectroscopy (HREELS) post reaction, they observed the presence of CHx species on the surface, particularly CH and CH_2 surface species.

Lo and Ziegler [37] created a microkinetic model to study the methanation of syngas over Fe(100). To account for lateral interactions, they treated groups of species on the surface as unique species themselves with their own reactions and energetics, demonstrated in Table 6-2. Several p(2x2) supercell configurations were calculated; for the configurations in Table 6-2 [CO_s] is at 0.25 ML, [CO_s + CO_s] is at 0.5 ML (similar to the diagonal configurations in Chapters 3-5), and [CO_s + CO_s + CO_s] is a 0.75 ML configuration. As CO coverage increase, the heat of adsorption decreases, which is consistent with the results from this study (see Chapter 3). Lo and Ziegler [37] assumed that the lateral interactions are predominantly CO-X, H-X, C-X and O-X interactions and considered the effects of these interaction on the adsorption CO and H. No direct effect of lateral interactions on hydrogenation kinetics was investigated. Lo and Ziegler [37] varied several macro elements such as variations in partial pressures of CO and H_2 as well as variations in the feed ratio of CO:H_2 and Catalyst mass to CO flowrate ratio in order to compare their results with the experimental results of Lox and Froment [41][24]. The results from the study showed that the simulated CH_4 formation was comparable with experimental results. However, the simulated formation of CO_2 did not agree with experimental results, indicating this happens via a mechanism not included in their model.

Table 6-2: Lo and Ziegler [37] approach to incorporating lateral interactions

Reaction	E_{ads} (eV/mol)
CO_g + [*] ↔ [CO_s]	-2.01
CO_g + [CO_s + *] ↔ [CO_s + CO_s]	-2.12
CO_g + [CO_s + CO_s + *] ↔ [CO_s + CO_s + CO_s]	-1.12

In this section, a simplified syngas methanation model is used to study the effect of lateral interactions on the kinetics of the system. The model will consider CO and H_2 adsorption, CO dissociation, hydrogenation of C and O and desorption of CH_4 and H_2O. CO_2 formation is neglected in this model since CO_2 formation is more prevalent carbide surfaces then on iron catalysts [42].

6.3.1 Model setup

A batch reactor model was setup to simulate methanation and investigate the effects of lateral interaction and the effects different methods of incorporation of lateral interaction on the kinetics.

[24] Lox and Froment [41] investigated the kinetics of the Fischer-Tropsch reaction using commercial promoted precipitated iron catalyst in a tubular reactor

In chapter 5 tables 5.12 and 5.13 show the nearest neighbour interactions and next nearest neighbour interactions respectively for the species investigated at 600 K. The interactions are predominantly repulsive. The main exception to this being the C next nearest neighbour interactions. This is consistent with the work completed by Sorescu [38] who also showed that next nearest neighbour interactions of C on an Fe(100) surface are attractive. The lateral interactions for other temperatures can be calculated just as easily using the vibrational, rotational and translational energies.

The lateral interactions for surface CH_4 and H_2O have not been included in this model since it is assumed that these species will desorb almost instantaneously; there is initially no CH_4 and H_2O in the gas phase and the pre-exponential factor for adsorption is in the region of 10^1 - 10^3 Pa/s while the pre-exponential factor for desorption is in the region of 10^{10} - 10^{16} /s [14,15]. Furthermore literature shows weak adsorption of CH_4 on Fe(100) [17,38], less than 0.1 eV, which can be significantly influenced by the error expected in this model. The heat of adsorption of water of Fe (100) was found to be 0.53 eV by Govender [43] and 0.35 eV by Eder and Terakura [44]. Adsorption is typically a non-activated process, whereas desorption is activated. Given that the adsorption energies for H_2O and CH_4 are rather low (compared to CO) and the desorption pre-exponential factors are quite large, desorption is significantly favoured.

Table 6-3 shows ΔG of reaction and the forward barrier of the considered reactions used in this microkinetic model at 0 K with zero-point energy corrections. These steps are by no means a comprehensive list of the methanation reactions, we can still however examine the effects of the lateral interactions on the model and the effects of the different methods used to incorporate these interactions. The table includes results from several studies and which used different functionals and electronic implementations (USSP or PAW). It is good practise to use consistent functionals and methods for comparison. In this study, the lateral interactions and overall Gibbs free energy of reaction were investigated using the RPBE functional USSP.

The model was constructed at temperatures of 500 K, 550 K, 600 K and 650 K. The kinetics then include the vibrational, rotational and translational energies of the reactants and products. In this model, the activation energies and the Gibbs free energies of reaction[25] are dynamic, i.e. they change as the species on the surface change and as temperature changes. The vibrational frequencies of the reactants and transition states are available in the studies of Bromfield [33] and Govender [17,18,43] to describe the change in activation barrier with temperature. These were in good agreement with experimental results. The Gibbs free energies of reactions (ΔG_{Rxn}) generated in this study will be used along with the lateral interactions generated in this study will be used. For this study and the studies by Bromfield [33] and Govender [17,18,43] there is a margin of error, in DFT calculation and vibrational frequencies. The resulting forward barriers and ΔG of reaction at 600 K with no lateral interaction is shown in Table 6-4.

The alternative H_2O formation will be the preferred route of H_2O formation since the barrier is 0.4 eV lower then OH hydrogenation. Taking the energies from Table 6-4 and considering the changes in energy for pre-reaction diffusions, from configurations in chapters 4 and 5, energy profiles for the methanation of syngas is created in Figure 6-30. The energy profile at a temperature of 600 K is shifted towards higher energies relative to the energy of the reactants due to the contribution of translational, rotational and vibrational energy to the overall energy profile. The figure also includes the minimum and maximum lateral interactions the species at each respective point will experience, and hence a minimum and maximum profile was produced. These maxima and minima relating to the lateral interactions in chapter 5 tables 5.12 and 5.13. The calculated overall reaction energy was found to be -1.44 eV while the experimental results from Sandler [47] is -0.74 eV. The DFT gas energies at 0 K +ZPE were extrapolated

[25] The overall Gibbs free energy of reaction of methanation is fixed at a given temperature

using vibrational energies and Ideal gas translation and rotational energies, at 600 K this ideal gas Gibbs free energy of reaction is -0.80 eV.

Table 6-3: Comparison of Gibbs free energy of reaction calculated in this study (USPP-RPBE) with the other studies as well as the energy barrier for the forward reaction from other studies

	Reaction	ΔG_{Rxn} (eV)			E_a forward barrier (eV)		
		CASTEP RPBE USSP Present Work	**VASP PW91 PAW** [17,18,33,43]	**VASP PW91 USSP** [38,45,46]	**CASTEP RPBE USSP** [48]	**VASP PW91 PAW** [17,18,33,43]	**VASP PW91 USSP** [38,45,46]
Adsorption	CO + * ↔ CO*	-1.88	-2.53	-2.03	-	-	-
	H_2 + 2* ↔ 2H*	-0.63	-	-0.62	0.08	-	0.09
CO-dissociation	CO* + * ↔ C* + O*	-0.84	-0.33	-0.46		1.11	1.06
Hydrogenation	C* + H* ↔ CH*	0.07	0.41	0.13		0.76	0.63
	CH* + H* ↔ CH_2*	0.72	0.64	0.58		0.75	0.65
	CH_2* + H* ↔ CH_3*	0.36	0.38	0.39		0.86	0.85
	CH_3* + H* ↔ CH_4*	-0.76	-0.12	-0.17		0.71	0.50
	O* + H* ↔ OH*	0.89	0.52	-		1.14	-
	OH* +2H* ↔ H_2O*	0.64	0.94	-		1.1	-
Desorption	CH_4* ↔ CH_4 + *	0.08	0.05	0.02		-	-
	H_2O* ↔ H_2O + *	0.14	0.43	-		-	-
Alternative H_2O formation	OH* +OH* ↔ H_2O* + O*	0.65	0.61			0.65	

Table 6-4: The kinetics used in this study to build a microkinetic model of the methanation of syngas at 600K

	Reaction	E_a forward barrier (eV)	ΔG_{RXN} (eV) Present work
Adsorption	$CO + * \leftrightarrow CO*$	0	-0.97
	$H_2 + 2* \leftrightarrow 2H*$	0.16[1]	-0.11
CO-dissociation	$CO* + * \leftrightarrow C* + O*$	1.11[2]	-0.78
Hydrogenation	$C* + H* \leftrightarrow CH*$	0.72[3]	0
	$CH* + H* \leftrightarrow CH_2*$	0.84[3]	0.78
	$CH_2* + H* \leftrightarrow CH_3*$	0.93[3]	0.27
	$CH_3* + H* \leftrightarrow CH_4*$	0.60[3]	-1.20
	$O* + H* \leftrightarrow OH*$	1.09[3]	0.86
	$OH* + H* \leftrightarrow H_2O*$	1.11[3]	0.53
Desorption	$CH_4* \leftrightarrow CH_4 + *$	-0.24	-0.24
	$H_2O* \leftrightarrow H_2O + *$	-0.45	-0.45
Alternative H_2O formation	$OH* + OH* \leftrightarrow H_2O* + O*$	0.60[3]	0.42

[1] using vibrational frequencies and energies from van Helden [48]

[2] using vibrational frequencies and energies from Bromfield [33]

[3] using vibrational frequencies and energies from Govender [17,18,43]

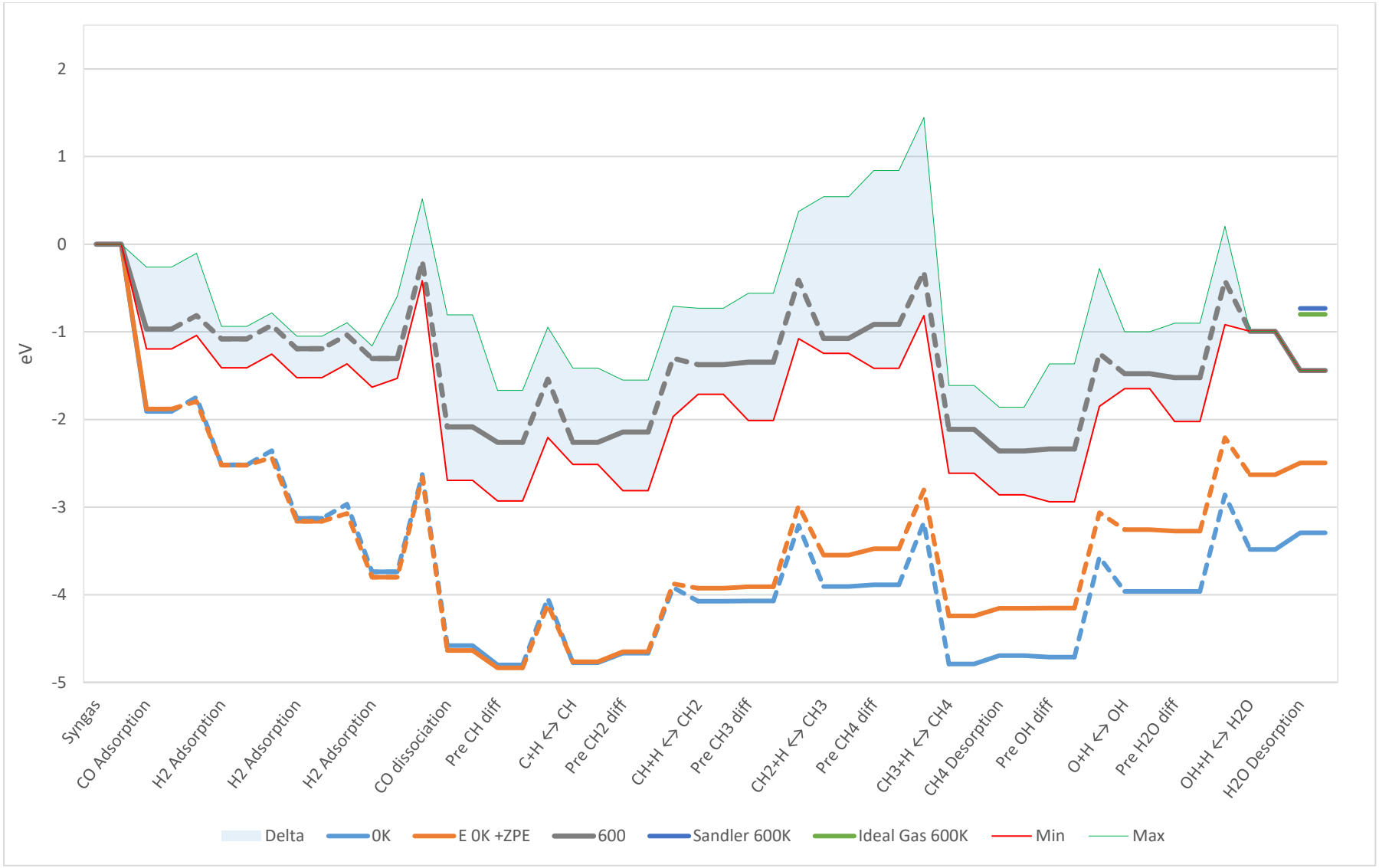

Figure 6-30: Energy profile of a simple methanation mechansim at 0K, 0K + ZPE and 600K. The energy profile at 600K also includes minimum and maximum interactions

CO, CH_4 and H_2O adsorption kinetics

$$r_{Ads,x} = k_{\mathrm{Ads,x}} P_x \theta_{ES} \quad (6.27)$$

$$k_{\mathrm{Ads,x}} = \mathrm{A}_s \sqrt{\frac{2\pi \cdot m_x}{kb \cdot T}} e^{-\Delta \mathrm{e}^{\mathrm{f}}(T,LI)/k_B T} \quad (6.28)$$

Where P_x is the partial pressure of either CO, CH_4 or H_2O, θ_{ES} is the coverage of empty sites, k_{Ads} is the rate constant derived from Collision frequency, A_s is the area of a single site, m_x is the molar mass of the gas, and e^f the forward activation energy, which is a function of both temperature and lateral interactions.

CO, CH_4 and H_2O Desorption kinetics

$$r_{Deso.,\mathrm{x}} = k_{\mathrm{Deso,x}} \theta_X \quad (6.29)$$

$$k_{\mathrm{Deso,x}} = \frac{k_B T}{h} e^{-\Delta G_{Desorption}(T,LI)/k_B T} \quad (6.30)$$

H_2 Desorption kinetics

$$r_{Deso.} = k_1 \theta_H^2 \quad (6.31)$$

$$k_{\mathrm{Deso}} = \frac{k_B T}{h} e^{-\Delta G_R(T,LI)/k_B T} \quad (6.32)$$

Dissociation kinetics

$$r_{Diss} = k_{\mathrm{Diss}} (\theta_{ES}\theta_{CO} - {\theta_C \theta_O}/{K_{e,\mathrm{Diss}}}) \quad (6.33)$$

$$k_2 = \frac{k_B T}{h} e^{-eb_2^f/k_B T} \quad (6.34)$$

$$Ke_2 = \prod Q_{v_i} Q_{T_i} Q_{R_i} e^{-(eb_2^f - eb_2^r)/k_B T} \quad (6.35)$$

$$eb^f = eb^{f0} \quad (6.36)$$

$$eb^r = eb^{r0} + (LI_{React.} - LI_{Prod.}) \quad (6.37)$$

Hydrogenation kinetics

$$r_{Hydrog-\beta H_x} = k_{\mathrm{Hydrog-\beta H_x}} (\theta_{\beta H_x}\theta_H - {\theta_{ES}\theta_{\beta H_{x+1}}}/{K_{e,\mathrm{Hydrog-\beta H_x}}}) \quad (6.38)$$

$$k_{\mathrm{Hydrog-\beta H_x}} = \frac{k_B T}{h} e^{-eb_2^f/k_B T} \quad (6.39)$$

$$Ke_{\mathrm{n}} = \prod Q_{v_i} Q_{T_i} Q_{R_i} e^{-(eb_{\mathrm{n}}^f - eb_{\mathrm{n}}^r)/k_B T} \quad (6.40)$$

If $\Delta G_{Rxn} > 0$ then $eb^f = eb^{f0} + (LI_{React.} - LI_{Prod.})$

If $\Delta G_{Rxn} < 0$ Then $eb^f = eb^{f0}$ (6.41)

If $\Delta G_{Rxn} < 0$ then $eb^r = eb^{r0} + (LI_{React.} - LI_{Prod.})$

If $\Delta G_{Rxn} > 0$ Then $eb^r = eb^{r0}$ (6.42)

where Θ_x is the coverage of species x, k_B is the Boltzmann constant, h is Planck constant, LI is the lateral interactions, eb^f is the forward barrier, eb^r is the reverse barrier and ΔG_{Rxn} is the Gibbs free energy of

reaction. The ΔG_{Rxn} is affected by temperature (rotation, translation and vibration energies) and the lateral interactions of the reactants and products.

$$\frac{d\theta_{CO}}{dt} = r_{\theta_{CO}} = r_{CO\ Ads} - r_{CO\ Diss} \quad (6.\ 43)$$

$$\frac{d\theta_{C}}{dt} = r_{\theta_{C}} = r_{CO\ Diss} - r_{CH\ form} \quad (6.\ 44)$$

$$\frac{d\theta_{O}}{dt} = r_{\theta_{O}} = r_{CO\ Diss} - r_{OH\ form} \quad (6.\ 45)$$

$$\frac{d\theta_{H_2}}{dt} = r_{\theta_{H_2}} = r_{H_2\ Ads.} - r_{CH\ form} - r_{CH_2\ form} - r_{CH_3\ form} - r_{CH_4\ form} - r_{OH\ form} - r_{H_2O\ form} \quad (6.\ 46)$$

$$\frac{d\theta_{CH}}{dt} = r_{\theta_{CH}} = r_{CH\ form} - r_{CH_2\ form} \quad (6.\ 47)$$

$$\frac{d\theta_{CH2}}{dt} = r_{\theta_{CH2}} = r_{CH_2\ form} - r_{CH_3\ form} \quad (6.\ 48)$$

$$\frac{d\theta_{CH3}}{dt} = r_{\theta_{CH3}} = r_{CH_3\ form} - r_{CH_4\ form} \quad (6.\ 49)$$

$$\frac{d\theta_{OH}}{dt} = r_{\theta_{OH}} = r_{OH\ form} - r_{H_2O\ form} - r_{H_2O\ form\ Alt} \quad (6.\ 50)$$

$$\frac{d\theta_{CH4}}{dt} = r_{\theta_{CH4}} = r_{CH_4\ form} - r_{CH_4\ Deso} \quad (6.\ 51)$$

$$\frac{d\theta_{H2O}}{dt} = r_{\theta_{H2O}} = r_{H_2O\ form} - r_{H_2O\ Deso} \quad (6.\ 52)$$

A differential equation for each surface species was setup for the different methods and different scenarios. The differential equations were then solved with ode23 solver[34], which was recommended for stiff ode's as part of the MatLab [35] package.

Batch models were setup with an initial partial pressure of CO at 1 bar and H_2 at 3 bar[26], a clean surface and temperatures of 500 K, 550 K, 600 K and 650 K. The reactor volume was set to 0.001 m^3, the site density of an Fe (100) surface is approximately 1.2 x 10^{19} hollow-sites/m^2 and a catalyst particle with 500 m^2 of surface area was used which relates to 0.01 mol of hollow-sites.

[26] A H_2:CO ratio of 3:1 is synonymous with methane formation while a ratio of approximately 1.8:1 is used for Fischer-Tropsch synthesis

6.3.2 Results and Discussion

As with the CO TPD, models with no lateral interactions, mean field and quasi chemical approximations were constructed. For all temperatures considered, the model with no lateral interactions displayed only adsorption of CO to a coverage of 1 ML and no further reactions, Figure 6-31.

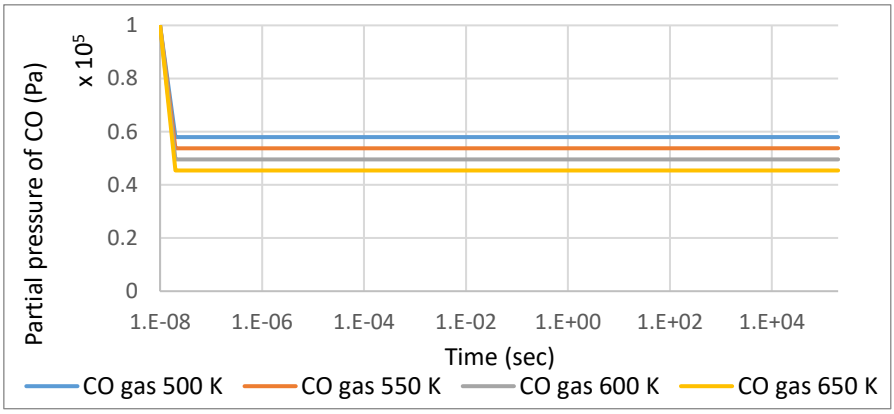

Figure 6-31: Change in partial pressure of CO for a model with no lateral interaction

The results that follow will discuss the partial pressure profiles, coverage profiles and equilibrium constant, and hence Gibbs free energy, profiles of the mean field (figures on the left) and quasi chemical approximation (figures on the right) microkinetic models at 500 K, 550 K, 600 K and 650 K. The results at 500 K are similar to the results of the model with no lateral interactions in that reactions beyond CO adsorption takes place at minimal rates.

For both mean field and quasi chemical approximations, CO is rapidly adsorbed, within $1x10^{-7}$ sec, onto the surface until the surface is virtually completely covered with CO adsorbates. In both systems, the partial pressure of CO drops from 1 bar to between 0.6 bar and 0.4 bar, depending on temperature. The system remains in this state until approximately 1 sec. Hydrogen also adsorbs rapidly but at much smaller scale than CO since the ΔG of adsorption is much smaller (From Table 6-4 at 600 K -0.97 eV for CO and -0.11 eV for H_2). While the hydrogen adsorbate coverage remains small, less than 0.005 ML for all temperatures and both mean field and quasi-chemical approximations, the hydrogenation steps still occur.

For both models at 550 K and above, the coverage of CO begins to drop while the coverage of O increases - this is associated with the dissociation of CO to C and O. The point at which the drop occurs is a function of temperature, the drop occurs earlier for higher temperature since the rates are higher, and lateral interactions. The coverage of C is orders of magnitude lower than the coverage of O indicating that hydrogenation of C is favoured over the hydrogenation of O.

The partial pressures of CH_4 and H_2O increases as CO dissociates. Additional CO is adsorbed on the surface for the mean field models at 550 K, 600 K and 650 K. For the quasi chemical approximation, additional CO adsorption is seen only at 650 K but CO is then repelled off the surface as the coverage of O increases. The partial pressure of H_2O is orders of magnitude smaller than that of CH_4. Even with the additional OH – OH combination reaction, the rate of H_2O formation is significantly smaller than that of CH_4. The magnitude of the partial pressures of the QCA model is smaller than that of the mean field model.

The coverage of O continues to rise as time increases and even surpasses the coverage of CO for 600 K and 650 K before the 48-hour mark is reached. At this point the predominantly repulsive O-X interactions are what dominate the energetic deviations. This build-up of O again confirms that the hydrogenation of C is favoured over the hydrogenation of O.

By comparing the equilibrium constants for the different reactions, the differences between mean field and QCA formulations become clear. The mean field approximation forces the inclusion of X-Y interactions if the coverage of either X or Y is large. The QCA approximation requires the coverage of both X and Y to be appreciable and hence a probability of X-Y is appreciable. For this reason, the mean field energetics are all affected early in the simulation, $1x10^{-8}$ to 1 sec, by the large CO coverage and hence CO-X interactions while for the QCA system only reactions directly concerning CO-CO interactions are affected.

The experimental study by van Steen et al. [49] argues that surface O may diffuse into the structure. For Fe based catalysts, surface O may result in the formation of nano-sized magnetite crystallite (i.e. O diffuses into the structure and break off). This was not included in the models generated here and could be a contributing factor to the build-up of surface O. To truly investigate this further the diffusion of O into the surface will need to be considered. The work here can then be taken as a further indication that the iron-based catalyst need to undergo phase change to complete the catalytic cycle.

6.3.2.1 CO and H Adsorption and dissociation

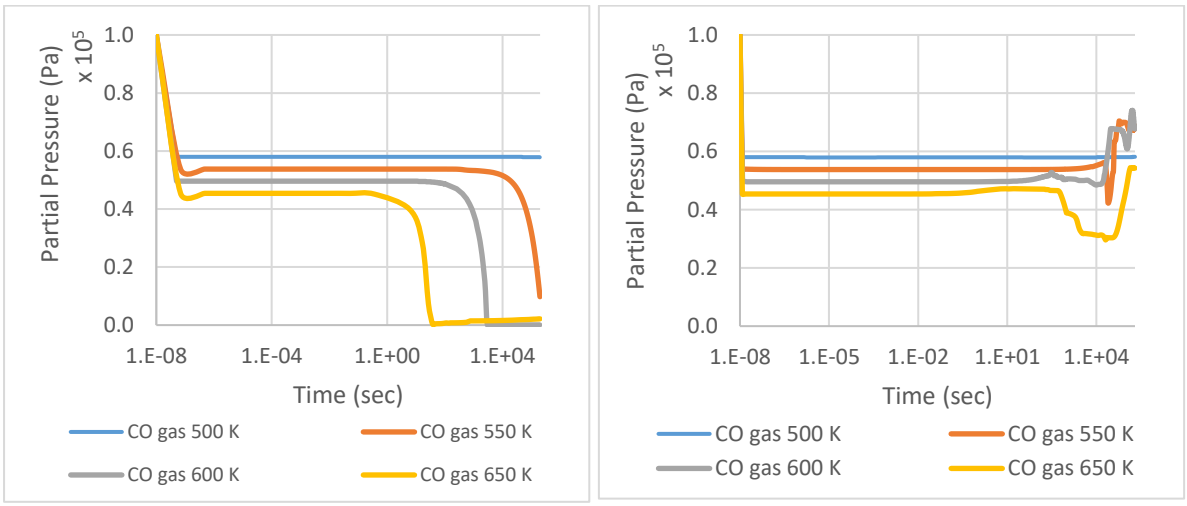

Figure 6-32: Change in partial pressure of CO for mean field model (Left) and QCA model (Right)

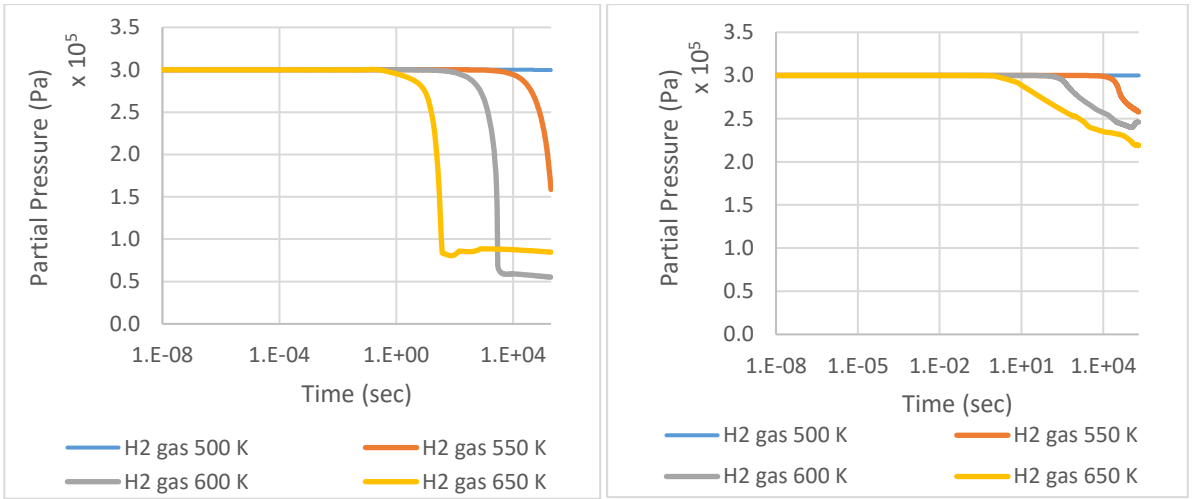

Figure 6-33: Change in partial pressure of H_2 for mean field model (Left) and QCA model (Right)

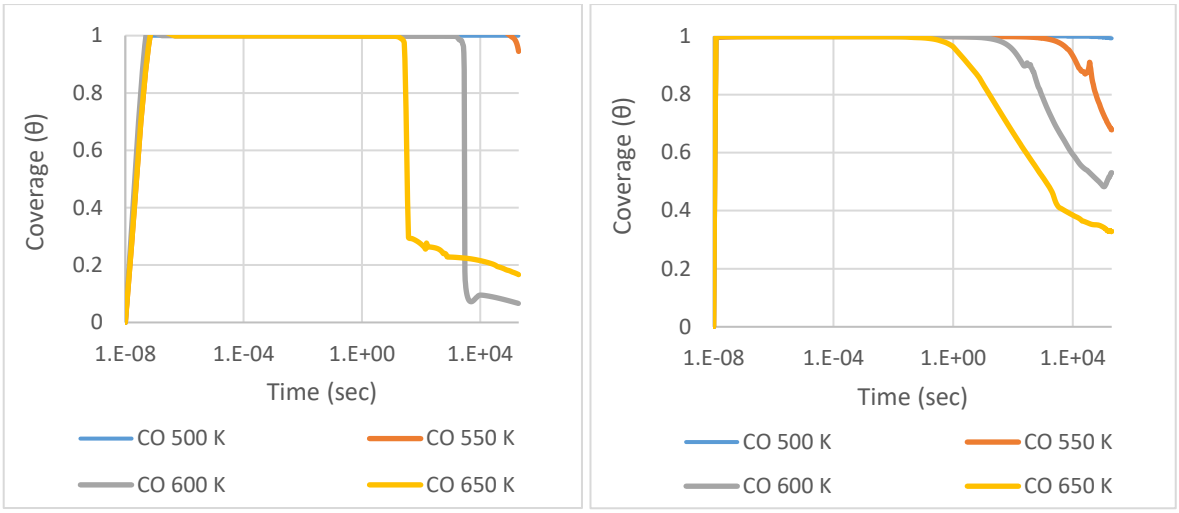

Figure 6-34: Change in coverage of CO for mean field model (Left) and QCA model (Right)

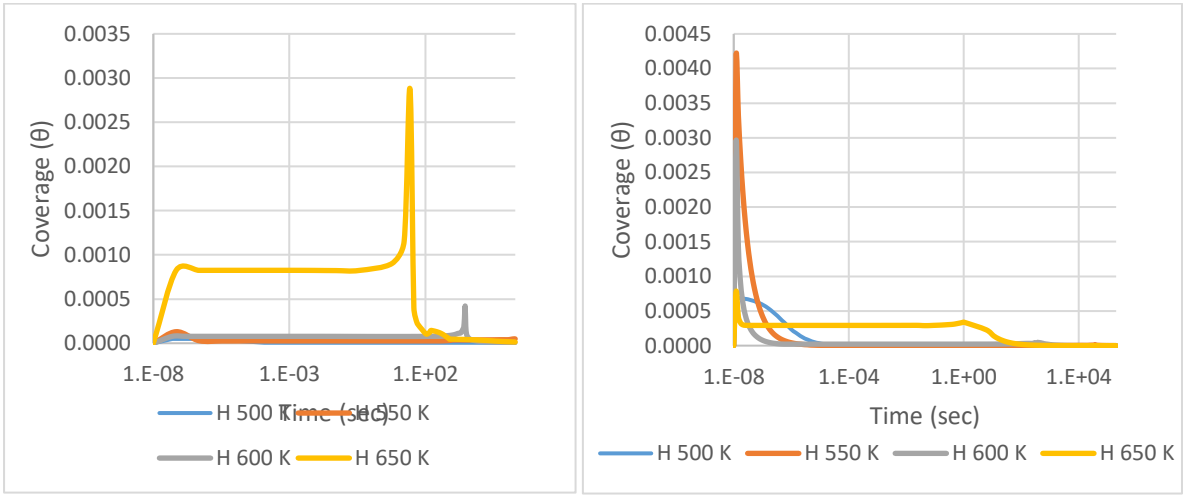

Figure 6-35: Change in coverage of H for mean field model (Left) and QCA model (Right)

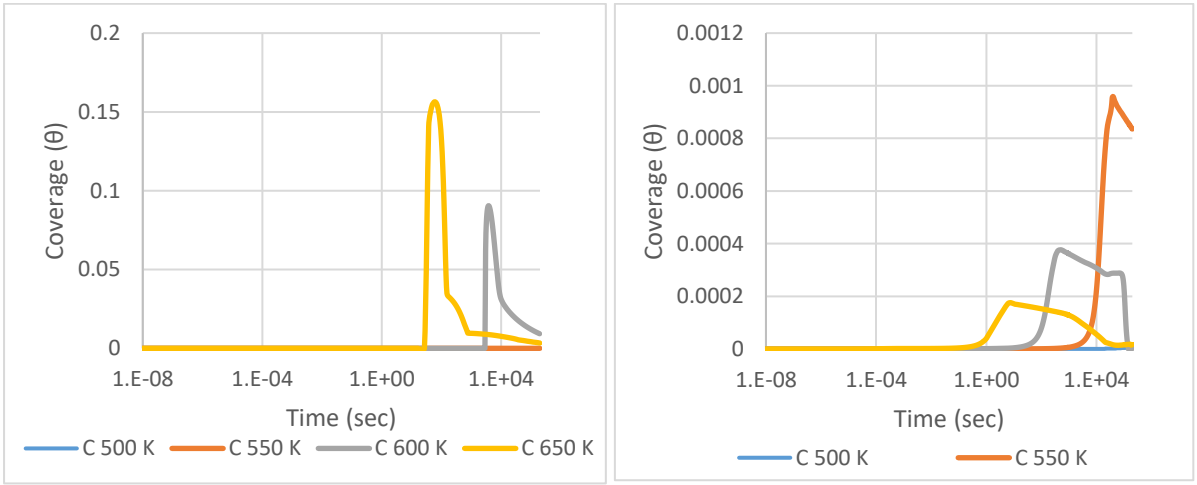

Figure 6-36: Change in coverage of atomic C on the surface for mean field model (Left) and QCA model (Right)

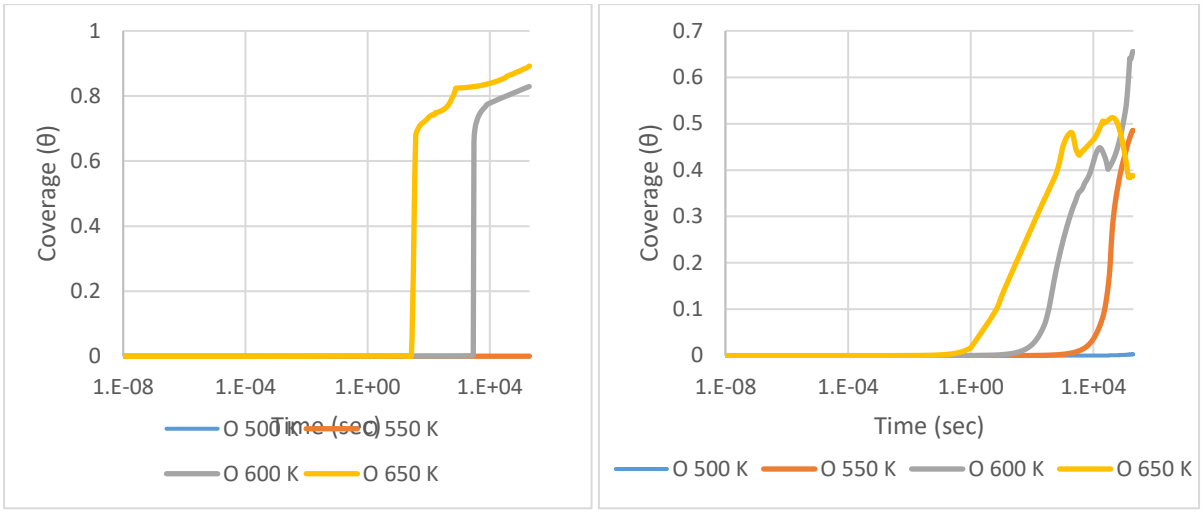

Figure 6-37: Change in coverage of atomic O for mean field model (Left) and QCA model (Right)

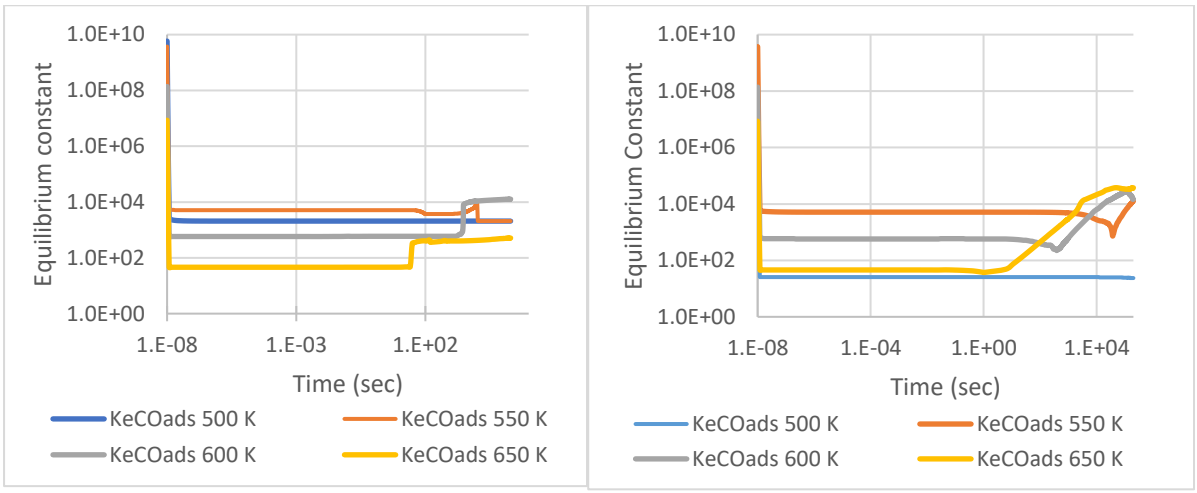

Figure 6-38: Change in equilibrium constant for CO adsorption for mean field model (Left) and QCA model (Right)

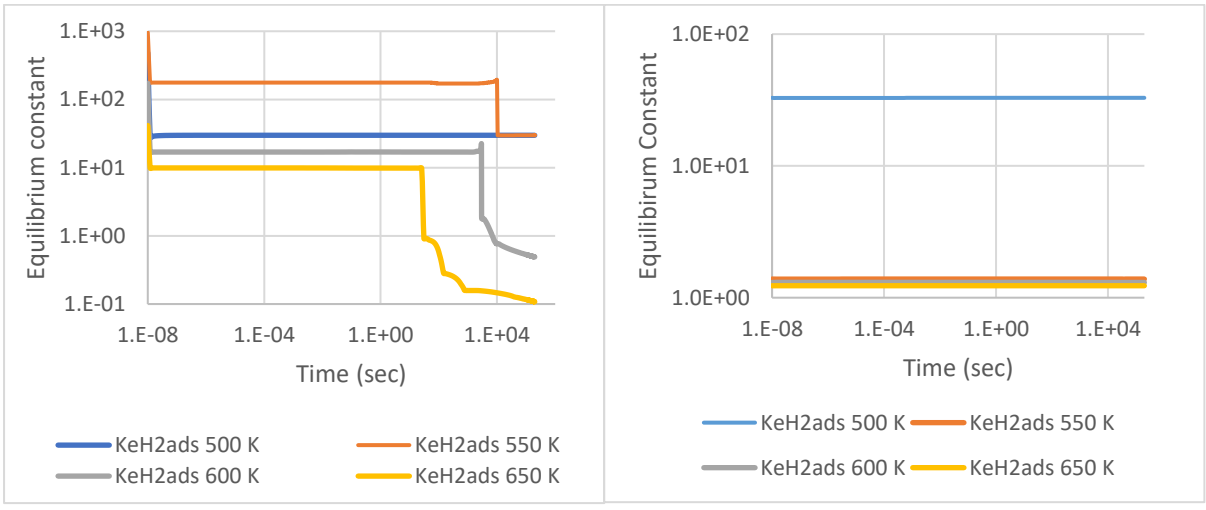

Figure 6-39: Change in equilibrium constant for H_2 adsorption for mean field model (Left) and QCA model (Right)

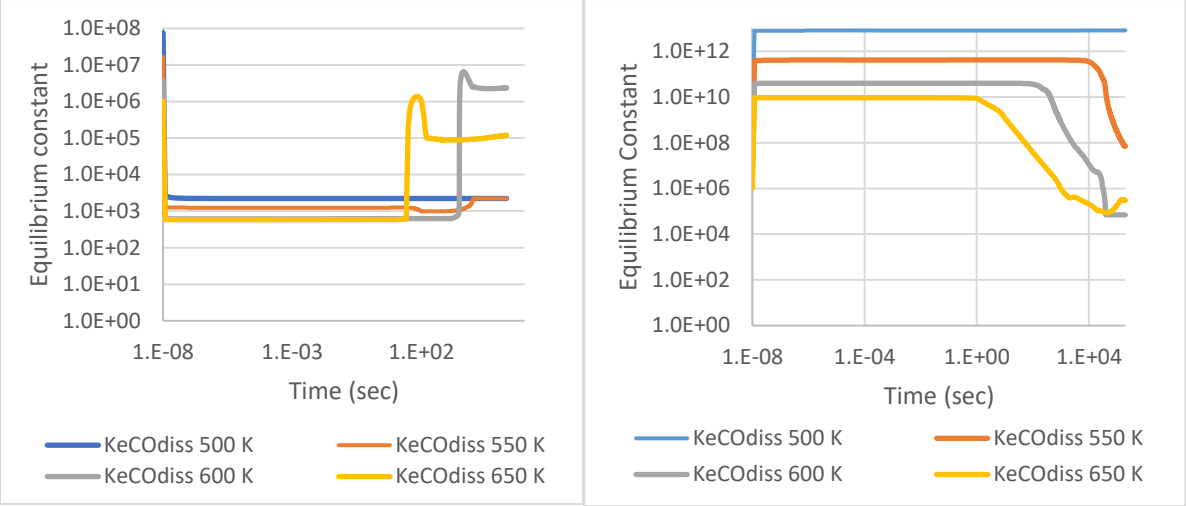

Figure 6-40: Change in equilibrium constant for CO dissociation for mean field model (Left) and QCA model (Right)

Adsorbed CO and atomic O are the dominant species on the Fe (100) surface during CO hydrogenation. This is a result of CO adsorption being favourable due to the large heat of adsorption and then consequently dissociated resulting in surface C and O adsorbates which are available for hydrogenation.

Within the first second, the partial pressures of CO drop while the H_2 partial pressures have negligible change, Figure 6-32 and Figure 6-33, for both the mean field and QCA models. This was to be expected as the heat of adsorption for CO is larger than that of H_2 (from Table 6-4 at 600 K -0.97 eV for CO and -0.11 eV for H_2). Furthermore, the existence of a forward barrier, which is significantly higher in the presence of high CO coverage, for the dissociate adsorption of H_2 further hinders the formation of surface H. The extent to which the CO partial pressure drops is dependent on the temperature, in all cases this relates to approximately 0.01 mol of CO (for all models the catalysts surface has 0.01 mol of hollow site).

This results in a rapid adsorption of CO to a coverage of >0.99 ML for both the mean field and QCA models, shown in Figure 6-34, and minimal adsorption of H (<0.005 ML), in Figure 6-35. At these high coverages of CO, CO-X interactions are significantly repulsive, changing the adsorption energies of both CO and H. The hydrogen coverages show that Hydrogen adsorption spikes but to a significantly lower coverage than CO, less than 0.01 ML, for both systems. The CO repulsions further lower this coverage to less than 0.001 ML for both systems and when the coverage of O begins to increase the mean field coverage of H drops even further as a result of O-H repulsions.

The equilibrium constants of adsorption of CO in Figure 6-38 and adsorption of H_2 in Figure 6-39, decreases, and hence the Gibbs free energy of adsorption decreases, upon CO adsorption for both the mean field and QCA models. Once CO starts dissociating the equilibrium constant of adsorption for H_2 decreases further as a result of more repulsive O-H interactions, while the equilibrium constant of adsorption for CO increases as O-CO interactions are less repulsive than CO-CO interactions.

The coverage of atomic C, Figure 6-36, and atomic O, Figure 6-37, rises as CO dissociates. For the mean field model, the coverage of atomic C rises sharply, passes through a maximum and then drops sharply and tails off. The coverage of atomic O also rises but to a much higher coverage than atomic C (0.7 ML for O and 0.15 ML of C at 650 K) and then increases gradually as more CO dissociates. For the quasi chemical approximation model, atomic C rises to a maximum, decreases moderately at first and then decreases to less than 0.01 ML. For the coverage of atomic C, maximum coverage is seen at 550 K but it does occur much later than the 650 and 600 K maximums. The coverage of atomic O also rises as CO dissociates and for 600 K and 650 K passes through a local minimum (almost a kind of peak separation) then continues to rise and for 650 K passes through a maximum and begins to decrease as O is

hydrogenated and possibly recombines with C to form surface CO again. For both models the decreases of atomic C is a result of C hydrogenated and the build-up of atomic O, which occupies sites needed for CO dissociation. The build-up of atomic O over atomic C indicates that carbon hydrogenation occurs faster than oxygen hydrogenation. O hydrogenation does occur since OH and H_2O surface coverages are seen and H_2O eventually is seen in the gas phase.

In Figure 6-40, the equilibrium constant of CO dissociation drops sharply for the mean field system and rises sharply for the QCA model upon CO adsorption. This highlights an important difference between the two methods of implementation. The mean field system considers the effect of lateral interactions independently of the coverage of the species itself. i.e. Considering the energetics of C adsorbates, CO-C interactions is only a function of the interaction energy of CO-C and the coverage of CO. The QCA methodology considers both the coverage of C and CO to determine the probability of CO-C interactions. Once CO dissociates the equilibrium constant of the mean field model rises, as the coverage of C and O rises, and goes through a maximum, decreases and stabilises. For the QCA model once CO starts to dissociate the equilibrium constant decreases. With regard to the CO dissociation equilibrium constant the formulation of the mean field approximation forces the inclusion of CO-C and CO-O interactions even though the coverage of C and O are negligible. The QCA approximation, since it is based on the probability of there being a neighbouring adsorbate, will have negligible probabilities for CO-C and CO-O allowing CO-CO interaction to dominate. This means that product interactions are small and the reactant interactions are large, resulting in a ΔG of CO dissociation which is smaller.

6.3.2.2 *Hydrogenation*

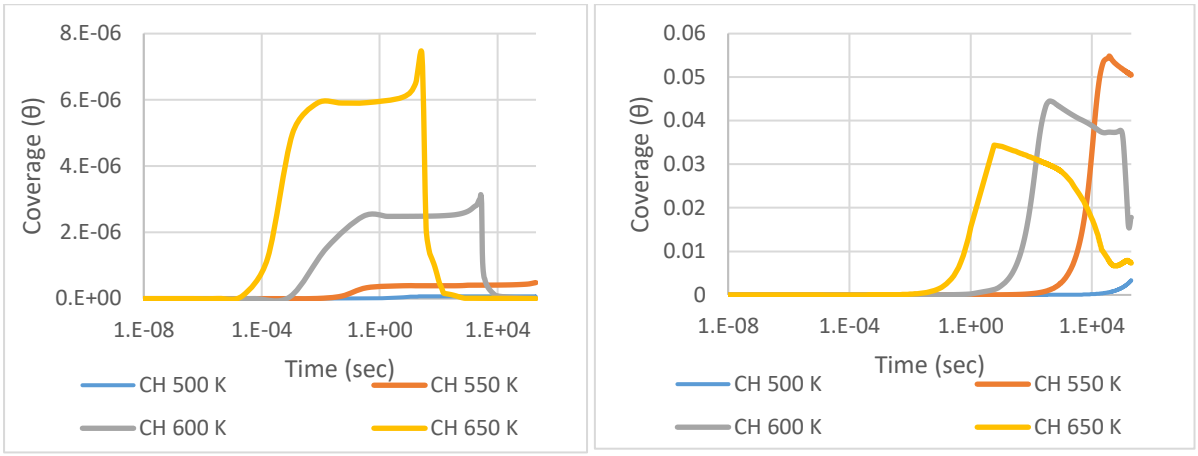

Figure 6-41: Change in coverage of surface CH for mean field model (Left) and QCA model (Right)

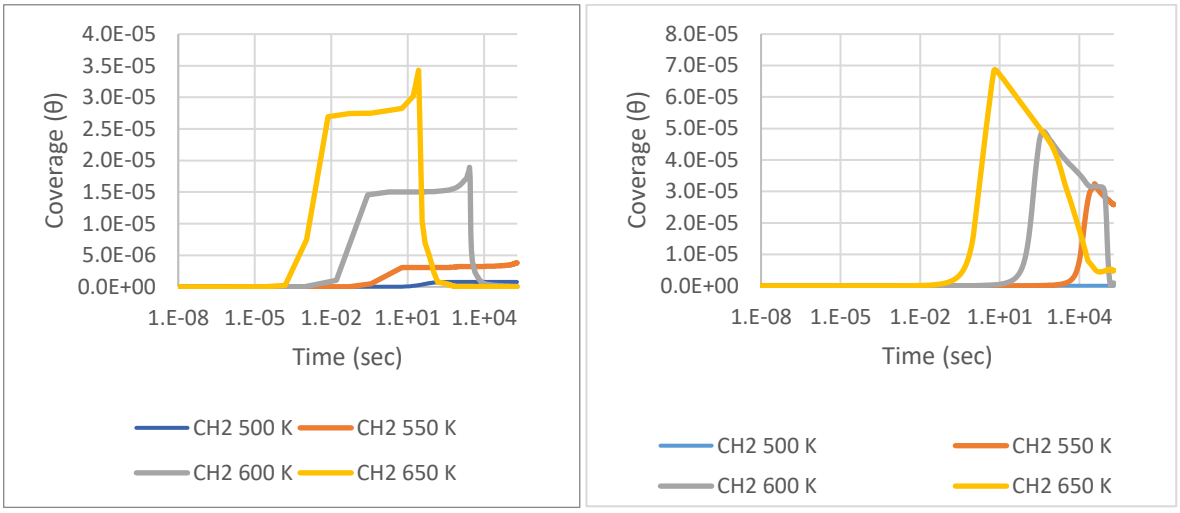

Figure 6-42: Change in coverage of surface CH_2 for mean field model (Left) and QCA model (Right)

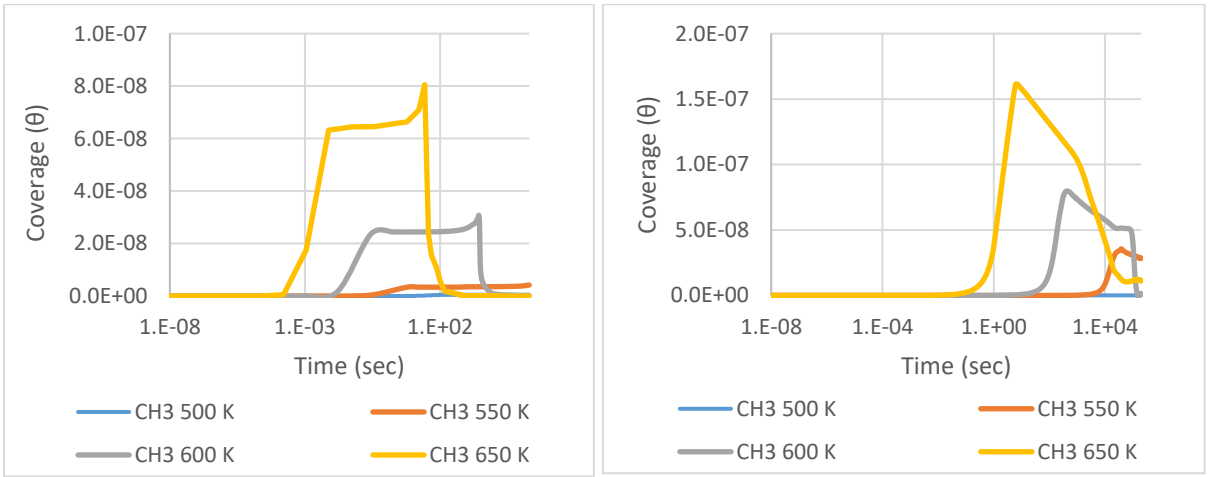

Figure 6-43: Change in coverage of surface CH_3 for mean field model (Left) and QCA model (Right)

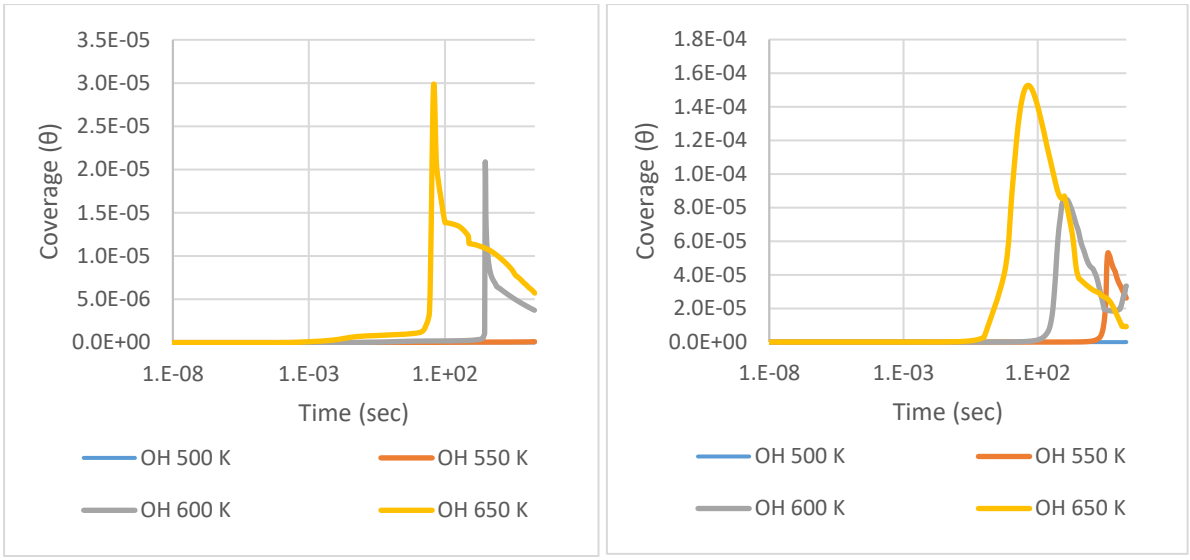

Figure 6-44: Change in coverage of surface OH for mean field model (Left) and QCA model (Right)

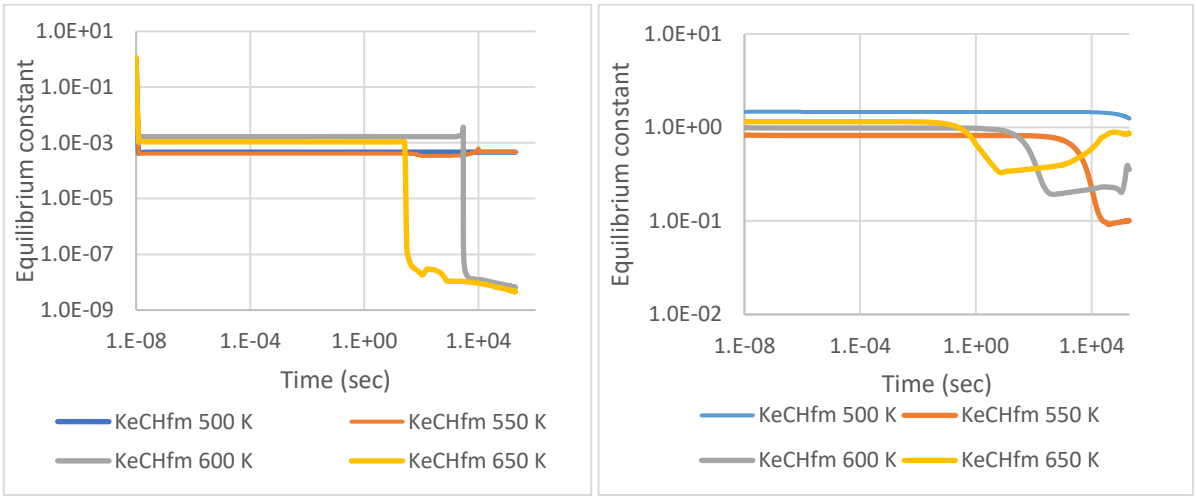

Figure 6-45: Change in equilibrium constant for CH formation for mean field model (Left) and QCA model (Right)

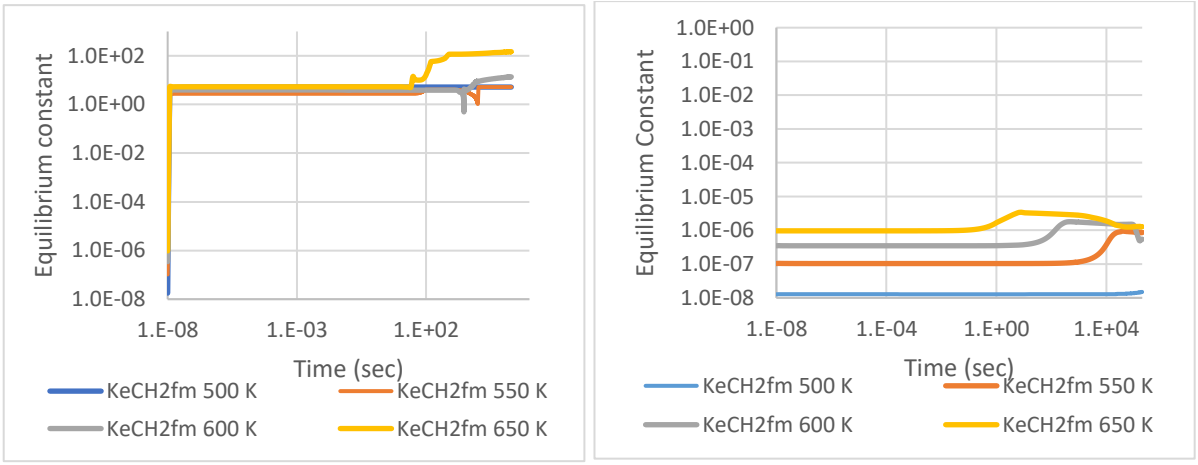

Figure 6-46: Change in equilibrium constant for CH_2 formation for mean field model (Left) and QCA model (Right)

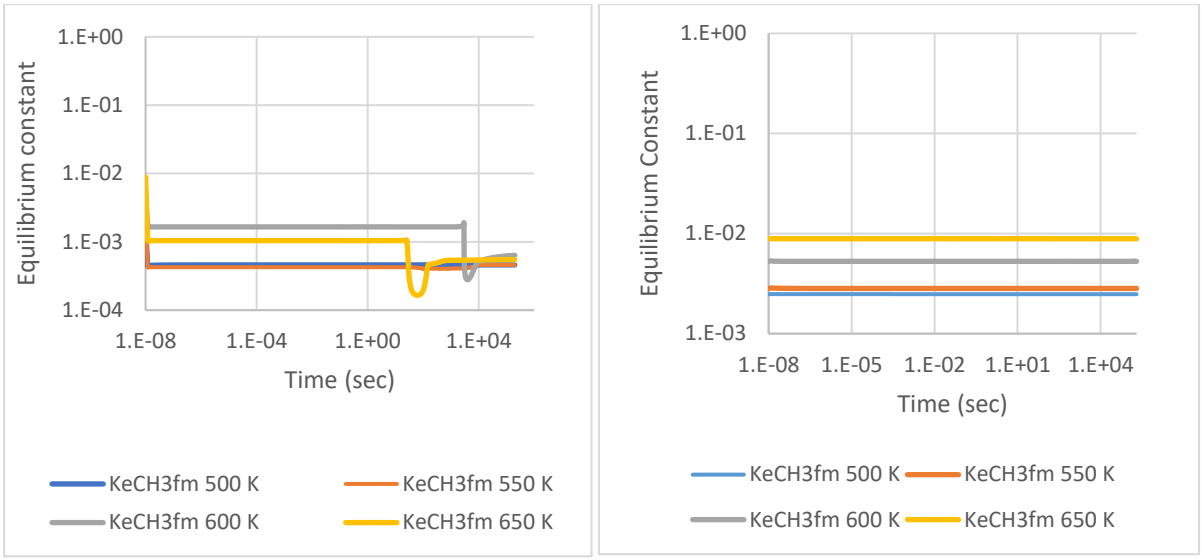

Figure 6-47: Change in equilibrium constant for CH_3 formation for mean field model (Left) and QCA model (Right)

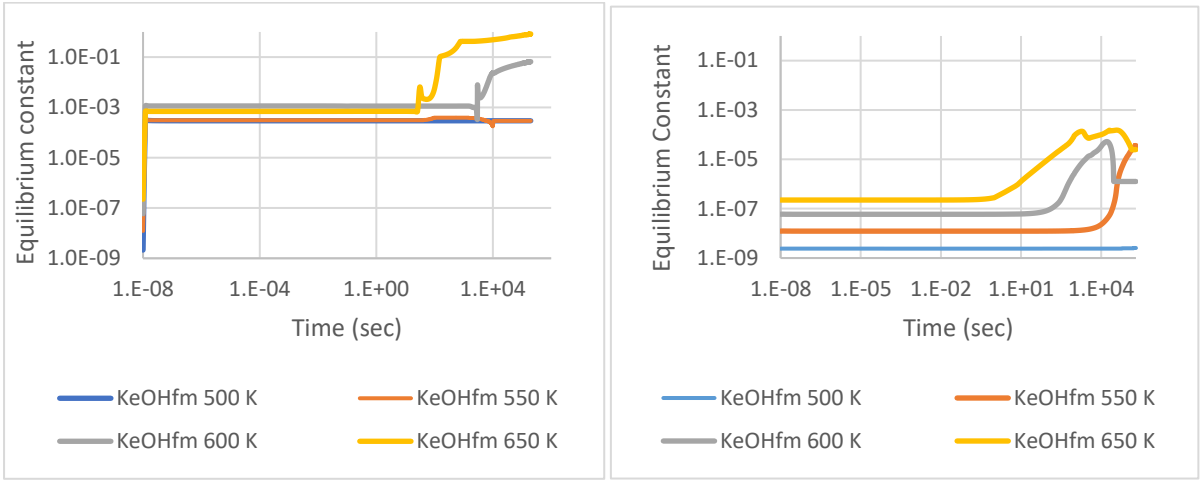

Figure 6-48: Change in equilibrium constant for OH formation for mean field model (Left) and QCA model (Right)

The coverages of CH, CH_2 and CH_3 are significantly lower than the coverages of CO and O. The coverage profiles of CH, CH_2 and CH_3 are also similar in shape but different in magnitude, with CH being larger than CH_2, being larger than CH_3 for the QCA system and CH_2 being larger than CH, being larger than CH_3 for the QCA system. The coverage of OH goes through a maximum for both systems and is the same order of magnitude as CH_2.

For the mean field system, we see the coverages of CH (Figure 6-41), CH_2 (Figure 6-42) and CH_3 (Figure 6-43) increase sharply within 1 sec and remain fairly constant. Once the coverages of C and O increase, the CH, CH_2 and CH_3 coverages increase again and go through a maximum and decreases significantly. For all three species, the coverages are larger at higher temperatures.

For the QCA system we see the coverages of CH, CH_2 and CH_3 begin to increase but slower than the mean field models. The coverages go through a maximum and then gradually decrease as the species get hydrogenated. For the CH species, maximum coverage is seen at 550 K but it does occur much later than the 650 and 600 K maximums, as with the coverage of atomic C. The CH_2 and CH_3 coverages are larger at higher temperatures.

In Figure 6-44 we see that for the mean field models the OH coverage increases as the coverage of O increases but decreases shortly afterwards. This is the result of OH being hydrogenated and the surface becoming saturated with atomic O and limiting H_2 adsorption. For the QCA system the OH

coverage begins to increase more gradually than the mean field models and goes through a maximum and decreases.

For the mean field models, the equilibrium constant of CH formation, Figure 6-45, drops from being slightly greater than 1 to being less than when, which relates to the Gibbs free energy changing from slightly exergonic to endergonic, when CO adsorbs on the surface. The equilibrium constant drops and mirrors the shape of the atomic O coverage profile as the O-X interaction dominate. For the QCA system the equilibrium constant also drops from being greater than 1 to being less than 1 but only as the coverages of C and CH change. The equilibrium constant profile resembles the shape of the CH coverage profile.

For the mean field models, the equilibrium constant of CH_2 formation, Figure 6-46, changes from being less than 1 to being more than 1 upon CO adsorption. Further increases in equilibrium constant are seen as the coverage of O increases on the surface. The QCA equilibrium constants remains less than 1, largely endergonic, and does resemble the shape of the CH_2 coverage profiles

The equilibrium constant of CH_3 formation, Figure 6-47, shows that the reaction remains endergonic in both models for the duration of the simulation. For the mean field system equilibrium constant decreases as CO is adsorbed on the surface and goes through a minimum, resembling the shape of the atomic C coverage profiles. The QCA equilibrium constant shows negligible change for the duration.

The equilibrium constant for OH formation, Figure 6-48, also remain endergonic for both systems for the duration of the simulation. For the mean field model, the equilibrium constant increases as CO is adsorbed on the surface and then increases again as the coverage of O increases on the surface. For the QCA model equilibrium constants only change once the coverage of OH and O change, which is after 1 sec.

The differences between the mean field and QCA systems are seen clearly in this section and more so by analysing the equilibrium constants for the different hydrogenation steps. Towards the end of the simulation atomic oxygen begins to dominate the coverages and the hydrogenation steps are slowed to a halt.

Practically the Fischer-Tropsch process is not halted by an increase in O coverage but rather the oxygen is consumed to form other oxygen containing hydrocarbons (alcohols, acids, olefins) and oxygen diffuses into the surface to form magnetite, which is brittle and breaks off from the main crystal [49].

6.3.2.3 *Desorption*

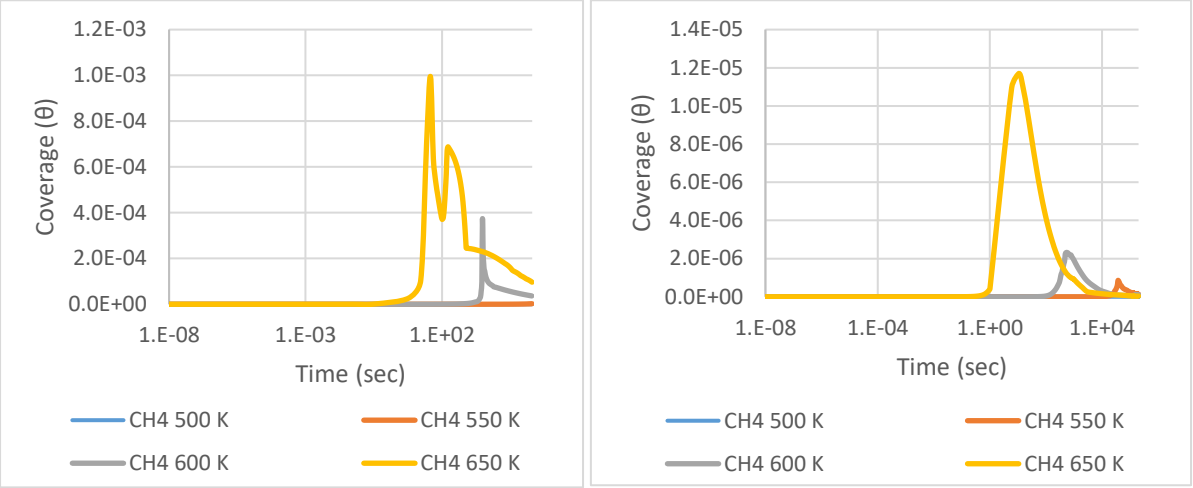

Figure 6-49: Change in coverage of surface CH_4 for mean field model (Left) and QCA model (Right)

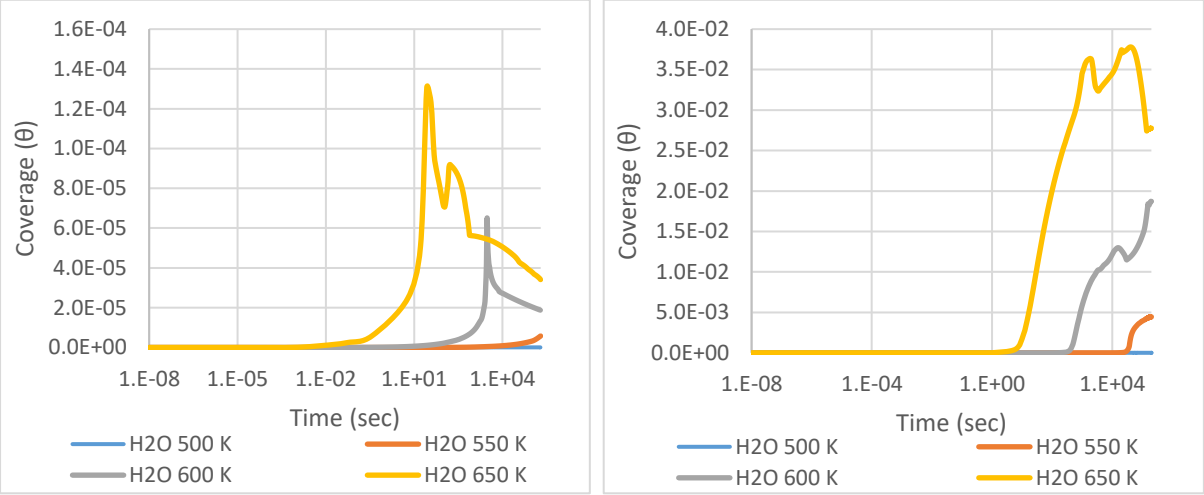

Figure 6-50: Change in coverage of surface H_2O for mean field model (Left) and QCA model (Right)

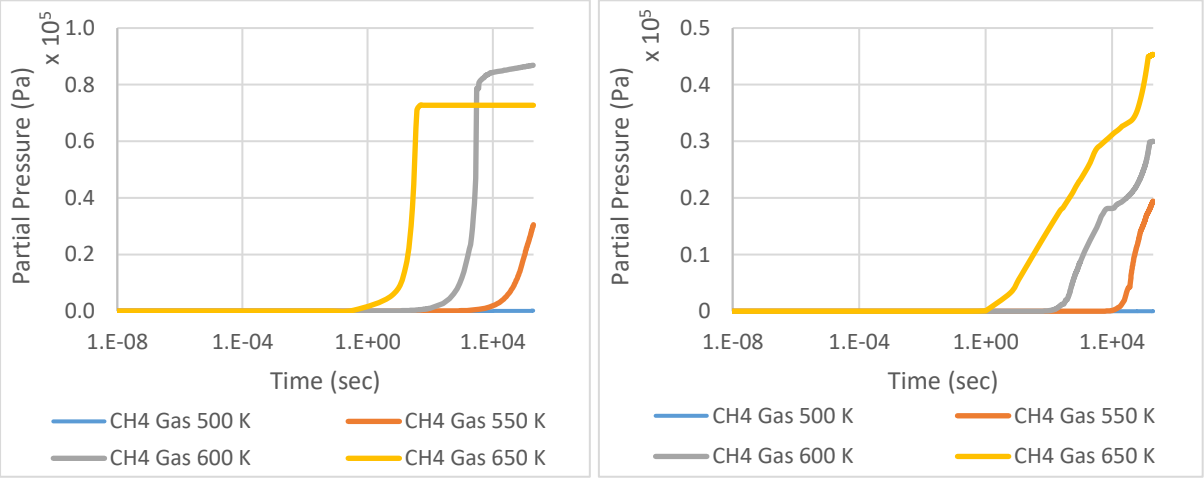

Figure 6-51: Change in partial pressure of CH_4 for mean field model (Left) and QCA model (Right)

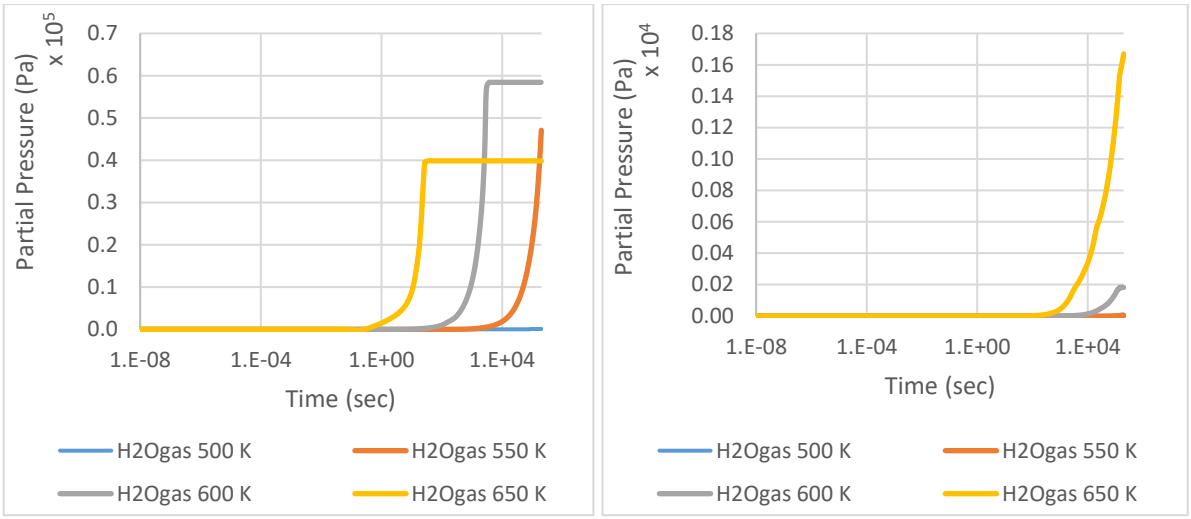

Figure 6-52: Change in partial pressure of H_2O for mean field model (Left) and QCA model (Right)

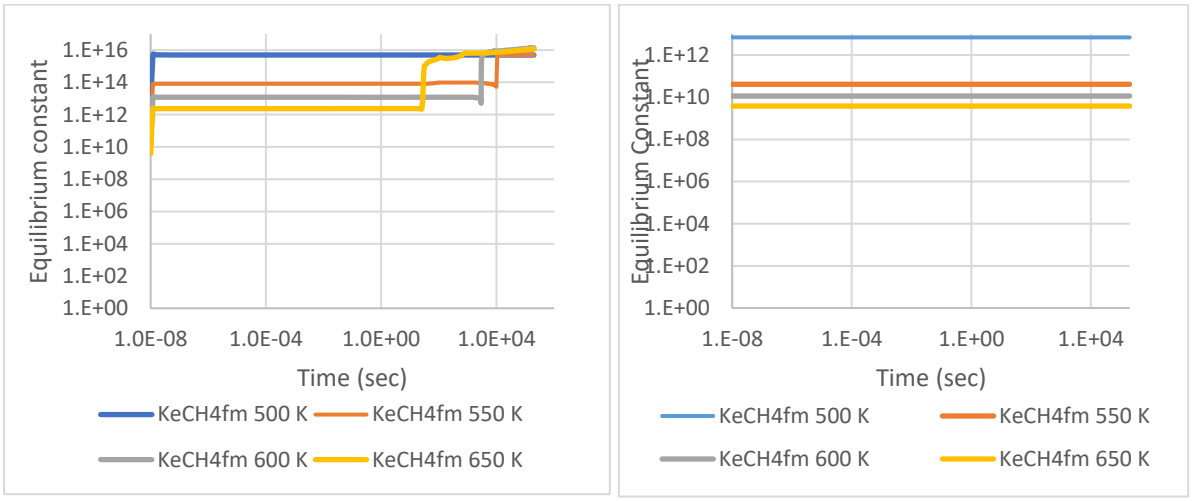

Figure 6-53: Change in equilibrium constant for CH_4 formation for mean field model (Left) and QCA model (Right)

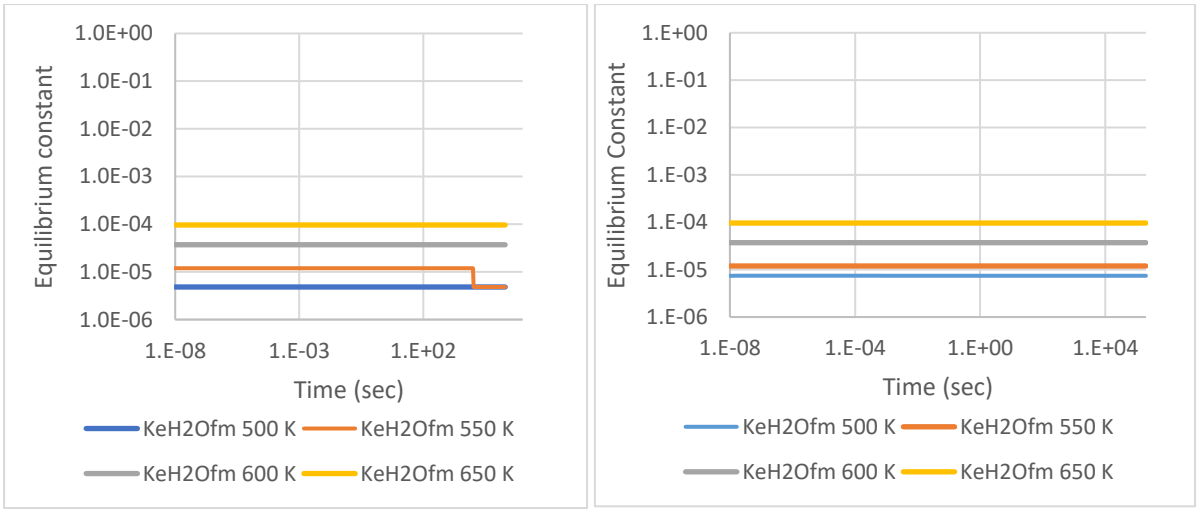

Figure 6-54: Change in equilibrium constant for H_2O formation for mean field model (Left) and QCA model (Right)

The coverage of CH_4, Figure 6-49, has similar features for both the mean field and QCA models but the mean field coverages are approximately two orders of magnitude larger. The mean field coverages are larger since additional CO is adsorbed and dissociated. The mean field coverages rise till there is

no more CO in the gas phase and decreases over time. For the QCA system the coverage of CH_4 increases as the coverages of CH, CH_2 and CH_3 increases but goes through a maximum and decreases as CH_4 is desorbed but CH_4 production is slowed due to increases in coverage of atomic O.

In Figure 6-50, for the mean field models, the H_2O coverage begins to increase gradually till there is no more CO in the gas phase and goes through a maximum and decreases till the end of the simulation, much like the mean field OH coverage. The QCA model coverages of H_2O is larger than the mean field model coverages. The coverage increases as the coverage of OH and O increases and goes through a local maximum and shortly after a local minimum (almost a kind of peak separation) where after the coverage increases with time and decreases for the 650 K model.

The partial pressures of CH_4, Figure 6-51, and H_2O, Figure 6-52, build up over time but the CH_4 partial pressures much larger than the partial pressures of H_2O, hence, rate of formation of H_2O is lower than that of CH_4. For the mean field model, the partial pressure increase and for the 600 K and 650 K models plateau once there is no more CO in the gas phase and the high coverage of atomic O hinders further CH_4 production. The same trends are seen for the partial pressure of H_2O but at a lower coverage. The quasi chemical models show increases in partial pressures of CH_4 and H_2O but at much lower magnitudes than the mean field models.

The equilibrium constant of CH_4 formation, Figure 6-53, show that the reaction remains largely endergonic in both systems for the duration of the simulation. The mean field system equilibrium constant increases as CO is adsorbed on the surface and again when atomic O builds up on the surface. The QCA model equilibrium constants remains fairly constant.

The equilibrium constant of H_2O formation, Figure 6-54, is constant for both systems at all temperatures except for the mean field model at 550 K where the equilibrium constant drops quickly as CO dissociates to approximately the same value as the 500 K model. The lateral interactions were included for this reaction but appear to balance out except for the mean field 550 K instance.

6.3.3 Conclusion

Microkinetic models of syngas methanation at 500 K, 550 K. 600 K and 650 K were investigated using different methods of lateral interactions implementation. Not only did the lateral interactions affect the kinetics of the model, but the methods of incorporating the lateral interactions showed different results.

The major differences include complete adsorption of CO on the surface at higher temperatures and larger partial pressures of products for the mean field models. The differences are evident from the differences in coverages and equilibrium constants of the reactions. The mean field approximation forces the inclusion of X-Y interactions if the coverage of either X or Y is large. The QCA approximation requires the coverage of both X and Y to be appreciable and hence a probability of X-Y is appreciable.

For both methods, a build-up of oxygen on the surface can be seen towards the end of the simulation, the results confirm that the iron-based catalyst need to undergo phase change to complete the catalytic cycle. The current set of works can be taken further by include catalytic phases changes i.e. Carbon diffusing into the surface and forming Iron carbides and Oxygen diffusing into the surface to form brittle magnetite.

Additional reaction steps such as hydrogen assisted CO dissociation, alcohol synthesis and longer hydrocarbon chains formation need to be included in the current models before any direct comparisons between the experimental and theoretical studies.

Concerning basic atomic hydrogenation as used here, it appears that carbon hydrogenation is much more favourable than oxygen hydrogenation. OH-OH combination to form H_2O does increases the

formation of water but not nearly to the same rates as methane formation. In order for water formation to occur at a similar rate to methane formation different reaction schemes need to be considered.

6.4 References

[1] Dumesic, J.A., *The microkinetics of heterogeneous catalysis*, An American Chemical Society Publication, **1993**.

[2] Davis, M.E., Davis, R.J., in:, *Fundam. Chem. React. Eng.*, vol. 217, MGraw-Hill Companies, New York **1993**, pp. 240–259.

[3] Hellman, A., Honkala, K., *J. Chem. Phys.* **2007**, 127, 194704: 1-6.

[4] Storsæter, S., Chen, D., Holmen, A., *Surf. Sci.* **2006**, 600, 2051–2063.

[5] Hansen, A.G., Well, W.J.M., Stoltze, P., *Top. Catal.* **2007**, 45, 219–222.

[6] Corma, A., Llopis, F., Monton, J.B., Weller, S.W., *Chem. Eng. Sci.* **1988**, 43, 785–792.

[7] Stoltze, P., Nørskov, J.K., *J. Catal.* **1988**, 110, 1–10.

[8] Stoltze, P., Nørskov, J.K., *Phys. Rev. Lett.* **1985**, 55, 2502.

[9] Ovesen, C. V, Clausen, B.S., Hammershøi, B.S., Steffensen, G., Askgaard, T., Chorkendorff, I., Nørskov, J.K., Rasmussen, P.B., Stoltze, P., Taylor, P., *J. Catal.* **1996**, 158, 170–180.

[10] Fishtik, I., Datta, R., *Surf. Sci.* **2002**, 512, 229–254.

[11] Honkala, K., Hellman, A., Remediakis, I.N., Logadottir, A., Carlsson, A., Dahl, S., Christensen, C.H., Nørskov, J.K., *Science* **2005**, 307, 555–8.

[12] Grabow, L.C., Gokhale, A. a., Evans, S.T., Dumesic, J. a., Mavrikakis, M., *J. Phys. Chem. C* **2008**, 112, 4608–4617.

[13] Ciobîcă, I.M., Frechard, F., van Santen, R.A., Kleyn, A.W., Hafner, J., *Chem. Phys. Lett.* **1999**, 311, 185–192.

[14] Chorkendroff, I., Niemantsverdriet, J.W., *Concepts of modern catalysis and kinetics*, vol. 2, Wiley-VCH, **2007**.

[15] Boudart, M., Djega-Mariadassou, G., *Kinetics of heterogeneous catalytic reactions*, Princeton University Press, Princeton **1984**.

[16] Govender, A., Ferré, D.C., Niemantsverdriet, J.W.H., *Chemphyschem* **2012**, 13, 1591–1596.

[17] Govender, A., Ferré, D.C., Niemantsverdriet, J.W.H., **2009**.

[18] Govender, A., Towards a Mechanism for the Fischer-Tropsch Synthesis on Fe(100) Using Density Functional Theory. Eindhoven University of Technology, **2010**.

[19] Hammond, S., *J. Am. Chem. Soc.* **1955**, 77, 334–338.

[20] Bartholomew, C.H., Farrauto, R.J., *Fundamentals of industrial catalytic processes*, John Wiley & Sons, **2011**.

[21] Moon, D.W., Dwyer, D.J., Bernasek, S.L., *Surf. Sci.* **1985**, 163, 215–229.

[22] Moon, D.W., Bernasek, S.L., Dwyer, D.J., Gland, J.L., *J. Am. Chem. Soc.* **1985**, 107, 4363–4364.

[23] de Jong, A.M., Niemantsverdriet, J.W., *Surf. Sci.* **1990**, 233, 355–365.

[24] Fichthorn, K., Miron, R., *Phys. Rev. Lett.* **2002**, 89, 2–5.

[25] Jansen, A.P.J., *Comput. Phys. Commun.* **1995**, 86, 1–12.

[26] Payne, S.H., Zhang, J., Kreuzer, H.J., *Surf. Sci.* **1992**, 264, 185–196.

[27] Meng, B., Weinberg, W.H., *J. Chem. Phys.* **1995**, 102, 1003–1013.

[28] Makeev, A.G., Kevrekidis, I.G., *Comput. Chem. Eng.* **2014**, 60, 172–181.

[29] Lehner, B., Hohage, M., Zeppenfeld, P., *Chem. Phys. Lett.* **2001**, 336, 123–128.

[30] Houle, F.A., *Surf. Sci.* **1995**, 338, 329–346.

[31] Van Helden, P., Van den Berg, J.-A., Weststrate, C.J., *ACS Catal.* **2012**, 2, 1097–1107.

[32] Zhdanov, V.P., in:, *Elem. React. Steps Heterog. Catal.*, Springer, **1993**, pp. 359–376.

[33] Bromfield, T.C., Ferré, D.C., Niemantsverdriet, J.W., *Chemphyschem* **2005**, 6, 254–60.

[34] Lamba, H., Stuart, A.M., *BIT Numer. Math.* **1998**, 38, 751–780.

[35] MATLAB User's Guide, *The mathworks*, vol. 5, **1998**.

[36] Nielsen, J., D'Avezac, M., Hetherington, J., Stamatakis, M., *J. Chem. Phys.* **2013**, 139, 224706.

[37] Lo, J.M.H., Ziegler, T., *J. Phys. Chem. C* **2007**, 111, 11012–11025.

[38] Sorescu, D., *Phys. Rev. B* **2006**, 73, 155420.

[39] Mavrikakis, M., Gokhale, A.A., *Am. Chem. Soc.* **2005**, 229, 861–865.

[40] Erley, W., McBreen, P.H., Ibach, H., *J. Catal.* **1983**, 84, 229–234.

[41] Lox, E.S., Froment, G.F., *Ind. Eng. Chem. Res.* **1993**, 32, 71–82.

[42] Lox, E.S., Froment, G.F., *Ind. Eng. Chem. Res. States)* **1993**, 32.

[43] Govender, A., Ferré, D.C., Niemantsverdriet, J.W., *Chemphyschem* **2012**, 13, 1583–90.

[44] Eder, M., Terakura, K., Hafner, J., *Phys. Rev. B* **2001**, 64, 115426.

[45] Sorescu, D.C., *Catal. Today* **2005**, 105, 44–65.

[46] Sorescu, D., Thompson, D., Hurley, M., Chabalowski, C., *Phys. Rev. B* **2002**, 66, 35416.

[47] Sandler, S.I., *Chemical, biochemical, and engineering thermodynamics*, vol. 1, John Wiley & Sons Hoboken, NJ, **2006**.

[48] van Helden, P., van Steen, E., *J. Phys. Chem. C* **2008**, 112, 16505–16513.

[49] Chonco, Z.H., Lodya, L., Claeys, M., Van Steen, E., *J. Catal.* **2013**, 308, 363–373.

7 Conclusions

The purpose of this work was to gain a better understanding of the interactions that exist between adsorbates on a catalytic surface, its magnitude and substance, and the effect they have on the adsorption and reaction energies.

Different configurations of CO, C, O, H, CH, CH_2, CH_3, were used to explore nearest-neighbour and next-nearest-neighbour adsorbate interactions on an Fe(100) surface using periodic density functional theory (DFT) calculations.

CO-CO interactions were studied to determine if lateral interactions could be understood at low coverages, less than 0.5 ML, and then extrapolated for larger coverages, 0.5 to 1 ML. The results showed that at a coverage of 0. 25 ML CO the heat of adsorption can vary by as much 0.28 eV/CO. The variation was a result of repulsive nearest-neighbour interactions which are approximately 0.10 - 00.15 eV/CO. Next nearest neighbour interactions showed little overall variation but significant variations in potential energy, which is for the most part electro static potential energy, and kinetic energy. For both nearest neighbour and next nearest neighbour interactions there was a strong relationship between the change in kinetic and potential energy. If this relationship is truly understood, then the total energy can be calculated knowing either kinetic or potential energy instead of both. To extrapolate the interaction for larger coverages an approximation of 0.15 eV/CO for nearest neighbour interactions was used over a distribution of unique configurations for all c(4x4) unit cells at coverages of 1/16 to 16/16 ML. The results were in agreement with literature studies at these coverages. To scale the model for temperature an average variation in vibrational frequency for nearest neighbour interactions was used for temperature corrections and a Quasichemical distribution with the same 0.15 eV nearest neighbour interactions was used to account for lateral interactions. The result was an energy surface that shows the decrease in heat of adsorption with increasing coverage and temperature.

The interspecies or same species interactions for basic methanation species showed that overall nearest neighbour interactions are typically repulsive, with the exception of OH, and overall next-nearest neighbour interactions are attractive but small enough to be considered negligible (i.e. within DFT calculation error). When these interactions are broken down into their electrostatic, kinetic and exchange-correlation components we see that even while the overall lateral interactions are small or negligible, large deviations of the individual components can exist. There again was a strong relationship between potential and kinetic energy. When scaled for temperature the interactions range from largely repulsive (CH_3-CH_3 nearest neighbours, repulsive interactions of 0.6 eV @ 600K) to negligible (H-H nearest neighbour, repulsive interaction of approx. 0.02 eV @ 600 K) and moderately attractive (OH-OH next nearest neighbour, attractive interaction of 0.16 eV @ 600K).

In Chapter 5 the intraspecies interactions were investigated and the results were similar to the interspecies interactions, overall nearest neighbour interactions are typically repulsive, with the exception of OH-H, and overall next-nearest neighbour interactions are small and a mix of repulsive and attractive interactions. C-X interactions showed significant attractive interactions. There again was a strong relationship between potential and kinetic energy.

Overall, nearest neighbour interactions are typically repulsive and much larger than next nearest neighbour interactions. While this is not a unique conclusion it did allow us to create lateral interaction matrices that vary with temperature for the initial stages of the Fischer Tropsch process.

The study has shown that lateral interactions can be broken down into kinetic and potential energy and a relationship exists between these component energies. This can be rationalized by recalling that the kinetic energy is related to the shape of the electron cloud and the shape of the electron cloud is related to the electrostatic potential energy.

A microkinetic model of CO TPD on Fe(100) was constructed. The mean field model does show an improvement from the model with no lateral interactions but when comparing it to the QCA model the additional refinement makes a significant difference. The QCA approximation shows a significant improvement to the mean field approximation since the lateral interactions are influence by local coverage, number of neighbours, and not necessarily global overage. The QCA TPD results were in good agreement with the experimental spectrum for desorpton of associatively adsorbed CO. The results here show that strong lateral interactions can create pre-shoulder and post-shoulders. It is important to distinguish between the effects of strong lateral interactions and the presence of adsorbed species on different sites.

Microkinetic models of syngas methanation over Fe(100) were also constructed showing that lateral interactions can have a significant effect on individual reaction steps.

It should be noted that even though the overall change in energy is different from the experimental results or even the ideal gas approximation, the largest sources of error in these calculations is the approximation of the gas phase. This is also why the largest differences between the literature work is for the adsorption energies. Variations in CO adsorption are as much as 0.6 eV. Furthermore, the physisorption of CH_4 on Fe(100) is requires additional precision and investigation to calculate at a molecular level.

The major differences between the methods of lateral interaction incorporation were seen when investigating the coverages and ΔG formation of CH_x species. The MF approximation forces the inclusion of X-Y interactions if the coverage of either X or Y is large. The QCA approximation requires the coverage of both X and Y to be appreciable and hence a probability of X-Y is appreciable.

For both methods, a build-up of oxygen on the surface can be seen towards the end of the simulation, the results confirm that the iron-based catalyst need to undergo phase change to complete the catalytic cycle. The current set of work can be taken further by include catalytic phases changes i.e. Carbon diffusing into the surface and forming Iron carbides and Oxygen diffusing into the surface to form brittle magnetite.

Appendix

A. Convergence and trends of component energies

The Kohn-Sham [1] energy functional can then be written as:

$$E(\rho) = \iint \frac{\rho(r')\rho(r)}{2|r'-r|} dr'dr + \int V(r) \cdot \rho(r)\, dr + T_0(\rho) + E_{XC}(\rho) \qquad \text{(A.1)}$$

Here T_0 is the kinetic energy of the reference system and E_{XC} is a combination of the exchange energy, correlation energy and the change in kinetic energy between the reference and real systems. It is important to note that the exact expression for E_{XC} is unknown[2]. Thus the accuracy with which the energy functional can be minimized is dependent on the accuracy of E_{XC}.

In order to quantify the lateral interactions all the terms included in the Hamiltonian will be considered. For CASTEP[3] the resulting energies are the kinetic energy, Hartree energy, local and non-local pseudopotential energies, exchange-correlation energy, Ewald energy and non-Coulombic energy.

The non-Coulombic energy accounts for this deviation [4]. Hartree, Ewald, pseudopotential and Non-Coulombic energies combined will give an overall electrostatic interaction.

The exchange-correlation potential includes the effects of the Pauli Exclusion Principle. It should be noted that all exchange-correlation functionals are only approximations. This will be considered a general correction energy term which accounts for the deviations from ideal systems.

The remaining energy is the kinetic energy. The kinetic energy operator is the sum of the Laplacian operator over all points, seen in equation 2.8 below. This means that the kinetic energy is the sum of the relative magnitude of the curvature of the wave function at each point. A simple analogy can be made with water waves where the water moves fastest in the regions of highest curvature, i.e. the peaks and troughs.

$$\hat{T} = \frac{1}{2}\sum_{i=1}^{N} \nabla_i^2 \qquad \text{(A.2)}$$

The kinetic energy gives us an idea of the shape of the electron density. A system with that has sharper changes in concavity will have a higher kinetic energy. This change in concavity could be the result of a number of changes to the system including large columbic interactions forcing a change in electron density and/or changes in position and geometry that brings about a large change in electron density.

Two case studies were considered to investigate the convergence of the component energies. The first will test the convergence of 1 ML CO on Fe(100) with vacuum spacing and the second will test the convergence of 1 ML CO on Fe(100) with number of relaxed layers. In each case the convergence of total, kinetic and potential energies are shown.

A.1 Methodology

The DFT calculations were completed using CASTEP [3], as implemented in the Materials Studio software package [5]. The exchange-correlation energy was calculated using the generalized gradient approximation (GGA), making use of the RPBE functional [6]. A Gaussian smearing width of σ = 0.1 eV was utilized in all calculations. The ion-electron interactions were approximated using ultrasoft pseudopotentials with core corrections and a cutoff energy was set at 400 eV. Spin-polarization was allowed for all calculations.

For the variation with vacuum spacing all 5 layers of the slab were left to relax. The vacuum spacing was systematically increased and each configuration underwent geometry optimization calculation.

For the conversion with number of layers relaxed the vacuum spacing was set to 12 Å. A geometry optimization calculation was conducted for each configuration considered.

A.2 Change in component energies with vacuum spacing

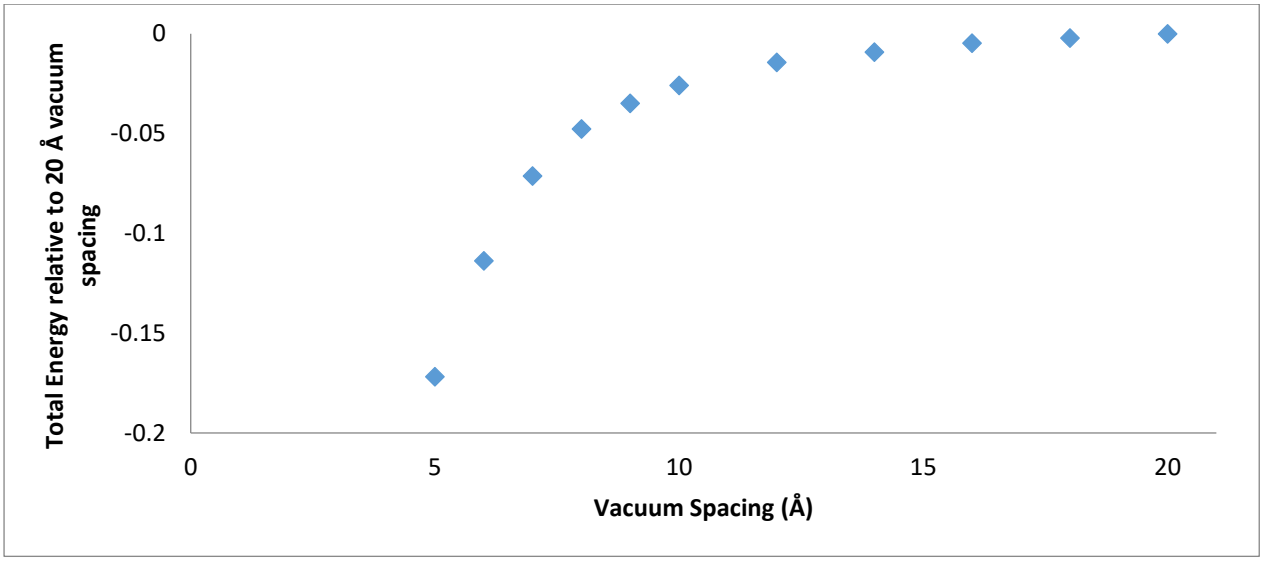

Figure A-1: The convergence of total energy with vacuum spacing

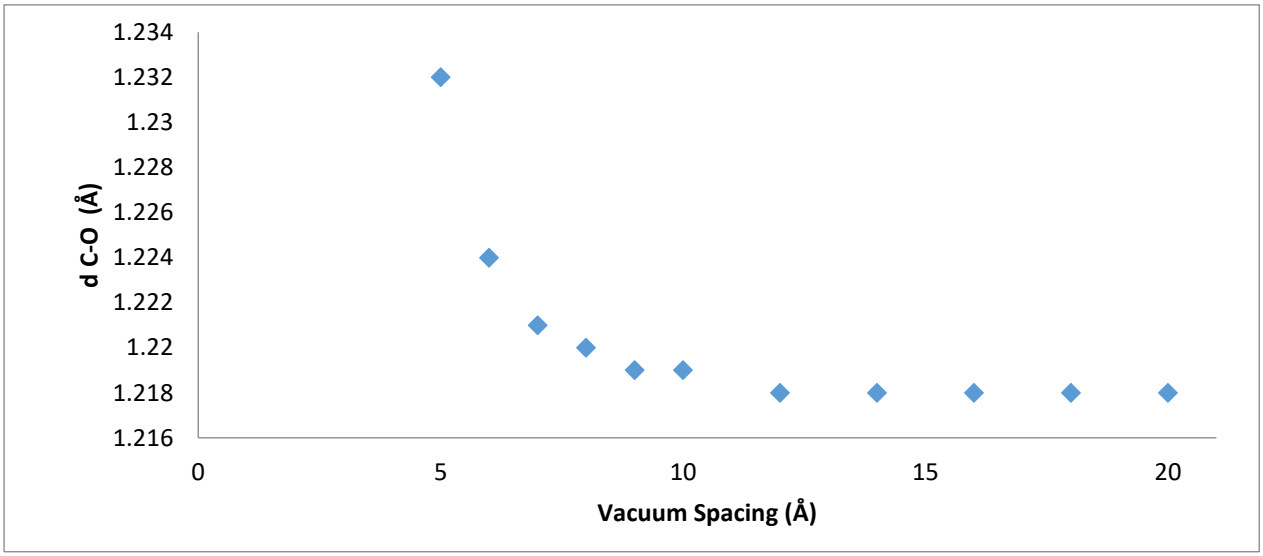

Figure A-2: The convergence of C-O distance with vacuum spacing

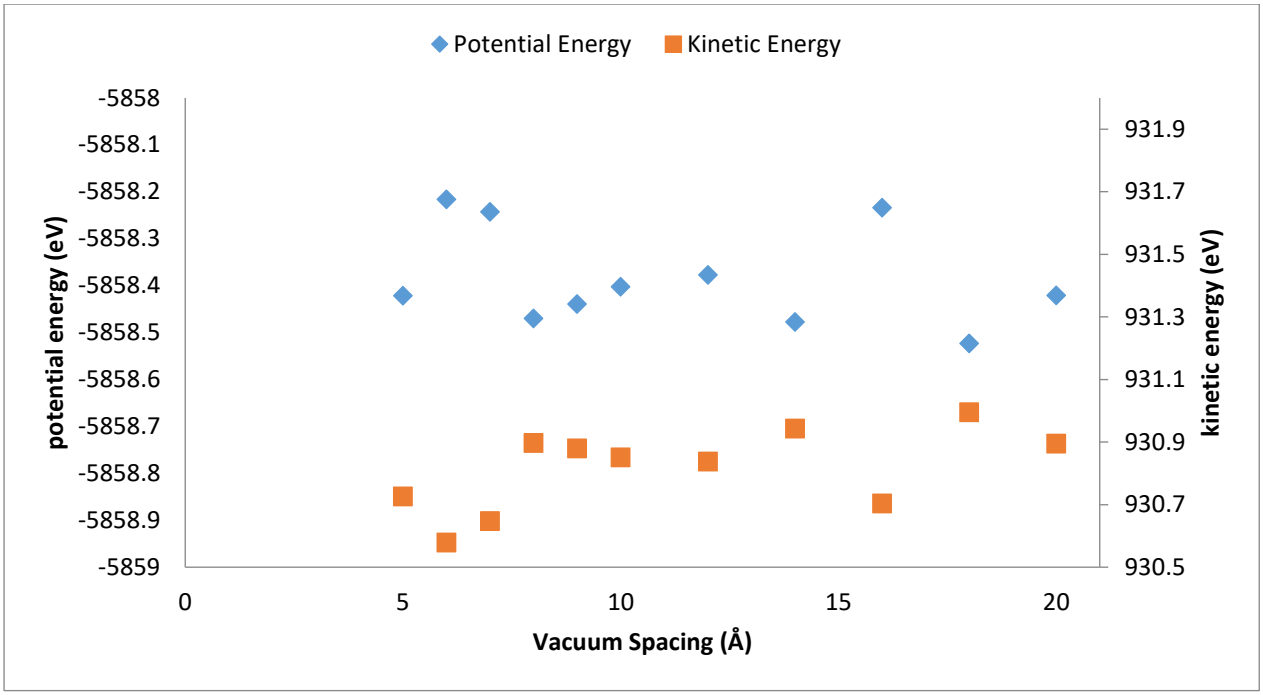

Figure A-3: Variation in kinetic and potential energies with vacuum spacing.

Figure A-1 shows total energy converges as the vacuum spacing is increased. This is the result of the metal slab of the neighbouring unit cells (above and below) displaying long range interactions. This interaction is diminished as the vacuum spacing and hence distance between the slabs increases. This interaction also has an effect on the C-O distance as it converges with increasing vacuum spacing, Figure A-2.

Interestingly the kinetic and potential energies don't appear to converge themselves with increasing vacuum spacing, Figure A-3. There does however appear to be a relationship between the change kinetic and potential energies. This could mean the it is the relationship between the kinetic and potential energies that is converged with increasing vacuum spacing.

A.3 Relaxed Layers

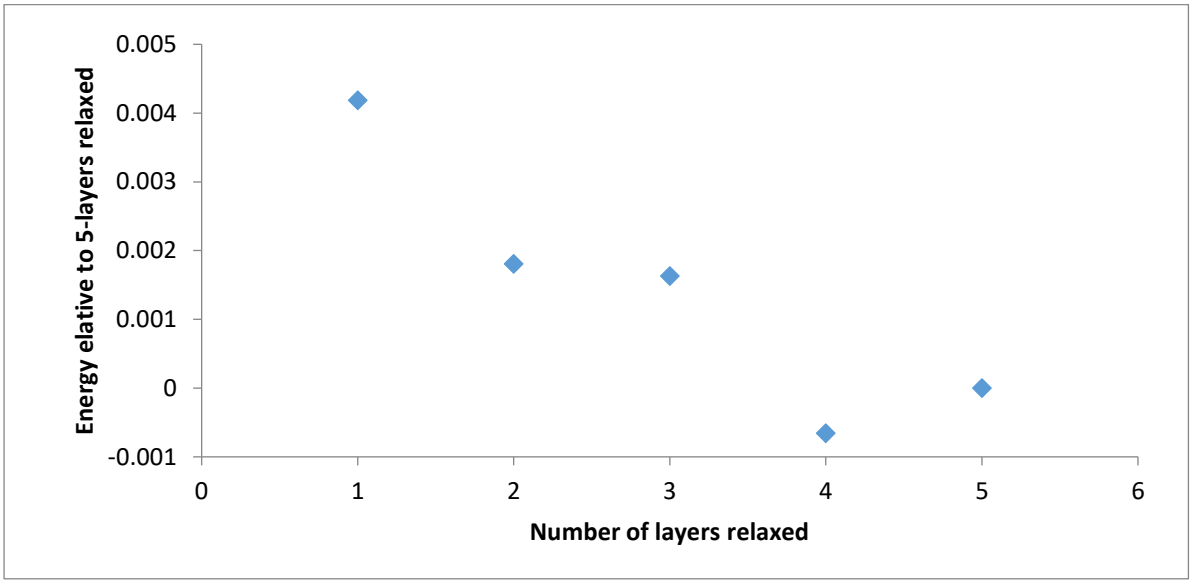

Figure A-4: The change in total energy with number of layers relaxed

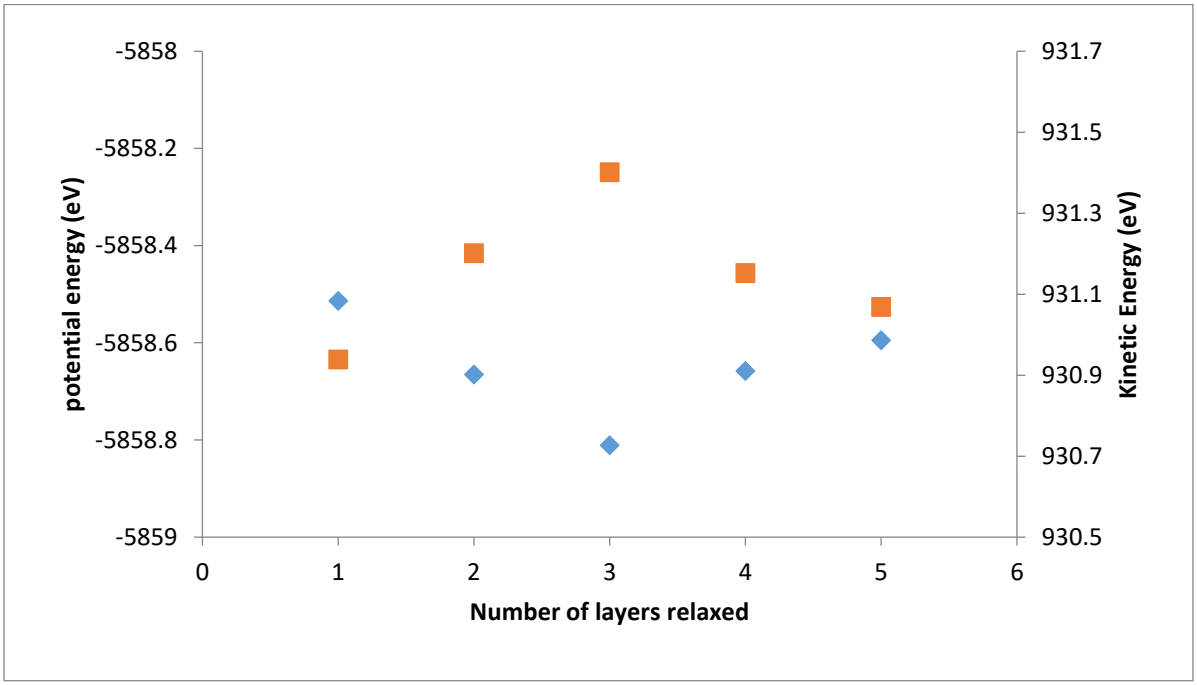

Figure A-5: The change in total energy with number of layers relaxed

The results from Figure B-4 show that the total energy varies by less than 0.005 eV as the number of relaxed layers is increased. This indicates the starting configuration was already a good approximation of 1 ML CO on Fe(100). The C-O distances remained constant at 1.219 Å for configurations tested. As with the vacuum spacing, we see the kinetic and potential energies don't appear to converge themselves with increasing numbers of layers relaxed, Figure B-5. Again, there appears to be a relationship between the change kinetic and potential energies.

The results from chapters 3-5, also show that there exists a relationship between the kinetic and potential energies. The relationship appears linear for all species but some species do appear to correlate better than others. It is interesting to note that the slope of this relationship can be used to find the binding energy of the species involved. This is

$$E_{bind} = E_{Kin-bind} + E_{Pot-bind} = (1 + \frac{1}{m}) \cdot E_{Pot-Ads} = (1 + m)E_{Kin-Ads} \qquad \text{(A.3)}$$

Where E_{bind} is the binding energy of and adsorbate, $E_{Kin-bind}$ is the kinetic energy of binding, $E_{Pot-bind}$ is the potential energy of binding and m is the slope $\frac{\Delta E_{Pot}}{\Delta E_{Kin}}$.

In both cases the total energy appears to converge, but the kinetic and potential component energies do not. If there is indeed a relationship between the kinetic and potential energies than the relationship must converge i.e. as the total energy converges, the relation between kinetic and potential energy becomes more accurate.

A.4 Component energies of interaction energies

In order to find an energetic breakdown for the lateral interactions, all the terms included in the Hamiltonian need to be considered. For CASTEP [26] the resulting energies are the kinetic energy, Hartree energy, local and non-local pseudopotential energies, exchange-correlation energy, Ewald energy and non-Coulombic energy.

Hartree, Ewald, pseudopotential and Non-Coulombic energies combined will give an overall electrostatic interaction. The exchange-correlation potential includes the effects of the Pauli Exclusion Principle and long range dipole interactions not described by the classical electrostatic interactions.

The kinetic energy gives us an idea of the shape of the electron density. A system with sharper changes in concavity will have a higher kinetic energy.

The energy contribution to the total electronic energy of each of the terms was considered and the change in each energy on adsorption was considered. This was calculated using the same procedure to calculate the integral adsorption energy was calculated. This means:

$$E_{i,ads} = \frac{E_{i,(Fe+nX)} - E_{i,(Fe\ Slab)} - n \cdot E_{i,X}}{n} \qquad (4.3)$$

Where i is either the kinetic energy, Hartree energy, local and non-local pseudopotential energies, exchange-correlation energy, Ewald energy or non-Coulombic energy.

In Figure A-6, the relationship between kinetic and potential energy is shown of all the species considered in this study. The relationship appears linear for all species but some species do appear to correlate better than others. It is interesting to note that the slope of this relationship can be used to find the binding energy of the species involved. This is

$$E_{bind} = E_{Kin-bind} + E_{Pot-bind} = (1 + \frac{1}{m}) \cdot E_{Pot-Ads} = (1 + m) E_{Kin-Ads}$$

The energy contribution to the total electronic energy of each of the terms was considered and the change in each energy with each lateral interaction was considered. This was calculated using the same procedure to calculate the excess energy:

$$E_{Excess\_i} = E_{AB\_i} - E_{A,0.25ML\_i} - E_{B,0.25ML\_i} + E_{xFe\_i} \qquad (A\text{-}4)$$

Where i is either the kinetic energy, Hartree energy, local and non-local pseudopotential energies, exchange-correlation energy, Ewald energy or non-Coulombic energy.

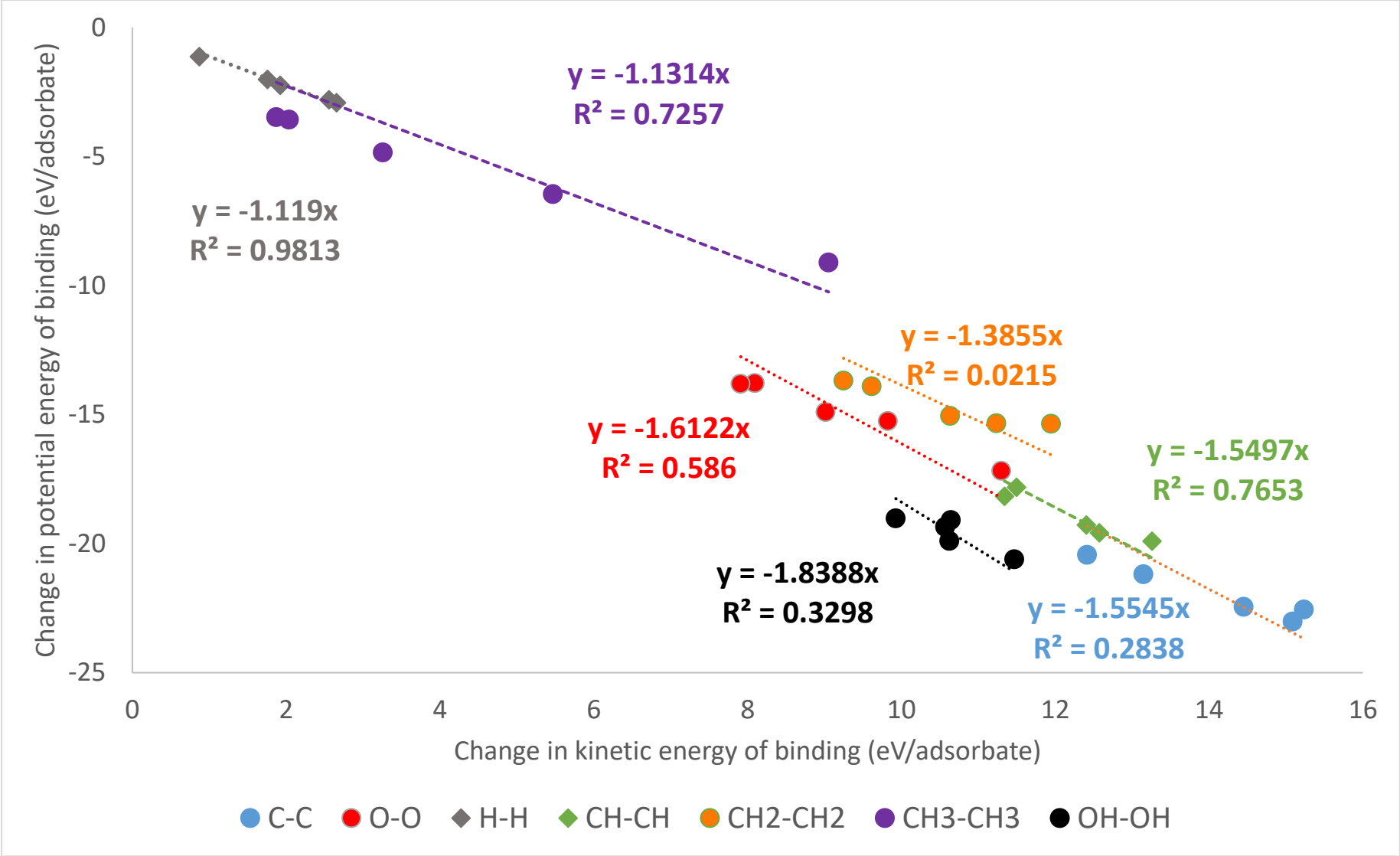

Figure A-6: The relationship between the kinetic and potential energy of binding

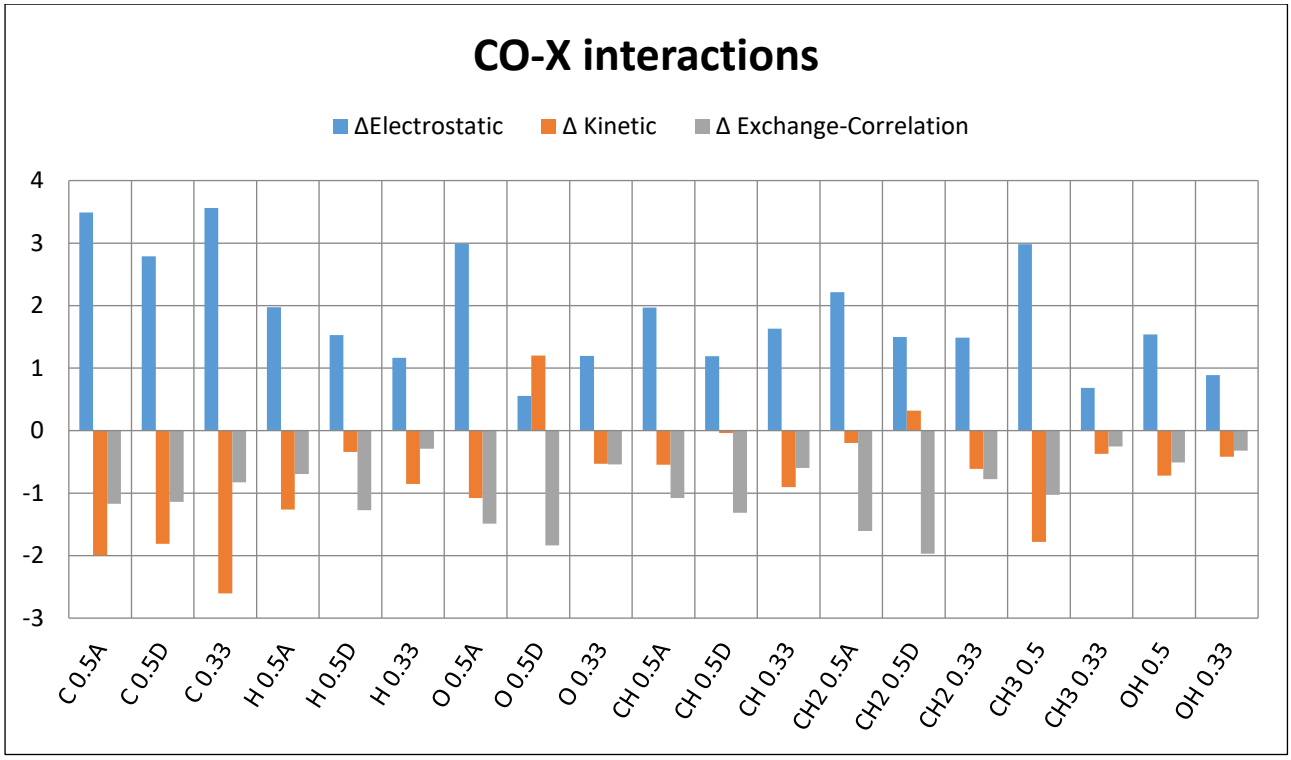

Figure A-7: Energetic breakdown of CO-X interactions on Fe(100)

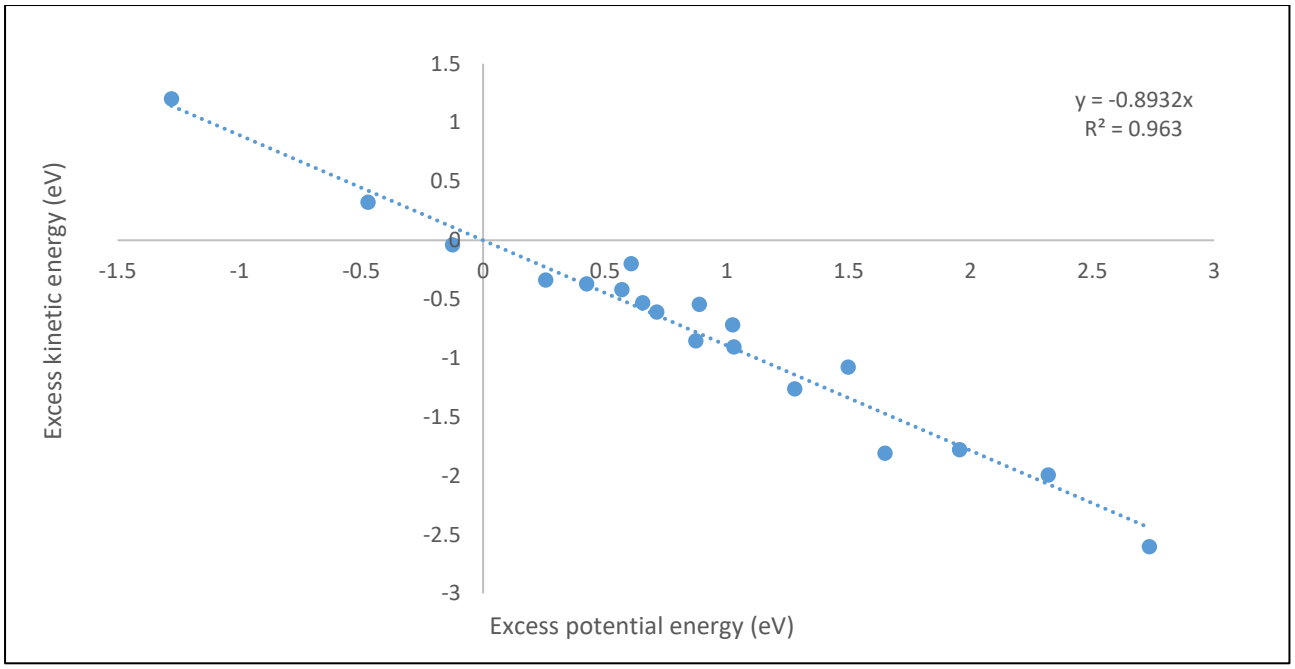

Figure A-8: linear relationship between excess kinetic and potential energy of CO-X interactions

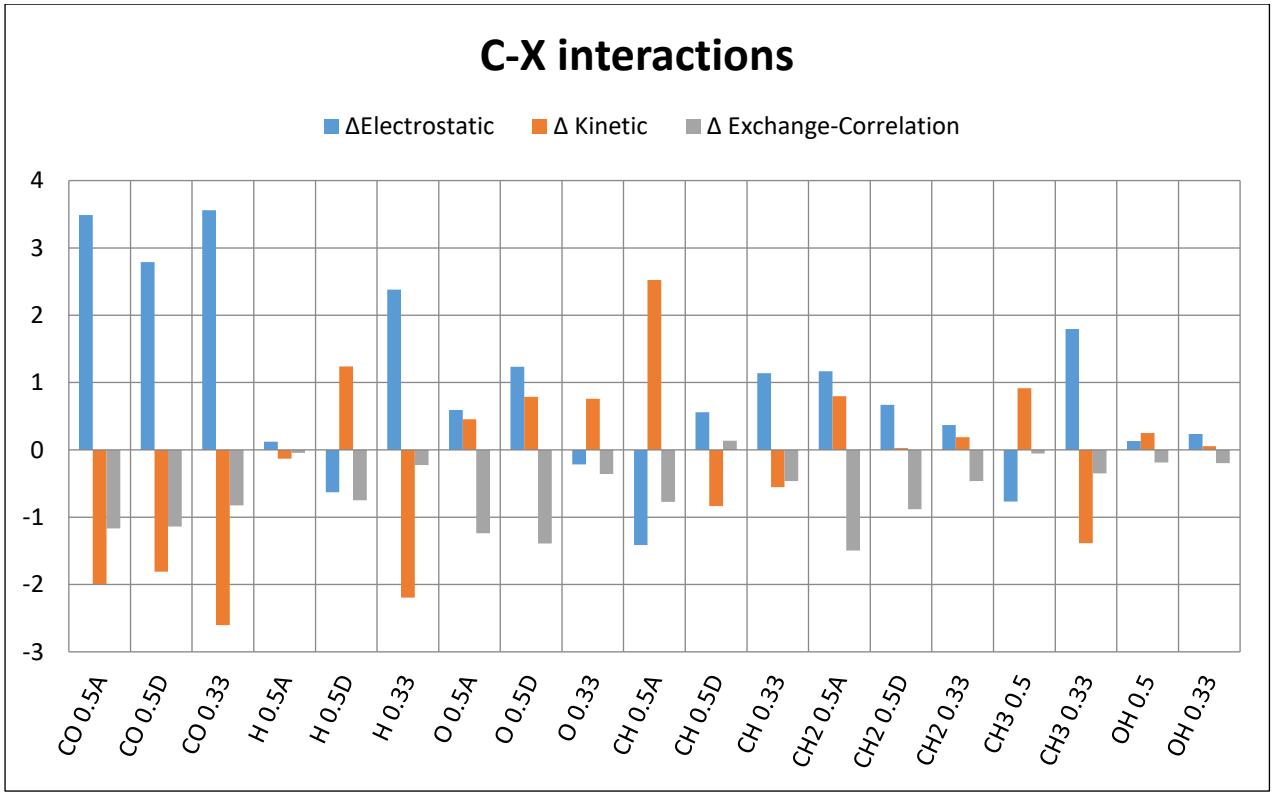

Figure A-9: Energetic breakdown of C-X interactions on Fe(100)

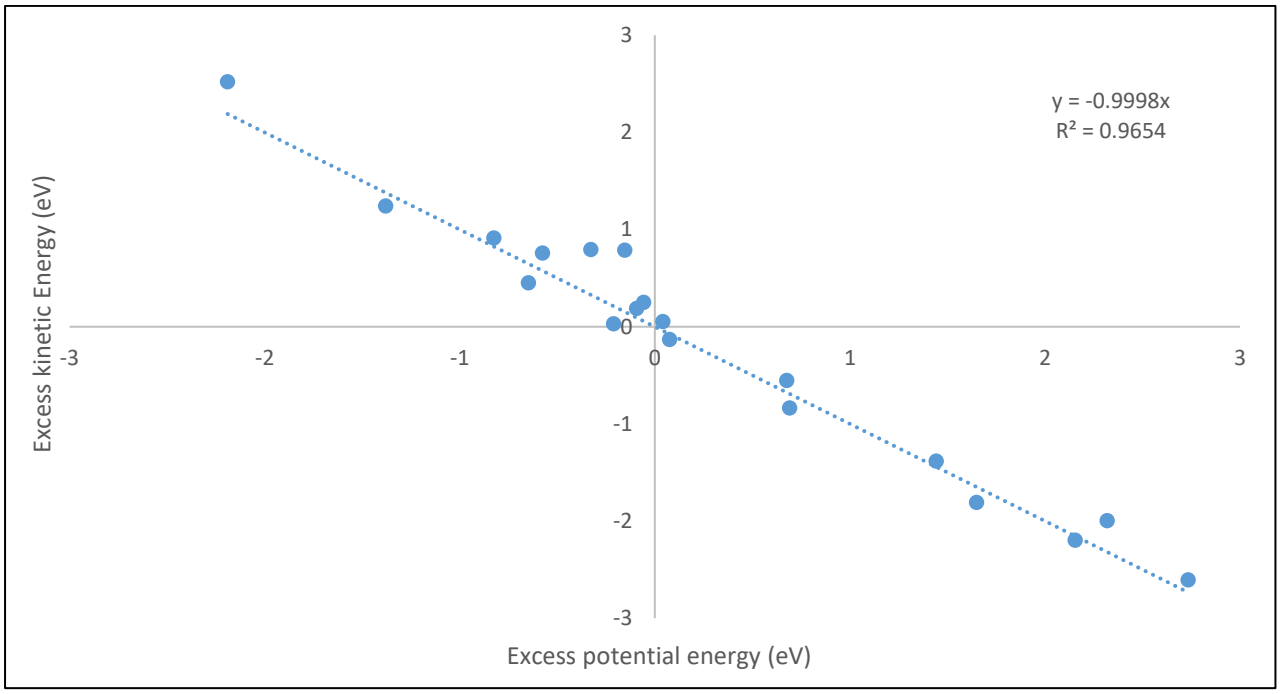

Figure A-10: linear relationship between excess kinetic and potential energy for C-X interactions

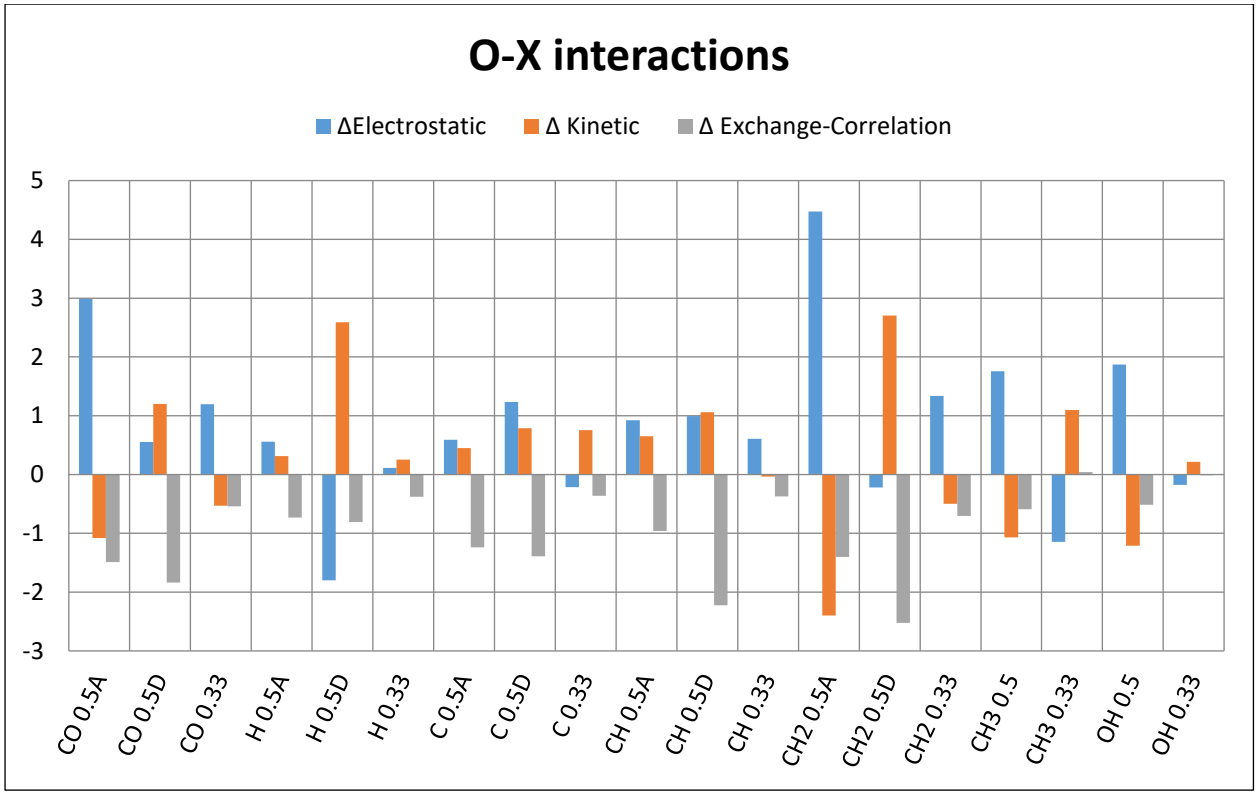

Figure A-11: Energetic breakdown of O-X interactions on Fe(100)

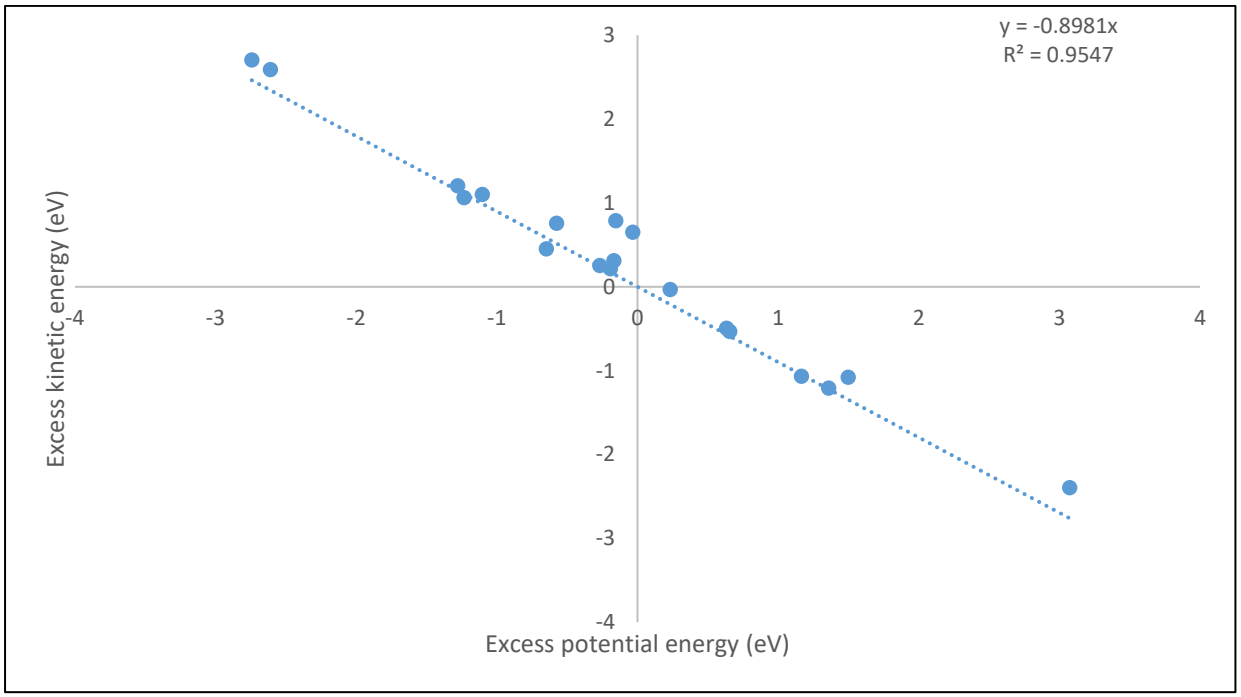

Figure A-12: Linear relationship between excess kinetic and potential energy for O-X interactions.

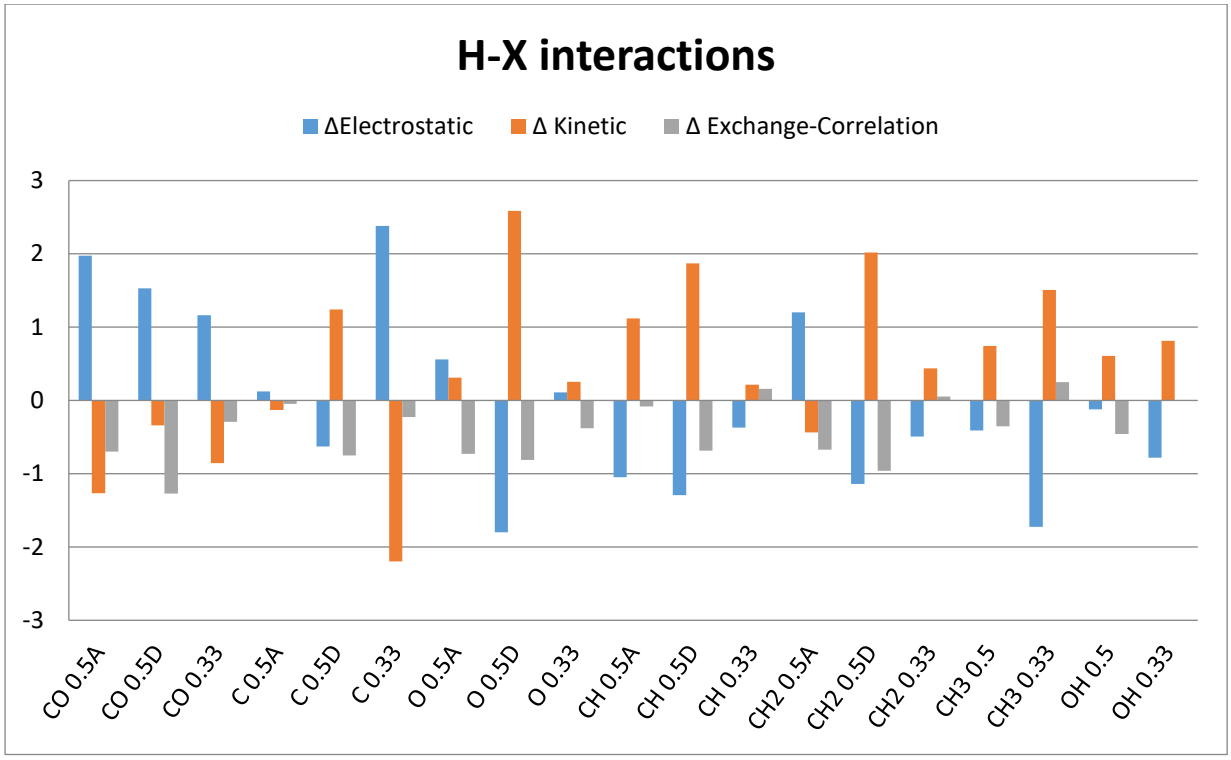

Figure A-13: Energetic breakdown of H-X interactions on Fe(100)

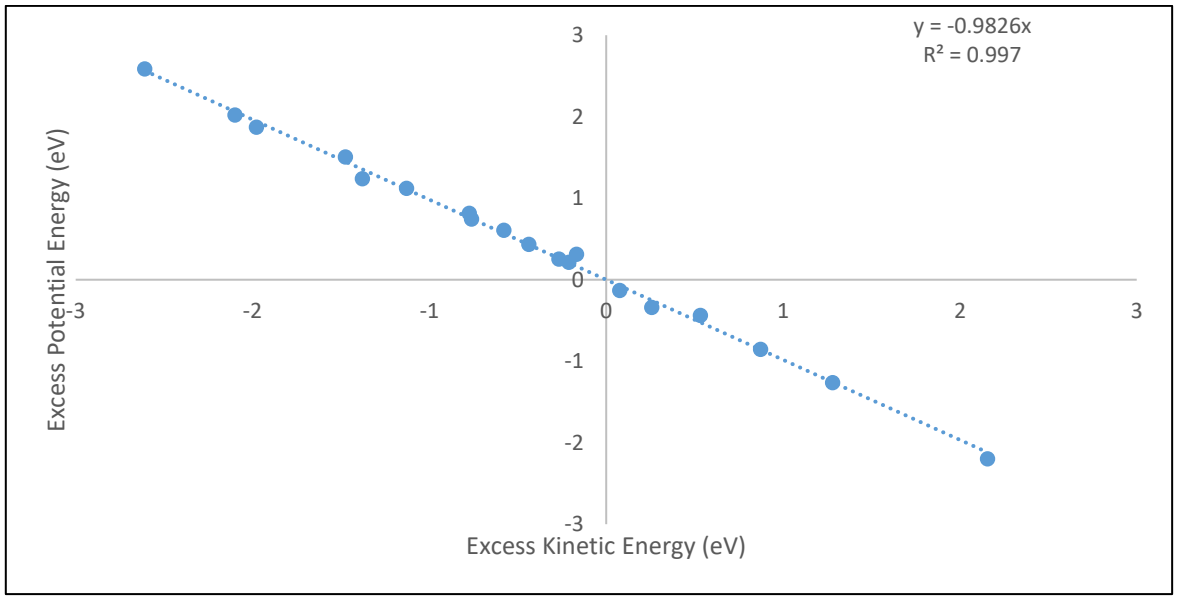

Figure A-14: linear relationship between excess kinetic and potential energy for H-X interactions

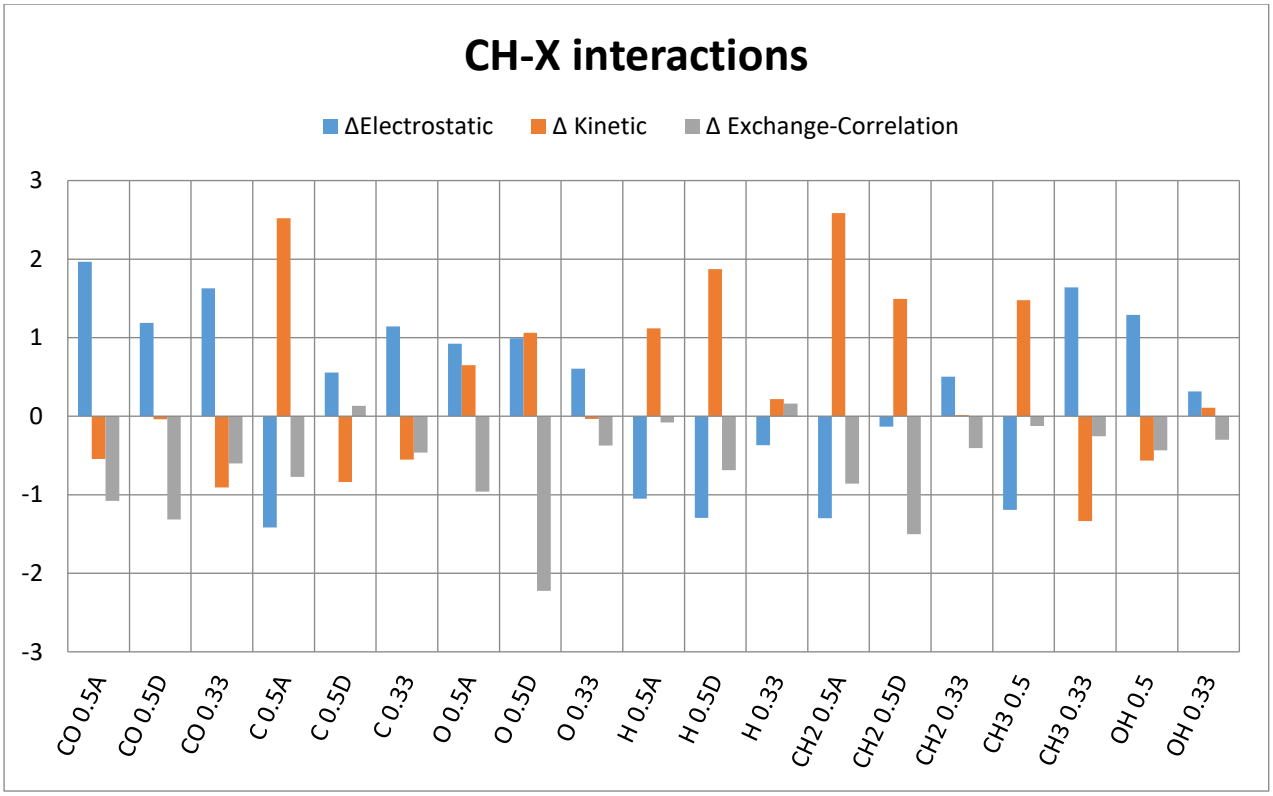

Figure A-15: Energetic break down of excess energies of CH-X interactions of Fe(100)

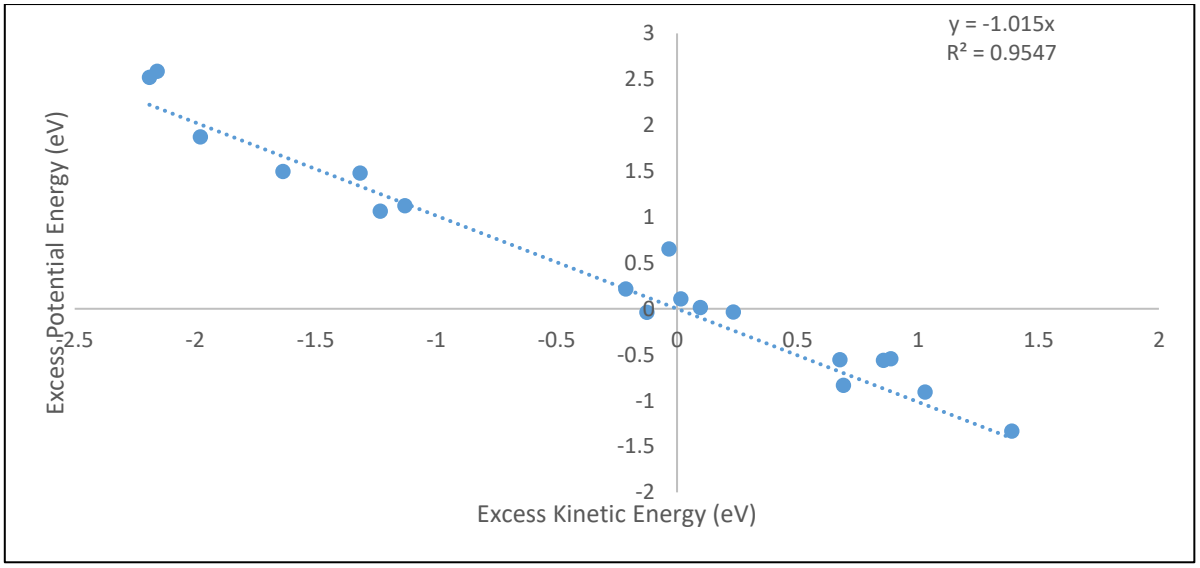

Figure A-16: linear relationship between excess kinetic and potential energy for CH-X interactions

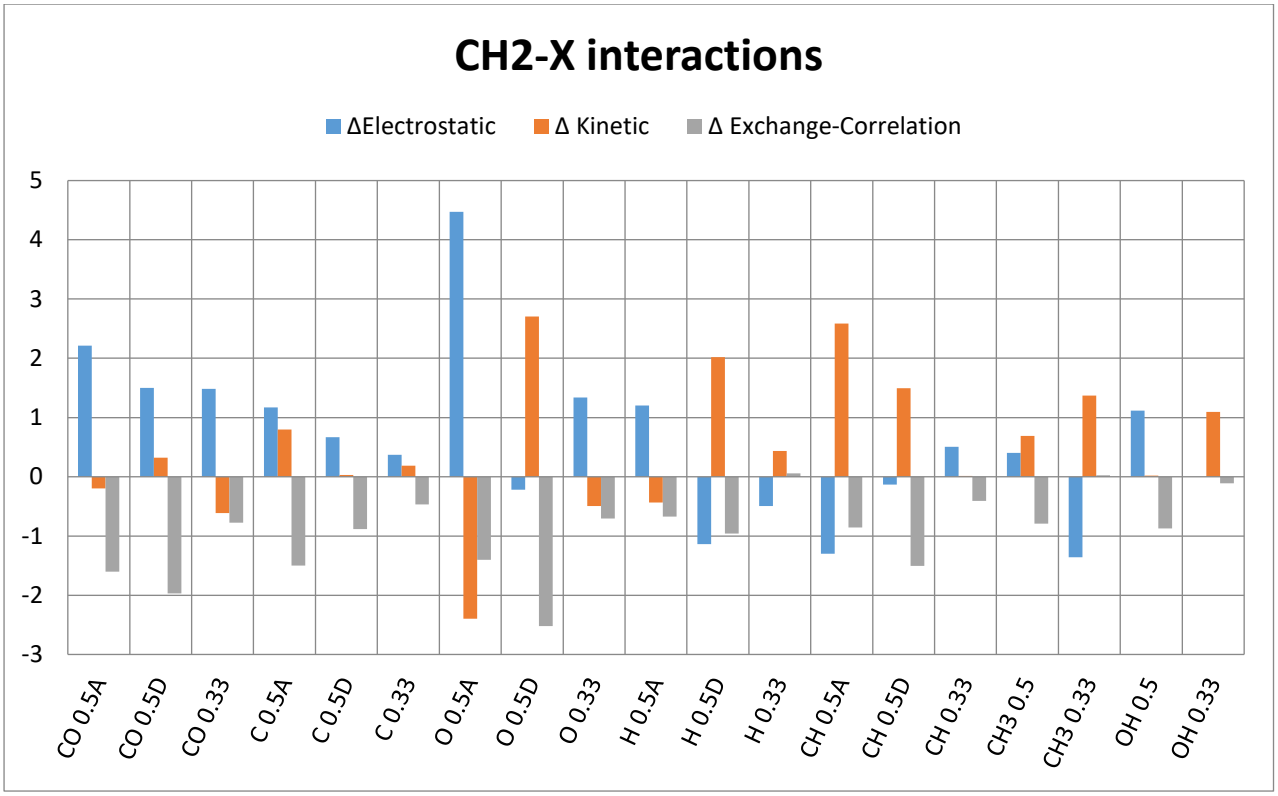

Figure A-17: Energetic breakdown of the Excess energy of CH_2-X interactions on Fe(100)

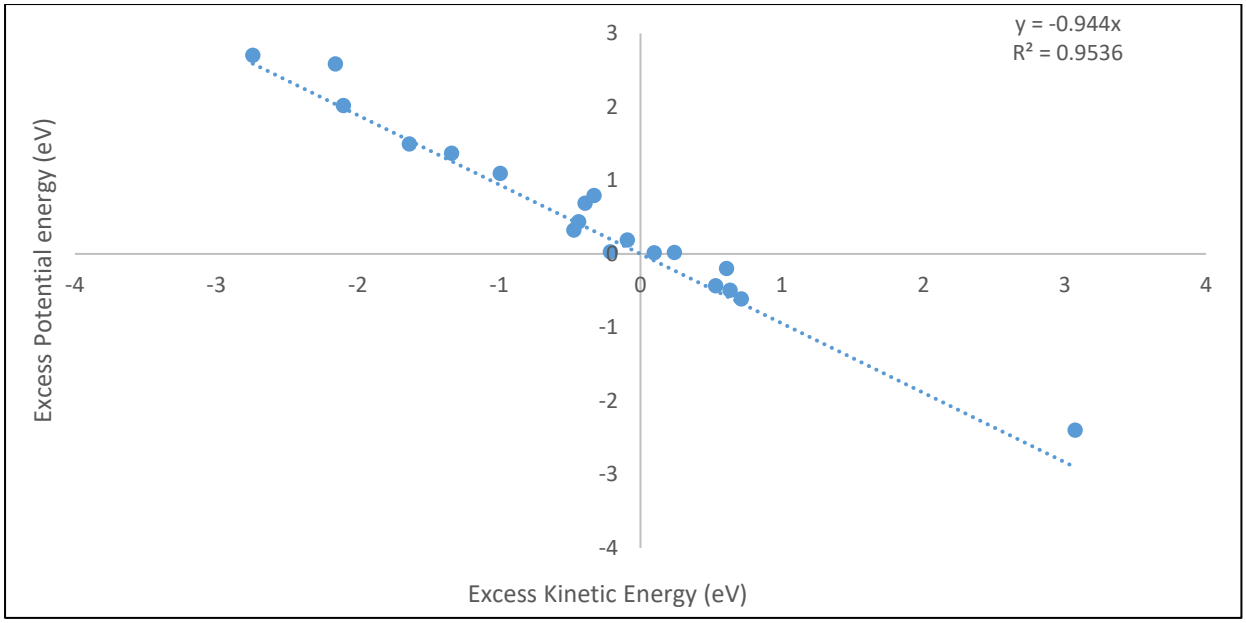

Figure A-18: Linear relationship between the excess kinetic energy and excess potential energy for CH_2-X

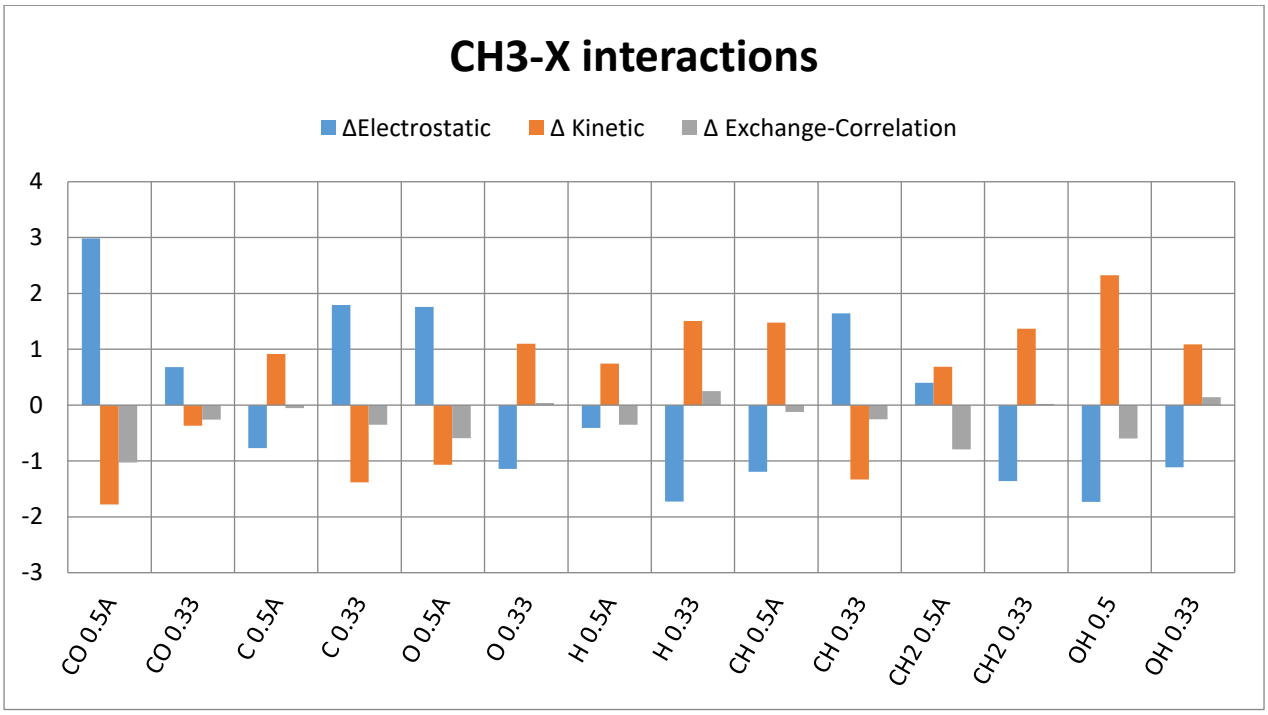

Figure A-19: Energetic breakdown of the excess energies of CH_3-X interactions on Fe(100)

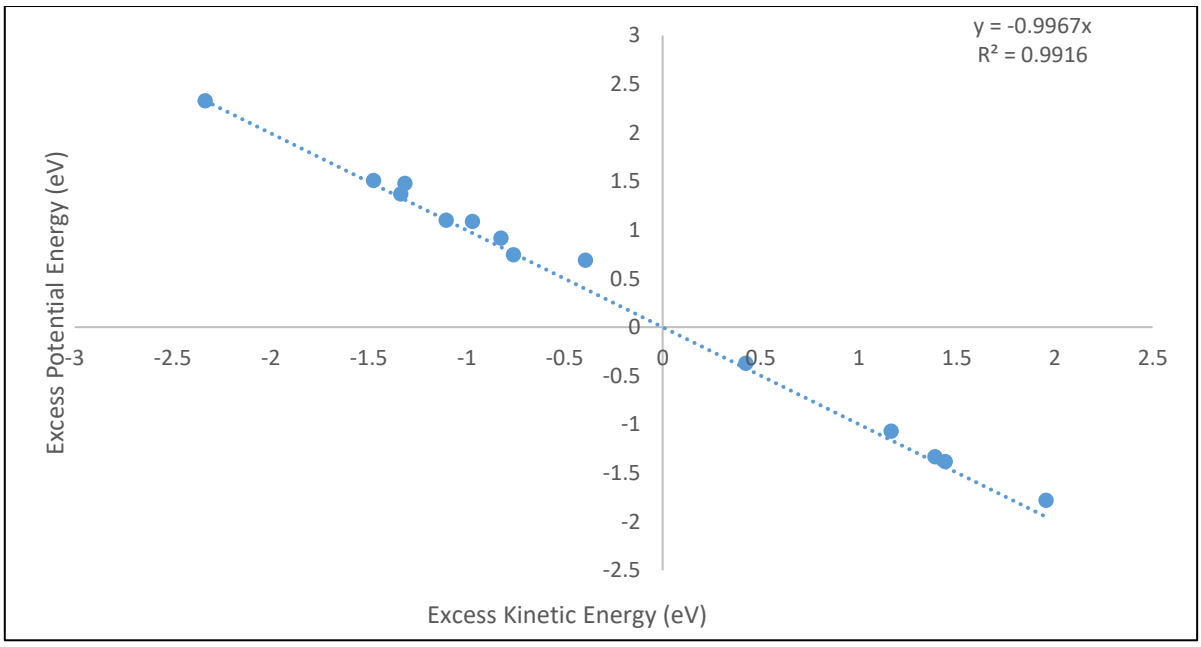

Figure A-20: Linear relationship between the excess kinetic energy and potential energy for CH_3-X interaction

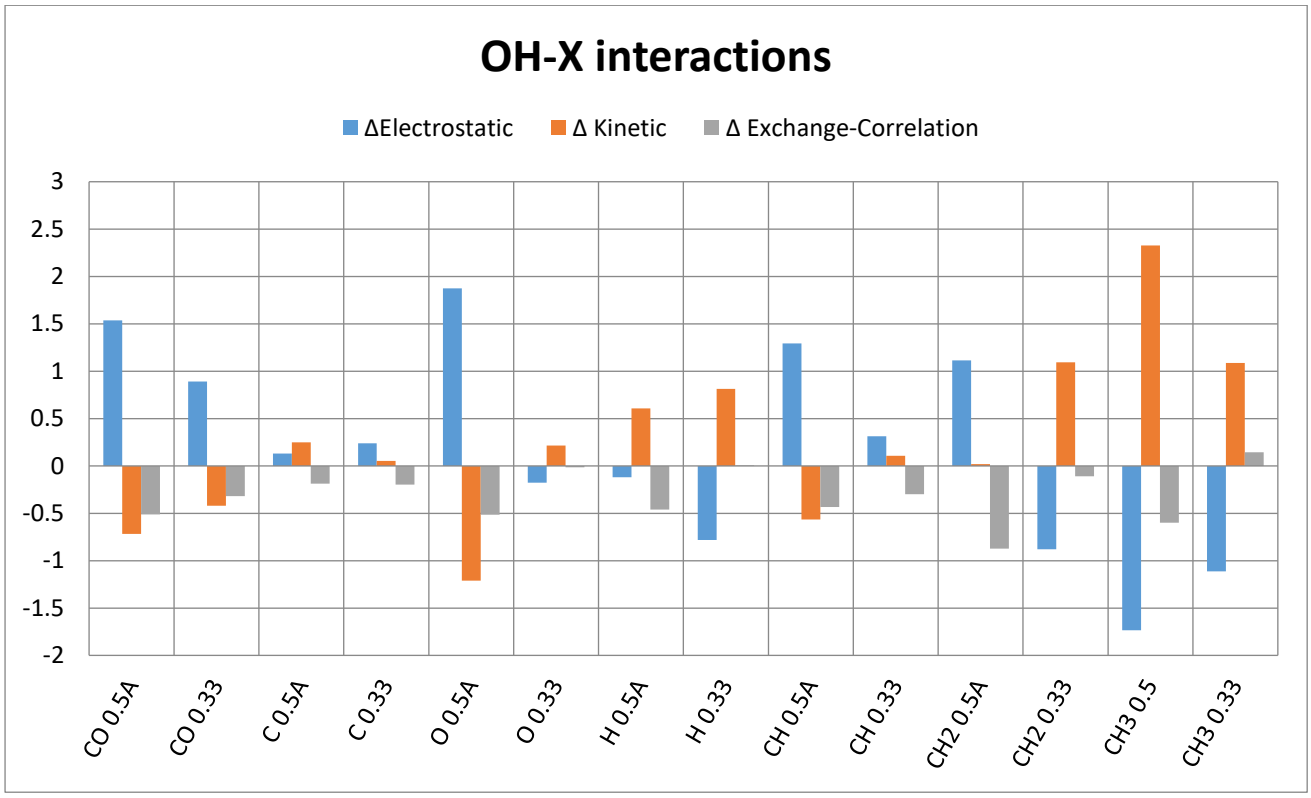

Figure A-21: The energetic breakdown of the Excess energies of OH-X interactions on Fe(100)

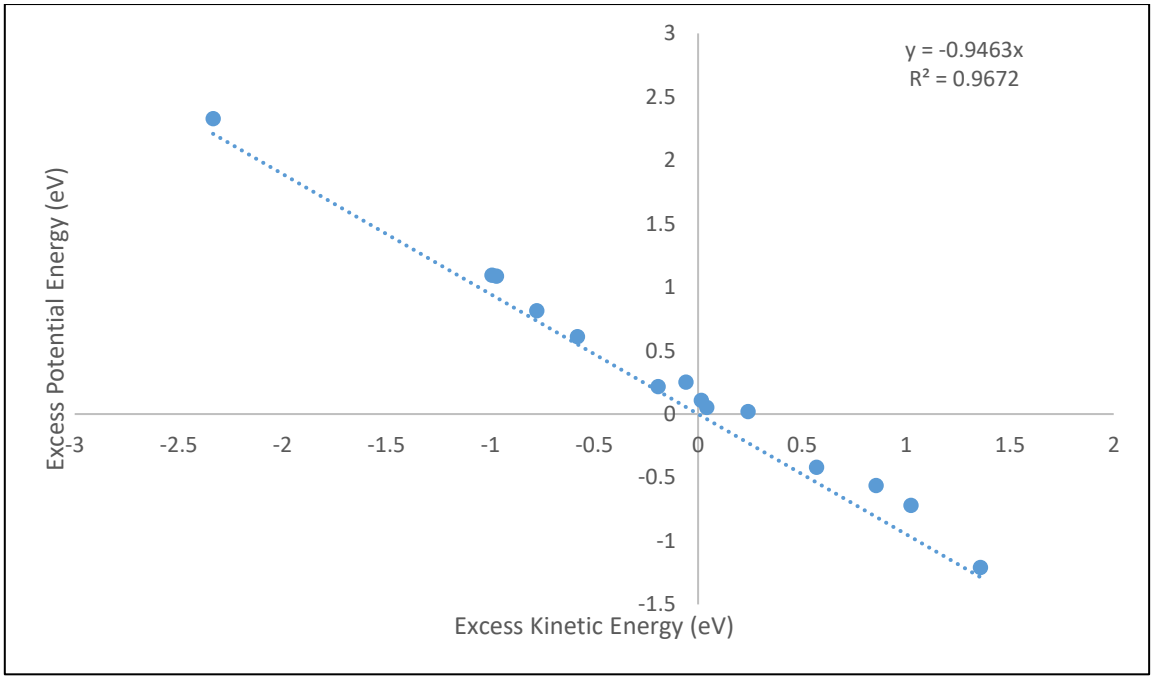

Figure A-22: Linear relationship between the excess kinetic energy and excess potential energy for OH-X interactions

Bibliography

[1] Kohn, W., Sham, L.J., *Phys. Rev.*, **140** (4A), **1965**, p. A1133–A1138.

[2] Dronskowski, R., *Computational chemistry of solid state materials*. Wiley. com, **2008**.

[3] Clark, S.J., Segall, M.D., Pickard, C.J., Hasnip, P.J., Probert, M.I.J., Refson, K., Payne, M.C., *Zeitschrift für Krist.*, **220** (5-6–2005), **2005**, p. 567–570.

[4] Payne, M.C., Arias, T. A., Joannopoulos, J.D., *Rev. Mod. Phys.*, **64** (4), **1992**, p. 1045–1097.

[5] Accelrys Software Inc., Material Studio Modeling Environment, San Diego: Accelrys Software Inc., **2010**.

[6] Hammer, B., Hansen, L., Nørskov, J., *Phys. Rev. B*, **59** (11), **1999**, p. 7413–7421.

B. Vibrational Frequencies

Obtaining the vibrational frequencies of a given configuration reveals much about the system. Firstly, they can be used to identify whether a system is a minimum, a transition state (1st order saddle point) or an unstable configuration (higher order saddle point). Once the vibrations are known the zero-point energies[27] can be calculated which improves the 0 K energy estimates [1]. Vibrations are also used to estimate temperature corrections[28].

A non-linear molecule containing N atoms will have 3N-6 vibrational modes, while a linear molecule containing N atoms will have 3N-5 vibrational modes.

The vibrational frequencies can be obtained either from molecular dynamics type calculations or by directly probing the Hessian Matrix with various algorithms. In this study a partial Hessian vibrational analysis was performed using density functional perturbation theory [3, 5]. Since the surface atoms are more ridged than the adsorbates, it is assumed that the phonons of the surface and the vibrational frequencies of the adsorbates in question can be decoupled and thus only a partial Hessian vibrational analysis is needed. This significantly reduces the complexity of the calculation much like the Born-Oppenheimer approximation reduces the complexity of solving the Schrodinger equation.

The vibrational analysis was performed using perturbations of 0.005 Å in the Cartesian space. From this analysis, we obtained the vibrational frequencies of the considered atoms.

The tables below show the vibrational frequencies (in cm^{-1}) for the configurations considered in this study with the zero-point energy corrections (in eV) in the last column. Only stable configurations that are minima were considered in this study, hence all the vibrations are positive real numbers. The 0.25 ML configurations are considered to have negligible lateral interactions, while the configurations with "Diag" in the name considered next-nearest-neighbour interactions and the other higher coverage configurations considered next-nearest neighbour interactions.

The magnitudes of the zero point energies are significant and, as discussed in literature [6], they can have a significant effect on the energy profiles. The vibrations are in good agreement with other literatures results focusing on methanation species on Fe(100) [2, 4, 6–9]**.**

By considering the vibrational frequencies of configurations which display lateral interactions and comparing them with the vibrational frequencies of the 0.25 ML configurations, argued to have little to no lateral interactions, we can estimate how the lateral interactions will change with temperature. Chapter 5 shows how the lateral interactions of each species changes with temperature.

[27] The inclusion of zero point energies implies that molecules are not completely stationary at 0 K.
[28] See section 2.5 for the incorporation of vibrations into temperature corrections

Table B-1: Vibrational frequencies of same species configurations

Name	v1	v2	v3	v4	v5	v6	v7	v8	v9	v10	v11	v12	v13	v14	v15	v16	v17	v18	v19	v20	v21	v22	v23	v24	ZPE (eV)
C 0.25 ML	494	525	526																						0.10
C 0.33 ML	496	514	533	549	557	607																			0.20
C 0.50 ML	536	538	574																						0.10
C 0.50 ML Diagonal	402	423	442	463	530	539																			0.17
C 1 ML	364	393	520																						0.08
O 0.25 ML	320	320	335																						0.06
O 0.33 ML	413	429	503	506	513	557																			0.18
O 0.50 ML	265	361	368																						0.06
O 0.50 ML Diagonal	304	307	317	327	350	358																			0.12
O 1 ML	352	382	383																						0.07
H 0.25 ML	405	414	1170																						0.12
H 0.33 ML	380	388	426	458	1121	1141																			0.24
H 0.50 ML	304	422	1150																						0.12
H 0.50 ML Diagonal	369	378	618	622	1208	1225																			0.27
H 1 ML	449	491	1153																						0.13
CO 0.25 ML	182	226	314	333	357	1177																			0.16
CO 0.33 ML	215	221	228	230	292	298	375	388	396	398	1207	1207													0.34
CO 0.50 ML	215	239	325	363	384	1208																			0.17
CO 0.50 ML Diagonal	174	174	237	242	305	305	319	329	359	373	1146	1175													0.32
OH 0.25 ML	116	297	380	502	690	3668																			0.35
OH 0.33 ML	122	157	304	312	364	378	500	502	670	674	3651	3679													0.70
OH 0.50 ML	118	313	369	511	684	3681																			0.35
OH 0.50 ML Diagonal	118	161	286	315	355	369	489	521	673	679	3653	3675													0.70
OH 1 ML	129	304	394	505	689	3676																			0.35
CH 0.25 ML	264	264	427	427	466	2949																			0.30
CH 0.33 ML	272	278	354	377	443	450	451	456	464	495	2942	2944													0.62
CH 0.50 ML	243	443	445	459	548	2946																			0.32
CH 0.50 ML Diagonal	258	285	320	331	410	453	459	461	474	532	2954	2966													0.61
CH 1 ML	353	360	497	545	546	2995																			0.33
CH2 0.25 ML	345	366	372	401	417	635	1193	2619	2677																0.56
CH2 0.33 ML	74	142	343	355	367	378	381	387	411	424	633	653	1165	1179	2561	2567	2664	2669							1.08
CH2 0.50 ML	288	352	392	430	441	734	1206	2516	2599																0.56
CH2 0.50 ML Diagonal	276	302	326	379	398	408	411	416	424	433	620	663	1174	1193	2607	2631	2660	2681							1.12
CH2 1 ML	216	283	438	627	775	882	1375	2498	2581																0.60
CH3 0.25 ML	102	110	192	336	525	531	1161	1324	1371	2758	2962	3007													0.89
CH3 0.33 ML	191	193	269	276	340	341	351	357	514	545	605	615	1081	1101	1347	1353	1380	1408	2933	2949	3025	3036	3182	3185	1.90
CH3 0.50 ML	200	266	346	360	529	606	1093	1362	1393	2933	3025	3182													0.95
CH3 0.50 ML Diagonal	90	100	215	330	508	523	1159	1303	1379	2793	2962	2990													0.89
CH3 1 ML	143	221	354	404	467	616	1087	1338	1553	3033	3114	3228													0.96

Table B-2: Vibrational frequencies of configurations with different species

	v1	v2	v3	v4	v5	v6	v7	v8	v9	v10	v11	v12	v13	v14	v15	v16	v17	v18	v19	v20	v21	v22	v23	v24	ZPE (eV)
CO + H 0.5 ML	200	276	304	337	411	504	623	1143	1243																0.31
CO + H 0.5 ML Diag	178	193	330	342	397	509	768	1221	1237																0.32
CO + H 0.33	79	256	298	320	337	406	467	1175	1228																0.28
CO + C 0.5 ML	196	316	318	347	450	496	536	620	1287																0.28
CO + C 0.5 ML Diag	181	229	330	341	358	508	541	574	1188																0.26
CO + C 0.33	237	306	371	415	499	543	583	622	1218																0.30
CO + O 0.5 ML	228	275	288	298	348	359	362	499	1303																0.25
CO + O 0.5 ML Diag	209	238	286	323	334	368	376	405	1195																0.23
CO + O 0.33	132	263	279	283	318	327	364	417	1253																0.23
CO + CH 0.5 ML	198	294	299	345	370	417	459	494	529	1250	1282	2965													0.55
CO + CH 0.5 ML Diag	200	223	246	313	338	357	370	448	465	486	1219	2967													0.47
CO + CH 0.33	207	213	227	323	354	384	441	449	451	563	1213	2944													0.48
CO + CH2 0.5 ML	196	266	279	312	325	337	379	439	453	512	727	1203	1287	2500	2702										0.74
CO + CH2 0.5 ML Diag	192	203	222	315	335	369	405	416	424	450	662	1167	1225	2594	2629										0.72
CO + CH2 0.33	232	230	296	362	395	1188	275	345	402	429	459	746	1222	2496	2605										0.72
CO + CH3 0.5 ML 3	23	52	161	212	299	319	334	362	374	418	525	1083	1293	1333	1342	2957	3024	3093							1.07
CO + CH3 0.33	46	177	239	258	326	371	425	484	585	602	738	1169	1225	1282	1389	1850	2158	3114							1.02
C + O 0.5 ML	302	342	385	503	517	618																			0.17
C + O 0.5 ML Diag	298	298	329	525	541	548																			0.16
C + O 0.33	309	393	474	495	530	605																			0.17
C + H 0.5 ML	478	494	531	533	609	1175																			0.24
C + H 0.5 ML Diag	233	256	504	559	560	1279																			0.21
C + H 0.33	508	550	572	659	718	1063																			0.25
C + CH 0.5 ML	225	280	312	461	473	556	637	1284	2627																0.42
C + CH 0.5 ML Diag	121	157	402	406	506	521	521	527	2995																0.38
C + CH 0.33	538	532	571	246	454	438	445	539	2964																0.42
C + CH2 0.5 ML	246	363	378	417	429	482	563	609	724	1201	2624	2651													0.66
C + CH2 0.5 ML Diag	246	337	368	370	412	518	532	548	630	1164	2632	2709													0.65

C + CH2 0.33	306	355	358	396	411	483	551	560	636	1191	2623	2699												0.66
	v1	v2	v3	v4	v5	v6	v7	v8	v9	v10	v11	v12	v13	v14	v15	v16	v17	v18	v19	v20	v21	v22	v23	v24	ZPE (eV)
C + CH3 0.5 ML Diag	123	173	259	321	381	487	523	528	581	1092	1321	1348	2909	2969	3101										1.00
C + CH3 0.33	535	540	587	200	252	362	350	521	605	1112	1381	1394	2935	3024	3190										1.05
O + H 0.5 ML	338	341	343	399	700	1194																			0.21
O + H 0.5 ML Diag	308	351	355	380	749	1336																			0.22
O + H 0.33	325	345	362	460	464	1161																			0.19
O + CH 0.5 ML	280	327	352	357	424	459	469	545	2939																0.38
O + CH 0.5 ML Diag	332	333	347	358	366	456	458	489	2949																0.38
O + CH 0.33	249	254	338	339	378	418	437	470	2947																0.36
O + CH2 0.5 ML	239	250	274	306	325	369	381	540	595	1278	2900	2931													0.64
O + CH2 0.5 ML Diag	151	337	360	372	393	400	405	432	675	1168	2597	2634													0.62
O + CH2 0.33	293	370	406	440	440	443	445	460	717	1206	2501	2591													0.64
O + CH3 0.5 ML Diag	281	342	385	195	270	351	365	542	606	1110	1362	1374	2931	3033	3169										1.01
O + CH3 0.33	279	363	357	206	258	332	342	522	593	1112	1374	1375	2939	3027	3182										1.01
H + CH 0.5 ML	234	276	349	441	450	465	548	1204	2936																0.43
H + CH 0.5 ML Diag	270	278	370	373	461	469	471	1299	2945																0.43
H + CH 0.33	252	306	415	426	429	474	558	1156	2939																0.43
H + CH2 0.5 ML	290	364	395	438	452	753	1216	2520	2593	300	435	1165													0.68
H + CH2 0.5 ML Diag	287	388	395	409	412	474	596	666	1167	1200	2522	2684													0.69
H + CH2 0.33	286	370	376	432	449	748	1208	2499	2593	321	440	1151													0.67
H + CH3 0.5 ML Diag	311	405	1164	211	269	359	342	530	621	1075	1350	1389	2919	3043	3201										1.07
H + CH3 0.33	305	404	1168	204	255	331	361	527	599	1078	1380	1382	2926	3034	3169										1.06
CH + CH2 0.5 ML	299	371	414	417	419	459	463	482	515	606	725	1208	2582	2608	2932										0.90
CH + CH2 0.5 ML Diag	279	294	317	384	388	392	436	455	456	494	669	1188	2599	2699	2956										0.87
CH + CH2 0.33	295	334	397	419	447	724	1222	2502	2599	244	461	427	455	543	2945										0.87
CH + CH3 0.5 ML Diag	202	286	355	356	534	608	1097	1380	1404	2913	3042	3183													0.95
CH + CH3 0.33	198	259	345	352	539	613	1077	1378	1374	2930	3034	3167													0.95
CH2 + CH3 0.5 ML	212	259	271	354	367	371	401	424	453	519	617	747	1084	1220	1343	1411	2510	2601	2948	3038	3170				1.51
CH2 + CH3 0.5 ML P	202	271	274	338	362	363	400	427	455	525	587	744	1083	1202	1353	1382	2502	2598	2948	3007	3170				1.50

CH2 + CH3 0.33	211	257	298	333	333	354	401	419	454	535	616	730	1079	1225	1373	1392	2524	2600	2916	3026	3193			1.50

	v1	v2	v3	v4	v5	v6	v7	v8	v9	v10	v11	v12	v13	v14	v15	v16	v17	v18	v19	v20	v21	v22	v23	v24	ZPE (eV)
OH + H 0.5 ML	103	257	320	341	424	446	685	1175	3648																1.50
OH + H 0.5 ML Diag	92	268	299	360	442	452	668	1135	3630																0.46
OH + H 0.33	88	258	323	345	434	460	652	1136	3632																0.46
OH + C 0.5 ML	70	262	329	494	546	550	575	642	3642																0.45
OH + C 0.5 ML Diag	111	267	327	471	522	538	558	649	3622																0.44
OH + C 0.33	99	284	373	492	514	558	584	689	3640																0.44
OH + O 0.5 ML	81	269	295	334	354	398	461	644	3661																0.45
OH + O 0.5 ML Diag	67	260	263	366	374	393	469	639	3636																0.40
OH + O 0.33	103	253	295	359	361	404	486	670	3654																0.40
OH + CO 0.5 ML	89	203	257	270	337	343	360	383	482	668	1217	3622													0.41
OH + CO 0.5 ML Diag	104	212	226	276	323	363	363	378	465	648	1203	3628													0.51
OH + CO 0.33	104	214	251	271	342	349	352	386	480	676	1222	3626													0.51
OH + CH 0.5 ML	91	251	272	353	428	457	457	469	519	651	2937	3628													0.51
OH + CH 0.5 ML Diag	108	245	272	341	421	458	470	475	532	639	2934	3615													0.65
OH + CH 0.33	92	243	246	338	442	446	461	476	546	637	2955	3627													0.65
OH + CH2 0.5 ML	67	254	267	355	366	376	430	445	461	649	734	1205	2526	2589	3656										0.65
OH + CH2 0.5 ML Diag	105	266	276	355	364	375	405	450	463	652	708	1196	2544	2616	3642										0.89
OH + CH2 0.33	97	270	292	360	361	385	428	467	473	635	727	1197	2545	2599	3621										0.89
OH + CH3 0.5 ML 3	88	191	243	260	341	345	356	451	521	584	649	1083	1365	1428	2912	3036	3205	3651							0.90
OH + CH3 0.33	95	193	250	257	340	350	373	479	516	576	672	1071	1347	1414	2937	3039	3198	3634							

References

[1] Govender, A., Ferré, D.C., Niemantsverdriet, J.W.H., *Chemphyschem*, **13** (6), **2012**, p. 1591–6.

[2] Bromfield, Ferré, D.C., Niemantsverdriet, J.W., *Chemphyschem*, **6** (2), **2005**, p. 254–60.

[3] Baroni, S., *Phys. Rev. Lett.*, **58** (18), **1987**, p. 1861.

[4] Govender, A., *Towards a mechanism for the Fischer-Tropsch synthesis on Fe(100) using Density Functional Theory*. Eindhoven University of Technology, **2010**.

[5] Gonze, X., *Phys. Rev. A*, **52** (2), **1995**, p. 1086.

[6] Govender, A., Ferré, D.C., Niemantsverdriet, J.W.H., *Chemphyschem*, **13** (6), **2012**, p. 1583–90.

[7] Sorescu, D., *Phys. Rev. B*, **73** (15), **2006**, p. 155420.

[8] Sorescu, D.C., *Catal. Today*, **105** (1), **2005**, p. 44–65.

[9] Sorescu, D., Thompson, D., Hurley, M., Chabalowski, C.., *Phys. Rev. B*, **66** (3), **2002**, p. 35416.

C. Methanation profiles

Several literature studies have used VASP to explore the adsorptions of methanation species and their reaction energies on Fe(100) [1–6]. Even though the same computational package was used the functionals, approximations and unit cell parameters should also be considered.

Table C-2: Details of computational methods used in studies by Govender [2, 3], Bromfield et al. [1] and Sorescu [4–6].

	Govender et al. [2,3]/ Bromfield et al. [1]	**Sorescu [4-6]**
Electron-ion interaction	Projector-augmented waves (PAW)	PAW and USPP
Code	VASP	VASP
Functional	PW91	PW91 and PBE
Kinetic energy cut off	400 eV	495 eV (usPP) 400 eV (PAW)
Exchange correlation energy	GGA	GGA
k-point setting	5x5x1 for p(2x2)	4x4x2 for p(2x2)
Smearing width	$\sigma \leq 0.1$ eV	$\sigma = 0.1$ eV
Vacuum thickness	10 Å	10 Å
Spin polarized	✓	✓
Slab approximations	4-layer slab (1 relaxed)	7-layer slab (2 relaxed)
Vibrational analysis	✓	✓

Bromfield / Govender VASP PW91 PAW [1–3]

Bromfield et al. [1] looked at the adsorption of CO on Fe(100) as well as the dissociation of CO to C and O on the surface. The study also considers different configurations of C and O after CO is dissociated. Much like in this study the next-nearest-neighbour configuration shows lower repulsions than nearest-neighbour interactions.

Govender [2] used the same computational method and parameters to investigate the successive hydrogenation of C to CH_4. This study also showed the effect of including the zero-point correction energies of the energy profile.

Govender [3] then completed the study by considering the formation of water from O and H on Fe(100), the study confirmed that $OH^* + OH^* \leftrightarrow H_2O^* + O^*$ is the energetically favour pathway for water formation and not successive hydrogenation of O.

All three studies include the vibrational frequencies of the configurations considered

Sorescu VASP PW91 USSP [4–6]

Sorescu [6] conducted an in depth study on the adsorption, diffusion and dissociation of CO on Fe(100). The study considered the PBE functional as well as the PW 91 function. To investigate the dissociation of CO, the process was broken into 18 successive configurations and the energetic changes at each step is determined. A clearly maximum can be seen, which relates to the transition state of the reaction.

Sorescu [5] then looked at the adsorption, diffusion and dissociation of Hydrogen on Fe(100). The study confirmed that hydrogen undergoes dissociative adsorption on Fe(100). Two methods of dissociative adoption were considered, one where H adsorbs on the bridge site and one where H is adsorbed in the hollow site. The processes were broken into several configurations and the energetic profiles were determined. The study also considered diffusion of hydrogen into the surface.

Sorescu [4] completed the study with by looking at the adsorption of methanation species on Fe(100) as well as the reaction energies for each hydrogenation steps. Like in the previous studies, the reactions were broken into several configurations and the energy profile can be mapped out. The diffusion of C into the surface was also considered in this study. The study also considered the C-X next-nearest-neighbour interactions and showed that they are mostly attractive.

Handling data gaps

Table C-2 shows the reaction energies of the reactions in question. The Govender / Bromfield profile did not explicitly investigate the adsorption of hydrogen. In this case the 0 K energies from Sorescu work was used. Sorescu did not explicitly investigate water formation and in this case the 0 K energies from Govender was used. In both cases, however the vibrational analysis was comprehensive and thus the ZPE and temperature correction profiles were completed using the studies own vibrations

Table C-2: Comparison of Gibbs free energy of reaction calculated in this study (USPP-RPBE) with the other studies as well as the energy barrier for the forward reaction from other studies

	Reaction	ΔG (eV)			E_{FWD} Barrier		
		CASTEP RPBE USSP Present Work	**VASP PW91 PAW** [1–3]	**VASP PW91 USSP** [4–6]	**CASTEP RPBE USSP** Present Work	**VASP PW91 PAW** [1–3]	**VASP PW91 USSP** [4–6]
Adsorption	$CO + * \leftrightarrow CO*$	-1.88	-2.53	-2.03	-	-	-
	$H_2 + 2* \leftrightarrow 2H*$	-0.63	-	-0.62	0.08	-	0.09
CO-dissociation	$CO* + * \leftrightarrow C* + O*$	-0.84	-0.33	-0.46		1.11	1.06
Hydrogenation	$C* + H* \leftrightarrow CH*$	0.07	0.41	0.13		0.76	0.63
	$CH* + H* \leftrightarrow CH_2*$	0.72	0.64	0.58		0.75	0.65
	$CH_2* + H* \leftrightarrow CH_3*$	0.36	0.38	0.39		0.86	0.85
	$CH_3* + H* \leftrightarrow CH_4*$	-0.76	-0.12	-0.17		0.71	0.50
	$O* + H* \leftrightarrow OH*$	0.89	0.52	-		1.14	-
	$OH* + 2H* \leftrightarrow H_2O*$	0.64	0.94	-		1.1	-
Desorption	$CH_4* \leftrightarrow CH_4 + *$	0.08	0.05	0.02		-	-
	$H_2O* \leftrightarrow H_2O + *$	0.14	0.43	-		-	-
Preferred H20 formation	$OH* + OH* \leftrightarrow H_2O* + O*$	0.65	0.61			0.65	

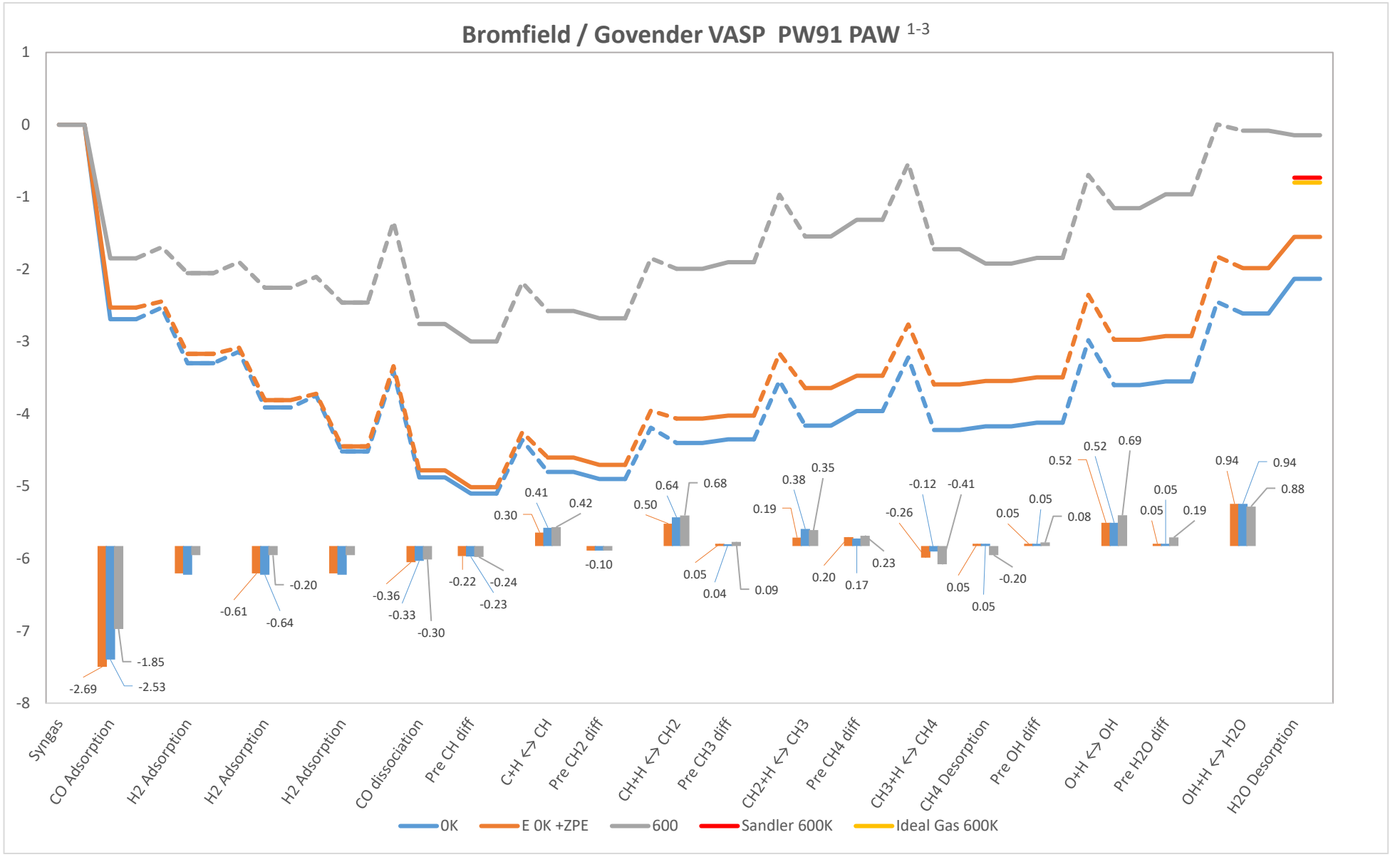

Figure C-1: energy profile for the methanation of syngas VASP PW91 PAW.

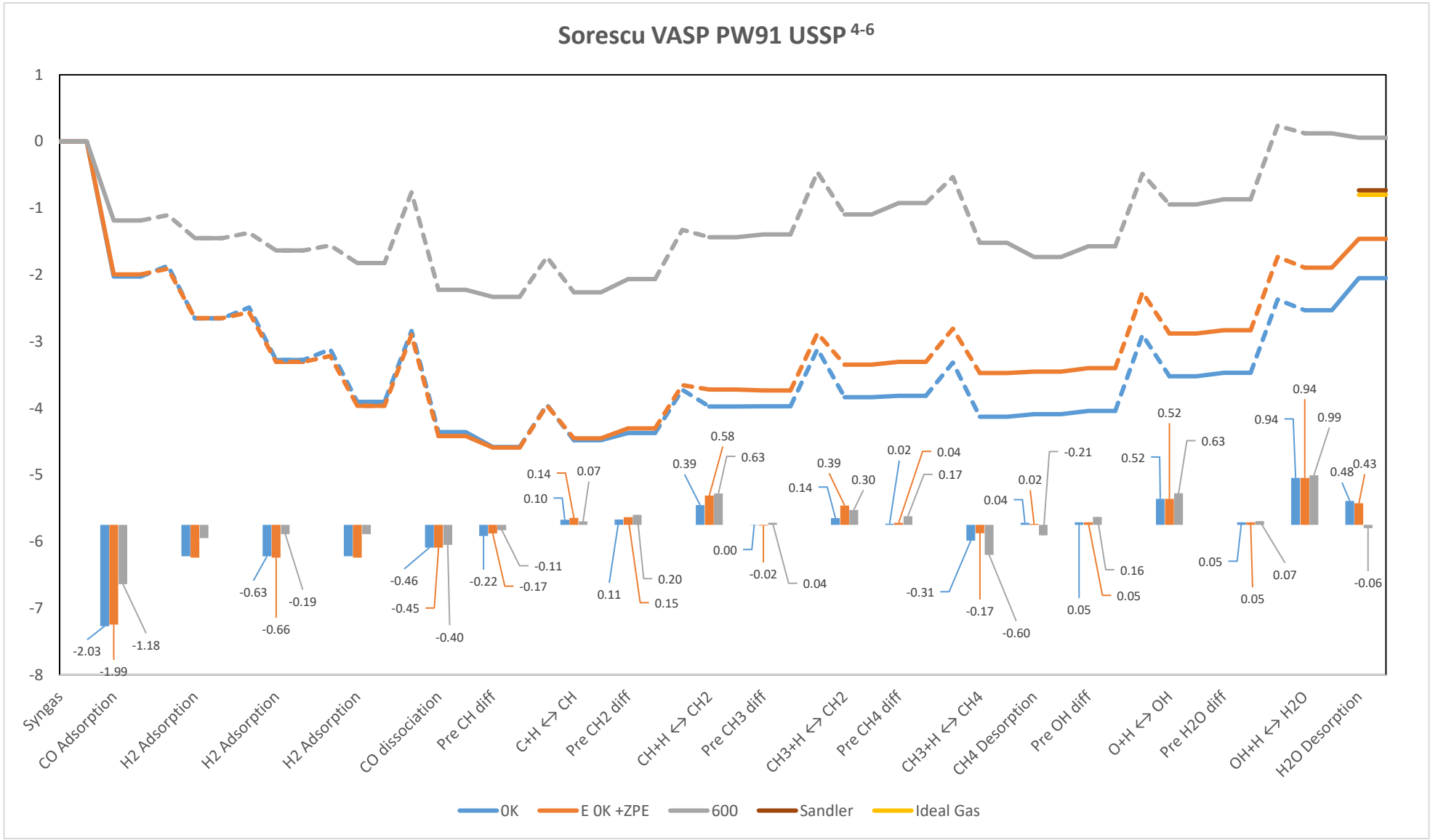

Figure C-2: energy profile for the methanation of syngas VASP PW91 PAW.

It should be noted that even though the overall change in energy is far away from the experimental results or even the ideal gas approximation, the largest sources of error in these calculations is the approximation of the gas phase. This is also why the largest differences between the literature work is for the adsorption energies. Variations in CO adsorption are as much as 0.6 eV. Furthermore, the physisorption of CH_4 on Fe(100) is not completely understood at a molecular level.

An additional source of error could be the approximations of temperature corrections using vibrational entropies and enthalpies. Even though individual errors may be small, a large amount of systems is considered and the errors accumulate.

References

[1] Bromfield, T.C., Ferré, D.C., Niemantsverdriet, J.W., *Chemphyschem*, **6** (2), **2005**, p. 254–60.

[2] Govender, A., *Towards a mechanism for the Fischer-Tropsch synthesis on Fe(100) using Density Functional Theory*. PhD thesis, Eindhoven University of Technology, **2010**.

[3] Govender, A., Ferré, D.C., Niemantsverdriet, J.W., *Chemphyschem*, **13** (6), **2012**, p. 1583–90.

[4] Sorescu, D., *Phys. Rev. B*, **73** (15), **2006**, p. 155420.

[5] Sorescu, D.C., *Catal. Today*, **105** (1), **2005**, p. 44–65.

[6] Sorescu, D. et al., *Phys. Rev. B*, **66** (3), **2002**, p. 35416.

Acknowledgements

Creating and writing this thesis would not be possible without the guidance, discussions and support from the following people and institutions.

I would like to thank my supervisor Prof. Eric van Steen for his guidance, patience and tutelage. Thank you for the opportunity to learn. I will never forget the endless sessions of back and forth “question and answer“ -ing.

My parents, Kevin and Fatima, for their support and guidance. While they may not have always understood my decisions and reasons, they have always supported me.

Peter van Helden, Jan Albert van den Berg, Melissa Peterson and Werner Janse van Rensburg for providing me with skills and knowledge to carry out the calculations in this work. They set the example for good practice.

Fellow engineering students Thaabit Nacerodian and Linus Naik and fellow molecular modelling students, Molefi Matsutsu, Junaide Karim, Thobani Gambu, Tracey van Heerden and Chris de Vries for their support and discussion.

The Centre for high performance computing (CHPC) for making the resources available for large calculations required in this work.

I would also like to thank the financial sponsors Sasol, the National Research Foundation and the University of Cape Town. Without them this project would not be possible.